# Modification of Titania Films by Chemical Vapour Deposition for Enhanced Photocatalysis

This thesis is submitted in partial fulfilment of the requirements for the Degree of Doctor of Philosophy (Chemistry).


**Carlos Sotelo-Vazquez**

*Supervised by Prof. Ivan P. Parkin*

**UCL**

**2016**

I, Carlos Sotelo-Vazquez confirm that the work presented in this thesis is my own. Where information has been derived from other sources, I confirm that this has been indicated in the thesis.

## Abstract

Titanium dioxide ($TiO_2$) is the leading material for self-cleaning applications due to its intrinsic properties, such as chemical inertness, mechanical robustness, high photocatalytic activity and durability to extend photocatalytic cycling. However, its *relatively* wide bandgap limits its outdoor applications. There has been a strenuous effort to try and improve the photocatalytic efficiency of $TiO_2$, in particular by modifying its electronic structure to enhance its function under solar illumination. The most commonly studied approaches for achieving this have been to incorporate anionic and/or cationic species into the $TiO_2$ structure and the design of $TiO_2$-based heterojunction systems.

The addition of nitrogen, phosphorus and sulfur species into the matrix of $TiO_2$ was investigated. Films were grown using atmospheric-pressure chemical vapour deposition (APCVD). The nitrogen-doped system has been investigated most prominently to enhance and extend the photocatalytic response of $TiO_2$ materials into the visible region of the electromagnetic spectrum. Nitrogen can either replace oxygen sites ($N_s$, substitutional doping) or sit within the $TiO_2$ structure ($N_i$, interstitial doping) and form N-O groups with lattice oxygen. Interestingly, these $NO_x$ groups, as well as $NH_x$ surface species present similar binding energies, *ca*. 400 eV, hindering the identification of the nitrogen species and their role in the photocatalytic response of the material. Various synthesis conditions were experimented using different nitrogen precursors (*tert*-butylamine, benzylamine and ammonia), which were used to establish a correlation between surface and bulk nitrogen species and the photocatalytic behaviour of the N-$TiO_2$ films. A loss of the $N_i$ environment (as observed by X-ray photoelectron spectroscopy), as well as a decrease in photoactivity over time was observed, suggesting a direct participation of the nitrogen species in photocatalytic

processes. In addition to traditional CVD methods, a pulse precursor approach was used for the first time, to the best of our knowledge, to synthesise stratified N-doped $TiO_2$ thin films, by adding nitrogen into specific regions of the N-$TiO_2$ film. Physical and functional comparison of stratified and non-stratified N-$TiO_2$ films with similar structural and morphological features allowed us to evaluate the benefits of this synthetic approach, which not only resulted in an increase in the photocatalytic efficiency of the stratified N-$TiO_2$ films but also did not affect the overall crystallinity of the films. The addition of phosphorus and sulfur was investigated as the most promising alternative to the use of nitrogen doping, as both could be added to the lattice of $TiO_2$ either as cations or anions. Through functional testing, it was found that both dopant species were beneficial from a photocatalytic point of view. Interestingly, the use of APCVD techniques to deposit P-$TiO_2$ thin films resulted in the addition for the first time, to the best of our knowledge, of $P^{3-}$ species, as well as $P^{5+}$, to the $TiO_2$ structure with the relative proportion being determined by the synthesis conditions. Through Hall effect probe, photocatalytic testing and transient absorption spectroscopy (TAS) analyses, it was found that the incorporation of $P^{3-}$ species was detrimental from an electrical conduction and photocatalytic point of view; however, the presence of solely $P^{5+}$ species resulted in P-$TiO_2$ films with enhanced self-cleaning and TCO properties. These results provide important insights on the influence of dopant nature and its location within a semiconductor's structure.

Heterojunction semiconductor materials are used in a wide range of applications including catalysis, electronic devices, sensors and solar-to-chemical energy conversion. These materials benefit from effective electron transfer processes, electron tunnelling, surface passivation and other synergistic effects to enhance their performance beyond the individual components. By using CVD methods, two different

heterojunction systems, rutile/ anatase $TiO_2$ and $WO_3/TiO_2$, were grown. The interposition of an amorphous $TiO_2$-based interlayer allowed direct vapour deposition of anatase on a rutile substrate, which is otherwise hindered by templating. The subsequent crystallisation of the amorphous interlayer after annealing, allowed us to investigate the impact of an efficient interface between the two rutile-anatase phases in the photodegradation of an organic model pollutant, stearic acid. Clear evidence on the synergy between the two polymorphs and more importantly, on the charge flow across the interface, which is against much conventional understanding, was evaluated through the photoreduction of silver particles. This charge flow involves electron transfer from rutile to anatase. Likewise, a conformal coating of $WO_3$ nanorods with $TiO_2$ was performed using APCVD techniques. The resulting $WO_3/TiO_2$ heterojunction films showed an electron transfer phenomenon, where electrons moved from $WO_3$ into $TiO_2$, against widely reported observation. State-of-the-art hybrid density functional theory (DFT) and hard X-ray photoelectron spectroscopy (HAXPES) were employed to elucidate the electronic interaction at the heterojunction of the $WO_3$ and $TiO_2$ crystalline phases. This vectorial charge separation reduces electron-hole recombination and most likely extends the lifetime and relative population of photogenerated charges. These results provide important insights on the influence of vectorial charge separation in heterojunctions. These phenomena had a dramatic impact on the photocatalytic efficiency of the heterojunction films, which are among the very highest ever reported by a thin film.

# List of publications

**Publications related to the work presented in this thesis.**

- Carlos Sotelo-Vazquez, Raul Quesada-Cabrera, Min Ling, David O Scanlon, Andreas Kafizas, Pardeep Kumar Thakur, Tien-Lin Lee, Alaric Taylor, Graeme W. Watson, Robert G Palgrave, James R. Durrant, Chris Blackman, Ivan P Parkin, *'Evidence and effect of photogenerated charge transfer for enhanced photocatalysis in WO3/TiO2 heterojunction films: a computational end experimental study'. Advanced Functional Materials*, **2017**, 1605413.
- Raul Quesada-Cabrera, Carlos Sotelo-Vazquez, Miguel Quesada-Gonzalez, Elisenda Pulido Melian, Nicholas Chadwick, Ivan P. Parkin, *'On the apparent visible-light and enhanced UV-light photocatalytic activity of nitrogen-doped TiO2 thin films'. Journal of Photochemistry and Photobiology A: Chemistry*, **2017**, 333, 49.
- Carlos Sotelo-Vazquez, Nuruzzaman Noor, Andreas Kafizas, Raul Quesada-Cabrera, David O Scanlon, Alaric Taylor, James R Durrant, Ivan P Parkin, *'Multifunctional P-Doped TiO2 Films: A New Approach to Self-Cleaning, Transparent Conducting Oxides Materials'. Chemistry of Materials*, **2015**, 27, 3234.
- Raul Quesada-Cabrera, Carlos Sotelo-Vazquez, Jawwad A Darr, Ivan P Parkin, *'Critical influence of surface nitrogen species on the activity of N-doped TiO2 thin-films during photodegradation of stearic acid under UV light irradiation'. Applied Catalysis B: Environmenta*l, **2014**, 160-161, 582.
- Raul Quesada-Cabrera, Carlos Sotelo-Vazquez, Joseph C Bear, Jawwad A Darr, Ivan P Parkin, *'Photocatalytic Evidence of the Rutile-to-Anatase Electron Transfer in Titania'. Adv. Mater. Interfaces*, **2014**, 1, 1400069.
- Carlos Sotelo-Vazquez, Raul Quesada-Cabrera, Jawwad A Darr, Ivan P Parkin, *'Single-step synthesis of doped TiO2 stratified thin-films by atmospheric pressure chemical vapour deposition'. J Mater. Chem. A*, **2014**, 2, 7082.

**Other publications**

- Min Ling, Christopher S. Blackman, Robert G. Palgrave, Carlos Sotelo-Vazquez, Andreas Kafizas, Ivan P. Parkin, '*Correlation of Optical Properties, Electronic Structure, and Photocatalytic Activity in Nanostructure Tungsten Oxide*' *Advanced Materials Interface*, **2017**, DOI: 10.1002/admi.201700064.
- Nicholas Chadwick, Sanjayan Sathasivam, Carlos Sotelo-Vazquez, Salem Bawaked, Mohamed Mokhtar, Sulaiman Nasir Basahel, A. Y. Obaid, Claire J. Carmalt, Ivan P. Parkin, '*Dopant stability in multifunctional doped $TiO_2$'s under environmental UVA exposure*' *Envromental Science: Nano*, **2017**, Advance article DOI: 10.1039/C7EN00061H.
- Andreas Kafizas, Laia Francas, Carlos Sotelo-Vazquez, Min Ling, Yaomin Li, Emily Glover, Liam McCafferty, Christopher S. Blackman, Jawwad A. Darr, Ivan P. Parkin, *'Optimizing the activity of nano-needle structured $WO_3$ photoanodes for solar water splitting – Direct synthesis via chemical vapor deposition'. The Journal of Physical Chemistry C*. **2017**, DOI: 10.1021/acs.jpcc.7b00533.

- Nicholas Chadwick, Andreas Kafizas, Raul Quesada-Cabrera, Carlos Sotelo-Vazquez, Salem Mohammed Bawaked, Mohamed Mokhtar, Shaeel A. Al Thabaiti, A. Y. Obaid, Sulaiman Nasir Basahel, James R. Durrant, Claire J. Carmalt, Ivan P. Parkin, *'Ultraviolet radiation induced dopant loss in a $TiO_2$ photo-catalyst'*. *ACS Catalysis*, **2017**, DOI: 10.1021/acscatal.6b03170.
- Stella Vallejos, Nadezda Pizurova, Isabel Gracia, Carlos Sotelo-Vazquez, Jan Cechal, Christopher Blackman, Ivan Parkin, Carles Canes, *'ZnO nanorods with exposed {100} facets grown via a self-catalysed vapour solid mechanism, and their photocatalytic and gas sensing properties'*. *ACS Applied Materials & Interfaces*, **2016**, 8, 33335.
- Sultan Ben-Jaber, William J. Peveler, Raul Quesada-Cabrera, Emiliano Cortes, Carlos Sotelo-Vazquez, Nadia Abdul-Karim, Stefan A. Maier, Ivan P. Parkin, *'Photo-Induced Enhanced Raman Spectroscopy for Universal Ultra-trace Detection of Explosives, Pollutants and Biomolecules'*. *Nature Communications*, **2016**, 7, 12189.
- Andreas Kafizas, Xiuli Wang, Stephanie R Pendlebury, Piers Barnes, Min Ling, Carlos Sotelo-Vazquez, Raul Quesada-Cabrera, Can Li, Ivan P Parkin, James R Durrant, *'Where Do Photogenerated Holes Go in Anatase:Rutile TiO2? A Transient Absorption Spectroscopy Study of Charge Transfer and Lifetime'*. *The Journal of Physical Chemistry A*, **2016**, 120, 715.
- Sacha Noimark, Kristopher Page, Joseph C Bear, Carlos Sotelo-Vazquez, Raul Quesada-Cabrera, Yao Lu, Elaine Allan, Jawwad A Darr, Ivan P Parkin, *'Functionalised gold and titania nanoparticles and surfaces for use as antimicrobial coatings'*. *Faraday Discuss*, **2014**, 175, 273.

## Acknowledgements

First and foremost, I would like to thank my supervisor Prof. Ivan P. Parkin for his guidance, support and advice throughout my PhD. I couldn't have asked for a more supportive or helpful supervisor. It has been a great experience to work with you, I have learnt a lot from you in the past three years. I would also like to thank my second supervisor Prof. Jawwad A. Darr for all the help, advice and discussions.

I am very grateful to Dr. Raul Quesada-Cabrera for all the help, guidance and long hours and chats shared during my first steps at UCL, but especially I would like to say thank you for the friendship and good moments shared during these years. I am also very grateful to Dr. Andreas Kafizas for the discussions and help (especially with the TAS measurements and data interpretation), advice and friendship shared over the last three years. I am thankful to Dr. Chris Blackman for all the help and useful discussions during these years, I especially appreciate all the help during the last year related to our $WO_3/TiO_2$ heterojunction system work. I would like to thank Mr. Min Ling for all the help synthesising the $WO_3$ nanorods and for the TEM image borrowed in chapter 5. I am also very grateful to Dr. David O. Scanlon for all the advice, discussions and help (especially with the theoretical studies presented in this thesis). I am thankful to Dr. Allison Cross for all her help during the start of my PhD. I would like to thank Mr. Alaric Taylor for all the help with the AFM measurements and all the discussions and good moments shared. Finally, I would like to thank Dr. Pardeep Kumar Thakur and Dr. Tien-Lin Lee for assistance with the HAXPES measurements at the Diamond Lab.

I would like to say a huge thank you to all the staff of the chemistry department who have helped me during the past three years. In particular, I would like to thank Dr. Steve Firth for assistance and chats during Raman, SEM and TEM analyses; Mr. Martin Vickers for assistance with XRD analysis; Mr. Joe Nolan and Mr. Tom Bridges for all the help and assistance fixing the APCVD rig.

Special thanks to Nadia, Francesco, Nuru, Diana, Min, Sanjay, Miguel, Mark and all other friends in offices 320 and 310; your friendship and laughs have made the past years so special. I couldn't finish without saying that this thesis wouldn't have been possible without the *tripod*, you guys will be always in my heart and you became my family. Special thanks to my parents, grandparents, aunt, uncle and the two *little* cousins, for all your support and help. And last but no least special thanks to Azu, you know I couldn't have done all this without you, your constant support and encouragement helped me to go through all those difficult moments.

## Table of Contents

Chapter I

# INTRODUCTION

*"The following chapter presents the aim and motivation of this project, using photocatalysis for water treatment remediation. In this chapter, a brief introduction and historical review of $TiO_2$ photocatalysis and its potential new photocatalytic applications is presented. This chapter introduces the basics and principles of chemical vapour deposition techniques, which was used in the synthesis of the photocatalytic materials produced for the thesis."*

# 1. Introduction.

This thesis aims to explore and develop a method to enhance the photocatalytic properties of titanium dioxide ($TiO_2$) coatings, which will be used inside a photoreactor to purify wastewater in South East Asia from palm oil industries. In this thesis, the enhancing of the $TiO_2$ functionality will be investigated by using three different approaches, including chemical modification, coupling two dissimilar semiconductors and through the nanostructuring of metal oxides. The chemical modification of $TiO_2$ will be explored by adding different non-metal species, such as nitrogen, phosphorus and sulfur, to the $TiO_2$ structure, allowing us to acquire a better understanding of their effect on the photocatalytic performance of $TiO_2$ films. In addition, the coupling and nanostructuring of $TiO_2$-based semiconductors will be also investigated to identify and optimise the most beneficial approach for enhanced photocatalysis of $TiO_2$-based films.

## 1.1. Principles and aims of this thesis: The PCATDES project.

While the amount of fresh water on the planet has remained relatively constant over time, continually recycled through the atmosphere and back onto the earth, the human population has dramatically grown, increasing water demand. The shortage of clean water sources due to the rapid development of industrialisation and metropolitan areas has led to shortages that are exacerbated by droughts.

All this has made access to drinking water a major issue that needs to be solved by both developing and developed worlds. The amount of fresh water available to the world population represents only 2.5 % of all water on the planet. It is worth noting that most of this fresh water is trapped in glaciers and snowfields, leaving only 0.007 % of the planet's fresh water available to be used by human beings. It has been estimated that around 4 billion people worldwide have little to no access to clean and sanitised water

resources.[1] This world scenario is expected to get worse, due to the increase of industrialisation and farming, which will deliver micropollutants and contaminants into the natural water cycle.[2] All this has led to a vast investigation to optimise and improve water treatment processes. The wastewater problem could be addressed by using conventional water treatment methods, but they are highly expensive and energy intensive,[3] making them largely inaccessible in developing countries. Therefore, highly efficient and low cost water treatment technologies must be developed and optimised to address the fresh water shortage.

The most common approach to treat water consists of a two-step process, where firstly the contaminated wastewater is treated by separation, to decrease the amount of contaminants, and subsequently treated by biological degradation. These are cheap and effective methods that can reduce 95 % of water contaminants. However, there is a remaining 5 % of organic pollutants commonly named *recalcitrant* material, whose removal is challenging.[4] This *recalcitrant* matter includes humic and palmitic acid, as well as oleic and linoleic triglycerides. Therefore, further treatment processes are necessary to completely clean wastewater deposits. Currently there are different water treatment processes to destroy these remaining organic contaminants: ozonation, membrane bioreactors, electrocatalytic treatment and chlorination are the most common:

i. Ozonation consists of the oxidation of organic components by pumping ozone into the water stream. The very short half-life of ozone requires on-site production through a low efficiency process and consequently requires high investment and operational costs.
ii. Membrane reactors are intrinsically less energy intensive, however, these systems are affected by membrane fouling, increasing significantly the

hydraulic resistance of the system.[5,6] These systems require frequent membrane cleaning and maintenance processes, adding significant operational costs to the water treatment process. Therefore, this approach would be unsuitable for very high throughput systems.

iii. Electro-catalytic oxidation processes are based on the injection of suitable biological and chemical catalysts into the wastewater stream together with a concentrated oxygen source, creating an aerated water stream.[7,8] This stream is subsequently electrolysed using a controlled direct current. This water treatment approach has shown the highest efficiency to purify wastewater, but is highly expensive and energy intensive. Thus, its application is not affordable for small scale producers.

iv. Chlorination has been the most commonly and widely used water treatment method in the last decades to decontaminate wastewater streams. Unfortunately, this disinfection method generates mutagenic and carcinogenic by-products.[9]

Despite the fact that these treatment methods can remove the *recalcitrant* matter from wastewater streams, they are energy intensive and relatively expensive to meet the legislative and policy standards of Southern Eastern Asian countries.[10] In addition, small palm oil mills and olive oil pressing industries, as well as smaller scale fish farming businesses which are ubiquitous to South East Asia, as well as Southern Europe, are often situated in rural areas where power is scarce and/or expensive, making people unable to access drinking water. Therefore, there is a clear need to develop and implement cost-effectiveness and mobile water treatment technologies.[11] This could be addressed by using photocatalysis to treat wastewater streams. In the last few decades, photocatalysis has shown a great potential to remove persistent organic compounds and

micro-organisms from water. In addition, this is a low-cost and sustainable water treatment process.[12]

In this thesis, the application of photocatalysis for water purification applications was explored through the synthesis and design of new photocatalytic materials, which were tested in photoreactors designed by our project partners (Bath University and Rey Juan Carlos University). This thesis work was part of a multidisciplinary project, involving different teams across Europe and South East Asia, named the PCATDES project. The aim of the PCATDES project was to design, develop and build smart autonomous-mobile photoreactors based on innovative processes, novel engineering, solid-state lighting and materials with enhanced photocatalytic properties. Therefore, these photoreactors could be used in remote areas and potentially mineralise the *recalcitrant* organic pollutants, which cannot be removed from wastewater using biological methods.

The PCATDES project consists of two main phases. Firstly, it is focused on developing doped $TiO_2$ or other active photocatalytic materials (core shell systems, nanostructured metal oxides, heterojunction systems, etc.) to increase the photocatalytic efficiency through the enhancement of photon absorption and charge carrier separation. In particular, this increase will be accomplished by maximising the UV absorption *via* artificial irradiation using blue light emitting diodes (LEDs, developed by Bath University). Secondly, innovative electronic technologies will be used to build an autonomous and portable photoreactor for wastewater purification purposes. The reactor will be assisted by the blue LEDs which will enhance the photogenerated charge carrier separation of the photocatalytic material. These LED lights will be interconnected with high-tech sensors and microprocessor to enable continuous operations in remote areas. The input of UCL to this project was the synthesis and

optimisation of highly active new photocatalysts, as well as novel photocatalytic materials with high surface area. Photocatalytic tests were also carried out at UCL to assess the functionality of the photocatalysts.

## 1.2. Photocatalysis as an alternative and green method to purify water.

### 1.2.1. Photocatalysis: basis and fundamentals.

Photocatalysis has been one of the most investigated topics in the last five decades, due to its potential application in a wide range of different fields, such as photovoltaics, energy storage, remediation treatments, etc. Photocatalysis is understood as a photocatalysed reaction, however, this terminology can be incorrectly used since this terminology implies that light acts as a catalyst, whereas light should be thought and understood as a reactant which is photoconsumed during the chemical process. Therefore, photocatalysis has been chemically defined as the acceleration of a photoreaction when a catalyst is present. There are two different types of photocatalysis, depending whether photocatalysts and reactants are in the same phase or not. These two types are:

I. *Homogeneous photocatalysis*:

Homogeneous photocatalysis is a type of photocatalysis where the photocatalyst and the reactant are in the same phase. The most common photocatalysts used in homogeneous photocatalysis are ozone and photo-Fenton systems ($Fe^{+}$ and $Fe^{+}/H_2O_2$), and both mechanisms are driven by the formation of hydroxyl radicals (•OH). The generation of hydroxyl groups from ozone is given in Equation 1.1.[13]

$$O_3 + h\nu \longrightarrow O_2 + O(^1D) \qquad 1.1a$$

$$O(^1D) + H_2O \longrightarrow {}^{\bullet}OH + {}^{\bullet}OH \qquad 1.1b$$

$$O(^1D) + H_2O \longrightarrow H_2O_2 \quad 1.1c$$

$$H_2O_2 + h\nu \longrightarrow {}^{\bullet}OH + {}^{\bullet}OH \quad 1.1d$$

Likewise, in photo-Fenton systems, UV light would encourage the photolysis of $H_2O_2$ with the concomitant reduction of $Fe^{3+}$, to create active hydroxyl radicals. The mechanism is given in Equation 1.2.[14]

$$Fe^{2+} + H_2O_2 \longrightarrow {}^{\bullet}OH + Fe^{3+} + OH^- \quad 1.2a$$

$$Fe^{3+} + H_2O_2 \longrightarrow Fe^{2+} + HOO^{\bullet} + H^+ \quad 1.2b$$

$$Fe^{2+} + {}^{\bullet}OH \longrightarrow Fe^{3+} + OH^- \quad 1.2c$$

and

$$H_2O_2 + h\nu \longrightarrow {}^{\bullet}OH + {}^{\bullet}OH \quad 1.2d$$

$$Fe^{3+} + H_2O + h\nu \longrightarrow Fe^{2+} + HO^{\bullet} + H^+ \quad 1.2e$$

This process shows sensitivity up to 450 nm, making it active in the visible region and thus a cost-effective process as it can avoid the use of UV lamps and electrical energy. However, the main disadvantage of this process is that it can only be used at low pH values, since iron precipitates at high pH values, having to be removed after the treatment.

II. *Heterogeneous photocatalysis*:

Heterogeneous photocatalysis has both the photocatalyst and the reactant in different phases. The most common heterogeneous photocatalysts are transition metal oxides and semiconductors. Dissimilar to metals, semiconductors present an electronic structure characterised by a valence and a conduction band separated in energy. This difference in energy, between the top of the valence band and the bottom of the conduction band,

is the bandgap. If the valence band is completely full and the conduction band is completely empty some electrons can be promoted from the valence to the conduction band.[15] This electronic promotion is essential in photocatalysis. When a semiconductor is irradiated by a light source, with photons of energy ($h\nu$) equal to or superior to the bandgap energy, $E_g$, of the semiconductor, an electron ($e^-$) is promoted from the valence band (VB) into the empty conduction band (CB), creating a hole ($h^+$) in the VB (**Figure 1.1**). These photogenerated electrons and holes can follow different paths, they can recombine dissipating the energy as heat or getting trapped in metastable surface states (**Figure 1.1, reaction (a)**), with the concomitant loss of the photogenerated charge carriers. In contrast, if photogenerated carriers are promoted to the surface of the semiconductor, they will react with acceptors and donors adsorbed on the semiconductor surface (**Figure 1.1, reaction (b) and (c)**) to initiate the photocatalytic process. It is worth mentioning that in the absence of suitable electron and hole scavengers, the stored energy is dissipated within a few nanoseconds by recombination.[16]

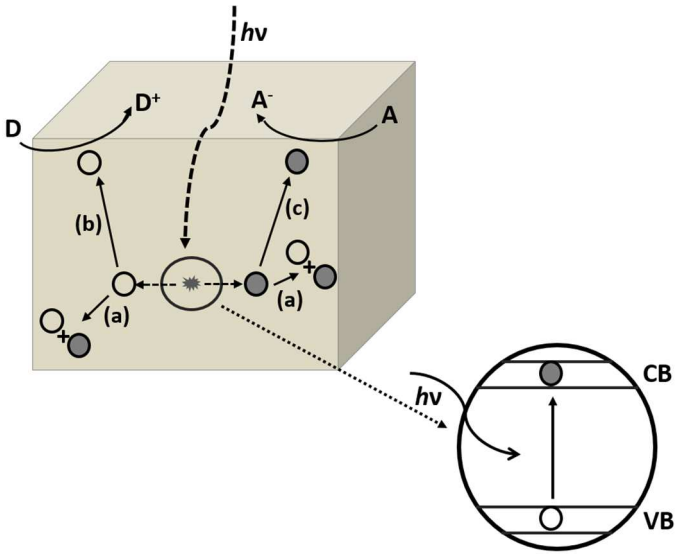


**Figure 1.1.** Scheme representing the processes that occur at the semiconductor photocatalyst upon irradiation and electronic excitation. Photogenerated electrons and holes can get recombined at the bulk or surface (a). Photogenerated holes promoted to the surface of the photocatalyst can oxidise an electron donor D (c), and photogenerated electrons will reduce an electron acceptor A (d).

### 1.2.2. Photocatalytic water purification. Heterogeneous photocatalysis.

As previously mentioned, heterogeneous photocatalysis is a photocatalytic application where both the photocatalyst and the reactant are in different phases. It can be performed in a wide range of different environments, such as, gas and liquid phase, as well as in aqueous solutions. Therefore heterogeneous photocatalysis can be used in different applications, such as; organic synthesis, water splitting, photoreduction, hydrogen transfer, metal deposition, disinfection and anti-cancer therapy, water detoxification, gaseous pollutant removal, etc.[17] Heterogeneous photocatalysis, also known as 'advanced oxidation technologies' (AOT), is based on reductive and oxidative reactions at the surface of the photocatalyst. This type of photocatalysis uses solar energy to generate *in-situ* highly reactive transitory species ($H_2O_2$, $OH^{\bullet}$, $O^{\bullet -}$, $O_3$) to mineralise organic compounds, pathogens and disinfection of by-products. All these properties make heterogeneous photocatalysis the most promising approach for air and water remediation treatments. The mechanism of photocatalysis can be divided in five different steps:

1. Transfer of the reactant species to the surface of the photocatalyst.
2. Adsorption of at least one of the reactant species.
3. Reaction in the adsorbed phase, where the reaction takes place.
4. Desorption of the products.
5. Removal of the products from the interface region.

Heterogeneous photocatalysis requires aerated conditions, therefore, oxygen will play an important role to degrade organic compounds and mineralise them to carbon dioxide and water. This process could be summarised by Equation 1.3.

$$\text{Organic pollutant} + O_2 \xrightarrow[h\nu \geq E_{bg}]{\text{semiconductor}} CO_2 + H_2O + \text{mineral acids} \qquad 1.3$$

The general mechanism of this photocatalytic process can be observed in Figure 1.2. However, the role of the photogenerated charge carriers and oxygen on the overall reaction has been a constant source of debate during the last few decades.[18] Some groups have reported that the oxidation of the organic compounds is directly linked to the photogeneration of holes and their transfer to the surface of the catalyst. Nevertheless, in recent years, it has been widely postulated that both photogenerated electrons and holes, generated in the photonic excitation, have a critical role in the oxidation of organic compounds. These charge carriers, promoted to the surface of the photocatalyst, would react with oxygen and water to form highly reactive radical groups, such as hydroxyl ($^{\bullet}OH$), hydroperoxyl radicals ($^{\bullet}OOH$) and superoxide ions ($^{\bullet}O_2^-$) radicals, which will finally react with nearby reactants.

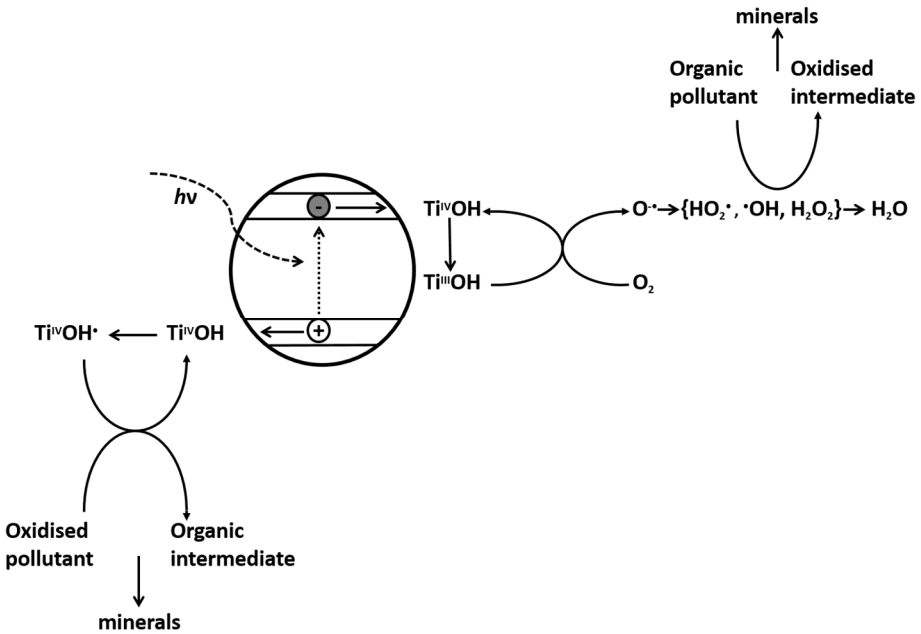


**Figure 1.2**. General processes for the photomineralisation of organic compounds, adapted from Mills *et al*.[17]

The use of semiconductor materials to mineralise organic matter was reported for the first time in the 1980's by Ollis and coworkers,[19,20] through the degradation of halogenated hydrocarbons. Since this first approach, there has been vast number of investigations to expand the use of photocatalysis to a wide range of organic compounds, being already reported more than 200 publications. In the last few decades, different semiconductors, such as $TiO_2$, ZnO, $Fe_2O_3$, CdS and ZnS, have been successfully reported as potential photocatalysts. It is commonly acknowledged that a semiconductor photocatalytic material should possess five essential property requirements, which are:

1. photoactive.
2. able to utilise visible and/or near-UV light.
3. biologically and chemically inert.
4. photostable.
5. inexpensive.

The use of solar energy, for water treatment applications, will reduce the impact on the environment, reducing the use of toxic oxidants, as well as the overall energy usage (reducing $CO_2$ emissions), facilitating its implementation in remote areas. In addition, it is important mentioning that the photocatalytic cleaning process of *recalcitrant* compounds occurs at the boundary between the photocatalyst and the aqueous environment. However, when light rays penetrate into the aqueous environment, they can be attenuated. Despite this limitation photocatalysis is a promising technology for water and air remediation treatments, as it can be supported by high surface area materials which can reflect and irradiate the photocatalyst material. Likewise, it can be also supported by additional lights (UV, etc.) inserted inside the photoreactor chamber. Therefore, the investigation and optimisation of the photocatalytic water treatment

process and semiconductor photocatalysts, is a key point in our project. It could be finally concluded that photocatalytic water treatment processes present great advantages over conventional methods.

## 1.3. Titanium dioxide: Functionality and efforts to improve its application in the water treatment process.

Titanium dioxide ($TiO_2$) is the most commercially utilised semiconductor material. It is widely used in industry as a pigment, *titanium white*, to provide whiteness and opacity to paints, plastics, papers, inks, food, etc. representing 70 % volume of the worldwide pigments' production. $TiO_2$ is also commonly used in cosmetic and skincare products, and it is present in many types of sunblock products to avoid the effect of UV light over the skin. However, despite the vast number of applications of $TiO_2$, the most studied and promising is its exceptional photocatalytic response for environmental remediation applications. Interestingly, this was causally found in the beginning of the 20$^{th}$ century, as a consequence of chalking paints upon light illumination. This finding led to different studies during the following years, being finally attributed to the photocatalytic degradation of the organic bonds within $TiO_2$.[21] However, it was not until the late 1960's that Fujishima *et al.*[22] reported for the first time the photoelectrochemical solar conversion using $TiO_2$ and its detailed photocatalytic mechanism.

$TiO_2$ exists in nature as three main crystalline polymorphs; anatase, rutile and brookite. Rutile is the most abundant and thermodynamically stable crystalline phase. Anatase and rutile polymorphs are commonly used in photocatalysis, both crystal phases consist of chains of $TiO_6$ octahedra. These two $TiO_2$ phases present different distortion of each octahedron, as well as a different assembly pattern of the chains (**Figure 1.3**). Both

rutile and anatase present a tetragonal structure, with rutile showing a cubic close packing (ccp) structure and anatase a hexagonal close packing (hcp) structure. These differences in the lattice structure cause different mass densities and electronic band structures. Rutile and anatase $TiO_2$ show different bandgap energies 3.0 eV and 3.2 eV, respectively. Despite the higher bandgap of anatase $TiO_2$, this is the most efficient crystal phase from a photocatalytic point of view. This difference in photoactivity is mainly due to the different surface behaviour of both polymorphs, which can be explained by the rapid coverage of the anatase $TiO_2$ surface with a layer of peroxo species during photo-oxidation processes. In contrast, rutile shows a negligible loading of peroxo species,[23] which suggests that the mechanism of the photooxidation reactions occurs differently in anatase and rutile crystal phases. In addition, it has been commonly reported a higher polaron effective mass for rutile than for that of anatase. The polaron effective mass is intimately associated to the exciton mobility, where only excitons that efficiently diffuse can reach the surface of the photocatalyst. Therefore, the anatase phase presents a lower photogenerated carrier recombination rate than the rutile phase.

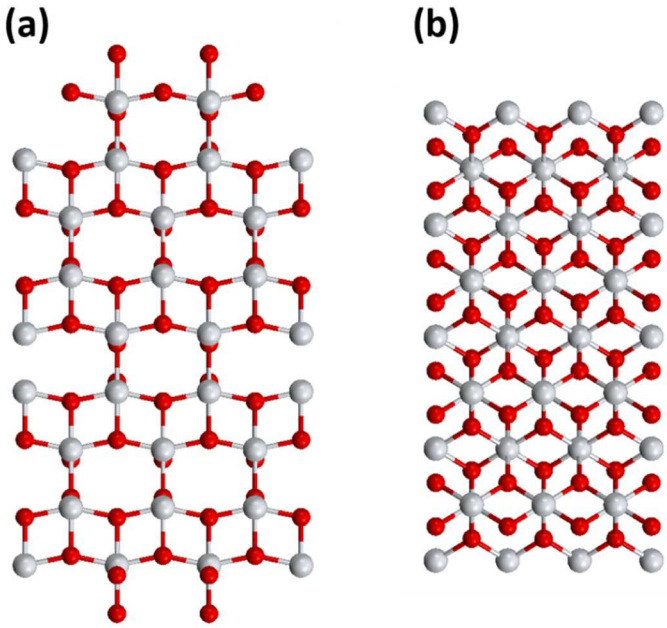


**Figure 1.3.** Scheme presenting the crystal structures of (a) anatase $TiO_2$ and (b) rutile $TiO_2$.

As previously mentioned, $TiO_2$ materials have shown high photocatalytic efficiency (within the UV range), chemical inertness, as well as mechanical robustness and relatively low-cost production,[17,24] making them an ideal material for photocatalysis applications.[17] The photocatalytic mechanism of $TiO_2$ is based on its photoexcitation upon UVA light illumination. The photoexcitation of $TiO_2$ generates photogenerated holes and electrons, which are transferred to the surface of the $TiO_2$ photocatalyst where they react with $O_2$ and $H_2O$ existing in the environment to produce the highly active radicals that are the responsible species for photocatalytic processes. These radical species are hydroxyl species ($OH^-$), formed from photogenerated holes, and superoxide ($O_2^-$) groups, produced from photogenerated electrons. It is generally accepted that photocatalysis in $TiO_2$ proceeds through two different avenues:

i) donor molecules, such as water, react with surface holes ($h^+$) to form highly reactive hydroxyl radicals that subsequently will degrade nearby organics, or;

ii) the reaction of electrons ($e^-$) with oxygen to create highly reactive superoxide radicals that can also degrade nearby organics.

These active radical species react with nearby organics, oxidising organic matter into water, carbon and mineral acids. The rate limiting step of this mechanism is the interfacial electron transfer process, which involves the reduction of oxygen.[17]

The degradation rate of the organic matter by $TiO_2$, when the illumination source is in steady state, follows Langmuir – Hinshelwood kinetics.

$$r_i = k_s \text{ x } \theta_s \text{ x } C_s / (1 + \theta_s \text{ x } C_s) \qquad 1.4$$

Where $r_i$ is the initial rate of substrate removal, $C_s$ is the initial concentration of the organic species, $k_s$ is the kinetic constant for the surface reaction and $\theta_s$ is the surface

coverage constant (absorption). It is generally assumed that $k_s$ is proportional to $I_a$ (rate of light absorbed) and to the fraction of $O_2$ adsorbed to the surface of the photocatalyst and the different constants are affected by the following factors:

i) Bandgap. The bandgap of the semiconductor photocatalyst defines the region of the solar spectrum where it will be active,

ii) Thickness. The thickness of the photocatalytic material is essential to understand the portion of photons that can be absorbed, $I_a$,

iii) Roughness. The morphology of the photocatalyst determines the number of active sites available to form radical groups, $k_s$, and the contact with the organic layer, $\theta_s$,

iv) Crystallinity. The crystallinity of the photocatalyst drives the transfer of the photogenerated electron-holes to the surface of the material, $k_s$. Therefore, different $TiO_2$ materials will show different rates of photocatalysis,

v) electron and hole diffusion length,

vi) average electron-hole lifetime,

vii) kinetics of reactions of electrons and holes with acceptor and donor molecules.

In the last few decades, there has been a constant investigation to make photocatalysis an energy-efficient process. This has been widely explored by improving the photocatalytic feature of $TiO_2$, especially by modifying its electronic structure to enhance its function under solar illumination.[24] The most investigated approaches have been chemical modification,[25] nanostructuring,[26,27] the addition of co-catalysts[28,29] and coupling semiconductors.[30–33]

The chemical modification of $TiO_2$, through the incorporation of anionic and cationic dopants into its structure, has been widely explored to alter the $TiO_2$ band structure and enhance its photocatalytic function. Different computational density of states calculations (DOS) have shown that the electronic band structure of $TiO_2$ consists of a valence band made primarily of O 2p orbitals and a conduction band made by Ti 3d orbitals. The dopant species can introduce band states within the bandgap of $TiO_2$, modifying its electronic structure. It has been commonly acknowledged that anionic species can substitute oxygen ($O^{2-}$) sites, but they can also be added into the $TiO_2$ framework as interstitial sites. Computational studies have shown that both doping forms can modify the band arrangement of $TiO_2$ materials, non-metal modification in substitutional positions generates interband states just above the valence band maximum (VBM), allowing their interaction with O 2p orbitals to spread the VBM to higher energies, lowering the bandgap (**Figure 1.4(b)**). However, dopants in interstitial positions create interband states between the valence and conduction band of $TiO_2$ (**Figure 1.4(c)**), resulting in a dual-electron process with electrons initially excited to the interband state and subsequently to the conduction band. $TiO_2$ has also been modified using cationic species, which replace titanium (Ti) sites, these cationic species generate electronic states close to the conduction band minimum (CBM) of $TiO_2$; forming interband states between the VBM and CBM of $TiO_2$ (**Figure 1.4(d)**).

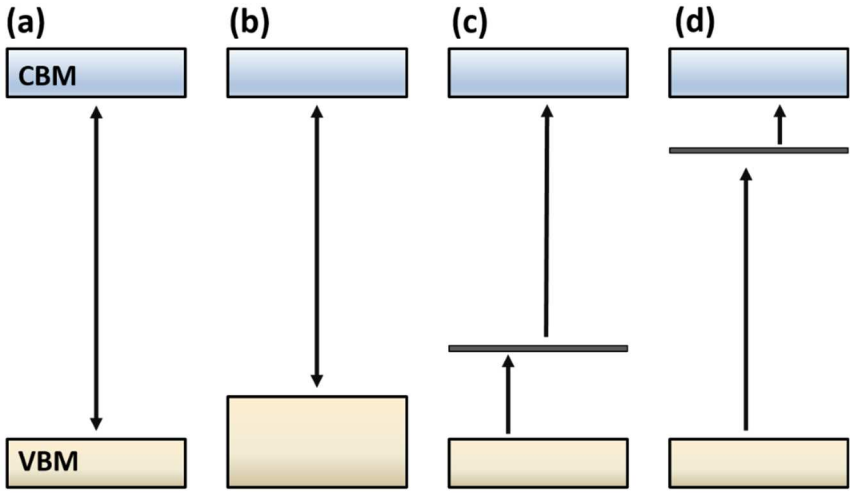


**Figure 1.4**. Scheme to illustrate the different changes that the bandgap of $TiO_2$ could show upon doping with different chemical species. (a) bandgap of pristine anatase $TiO_2$; (b) anatase $TiO_2$ doped with anionic species in substitutional positions; (c) anatase $TiO_2$ doped with anionic species in interstitial positions and (d) anatase $TiO_2$ doped with cationic species.

Different theoretical studies have reported shifts in the absorption edge of $TiO_2$, as well as visible-light activity through these changes in the electronic structure of $TiO_2$.[34–36] However, it is important mentioning that the optical shift observed through interstitial and cationic modification is mainly due to excitations from the intermediate states to CBM. It is also worth noting that the chemical modification of $TiO_2$ can lead to the production of oxygen deficient materials, commonly known as oxygen vacancies ($O^{2-}$), they can also generate intermediate states below the CBM, potentially resulting in the visible activation of $TiO_2$.[37] This has led to a broad debate about which modification is responsible of the activation of $TiO_2$. Although many different dopants have been examined, there is still no consensus as to which dopant produces the best desired effect. In many cases, the acquisition of visible light activity through chemical modification is often coupled with a decrease in UV light activity, with little or no overall benefit for outdoor use. In chapters 2 and 3, we present an exhaustive investigation on the effect that different non-metal species have on the functional and structural properties of $TiO_2$.

Nanostructuring of $TiO_2$-based materials enables formation of a solid solution which can enhance the photocatalytic performance. By structuring $TiO_2$ in different arrangements, such as nanorods, nanobelts, nanotubes, etc., confined conductive channels, with longer charge diffusion lengths, are created within the $TiO_2$ matrix. This can drastically increase the separation of photogenerated charge carriers and their availability to react with nearby reactants.[38] All these features make these hierarchical structures with high and accessible specific surface area desirable for photocatalytic applications.[39] Nevertheless, the main limitation of this approach is that the absorption onset of the nanostructured $TiO_2$ cannot be extended to the visible region. However, it could be bypassed by the addition of dopant species.

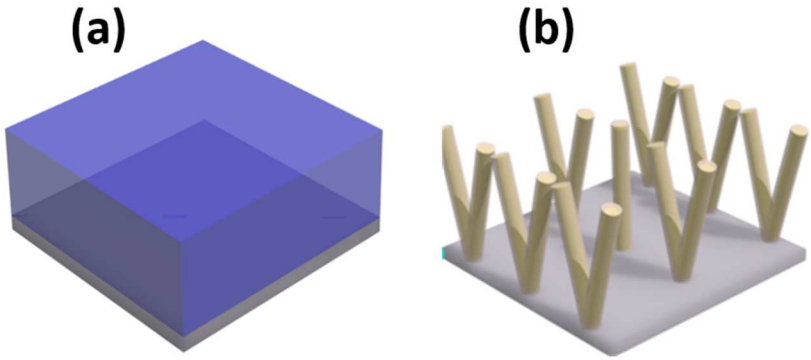


**Figure 1.5**. Illustration of a conventional $TiO_2$ film (a) synthesised by a CVD process and a CVD nanoengineered $TiO_2$ film (b), with high specific area.

Heterostructured materials have garnered attention in the field of photocatalysis, as an alternative to the chemical modification of $TiO_2$. The success of this approach is supported by the fact that the most active form of $TiO_2$ is a commercial heterojunction system, P25 *Evonik*, which is composed of ~ 3:1 ratio of the anatase and rutile phases of $TiO_2$.[40] A heterojunction system allows engineering of the band structure of the two joining semiconductors, making it energetically favourable to transfer photogenerated electrons and holes in opposite directions across the heterojunction boundary. The position of the band potential of the heterostructured material is essential to understand

the flow of the photogenerated charge carriers, as either the photogenerated holes can leap down into the valence band of the top layer semiconductor (**Figure 1.6(a)**) or electrons can jump up into the conduction band of $TiO_2$ (**Figure 1.6(b)**). This spatial separation in charge can inhibit electron-hole recombination and increase photocatalytic efficiency.[313238] In addition, depending upon the respective band energies, a heterojunction can extend the photocatalytic response into the visible region of the solar spectrum through complementary absorption of solar light. The benefits of using these heterostructured systems in photocatalysis have been demonstrated for a wide range of heterojunction systems, including $Cu_2O/TiO_2$,[41] $WO_3/BiVO_4$,[42] $ZnO/BiVO_4$,[43] which have shown synergetic enhancements in their photoresponse compared to that of their individual analogues. In chapter 4, we will present the synthesis of a rutile/anatase $TiO_2$ heterojunction film to investigate its impact on the functional properties of $TiO_2$-based materials.

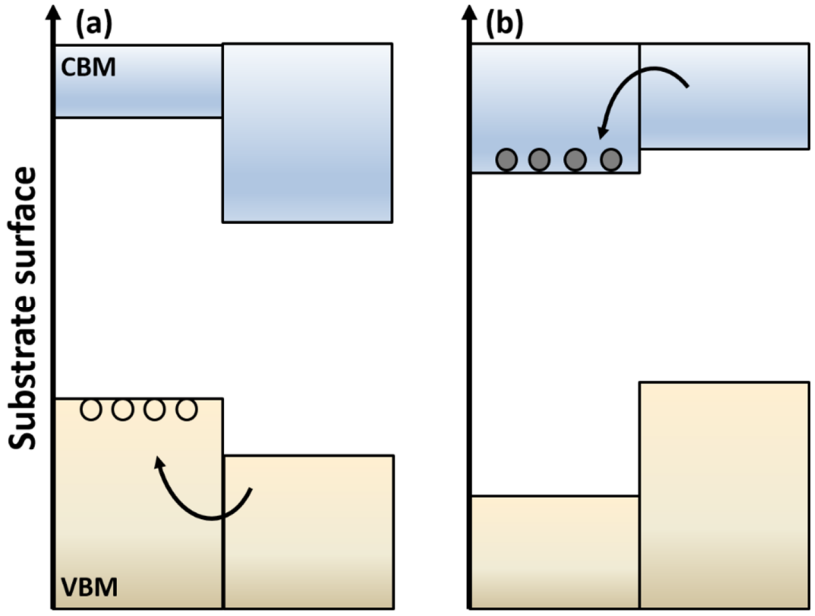


**Figure 1.6**. Characteristic band alignment for heterostructured photocatalysts. Heterostructured materials coupled with semiconductors of lower energy can result in the straddle of the (a) conduction band or (b) valence band.

In addition, in chapter 5 we will investigate the combination of both nanostructuring and heterostructuring approaches, through the synthesis of a metal oxide with high specific area, nanorods of $WO_3$, coupled with a overlayer of $TiO_2$.

## 1.4. Synthesis of photocatalytic materials. Chemical vapour deposition.

### 1.4.1. Basics and history.

Chemical vapour deposition (CVD) of thin films and surface coatings involves the chemical reaction from precursors transported in the gas phase, to a heated substrate material to produce a solid deposit. CVD is a well-known and versatile technique employed for more than a century to synthesise a vast number of metal and non-metal chemical species, as well as carbides, nitrides, oxides, and many others. One of the earliest uses of CVD was reported by Wohler *et al*.,[44] where tungsten metal films were produced using tungsten hexacarbonyl [$W(CO_6)$] and hydrogen. During the beginning of the 19$^{th}$ century, CVD was extensively used in industrial applications to produce high purity refractory metals, such as Ti, Ni and Zr. However, it was not until the late 1950's when the mechanism of CVD was better understood, leading to improvements in the synthesis of surface coatings, as well as their functional properties, such as protection against wear, corrosion, oxidation, chemical reaction, etc.[45,46]

Nowadays, CVD is an important industrial tool, as it can be easily scaled-up. One of the most proactive companies to implement it has been Pilkington *NSG* Group *via* an on-line CVD process,[47] through the synthesis of surface coatings at a very large scale, which reduced both cost and production time. These advances resulted in a breakthrough in the production of self-functional windows. Two of the most notable surfaces deposited by this methodology are:

i. Fluorine-doped tin oxide (F:$SnO_2$, FTO). FTO coatings are used in windows to prevent heat loss from houses, with the concomitant ecological energy saving.

ii. $TiO_2$ coatings. *Self-cleaning* glass surfaces were designed by coating windows with a very thin layer of transparent $TiO_2$, which can degrade and clean dirt upon solar illumination.

Despite all the advances and improvements seen by CVD technology, it was not until three decades ago when CVD technology garnered significant success in the microelectronic industry, which required to have a very accurate control of the uniformity, composition and doping of the coatings to deliver very thin coatings with high purity. This led to the introduction to two new concepts of CVD methodology; metalorganic chemical vapour deposition (MOCVD)[48,49] and atomic layer deposition (ALD).[50,51] MOCVD allows the thermodynamically stable deposition of metastable alloys on different surface substrates, introducing the use of semiconductors in optoelectronic applications. Likewise, ALD has recently shown great potential in the field of optoelectronics, as it allows deposition of very thin and conformal coatings controlled at an atomic level. All these advances in CVD technology has allowed its exportation to many different applications, such as surface modification, ceramic fibre production, as well as aerospace and military applications.

It is also worth mentioning that CVD presents important advantages compared to other sputtering or vapour deposition techniques (physical vapour deposition, PVD), as it allows surfaces to be coated with high specific area, including three-dimensional configurations. In addition, CVD normally does not always require high vacuum systems and it can be easily modified to different configurations, making it a most economical process.

### 1.4.2. Principles of chemical vapour deposition processes.

The mechanism of CVD processes is complex and requires gas-phase reactions, as well as surface reactions with the surface substrate. The key points of this mechanism can be summarised in the following steps:

1. Transport of the gaseous reagents to the CVD reactor chamber.
2. Gas phase reaction of the different reagents in the reactor chamber to create reactive intermediate species and by-products, which are removed from the reaction chamber through the exhaust system.
3. Mass transport of the intermediate reactants to the substrate surface.
4. Adsorption of the reactant species on the substrate surface.
5. The reactant deposits will diffuse through the substrate surface to nucleation sites, where surface chemical reactions will lead to the growth of a coated film.
6. Desorption of unreacted deposits from the substrate and transport from the reaction chamber through the exhaust system.

A representative scheme of the mechanism of a CVD process is shown in Figure 1.6.

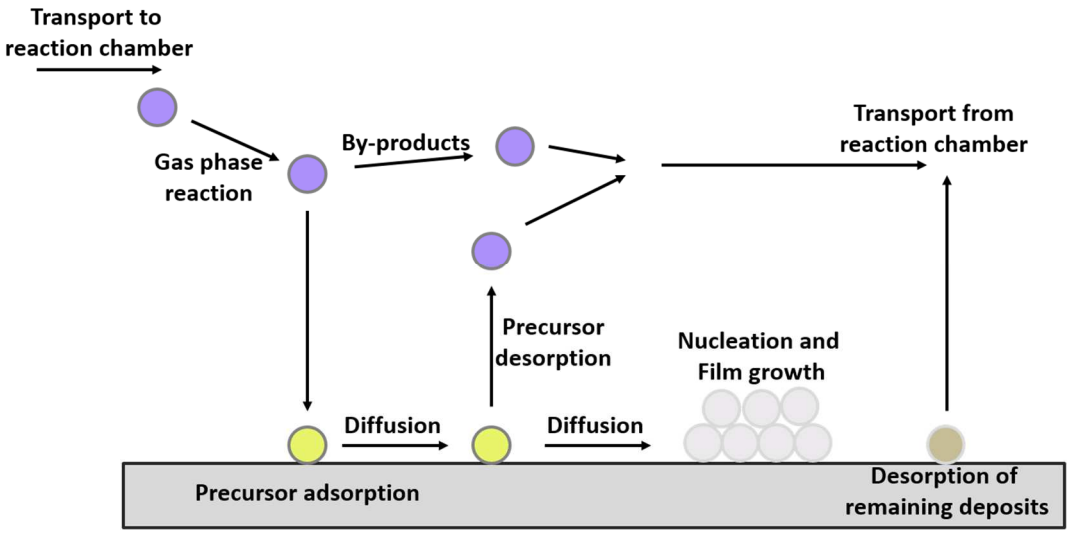


**Figure 1.6.** Schematic illustration of the precursor transport and reaction processes in CVD technology.

### 1.4.3. Types of chemical vapour deposition processes.

CVD can be carried out in a variety of different configurations. The main difference between these different configurations is that the chemical reaction can be activated by several methods, being the most important:

1. Thermal activation. Thermal CVD typically takes place at high temperatures, however this temperature can be lowered if metal-organic precursors are used. It is worth mentioning that this thermal CVD category can be further subdivided depending on the configuration of the CVD reactor:
    i. Pressure. CVD can be either performed at atmospheric-pressure CVD (APCVD);[52–54] at sub-atmospheric-pressure CVD (LPCVD)[55,56] which could reduce gas phase reactions or under very low pressure, ultra-high vacuum CVD (UHVCVD).[57,58]
    ii. Physical properties of the precursor. The precursor can be transported as a gas (APCVD),[52,53] aerosol (AACVD)[59,60] or injected as a liquid solution (DLICVD).[61]
    iii. Reactor chamber configuration. Thermal CVD can either use a hot-wall or cold-wall configuration. A hot-wall reactor consists of an isothermal furnace which allows it to achieve a homogenous heating of the different parts of the reaction chamber. On the contrary, in a cold-wall reactor there is only one heating source, whilst the rest of the reaction chamber remains cool.
    iv. Precursor mixing. Almost all thermal CVD configurations transport the precursors to the reaction chamber where they react, depositing a coating on the substrate surface. However, there is a thermal CVD

modification, where precursor reactants are pulsed to the reaction chamber alternatively: atomic layer deposition (ALD).[51]

2. Plasma activation. CVD techniques can be activated by plasma sources which can work at much lower substrate temperatures than thermal CVD, allowing polymers to be coated. There are three different modifications of plasma-assisted CVD techniques; microwave plasma-assisted CVD (MPCVD),[62,63] plasma-enhanced CVD (PECVD)[64,65] and remote plasma-enhanced CVD (RPECVD).[66,67]
3. Photo-activation. Photo-initiated CVD is a process activated by UV light to stimulate chemical reactions.[68,69] This process is similar to plasma-enhanced techniques. However, PICVD presents an advantage compared to plasma-enhanced CVD, under specific conditions it can be operated at atmospheric pressure.

### 1.4.4. Chemical vapour deposition kinetics.

The CVD processes employed in this thesis were atmospheric-pressure and aerosol-assisted chemical deposition, APCVD and AACVD, respectively. Both CVD methods are characterised as "thermal CVD". The film growth rate of these CVD processes is controlled by the substrate temperature, pressure of the reactor chamber, as well as the chemistry of the gas-phase.[70] The growth rate is intimately correlated to the temperature of the reaction chamber, exhibiting three well differentiated growth regions. The first region corresponds to growths at low temperatures, following the Arrhenius equation, where $E_A$ is the activation energy, $R$ is the gas constant and T is the temperature. CVD systems working within this region can produce film depositions by maintaining

constant temperature. In this region, the growth rate increases exponentially with substrate temperature and it is mainly controlled by the kinetics of chemical reactions.

$$\text{Growth rate} = \exp(E_A / RT) \quad 1.5$$

Upon an increase in temperature, there is a region where the surface kinetic processes become so rapid that the growth rate stops being temperature dependant and it is only controlled by the transport of the gaseous reactants. This region is commonly called the mass transport limited region. This type of film growth is beneficial for cold-wall CVD processes, where it is more difficult to achieve a homogenous heating gradient across the substrate surface. The growth rate of the as-synthesised coating can be controlled by monitoring the flux of the limiting reactant precursor.

The mass transport limited region is controlled by the diffusion of the gas phase precursors species through a boundary layer to the deposition surface. The diffusion rate in this region is given by Fick's law of diffusion:

$$J_i = -D\frac{dC_i}{dx} = -D\frac{[A]}{dx} \quad 1.6$$

where $J_i$ is the precursor diffusion flux, $D$ is the diffusion coefficient or diffusivity, $Ci$ is the concentration of the precursor species and $x$ is the direction perpendicular to the substrate surface. This equation can be summarised to a first order equation in respect to the concentration of the precursor species on the substrate surface, [A]. The rate of diffusion of gas phase precursors to the surface is expressed in molecules / $cm^2s$.

Further an increase in temperature results in a region where the growth rate starts decreasing. This decrease is due to side reactions through depletion of reactants on the walls of the reactor, promoting reactions outside the substrate surface. Likewise, this growth region increases the desorption rate of the film from the substrate due to

delamination effects. Higher temperatures in the reactor chamber promotes particle formation instead of film generation due to gas phase reactions, producing powdery film deposits.[70,71]

### 1.4.5. Layer morphology.

Layer morphology is extremely critical to determine the physical properties of a thin film. The morphology of the film is directly associated to the diffusion and nucleation processes, which are also influenced by different CVD parameters, such as deposition temperature, total pressure of the CVD system, as well as the partial pressure of the gaseous reactants. An increase in the deposition temperature is associated with an increase in the mobility of the species adsorbed on the substrate surface.

Typically, CVD processes can be driven by two different type of reactions, homogeneous (gas phase) or heterogeneous (near the heated substrate surface) reactions. Gas phase reactions commonly generate homogeneous nucleation, which normally takes place at high deposition temperatures, leading to the production of a stable solid powder. This effect is due to the presence of powdery particles, generated in the gas phase reaction, which will sit on nucleation sites of the substrate surface, stopping nucleation and growth processes. Therefore, this type of chemical reaction will produce powdery coatings. In contrast, heterogeneous reactions near to the substrate surface lead to adsorption of mobile monomers onto the substrate, which diffuse to preferred sites on the substrate surface to start the nucleation process. Subsequently, more monomers will be added to these nucleation sites, leading to crystallite growth with the concomitant formation of a thin crystalline layer.

There are three main types of layers growth by CVD methods, epitaxial, amorphous and polycrystalline:[70,71]

i. Epitaxial layers. Film layers are single crystals grown with the same direction as the substrate. This growth is only possible if the substrate is defect and contamination free. Epitaxial deposition requires low growth rates which allow diffusion of the adsorbed species to nucleation sites that replicate the orientation of the substrate. Low growth rates are generally achieved by low amounts of reactive species (controlled by the partial pressure of the reactants) and fast surface diffusion. Low-vacuum systems are ideal for this type of growth.

ii. Polycrystalline layers. Polycrystalline substrate surfaces present this growth, where polycrystalline layers are grown by nucleation on different sites of the substrate. This type of growth is controlled by the size and nature of the crystallites, presenting two different structure morphologies: a) Columnar structure: particle grains arranged in the same preferred orientation than the first nucleated layer deposited on the substrate surface. b) Equiaxed structure: particle grains randomly arranged across the substrate surface.

iii. Amorphous layer. In this growth arrangement, the transfer of the precursors to the reaction chamber is much more rapid than the diffusion of reactant species along the substrate surface. This is favoured by high growth rates and low temperatures inside the reaction chamber.

In addition, the quality and functionality of the as-deposited films in a CVD process, are influenced by the following parameters:

i. Thickness and density. Film thickness in CVD vary from a few nanometres to several microns. The film thickness is intimately related to the type of CVD process and different deposition parameters (substrate temperature and pressure of the CVD system) employed. It is commonly acknowledged that high growth

rates, which are associated with high temperatures and partial pressure values, will produce thick films. In contrast, low growth rates are associated with the synthesis of very thin films. Likewise, the density of a film is very important in terms of the film quality and functionality, where low values are associated to highly porous films with impurities in the crystal lattice.

ii. Adhesion. This parameter is essential in thin films synthesis, as the film functionality is extremely dependent on the strength of the adhesion between the substrate and the as-deposited film. Although this mechanism is not always totally understood, it is widely acknowledged that the substrate surface needs to be thoroughly cleaned before the deposition process.

iii. Composition and purity. These two factors are also really important to produce highly functional films. Small changes in film composition can drastically change the physical properties of the film. Likewise, the presence of even very small traces of impurities can have a dramatic impact on the formation of the film. These impure particles can consume the precursors decreasing the amount available to react. Likewise, they are potential source of defects, inducing to pin-hole effect and the concomitant delamination of the as-deposited film.

### 1.4.6. Atmospheric-pressure chemical vapour deposition (APCVD).

Atmospheric-pressure CVD is the most common form of CVD, where pure precursor species are heated in a bubbler to form enriched vapour, which are delivered by an inert carrier gas to the reaction chamber. These gaseous reactants chemically react when they pass through the reaction chamber, with the subsequent deposition of a solid product (thin film) on the substrate surface. The precursor supply rate to the reaction chamber is controlled by the vapour pressure of the precursor, operating temperature of the

bubbler, as well as the flowing rate of the inert carrier gas. The use of vapour reactants requires that the precursor species should have a relatively high vapour pressure to facilitate the phase change transfer, from liquid to gas phase.

In APCVD the growth rate of the as-deposited films can be controlled by monitoring the gas transport of the gaseous reactants to the reaction chamber. To determine this gas flow, it is generally assumed that the gaseous species follow the ideal gas law, which is valid for APCVD processes, as it works at atmospheric-pressure and therefore, there will not be gas phase reactions occurring. The ideal gas law equation is:

$$\frac{N_p}{N_c} = \frac{P_p}{P_c} \tag{1.7}$$

where $N_p$ and $N_c$ are the amount (moles) of precursor reactants and carrier gas, respectively; and $P_p$ and $P_c$ are the partial pressures of precursor reactants and carrier gas, respectively. Assuming that an APCVD system will only contain precursor and carrier gas species, it is commonly acknowledged that the partial pressure at the outlet of the bubbler is equal to the sum of the partial pressure of the precursor species, $P_p$, and the partial pressure of the carrier gas, $P_c$.

$$P_{total} = P_p + P_c \longrightarrow P_c = P_{total} - P_p \tag{1.8}$$

$$N_p = \frac{N_c \text{ x } P_p}{P_{total} - P_p} \tag{1.9}$$

As previously mentioned APCVD works at atmospheric-pressure, therefore the total partial pressure can be substituted by 760 torr. In APCVD processes the gas flow is measured in litres per minute. Considering that one mole of gas is equivalent to 22.4 litres, it can be concluded that dividing the carrier gas volume-flow rate, $N_c$, by 22.4 litres would give the flow rate of the carrier gas, $F_c$, which is independent of temperature and pressure, and thus it can be used to calculate the flow rate of the precursor species,

$F_p$. Therefore, Equation 1.10 can be used to determine the flow rate of the precursor species transferred to the reaction chamber.

$$F_p = \frac{F_c \text{ x } P_p}{22.4(760 - P_p)} \qquad 1.10$$

### 1.4.7. Aerosol-assisted chemical vapour deposition (AACVD).

As previously mentioned, in conventional CVD the precursor reactants are delivered to the reaction chamber by heating a stainless steel bubbler, wherein these precursors are contained, to create reactant vapours. Despite the advantages of conventional CVD, such as scalability and relative fast production of high quality coatings, there is a main limitation associated to this type of CVD; the availability of suitable chemical precursors, as it requires the use of highly volatile chemical species.

Aerosol-assisted CVD was designed as a liquid-phase modification of CVD, where non-volatile precursors can be used. These non-volatile precursors are mixed with a solvent to produce a precursor-mist, which is transferred to the reaction chamber by nebulising it using an ultrasonic generator. Therefore, the major advantage of AACVD over conventional CVD processes is the wider range of potential precursors that can be investigated, as they depend on their solubility rather than volatility.[72] In addition, AACVD does not require heat lines to transport the precursor-mist and its cost is relatively low compared to conventional CVD processes. In a typical AACVD deposition, the precursor solution is placed in an ultrasonic generator, which consists of a piezoelectric transducer element in a water bath to generate standing waves and aerosol droplets. These precursor droplets are transferred to the reaction chamber, where a solid thin film will be deposited on the substrate surface.

In the following chapter, we will explore the chemical modification of $TiO_2$ thin films by adding nitrogen species to its structure. These nitrogen-doped $TiO_2$ films will be investigated to study the effect of surface and bulk nitrogen species on the physical and functional properties of N-$TiO_2$ thin films. In addition, the engineering and synthesis of stratified N-$TiO_2$ thin films will also be investigated, which will allow high concentrations of nitrogen in selective positions of the N-$TiO_2$ thin films.

Chapter II

# NITROGEN DOPED $TiO_2$ THIN FILMS

*'The following chapter presents the results from a series of experiments for growing nitrogen-doped $TiO_2$ thin films using atmospheric pressure chemical vapour deposition (APCVD) processes. This chapter will be divided in two different sections. In the first section, different nitrogen precursor sources (tert-butylamine, benzylamine and ammonia) are used to create different synthesis environments, which will help to study the effect that surface and bulk nitrogen species will have on the functional properties of N-$TiO_2$ thin films. In the second section of this chapter, the use of APCVD processes in a pulsed precursor mode to deliver stratified N-$TiO_2$ thin films is explored. This approach allows high concentrations of nitrogen to be added in selective positions of the N-$TiO_2$ films with minor impact on their physical properties. These stratified N-$TiO_2$ films showed an increase of the photocatalytic efficiency compared to that of undoped and non-stratified N-$TiO_2$ films. The enhanced photocatalytic properties of this systems can be explained by engineering layers of undoped and N-doped $TiO_2$, resulting in an enhancement of charge carriers photogeneration and mobility.'*

## 2. Nitrogen doped $TiO_2$ thin-films.

### 2.1. Introduction.

As previously mentioned, anatase $TiO_2$ presents a range of intrinsic properties, such as high photocatalytic activity, durability to extended photocatalytic cycling, mechanical robustness and chemical inertness over a wide range of pH and voltage, which has made it the most studied photocatalyst.[17,73–75] However, this photocatalytic material shows some drawbacks, such as its *relative* wide band gap (~ 3.2 eV) which lies in the UV region of the electromagnetic spectrum, minimising its outdoor applications (as < 4 % of solar photons can excite the material), leading to a vast number of studies aimed at enhancing the visible light activity of anatase $TiO_2$.

The use of non-metal species to chemically modify $TiO_2$ materials is the most common method of expanding its absorption onset into the visible region. Over the last few decades, it has been commonly assumed that non-metal acceptor doping should simultaneously raise the valence band of $TiO_2$ (red-shifting the absorption onset of $TiO_2$) and reduce the number of recombination centres.[76] From all different non-metal acceptor species, nitrogen has become the most studied dopant source.[35,77–81] However, the origin of this visible activity is still a matter of debate. This is due to the ambiguous assignment of N species by X-ray photoelectron spectroscopy (XPS) studies.[35,77,82] Nevertheless, general consensus has resulted in the assignment of two types of nitrogen dopants; substitutional ($N^{3-}$, replacing oxygen) and interstitial ($N^0$/ N-$O^{2-}$ groups within the lattice), with binding energies of *ca*. 396 and 400 eV, for substitutional (Ns) and interstitial ($N_i$) dopant species.[83,84]

In this chapter, the use of atmospheric-pressure chemical vapour deposition (APCVD) processes to synthesise N-doped $TiO_2$ thin films, using either *tert*-butylamine,

benzylamine or ammonia ($NH_3$) as nitrogen sources, is explored. The use of APCVD will facilitate N-doping of $TiO_2$ thin films with a homogeneous content of the dopant specie throughout the material bulk. The effect of adding nitrogen to the lattice of $TiO_2$, will be investigated through physical and functional studies. In addition, the selective incorporation of the N dopant into the $TiO_2$ lattice by pulsed precursor delivery using APCVD is also investigated. This approach will deliver stratified N-doped $TiO_2$ thin films, which will allow investigation of the addition of high concentrations of N in localised positions throughout the lattice of $TiO_2$.

## 2.2. Experimental methods.

All chemicals were purchased from *Sigma-Aldrich*. Titanium (IV) chloride ($TiCl_4$, 99.9 %) and ethyl acetate ($C_4H_8O_2$, 99.8 %) were utilised as titanium and oxygen precursors, respectively. *Tert*-butylamine ($C_4H_{11}N$, 99.5%), benzylamine ($C_7H_9N$, 99%) and ammonia ($NH_3$, oxygen free) were used as nitrogen sources. Nitrogen carrier gas was supplied by BOC. Glass substrates, provided by Pilkington *NSG* Group, contain a thin $SiO_2$ barrier (50 nm), which prevents ion diffusion into the as-deposited photocatalyst.

### 2.2.1. Nitrogen-doped $TiO_2$ thin films synthesis.

As previously mentioned, APCVD processes, in a cold-wall configuration, were used to synthesise N-doped and undoped $TiO_2$ films. All thin films used in this chapter, were deposited on float glass substrates. Each substrate was carefully washed with acetone ($C_3H_6O$, 99 %), isopropanol ($C_3H_8O$, 99 %), distilled water and finally dried with air prior to their use.

In APCVD, precursors are volatised thermally. In our set-up, each different precursor source was stored in a stainless steel bubbler. The precursors were heated to achieve a

particular vapour pressure, so that the gaseous vapours could be transported to the reaction chamber by an inert carrier gas ($N_2$). A schematic figure of the APCVD apparatus is shown in Figure 2.1.

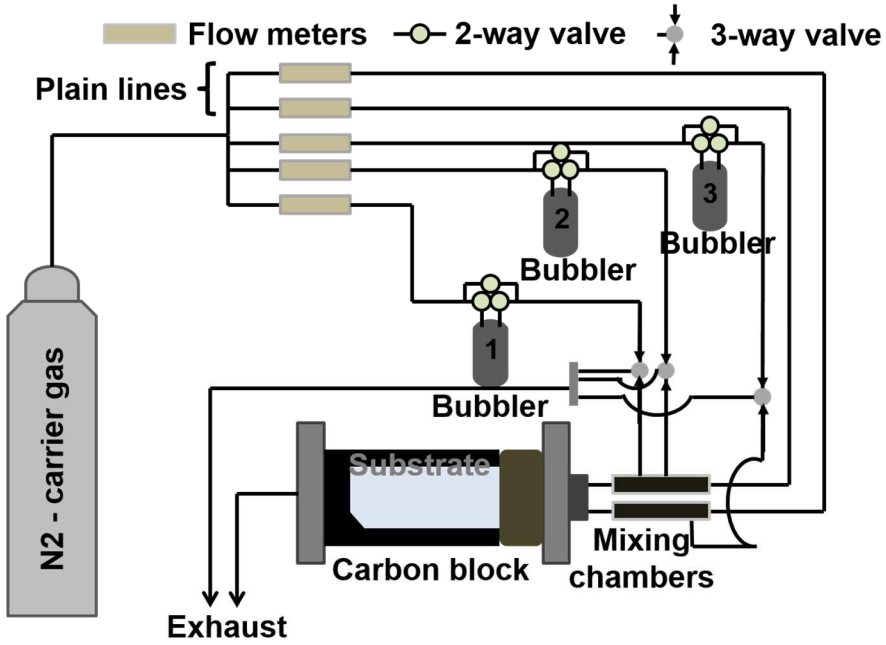


**Figure 2.1.** Scheme of the atmospheric-pressure chemical vapour deposition (APCVD) apparatus. Undoped and N-doped thin-films were synthesised from volatile precursors carried by di-nitrogen gas from bubblers; where bubbler 1 contained $TiCl_4$, 2 contained ethyl acetate and 3 contained a nitrogen source (either *tert*-butylamine, benzylamine or $NH_3$).

All pipelines of the APCVD reactor, were maintained at 200 °C to inhibit condensation of the precursors as they were carried to a pre-mixing chamber. The pre-mixing chamber was held at 250 °C, where the two gas streams of $TiCl_4$ and ethyl acetate met before being carried through a triple baffle manifold into the reaction chamber. The $N_2$ gas carrier gas was pre-heated. The CVD reaction chamber consisted of a 320 mm-long graphite block with three inserted heater cartridges (*Whatman*). Pt-Rh thermocouples were used to control the temperature at different stages of the CVD system. In a standard $TiO_2$ synthesis, the temperatures of the bubblers, containing the titanium and oxygen precursors, were held at 68 and 38 °C, respectively. The temperature used for

the nitrogen dopant was adapted in order to produce enough gaseous reactants. Low temperatures were used for *tert*-butylamine and benzylamine (~3-5 °C), using an ice-bath.

### 2.2.2. Physical characterisation.

The structural properties of the as-synthesised thin films were investigated using X-ray diffraction (XRD) and Raman spectroscopy analyses. XRD measurements were carried out using a Bruker-Axs D8 (Lynxeye XE) diffractometer, which consists of a monochromated Cu X-ray source ($K_{\alpha 1}$, 1.54 Å) and a glancing incident angle ($\theta$) of 1°. Raman spectroscopy was performed using a Renishaw 1000 spectrometer equipped with a 633 nm laser, which was calibrated using a silicon reference. UV/vis spectroscopy analyses were evaluated using a double monochromated Perkin Elmer Lambda 950 UV/Vis/NIR Spectrophotometer in the 250 – 2500 nm range. The UV/vis measurements were calibrated using a *Labsphere* reflectance standard as reference. In addition, a Helios double beam instrument was used to record reflectance values, within the 300 – 2500 range, at different positions, allowing to evaluate the thickness of the films via *Swanepoel* method.[85] These thickness measurements were also corroborated by side-view scanning electron microscopy (SEM) analysis. Two different SEM systems, a JEOL 6301 (5 KV) and a JEOL JSM-6700F field emission instruments, were used to collect the data, which were analysed using the Oxford software INCA. X-Ray photoelectron spectroscopy (XPS) analyses were carried out using a Thermo K alpha spectrometer with monochromated Al K alpha radiation, a dual beam charge compensation system and constant pass energy of 50 eV. A binding energy range of 0 – 1200 eV was used to collect survey scans. The principal peaks of the elements present in the as-synthesised thin films Ti (2p), O (1s) and N (1s), as well as C (1s) and Si (2p),

were investigated by acquiring high-resolution peaks. These peaks were used to evaluate the concentration of element within the analysis region (spot size 400 μm). CASAXPS software was utilised to model the area underneath these peaks, using relative sensitivity factors to calculate the thin film composition and referenced to adventitious carbon at a binding energy (B.E.) of 284.4 eV.

### 2.2.3. Functional properties characterisation.

#### 2.2.3.1.1. Band gap determination.

Transmittance spectra were recorded over the 300 – 2500 nm range on a Helios double beam instrument. Band gap energies were determined through Tauc plots.[86]

#### 2.2.3.1.2. Photocatalytic test.

A model organic pollutant, octadecanoic (stearic) acid (95 %), was used to evaluate the photocatalytic response of the thin film coatings deposited in this chapter. A 0.05 M solution of stearic acid in chloroform was used to deposit a layer of this organic pollutant in the undoped and N-doped thin films, using a dip-coating process. UVA (*Vilber-Lourmat*, 2 x 8 W, 365 nm, 1.2 mW $cm^{-2}$) and/ or visible (*GE lighting 2D fluorescent GR10q-835 white, 28 W*) irradiation were used to evaluate the photocatalytic performance of the thin film photocatalysts. The loss of the dip-coated stearic acid layer was followed by measuring its characteristic C-H infrared bands at 2958, 2923 and 2853 $cm^{-1}$, which were integrated using a Perkin Elmer RX-I Fourier transform infrared (FTIR) spectrometer. The degradation of the stearic acid bands needs to be converted to the number of molecules of stearic acid degraded during the photocatalytic process. This conversion was performed following a work reported by Mills *et al*.,[87] where it was estimated that 1 $cm^{-1}$ of integrated area corresponds to 9.7 x $10^{15}$ molecules of stearic acid. A linear regression of the degradation process, at its

initial step (30 – 40 %), was used to assess the photocatalytic rate, which has been shown to possess zero-order reaction kinetics above a critical stearic acid concentration. The photocatalytic response was expressed as formal quantum efficiency (ξ), which has been described as molecules of acid degraded per incident photon (molec. photon$^{-1}$), and estimated accepting that all incident photons had the same energy (3.4 eV).

## 2.3. N-doped $TiO_2$ thin films: A study of the effect of the different nitrogen species (bulk and surface) on the photocatalytic properties of N-$TiO_2$ thin films.

### 2.3.1. Introduction.

No dopant within $TiO_2$ has been investigated more than nitrogen, producing a vast list of reports in photocatalysis, including a good number of reviews[35,77,79,80] and patents.[81] These materials have become the archetypical visible-light-active $TiO_2$-based photocatalysts for a wide range of applications,[77] although the origin of their visible light activity is still a matter of debate. This is due to the ambiguous assignment of N species by X-ray photoelectron spectroscopy (XPS).[35,77,82] Nevertheless, general consensus has assigned two main positions as substitutional ($N^{3-}$, replacing oxygen) and interstitial ($N^0$, N…O groups with lattice oxygen) nitrogen, henceforth referred to as $N_s$ and $N_i$, with respective binding energies of *ca.* 396 and 400 eV.[83,84]

It has been commonly acknowledged that adding N within the lattice of $TiO_2$ results in a red-shift of the optical absorption and often additional features in the visible range. This effect has been widely explained on the basis of localised N 2p interband energy states above the upper O 2p valence band in $TiO_2$.[36,78,88] Different theoretical studies have reported that $N_s$ species raise the valence band energy due to the mixing between N 2p and O 2p orbitals, narrowing the bandgap energy of N-$TiO_2$ materials.[34,88,89] In contrast, it has been postulated that $N_i$ species form interband states (~ 0.74 eV) above the valence band, resulting in a dual-electron process, where electrons are initially

excited to the interband state and subsequently to the conduction band.[34] However, it is worth mentioning that narrowing the band gap of $TiO_2$ usually requires the use of high amounts of the dopant reagent which can be negative for photocatalytic applications as result of the increase of impurities added to the $TiO_2$ lattice.

The scientific community has been historically divided in regards to which N species, in particular substitutional ($N_s$) or interstitial ($N_i$) nitrogen, are allegedly responsible for the enhanced sensitivity of N-$TiO_2$ photocatalysts.[77] In the last few years, there have been a wide number of works attributing the visible light activity of N-doped photocatalysts to the narrowing of the bandgap energy of $TiO_2$ upon the substitution of $O^{2-}$ by $N^{3-}$ species.[36] In contrast, the presence of $N_i$ within the $TiO_2$ lattice has been reported to beneficially enhance the UV light sensitivity of N-$TiO_2$ films.[90] The latter forms N-O groups with lattice oxygen in the $TiO_2$ structure. Unfortunately, a range of different $NO_x$ groups, chemisorbed molecular nitrogen ($\gamma$-$N_2$) and $NH_x$ species with similar binding energies (*ca.* 400 eV) are often present,[34,35,77,83,91] hindering the assignment of the nitrogen species, as well as their role in the photocatalytic activity. It has also been suggested that the visible light activity is due to inherent oxygen vacancies ($V_0$) formed in the incorporation of $N^{3-}$ anions in the $TiO_2$ structure.[35,92] Furthermore, other authors have observed correlation between visible light activity and an optimum loading of defect sites in the form of Ti≡N triple bonds in *modified* N-$TiO_2$ materials containing a single surface peak at *ca.* 397.5 eV.[93]

The photocatalytic performance of N-$TiO_2$ materials has been commonly missed by arguable assessments of visible light activity, which is often determined in the photocatalytic process (photo-oxidation and /or photo-reduction) of dyes, as well as using irradiation conditions which could lead to a dye-sensitised process through the direct participation of the dye in the reaction. However, visible-active photocatalysis of

organic pollutants has been claimed by many authors.[88,94–96] It is worth mentioning that these processes require the engineering and design of an appropriate photoreactor with cut-off filters, which would prevent any secondary bands at half-wavelength in the UV range (even for monochromated light), and control of any potential thermal degradation of the target organic pollutant, *etc*. Further, many of photocatalytic studies involve the use of materials with varied physical properties, such as crystallinity, morphology, surface area, *etc.*; as well as unknown ratios of $TiO_2$ polymorphs, *etc.* This would inhibit an adequate comparison between the photocatalytic efficiencies of undoped and N-doped photocatalysts. Moreover, the addition of nitrogen (*doping*) within the $TiO_2$ structure can often be argued, especially when the dopant specie is added as a post-treatment process.

In this section, we will explore the photocatalytic performance of N-$TiO_2$ thin-films using different N precursors (*tert*-butylamine, benzylamine and ammonia), to the photocatalytic degradation of stearic acid, a model organic pollutant. The use of these precursors was intended to create different synthesis environments, helping to clearly establish a correlation between surface and bulk nitrogen species and the photocatalytic behaviour of the N-$TiO_2$ films. We observed a loss of the XPS peak at *ca*. 400 eV ($N_i$), as well as a decrease in photoactivity upon UV cleaning and after sequential stearic acid tests, which suggests the direct participation of N species in enhancing the UV light activity. The N-doped species predominantly enhance the UV photocatalysis of the films- however we observe that these dopants are partially consumed in the photocatalytic process through a minor degradation pathway- which results in the activity diminishing over time. It is worth noting that O-rich conditions, such as those used in wet processes induce the formation of interstitial $N_i$ and $NO_x$ species, whilst O-deficient (reducing) conditions would favour the incorporation of $N_s$ in O lattice sites.

### 2.3.2. N-doped $TiO_2$ films synthesis.

All $TiO_2$ thin films used in this chapter, N-doped and undoped, were synthesised using APCVD processes. Undoped $TiO_2$ thin films were synthesised using titanium (IV) chloride ($TiCl_4$, 99.9 %) and ethyl acetate ($C_4H_8O_2$, 99 %) as titanium and oxygen sources, respectively. N-$TiO_2$ films were formed using either *tert*-butylamine ($C_4H_{11}N$ 99.5%), benzylamine ($C_7H_9N$ 99%) or ammonia ($NH_3$, oxygen free) as nitrogen sources. All precursors were contained in stainless steel bubblers at appropriate temperatures to create gaseous reactants which were carried through the CVD rig. The enriched gases were combined in stainless steel mixing chambers at 250 ºC and carried through a triple baffle manifold into the APCVD reaction chamber using pre-heated $N_2$ gas. In a standard N-$TiO_2$ deposition, the temperatures of the bubblers containing the titanium, oxygen and nitrogen sources were hold at 68, 38 and 5 ºC, respectively. The temperature of the nitrogen bubbler (5 °C) was achieved using an ice-bath and it was applied to both *tert*-butylamine and benzylamine chemical reagents; ammonia flowed under its own vapour pressure from a gas cylinder. The corresponding mass flow rates of titanium and oxygen sources were 6.7 x $10^{-3}$ and 3.1 x $10^{-3}$ g $min^{-1}$. The flow rate conditions of the N precursors are indicated in Table 2.1. The films were deposited at 500 °C on float glass substrates (225 x 90 x 4 mm; length x width x thickness). Further experimental details are also included in Table 2.1, such as N source, atomic concentration of each N specie at the photocatalyst surface and bulk, deposition time, thin film thickness (obtained from Swanepoel method and side-on view SEM), as well as photocatalytic values expressed as formal quantum efficiency ($\xi$).

All $TiO_2$ thin films, both undoped and N-doped, showed interference fringes, which are typical of thin film materials with high refractive indices. These interference bands are

associated to a varying film thickness across the substrate, with the bands peaking within the centre of the film (**Figure 2.2**). This indicates an increase in thickness towards the middle section of the film. Undoped $TiO_2$ thin films were colourless and translucent, whereas N-$TiO_2$ thin films presented a yellowish tint, characteristic of nitrogen-doped $TiO_2$ materials. All thin films used in this chapter were adhesive and resistant to the Scotch tape test,[97] with no particles being peeled off, as well as resisting a scratch test using a steel scalpel[98] and are indefinitely stable in air. It is worth noting that all as-synthesised coating surfaces showed no pin-hole defects and no particulates were observed in the exhaust gas.

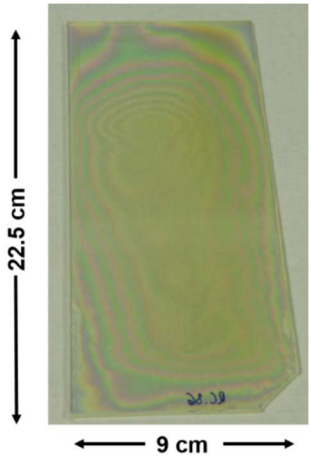


**Figure 2.2.** Picture of a characteristic N-doped $TiO_2$ thin-film. The interference fringes observed in the thin-film are characteristic of thin-film materials with high refractive indices. These different interference bands allowed an investigation at the effect of different thickness on the physical and functional properties of undoped and N-doped titania thin-films.

**Table 2.1**. Experimental and synthesis details of the as-synthesised films used in this section, undoped and N-doped $TiO_2$ thin films. The metal ($TiCl_4$) and oxygen ($C_4H_8O_2$) sources were set at constant temperature and mass flow parameters: 68 and 38 °C and 6.7 x $10^{-3}$ and 3.1 x $10^{-3}$ g $min^{-1}$, respectively.

| Sample # | N source | N Mass Flow/$10^{-4}$ (g $min^{-1}$) | Bulk N species (at%)[a] | | Surface N(i) (at%) | Deposition time (s) | d[b] (nm) | $\xi/10^{-4}$ (molec $photon^{-1}$)[c] |
|---|---|---|---|---|---|---|---|---|
| | | | N(i) | N(s) | | | | |
| Ti1 | – | – | – | – | – | 60 | 253 | 0.63 |
| Ti2 | – | – | – | – | – | 120 | 744 | 0.92 |
| NTi1 | $NH_3$ | 4040 | 1.69 | 7.75 | 3.70 | 60 | 370 | 0.10 |
| NTi2 | $NH_3$ | 760 | 0.21 | 0.41 | 3.79 | 60 | 370 | 0.04 |
| NTi3 | BA | 0.08 | 0.15 | 0.18 | 1.82 | 60 | 555 | 0.07 |
| NTi4 | BA | 0.03 | 0.41 | 0.27 | 3.04 | 60 | 461 | 1.01 |
| NTi5 | BA | 0.02 | 0.11 | 0.13 | 3.19 | 60 | 468 | 2.30 |
| NTi6 | BA | 0.11 | 0.10 | 0.14 | 2.46 | 60 | 584 | 0.05 |
| NTi7 | BA | 0.02 | 0.08 | 0.13 | 1.80 | 60 | 357 | 0.07 |
| NTi8 | BA | 0.02 | 0.01 | 0.11 | 0.64 | 60 | 416 | 1.24 |
| NTi9 | BA | 0.02 | 0.08 | 0.15 | 0.66 | 60 | 483 | 1.11 |
| NTi10 | TBA | 13.50 | 0.23 | 0.65 | 3.06 | 60 | 334 | 1.23 |
| NTi11 | TBA | 13.50 | 0.11 | 0.26 | 1.56 | 120 | 665 | 2.45 |
| NTi12 | TBA | 13.50 | 0.06 | 0.14 | 0.93 | 120 | 703 | 1.30 |
| NTi13 | TBA | 12.70 | 0.37 | 1.51 | 4.13 | 60 | 237 | 1.06 |
| NTi14 | TBA | 59.40 | 0.94 | 4.43 | 2.08 | 60 | 290 | 0.35 |

$NH_3$= ammonia, BA= benzylamine and TBA= *tert*-butylamine. [a]$N_{(i)}$= interstitial nitrogen and $N_{(s)}$= substitutional nitrogen. The atomic concentration of each N specie was measured using XPS analysis and CASAXPS software. [b]d= Film thickness estimated from cross-sectional SEM and Swanepoel method. [c]ξ= Formal quantum efficiency.

### 2.3.3. Results and discussion.

#### 2.3.3.1. Structural properties.

X-ray diffraction and Raman analyses showed that all undoped and N-doped $TiO_2$ thin films were only composed of the anatase phase structure, with no traces of other $TiO_2$ polymorphs or nitrogen-based materials, such as titanium nitride or any other nitrogen-containing structures, being detected (**Figure 2.3 (a) and (b)**). The XRD patterns of N-doped and undoped films showed comparable peak broadening (FWHM ~0.5°), peak intensities and peak area ratios at low concentrations of N (**Figure 2.3 (a)**), which ruled

out the influence of long-range order crystallinity as responsible for the drastic changes in photoactivity.

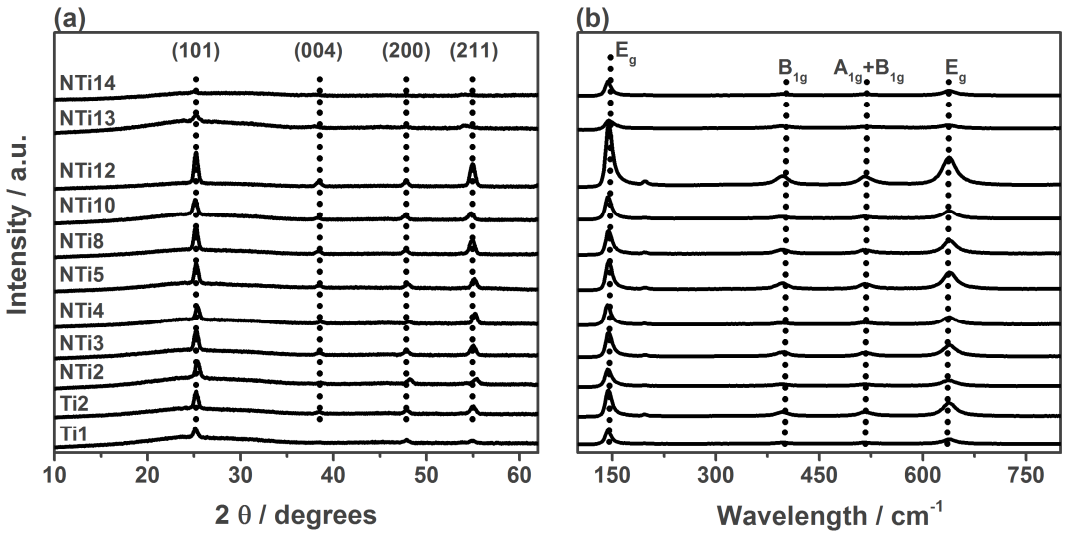


**Figure 2.3**. Representative films from the different nitrogen sources used to synthesise N-$TiO_2$ thin-films, ammonia, benzylamine and *tert*-butylamine. (a) X-ray analysis diffraction patterns showed that the different nitrogen precursors did not have a drastic impact on the crystallinity of the films using low concentrations of N, when compared with undoped $TiO_2$ (Ti1 and Ti2). However, upon an increase in the N concentration it can be observed an important decrease in the crystallinity of the films. (b) Raman spectroscopy analysis also confirmed the presence of solely anatase phase and that low concentrations of N do not change drastically the physical properties of $TiO_2$ films.

In contrast, it can be clearly observed in Figure 2.3 how XRD patterns turned into less intense and broader peaks upon an increase in N content, which agrees with previous reports in the literature where the physical properties of N-$TiO_2$ thin films was affected by the doping process.[75,90,99] These results were corroborated by Raman spectroscopy, where only anatase phase of $TiO_2$ was observed in all films and the major scattering $E_g$ band, typically found at 144 $cm^{-1}$ in undoped anatase, was shifted to lower wavenumbers when $TiO_2$ was doped with nitrogen (**Table 2.1**). The $E_g$ mode represents phonons operating primarily in the *a*-axis of the tetragonal unit cell. In this section, it was found that the use of high concentrations of nitrogen (> 12 at. %) showed traces of additional phases, which likely corresponded to oxynitride compounds. Therefore, only

N-$TiO_2$ films with nitrogen levels lower than 12 at.% were considered for the photocatalytic studies in this chapter.

Scanning electron microscopy (SEM) images of undoped $TiO_2$ thin films (**Figure 2.4**) revealed a relatively rough surface formed by large diamond-like aggregated particles. It can be observed in Figure 2.4 that N-$TiO_2$ films deposited using *tert*-butylamine and benzylamine showed similar surface morphologies, being slightly more compact than that of undoped $TiO_2$ films with flat particles merged together, particularly in the case of *tert*-butylamine. In contrast, the use of ammonia, as a nitrogen source, showed a dramatic changed in the morphology of the N-$TiO_2$ films, agreeing with previous studies.[36,99] Overall, it can be concluded that N-doping decreased the crystallite size of the N-$TiO_2$ films, resulting in an increase of the particle size.

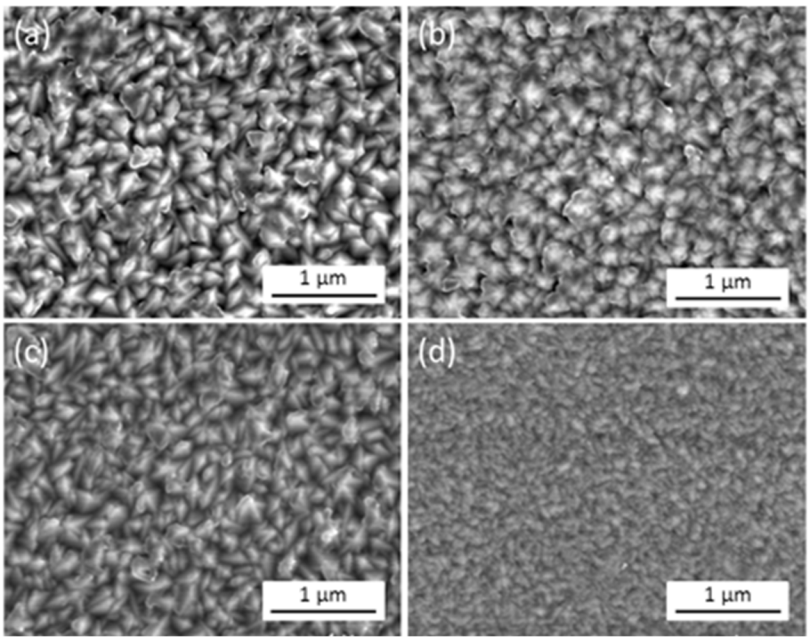


**Figure 2.4**. Scanning electron microscopy (SEM) images (x25,000 magnification) of (a) undoped and (b-d) N-$TiO_2$ films deposited using (b) tert-butylamine, (c) benzylamine and (d) ammonia as nitrogen precursors.

### 2.3.3.2.Optical properties and band gap determination.

UV-Visible absorption spectroscopy was used to determine the reflectance and transmittance of our undoped and N-doped $TiO_2$ films. These two optical measurements were used to calculate the light absorbed by the N-$TiO_2$ thin films, and thus determine the band gap through a Tauc plot.[86] This analysis plots $(\alpha h\nu)^{1/2}$ against light energy (eV), where α is the absorbance of the thin film, *h* is the Planck's constant and ν is the frequency of the light at the absorbing wavelength. The change in absorbance with wavelength was measured from 250 to 2500 nm, completely encapsulating the band gap of undoped $TiO_2$, *ca.* 380 nm. This approach to measure the band gap of semiconductors is a straight forward approach for semiconductors with an indirect bandgap, as $TiO_2$,[100] this plot is linear close to the absorption onset point of the semiconductor material. Thus a simple extrapolation of the intersection between the two different axis, energy (x axis) and $(\alpha h\nu)^{1/2}$ (y axis), generates the band gap energy.

UV-Visible spectra of undoped $TiO_2$ samples showed colourless and transparent films, with an absorption onset at *ca*. 380 nm and maximum absorbance at 330 nm and below, whereas the N-$TiO_2$ films showed a yellow tinge, typical from N-doped materials, and their corresponding absorption onsets were red-shifted with respect to that of the undoped films (**Figure 2.5**). Figure 2.5 shows the transmittance and the Tauc plot determination, as an inset, performed by the different N-doped thin-films using different nitrogen sources. It is worth mentioning that when benzylamine was used as nitrogen source no changes in the optical properties of N-$TiO_2$ were observed compared to undoped $TiO_2$ films. These N-$TiO_2$ thin films presented mainly $N_i$ incorporated into the lattice of $TiO_2$, determined through depth profiling XPS analysis, which agrees previous theoretical studies,[101,102] where computational modelling showed the

formation of an interband state above the valence band of $TiO_2$ materials. It is worth mentioning that this interband state was found difficult to assess by experimental groups. Ananpattarachai *et al.*[103] reported no changes in the absorption onset of their N-doped materials, suggesting that these N-$TiO_2$ materials did not present a narrowing of its bandgap energy. Interestingly, both groups found a slight red-shift in the tail onset of the N-$TiO_2$ materials, which could explain the enhanced photocatalytic efficiency of the N-$TiO_2$ materials. However, such a tail shift was not observed in our N-$TiO_2$ films.

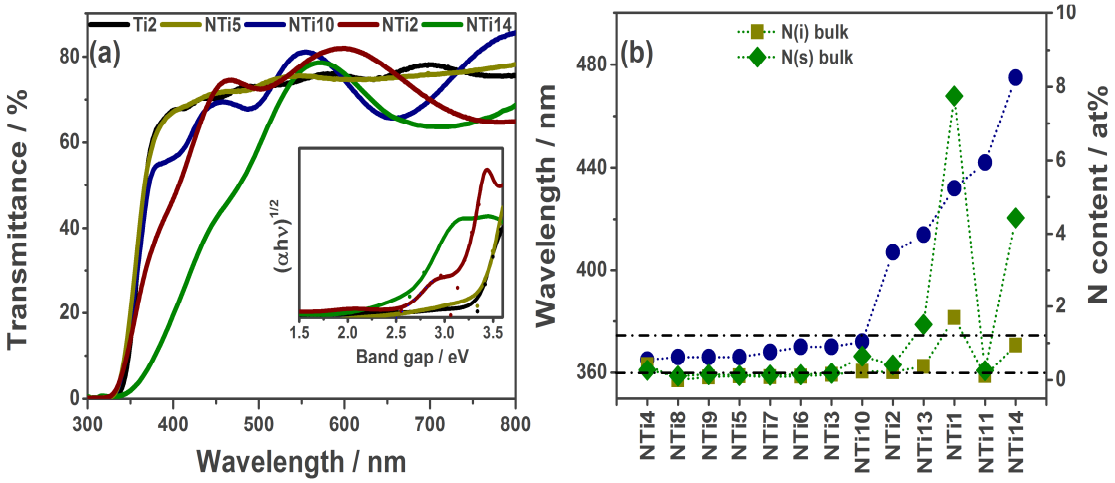


**Figure 2.5.** (a) UV/Vis spectra of pristine (black line) and selected N–$TiO_2$ films: Ti2 (undoped $TiO_2$, black line), NTi5 (using benzylamine as N source, yellow line), NTi10 (low concentration of N using *tert*-butylamine as N source, blue line), NTi2 (low concentration of N using ammonia as N source, red line) and NTi14 (high concentration of N using *tert*-butylamine as N source, green line). Inset: Tauc plots assuming all films are indirect bandgap semiconductors. (b) Shift in optical transmission at 50 % (blue line) and corresponding nitrogen content in the films, given as interstitial (N(i), full green diamonds) and substitutional (N(s), full green triangles) nitrogen species. The dashed horizontal lines indicate the optical shift (50 %) for a range of undoped $TiO_2$ films of different thicknesses. The film description and experimental details of the samples are given in Table 2.1.

In contrast, we observed that the use of the other nitrogen sources, *tert*-butylamine and ammonia, resulted in N-$TiO_2$ films with relatively high content of nitrogen (> 4 at. %)

These N-$TiO_2$ films contained both $N_i$ and $N_s$, showing additional absorption bands in the range of 400 – 450 nm (related to several optical absorption edges of the film), and a red-shift of the absorption onset. It is not surprising that the presence of this substitutional species (N-$TiO_2$ films synthesised using *tert*-butylamine and ammonia) showed a change in their absorption onset, as well as in their light transmittance (**Figure 2.5 (a) and (b)**), resulting in a red-shift of the band gap of N-$TiO_2$ films. This is because these $N_s$ species narrow the band gap energy by mixing N 2p and O 2p orbitals, resulting in a raise of the energy of the valence band towards the conduction band. Therefore, it can be concluded that increasing the amount of $N_s$ species, within $TiO_2$, resulted in narrower bandgap energies. The absorption features observed in this chapter are consistent with previous works.[35,36,89,104,105]

#### 2.3.3.3. Impact of nitrogen species on the photocatalytic activity of N-$TiO_2$ films.

X-ray photoelectron spectroscopy (XPS) studies at the surface of the N-doped $TiO_2$ films (**Figure 2.6**), showed a predominant peak at 400 eV, which is generally attributed to the overlap of different N species, such as $N_i$, $NH_x$ groups and chemisorbed molecular nitrogen ($\gamma$-$N_2$). It is worth mentioning that additional peaks were sometimes observed at the surface of the films, particularly when using ammonia and benzylamine as nitrogen precursors. For instance, Figure 2.6 shows additional peaks at *ca*. 402 eV, assigned to adsorbed N–O groups (N–O–Ti–O or O–N–Ti–O),[106] which was found detrimental from a photocatalytic point of view, as it will be discussed in detail in this section.

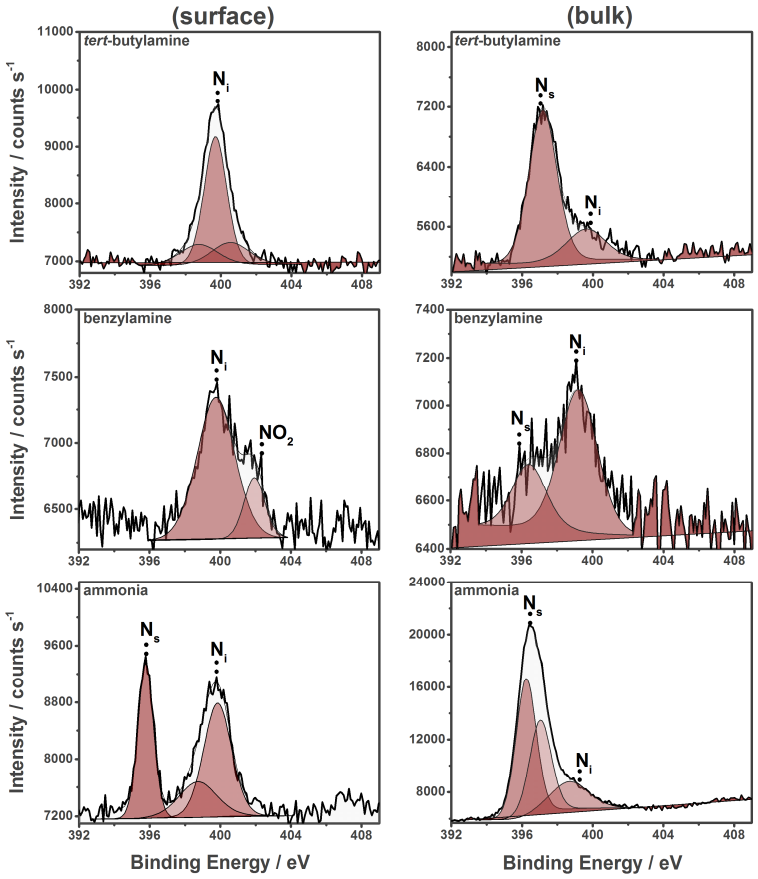


**Figure 2.6.** X-ray photoelectron spectra (XPS) of the N 1s environment for representative N-doped $TiO_2$ films as-synthesised *via* tert-butylamine, benzylamine and ammonia. The left column shows XPS spectra of the surface of N-$TiO_2$ films and the right column shows XPS average spectra collected during depth profiling analysis (right column). $N_s$ and $N_i$ correspond to $N^{3-}$ (substitutional) and $N^0$ (interstitial) species, respectively.

The photocatalytic performance of the N-doped and undoped $TiO_2$ films was evaluated during the degradation of stearic acid, a model organic pollutant, under UVA and visible light irradiation (**Figure 2.7**). Comparison between these activities and their corresponding bandgap energies, as estimated from Tauc plots (**Figure 2.5**), was attempted (**Table 2.1**). However, no correlation was clearly observed under the irradiation conditions used in the preliminary tests. The main reason for this divergence is likely due to the role of surface species which are inherently formed in the deposition of the films. The surface chemistry of the doped materials and the photocatalytic testing method employed must be considered before any conclusion can be raised regarding

the influence of the dopant in the electronic properties of $TiO_2$ films. For instance, in this chapter we have observed direct correlation of surface nitrogen-containing species and degradation of stearic acid, which results in *apparent* photocatalytic activity under UVA irradiation. This surface reaction likely occurs via formation of N-containing radicals under the experimental conditions used in this chapter.

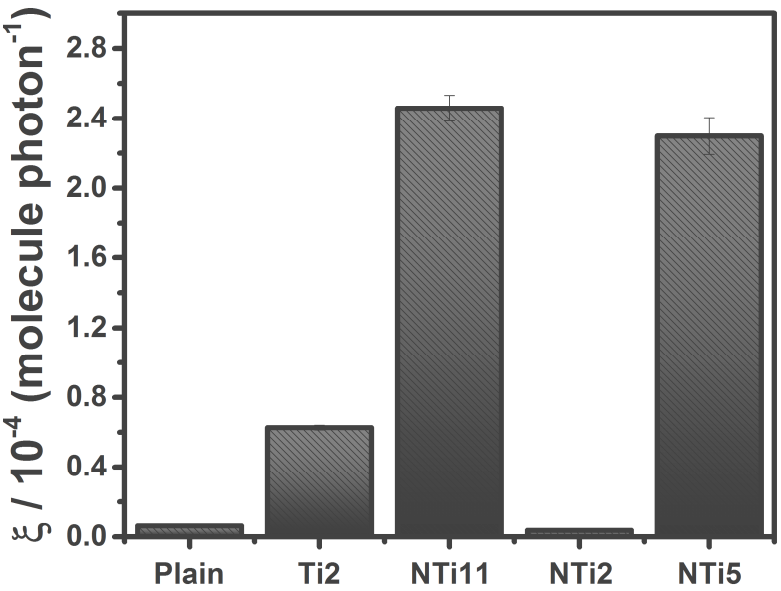


**Figure 2.7.** Formal quantum efficiencies (FQE) of typical undoped and N-doped $TiO_2$ films, as deposited using low concentration of *tert*-butylamine (NTi11), low concentration of ammonia (NTi2) or low concentration of benzylamine (NTi5) as nitrogen precursors, determined from the photodegradation of stearic acid under UVA irradiation (1.2 mW $cm^{-2}$). The apparent activity of plain glass is included for reference. Full experimental details of the samples are given in Table 2.1.

The apparent enhanced activity of the doped samples deposited using *tert*-butylamine could be discussed in terms of reactive N species present on the surface of the photocatalyst. In particular, a correlation was established between the performance of the photocatalyst and the concentration of N species with binding energies at *ca*. 400 eV, as identified using XPS analysis, which likely correspond to surface $NH_x$ groups. The material is thus sensitised for as long as these surface species are present on the surface, but this extrinsic activity drastically decreases once the active surface groups are consumed in the reaction. This finding is also consistent with the moderate activities observed in the case of N-doped samples deposited from benzylamine (**Figure 2.7**).

The latter showed relatively low amounts of nitrogen within the bulk, as evidenced by XPS analysis (**Figure 2.6**), and the corresponding apparent activities were only slightly improved compared to those of pure $TiO_2$ films. The negligible average activity of the doped films deposited from ammonia, for instance sample NTi2, as shown in Figure 2.7, could be explained considering the critical surface deterioration of these films upon the doping process (**Figure 2.4**).

In addition, the presence of N–O surface species was found highly detrimental in the photocatalytic performance of the N-doped films. Figure 2.8 shows the photocatalytic activity, given as formal quantum efficiency, of typical N-$TiO_2$ films. It was observed that those films containing N–O–Ti–O (or O–N–Ti–O), $NO_2^-$ and/or $NO_3^-$ groups, with binding energies at *ca*. 401, 403 and 408 eV, respectively, showed no (or low) activity under UVA light irradiation. This effect is illustrated in the schematic Figure 2.8. Only N-$TiO_2$ films containing N surface species with binding energy at *ca*. 400 eV *alone* were highly active compared to pure $TiO_2$ films under UVA illumination and their activity correlated with the concentration of these surface species, as evaluated by XPS. In this case, the activity of the films could be *sensitised* by surface groups rather than influenced by an intrinsic mechanism in the *doping* of the semiconductor.

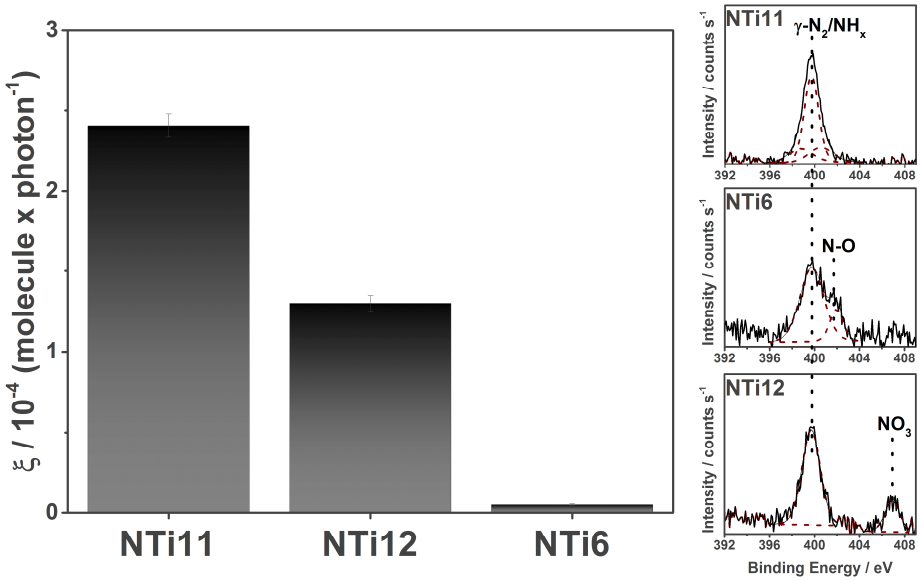


**Figure 2.8.** Photocatalytic activity (given as formal quantum efficiencies) of N–$TiO_2$ films deposited using low concentrations of *tert*-butylamine as nitrogen precursor (samples NTi11 and NTi12) and high concentrations of benzylamine (sample NTi6), and corresponding surface XPS data in the N 1s environment (right column), showing the presence of different $NO_x$ groups. The film description and experimental details of the samples are given in Table 2.1.

Further photocatalytic testing of the N-doped $TiO_2$ films was carried out under visible light (75 Xe lamp, AM 1.5 G), with a long-pass filter (cut-off $\lambda > 420$ nm, *Melles Griot*). The rates of degradation of stearic acid molecules ($R_{SA}$, units: molec $cm^{-2}$ $s^{-1}$) on selected N-$TiO_2$ films are shown in Figure 2.9. Similar results have been reported in the literature, and thus it could be tempting to correlate these activities with the N content in the films. Nevertheless, the results reported in this chapter are compromised by the *apparent* activity of the undoped film (Ti2), which points to potential UV leaking through the cut-off filter, and the poor fitting of the degradation curves ($r^2 < 0.90$), suggesting that no visible light activity could be determined beyond instrumental error. Indeed, as shown in Figure 2.9(b), the apparent activity of NTi13 was negligible compared with that of a standard P25 *Evonik* dip-coated film, synthesised following the optimal conditions reported by Mills *et al.*,[107] under identical conditions. It is worth mentioning that P25 consists of a ~ 3:1 ratio of anatase and rutile,[108] the bandgap of

either material falls below 420 nm, therefore, some light was certainly leaking through for this material to be so active.

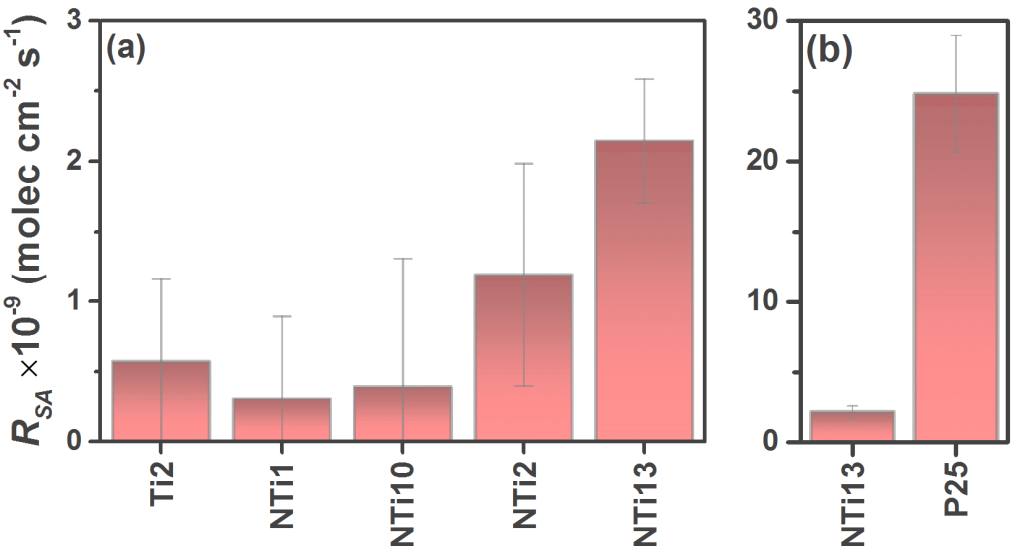


**Figure 2.9.** (a) Photocatalytic performance of undoped and N-doped $TiO_2$ films under visible light illumination (75 Xe lamp, AM 1.5 G, $\lambda > 420$ nm). (b) Comparison between the corresponding activities of the best N–$TiO_2$ sample (NTi3) and a dip-coated P25 $TiO_2$ film. The film description and experimental details of the samples are given in Table 2.1.

It could be finally concluded that the potential visible light sensitation mechanism with participation of $NH_x$ groups, as described by Shishido *et al.*[109] could not be confirmed. The implementation of visible-active N–$TiO_2$ compounds seems to involve several crucial elements, including a selective type of surface species and a restricted number of lattice defects for the promotion of charge diffusion. As such, the occurrence of only one element would not result in visible light activity. For instance, assuming the sensitising N species to be those with binding energy at 400 eV, the co-existence of other N species could deactivate the sensitisation mechanism, as observed in the UV light experiments. Likewise, the conditions that would result into appropriate N species may also induce lattice defects, which may act as charge recombination centres and thus counteract the visible-light sensitisation.

### 2.3.3.4. Photostability of N-$TiO_2$ films.

In this chapter, we evaluated the photostability of the as-synthesised N-$TiO_2$ films by carrying out sequential photocatalytic tests under UVA irradiation. The samples were cleaned using chloroform, under stirring conditions, to remove any remain of stearic acid before a fresh layer of stearic acid was dip-coated; herein, the sample will be labelled as NTi5-chloro. Interestingly, it was observed a linear decrease of the photoactivity rates (**Figure 2.10**) until a minimum value, which was similar to the photoactivity efficiency of the analogue undoped $TiO_2$ films. XPS analysis was used to study the influence that photocatalytic cycling has on the nitrogen species at the surface of the NTi5-chloro film. Figure 2.10 shows a concomitant decrease of the interstitial nitrogen peak (400.6 eV, $N_i$), as well as the formation of a weak new peak at 407.6 eV, which is assigned to nitrate species ($NO_3^-$, $N^{5+}$).

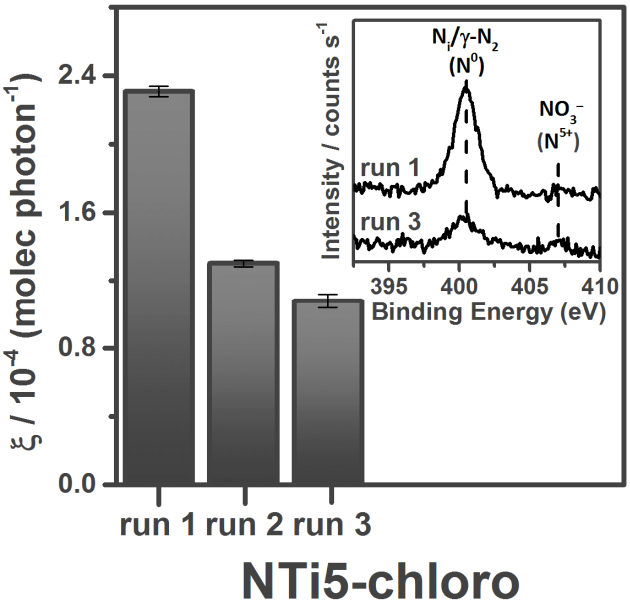


**Figure 2.10.** Formal quantum efficiencies (ξ), of sequential photocatalytic tests of a selected N-$TiO_2$ (NTi5) film using UVA irradiation. The sequential runs were labelled as run 1, 2 and 3. The changes of the N 1s environment at the surface of the N-$TiO_2$ film, before (run 1) and after (run 3) the photocatalytic cycling, are included as an inset. The binding energies of $N_i$ and $NO_3^-$ are included for reference. Sample NTi5 was synthesised using low concentrations of N and benzylamine as N source, further experimental details are given in Table 2.1.

The N-$TiO_2$ films used in this section were UV *cleaning*, using UVA (or UVC) irradiation, which is a common method to degrade (*clean*) organic contaminants from the surface of photocatalytic materials. This method was used to study the nature of the N 1s environment peak observed on the surface of as-synthesised N-$TiO_2$ films at 400.6 eV, as well as its role in their photocatalytic response. Surprisingly, XPS analyses of the surface of N-$TiO_2$ films showed relevant changes of the surface N species upon UVA cleaning of the N-$TiO_2$ films, using high humidity conditions, wet-air was flushed through the samples. Figure 2.11(a) illustrates the effect of UVA illumination (1.2 mW $cm^{-2}$) on a typical N-$TiO_2$ film (NTi10). It can be observed that, after irradiation for 48 h, the initial surface peak at 400.6 eV ($N_i$) decreased to approximately half of the initial area (NTi10/UV) and a new XPS peak at 407.6 eV ($NO_3^-$) appeared. This observation suggests that a partial photo-oxidation of the N species, with binding energy of 400.6 eV, resulted in the formation of $NO_3^-$ groups on the surface of the film. It is worth mentioning that these changes in the oxidation state of the surface N species decreased the photocatalytic performance of the N-TiO2 film (**Figure 2.11(b)**). These nitrate species may be formed and sat on active sites within the surface of the N-$TiO_2$ film, poisoning its photocatalytic performance. However, it is worth noting that regardless of removing the $NO_3^-$ species from the surface of the photocatalyst, upon washing the film in distilled water (NTi10/$H_2O$), the photocatalytic response of the film remained at low photoactivity values (**Figure 2.11(a)**). Interestingly, Figure 2.11 shows a correlation between the decrease of the surface N species at 400.6 eV and the photocatalytic values of the washed NTi10/$H_2O$ film, suggesting that the adsorbed N

species ($N_i$) may have a *direct* influence on the mechanism of stearic acid oxidation.

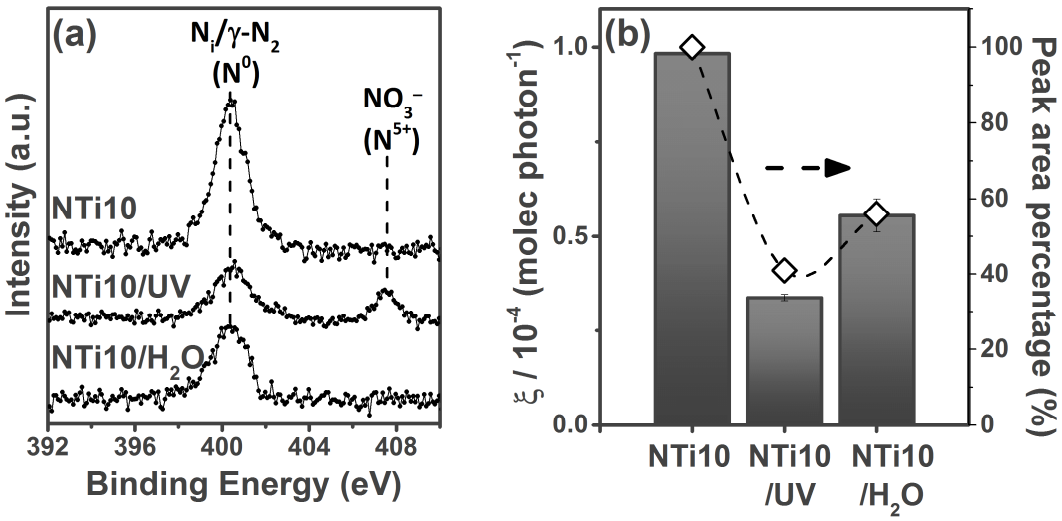


**Figure 2.11.** (a) X-ray photoelectron spectroscopy (XPS) spectra of N 1s environment at the surface of a selected N-$TiO_2$ film (sample NTi10, synthesised using low concentrations of N and *tert*-butylamine as N source), after being *cleaned* using UVA light (48 h, BLB lamp, 1.2 mW $cm^{-2}$) (NTi10/UV) and DI water (NTi10/$H_2O$). The binding energies of the surface N species at *ca*. 400 ($N_i/\gamma$-$N_2$) and 407.6 eV ($NO_3^-$) are included for reference. (b) Changes in the photocatalytic performance of sample NTi10 using identical UV illumination after each *cleaning* process with its corresponding XPS data (peak area percentage, calculated from CASA XPS fitting). Further experimental details and description of the photocatalyst are given in Table 2.1.

Further tests to investigate the photo-oxidation of the surface N species at 400.6 eV were carried out using XPS analyses and prolonged UVA irradiation (*ca*. 7 days), finding that these species were not completely photo-oxidised to $NO_3^-$ species after reaching a minimum value. Interestingly, once the surface N species were photo-oxidised to this minimum, it was observed that the activity of the NTi10 film was similar to that of undoped $TiO_2$ film analogue (Ti1). This effect may be explained due to the presence of different surface N species at comparable binding energies (*ca*. 400 eV) but with a very dissimilar chemical nature, $NH_x$ species. Therefore, the photo-oxidation of these species ($NH_x$) could potentially produce ·NO radicals, as well as highly oxidising species, including products of the reaction with superoxide ($O_2^{\bullet-}$) and hydroxyl radical groups, which may oxidise nearby organic molecules (**Figure**

**2.12(a)**). However, in the absence of nearby organic pollutants, the $NH_x$ species could also be photoconsumed, being oxidised into nitrate species (**Figure 2.12(b)**), while unreactive $N_i/N_2$ groups (also at *ca*. 400 eV) would remain on the surface. Therefore, the enhancement observed in the photocatalytic performance of N-$TiO_2$ photocatalysts could be the presence of active $NH_x$ species are present on the surface of the photocatalyst.

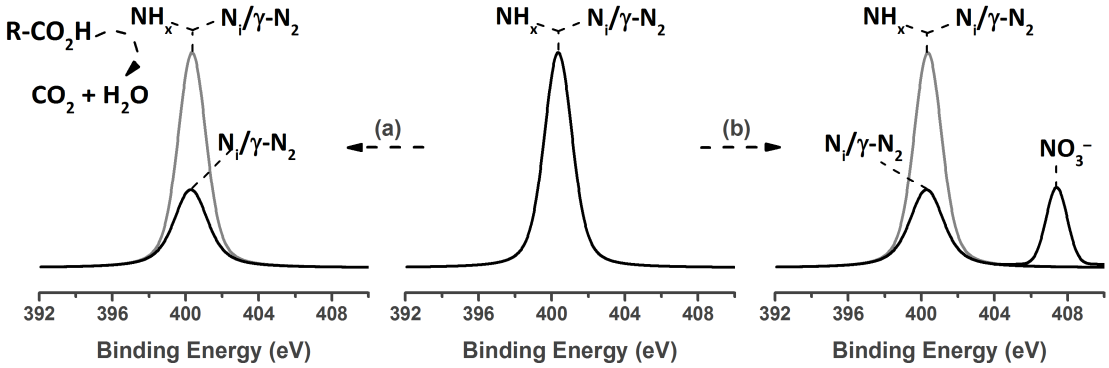


**Figure 2.12.** Schematic figure illustrating the proposed reactions of surface nitrogen species with binding energy at *ca*. 400 eV. The central XPS peak could be originated from concomitant N species such as (inactive) $N_i/\gamma$-$N_2$ and (active) $NH_x$ groups. (a) The mineralisation of an organic pollutant may be intermediated by highly oxidising species (N-O radicals) formed during photo-oxidation of $NH_x$ species. (b) In the absence of organic molecules, these radicals may readily form salt ($NO_3^-$) groups, as observed in this work. In both cases, (a) and (b), the remaining peak at 400 eV after the respective reactions is probably due to the inactive $N_i/\gamma$-$N_2$ species.

Interestingly, photoinduced deactivation of N-$TiO_2$ compounds has also been reported during visible light irradiation. *Nosaka et al*.[94] observed that the activity of their N-$TiO_2$ materials decreased to one half of the initial rate during degradation of 2-propanol after prolonged visible light illumination (100 h) using a 500 W super high-pressure Hg lamp with a glass UV filter. Consistent with our observations, these authors also observed a concomitant decrease of the main XPS peak in the N 1s environment. It is therefore possible that surface N species would have a role in the reported visible-light-driven reactions involving N-$TiO_2$ materials in the literature.

### 2.3.3.5. Conclusions.

A range of N–$TiO_2$ thin films were deposited *via* APCVD using a range of different N precursors, such as ammonia, benzylamine and *tert*-butylamine. The latter was found to be the most convenient precursor as N donor and also in terms of preserving the physical properties (crystallinity and microstructure, when the N concentration levels were kept below 1 *at*. %) compared to that of their undoped analogue films. Nitrogen was preferentially incorporated as substitutional nitrogen, $N_s$ (*ca*. 396-397 eV), in O sites, by replacing O within the $TiO_2$ lattice. In addition, nitrogen was also added to the $TiO_2$ structure as interstitial nitrogen, $N_i$ (*ca*. 400 eV), which were also clearly shown by XPS analysis.

The photocatalytic activity of the N-$TiO_2$ films was evaluated during mineralisation of stearic acid under UVA and visible light illumination. In this chapter, we have found that the presence of N is beneficial to enhance the photocatalytic properties of $TiO_2$. However, we also found that surface N species would have a main impact on the photocatalytic performance of the films under UVA illumination. Therefore, the enhanced activity observed may be attributed to a sensitisation mechanism with participation of surface species with binding energies of *ca*. 400 eV. Interestingly, XPS analyses showed that the presence of nitrate ($NO_3^-$) or nitrite ($NO_2^-$) groups on the surface of the films had a detrimental impact on the photocatalytic efficiency of N-$TiO_2$ films, since these species likely will be allocated on active sites of the photocatalytic material. In addition, we also found that other N–O groups, such as N–O–Ti–O or O–N–Ti–O, with binding energy of *ca*. 401 eV, were also detrimental from a photocatalytic point of view. Nitrogen leakage was also noticed for many samples before and after UVA irradiation, although it could not be confirmed unequivocally in some cases due to thickness gradients and N distribution across the films.

Finally, no visible light activity was observed for any of the N–$TiO_2$ films tested against the photo-degradation of stearic acid, despite the different APCVD conditions (precursor, and environment) used in this chapter. The idea of direct participation of surface N species on the photocatalytic activity of N–$TiO_2$ materials under visible light (visible-induced sensitisation) may be reinforced by the many reports claiming visible light activity from N-*modified* compounds, such as those obtained after post-treatment of pure $TiO_2$ materials.

In the following section of this chapter, we will explore the use of APCVD processes in a pulsed deliver mode to deliver stratified N-$TiO_2$ thin films, allowing to control the position, within the $TiO_2$ lattice, where the nitrogen precursor will be allocated. The stratified N-$TiO_2$ films will be physically and functionally investigated.

## 2.4. Stratified N-doped $TiO_2$ thin films.

### 2.4.1. Introduction.

As previously mentioned, the use of nitrogen to modify $TiO_2$ has been reported beneficial to broad the photoresponse of $TiO_2$, for solar photocatalysis applications. This has been widely explored by using different approaches, such as the design of $TiO_2$-based composite materials,[110,111] the modification of $TiO_2$ using dye sensitizers[112] and metal or non-metal species.[25,88,113–115] An interesting strategy, particularly adopted in recent years, is the selective incorporation of dopants (local doping) into semiconductor photocatalytic materials.[116–119]

The use of local doping would allow control over structural defects, contributing to a better understanding that the doping process has on the physicochemical and functional properties of N-doped $TiO_2$. Despite the potential benefits of doping to modify the band structure of $TiO_2$ materials, the indiscriminate addition of *impurities* (dopant species)

within the $TiO_2$ lattice could produce a severe impact on the structural properties (crystallinity, morphology, *etc*.) of the photocatalyst, which would potentially decrease its photocatalytic response. This has been widely reported by different groups when CVD methods were employed to synthesise doped $TiO_2$ thin films.[75,99]

An APCVD local doping approach, to synthesise doped films, can be used to deposit photocatalytic materials comparable to those produced using atomic layer deposition methods (ALD), which may be beneficial to minimise any structural impairment in the material. It is worth mentioning that ALD processes have been commonly employed to deposit nanostructured coating surfaces with nanoscale control,[120] which would facilitate the engineering of stratified films containing *buffer* layers. This led to the synthesis of nanostructured $TiO_2$ shells[121] and/ or ZnO-$TiO_2$ films,[122,123] where the photogenerated charge carrier transfer was increased by ultrathin layers of $TiO_2$, improving the efficiency of these solar cell devices.

In this section, we report the selective incorporation of nitrogen dopant species into $TiO_2$ films by using a pulsed precursor APCVD approach, to synthesise stratified N-doped $TiO_2$ thin films. This synthetic method was designed by adding the dopant specie only during intermittent periods of the total deposition time, resulting in the formation of N-$TiO_2$ layers within the $TiO_2$ bulk. This is, to the best of our knowledge, the first example of the synthesis of stratified doped photocatalytic thin films using CVD processes, a scalable and efficient operation/production method compared to ALD processes, capable of producing highly crystalline and robust coatings. We will also report that this approach will allow to add *relatively* high nitrogen content within the locally doped regions of the stratified N-$TiO_2$ films, without affecting the overall crystallinity of the stratified N-doped films, as evidenced by X-ray diffraction analyses. This will allow to effectively compare the photocatalytic response of non-stratified,

stratified and undoped $TiO_2$ analogue thin films, correlating the atomic concentration and nature of the dopant and their influence on the photocatalytic efficiency of the films used in this section.

### 2.4.2. Synthesis of undoped and nitrogen-doped $TiO_2$ thin films using APCVD.

In a typical $TiO_2$ deposition *via* APCVD, titanium (IV) chloride ($TiCl_4$) and ethyl acetate ($C_4H_8O_2$) are used as titanium and oxygen sources, respectively. Non-stratified and stratified N-doped $TiO_2$ films, as well as their undoped $TiO_2$ analogues were synthesised using a constant set up for titanium and oxygen sources. The temperatures of the titanium and oxygen bubblers were set at 67 and 38 ºC, with mass flow rates of $6.7 \times 10^{-3}$ and $3.1 \times 10^{-3}$ g $min^{-1}$. All films, undoped and doped, were synthesised at 500 °C on glass substrates coated with a $SiO_2$ barrier. Each substrate was carefully washed with acetone ($C_3H_6O$, 99 %), isopropanol ($C_3H_8O$, 99 %), distilled water and finally dried with air prior to their use.

Stratified N-doped $TiO_2$ thin-films were synthesised using APCVD processes by controlling the temperature, mass flow rate and deposition time of the nitrogen dopant chemical reagent, *tert*-butylamine ($C_4H_{11}N$). In the previous section of this chapter, we observed that this chemical reagent did not show apparent diffusion from the bulk of the N-$TiO_2$ film, and therefore it will facilitate the addition of nitrogen in selecting positions across the bulk of the N-doped $TiO_2$ thin film. The deposition of the non-stratified and stratified N-dope $TiO_2$ films was performed by controlling the volatility of the nitrogen source, *tert*-butylamine, with an ice bath at 3 °C. The film growth of the as-synthesised thin films used in this section ranged between 300-340 nm $min^{-1}$, as determined from side on view SEM analysis and Swanepoel method.[85]

The synthesis of the stratified N-$TiO_2$ films was designed to selectively incorporate the N specie using a pulsed delivery of the nitrogen precursor. Therefore, areas highly doped with N were introduce within undoped regions in the synthesis of the stratified N-doped thin films. X-ray photoelectron spectroscopy (XPS) analyses of the N species within the as-synthesised N-$TiO_2$ thin films used in this section, non-stratified, single-layer and multi-layer, are shown in Figure 2.13. The presence of the N species is shown as yellow areas. The synthesis of the non-stratified N-$TiO_2$ films was designed by flowing the nitrogen precursor during the entire deposition time (**Figure 2.13(a)**). However, the synthesis of the single-layer stratified N-$TiO_2$ film (SL) was engineered by adding the nitrogen source only half time (30 s) of the total deposition time (60 s) (**Figure 2.13(b)**). This was accomplished by maintaining the tap that regulates the nitrogen flow, close during the first and last 15 s of the film synthesis. A similar method was used for the synthesis of the multi-layer stratified N-$TiO_2$ thin films (ML) (**Figure 2.13(c)**), where the N tap regulator was maintained close during the first and last 15 s of the coating process and open in 5 s intervals. Further experimental details, including mass flow rates are included in Table 2.2. All thin films used in this chapter were adhesive and resistant to the Scotch tape test[97] with no particles being peeled off, as well as resisting a scratch test using a steel scalpel[98] and are indefinitely stable in air. It is worth noting that all as-synthesised coating surfaces showed no pin-hole defects and no particulates were observed in the exhaust gas.

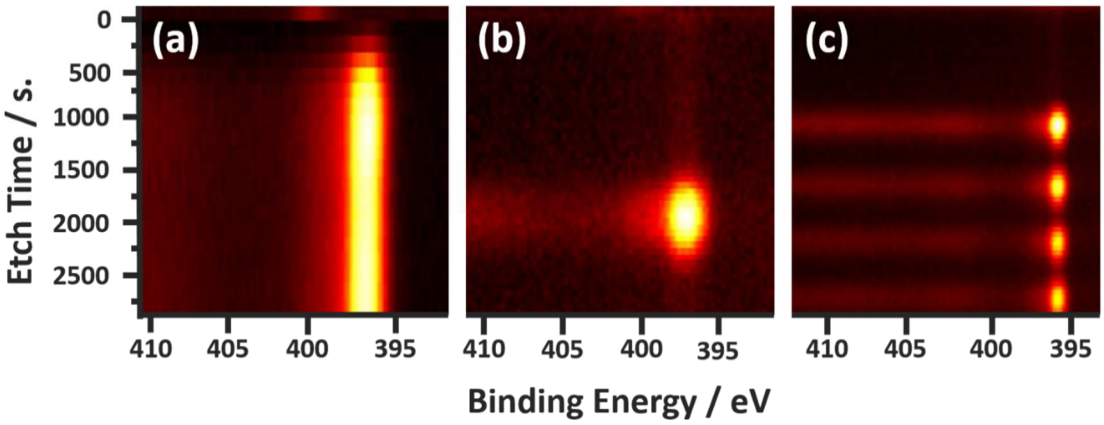


**Figure 2.13.** Depth-profiling X-ray photoelectron spectroscopy (XPS) analyses of the N 1s environment of selected N-$TiO_2$ thin films: (a) non-stratified, (b) single-layer stratified (SL) and (c) multi-layer stratified (ML) N-$TiO_2$ films. The regions with high amounts of nitrogen are represented by yellow areas. XPS fitting using the CASA XPS software showed that the N 1s environment corresponded to substitutional nitrogen species ($N_s$, 397 eV).

These locally N-doped $TiO_2$ thin-films were engineered by pulse precursor delivery APCVD, producing N-doped $TiO_2$ materials with high concentrations of nitrogen incorporated in specific positions within the bulk of the N-$TiO_2$ films. In this chapter, we will explore the use of this APCVD configuration to avoid the negative effect that high loadings of the dopant specie may have on the physical and functional properties of N-$TiO_2$ films. The impact of the stratified N-doping configuration and the influence of the type of nitrogen species on the enhanced photocatalytic activity will be discussed in the following sections. Several samples (more than 50), from each different thin film, were synthesised to prove the reproducibility of the method synthetic method reported in this section However, only selected thin films, with comparable thickness and physical properties, are presented.

**Table 2.2.** Sample description and experimental details for the deposition of undoped N-doped $TiO_2$ thin films. The temperature and mass flow conditions were constant for Ti and O precursors; being 68 °C, 6.7 x $10^{-3}$ and 37 °C, 3.1 x $10^{-3}$, respectively.

| Sample | Experimental Details | | | | |
|---|---|---|---|---|---|
| | Sample Description | N Mass Flow ($10^{-3}$) (g $min^{-1}$) | Deposition Time (s) | Film Growth (nm $min^{-1}$) | [N] (at. %) |
| Ti1 | Undoped | - | 60 | 305 | - |
| Ti2 | Undoped | - | 120 | 355 | - |
| N1 | Non-stratified | 5.9 | 60 | 265 | 2.0 |
| N2 | Non-stratified | 1.0 | 120 | 340 | 0.25 |
| SL | Single-layer | 1.3 | 60/30* | 390 | 0.60 |
| ML | Multi-layer | 1.3 | 120/25* | 330 | 0.65 |

*Fraction of total time for nitrogen precursor delivery.

### 2.4.3. Results and discussion.

#### 2.4.3.1.1. Physical and optical properties.

All undoped $TiO_2$ thin films, used in this chapter, were colourless and transparent with expected absorption edge values (~ 380 nm) (**Figure 2.14**). In contrast, N-$TiO_2$ thin films showed a yellow tinge, characteristic of N-doped $TiO_2$ films,[75] with their absorption onset red-shifted compared to that of their analogue undoped $TiO_2$ films (**Figure 2.14**). It is worth noting that this shift was not significant in the case of the single-layer N-$TiO_2$ film (SL), showing an absorption edge threshold similar to its undoped analogue films (~ 375-385 nm). Depth profiling XPS analysis of the SL film showed that the concentration of substitutional ($N_s$) and interstitial ($N_i$) nitrogen was comparable, agreeing previous theoretical and experimental works where an increase of the $N_i$ species showed negligible modifications of the absorption onset of N-$TiO_2$ thin films.[90,99,124] In contrast, the use of high concentrations of N resulted in an increase on the concentration of the $N_s$ species, leading to a red-shift of the optical properties of the N-$TiO_2$ films towards the visible range.[77,88,89] It is important mentioning that comparable non-stratified and stratified N-$TiO_2$ films showed similar optical properties, however, these estimations were made ignoring the scattering component in the spectra.

Interestingly, previous reports have shown similar changes upon the addition of high amounts of the dopant within the lattice of $TiO_2$,[116] however, correlation between these optical behaviour and the photocatalytic feature of N-$TiO_2$ photocatalysts has been a matter of historical controversy.[35]

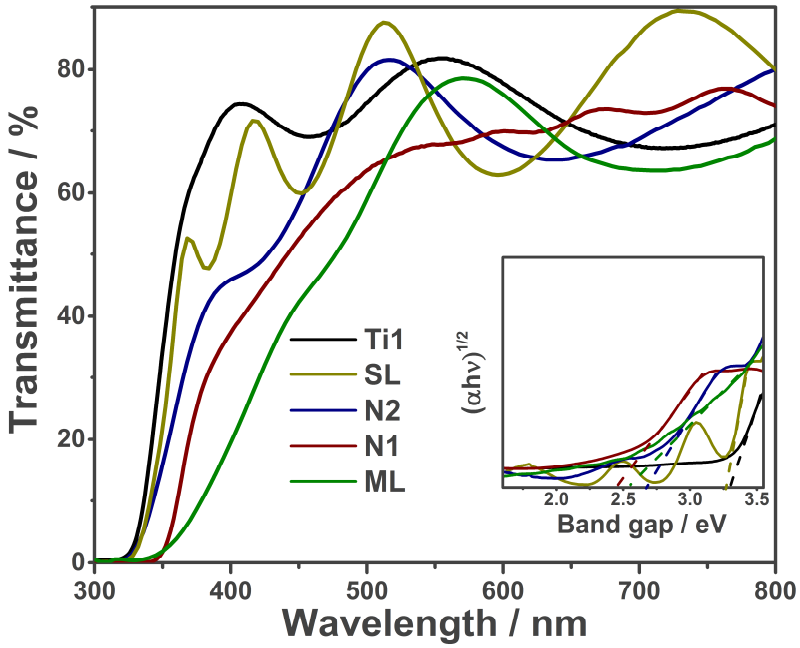


**Figure 2.14.** UV/Vis spectra of typical undoped (Ti1) and N-$TiO_2$ thin-films: non-stratified films with low (sample N2) and high (sample N1) concentrations of N (blue and burgundy patterns, respectively), as well as single-layer (SL, yellow pattern) and multi-layer (ML, green pattern) films, *tert*-butylamine was used as nitrogen source. The inset shows bandgap measurements derived from a Tauc plot of typical undoped $TiO_2$ and N-$TiO_2$ thin films synthesised by APCVD. Further sample and experimental details are given in Table 2.2.

Top-down view and cross-sectional scanning electron microscopy (SEM) analyses were used to investigate the surface morphology and film growth of the different films used in this chapter (**Figure 2.15**). It can be observed in Figure 2.15 that the nitrogen doping process did not affect the morphology of the as-synthesised thin films, showing large star-shaped aggregated particles. However, XRD studies of the N-$TiO_2$ films showed a drastic impact on the crystallinity of the as-synthesised thin films upon the addition of high amounts of the nitrogen dopant (**Figure 2.16(a)**). This effect was clearly observed upon comparison of the N-$TiO_2$ films and their undoped $TiO_2$

analogues, where the characteristic peaks of the anatase $TiO_2$ phase were broadened and decreased, agreeing previous works from the literature.[75,99,125] In contrast, XRD studies of the stratified N-$TiO_2$ films showed intense and sharp peaks (**Figure 2.16(c)**), suggesting that the overall crystallinity of the films was largely unaffected by the pulsed addition of high levels of nitrogen.

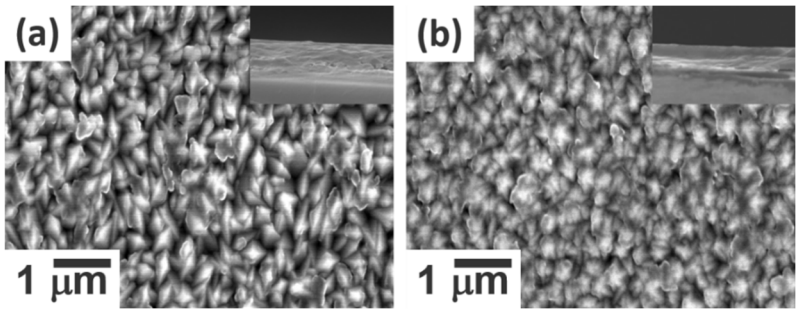


**Figure 2.15.** Scanning electron microscopy (SEM) images of typical (a) undoped and (b) stratified N-$TiO_2$ thin-films. Insets show cross-sectional SEM images of typical undoped and stratified N-doped $TiO_2$ thin-film.

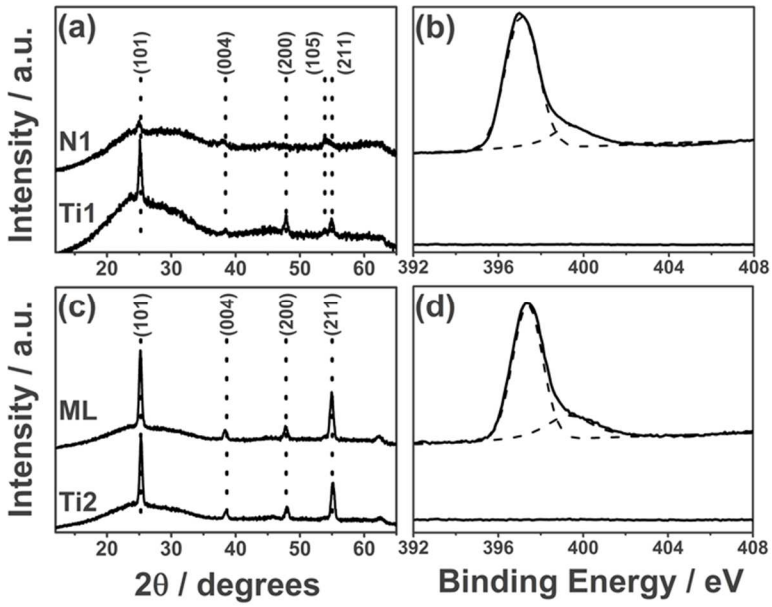


**Figure 2.16.** X-ray diffraction (XRD) and X-ray photoelectron spectroscopy (XPS) spectra of non-stratified, N1 (a and b) and stratified, ML (c and d) N-$TiO_2$ films containing highly N-doped regions. XPS data was obtained from averaging within *ca.* 50 nm. XRD and XPS spectra of their respective undoped analogues (Ti1, Ti2) are included as reference.

X-ray photoelectron spectroscopy (XPS) studies averaged from a similar thickness range of each different film (*ca.* 50 nm) are shown in Figure 2.16(b, d). CASA XPS software was used to fit the N 1s environment (397 – 400 eV) of each film, this fitting was employed to estimate the concentration of nitrogen within the as-synthesised films. In the case of the stratified ML thin film, the area studied includes one highly doped N layers. It can be clearly observed that the nitrogen levels within selective regions of both films were comparable, being 0.70 and 0.50, for N1 (non-stratified) and ML (stratified) samples, respectively. Therefore, a fair comparison can be made between samples made by a pulsed delivery strategy and those made using a constant delivery of nitrogen dopant.

### 2.4.3.2. Photoactivity of stratified vs. non-stratified N-$TiO_2$ thin films.

The photocatalytic activity, of each single film used in this chapter, was evaluated upon degradation of a model organic pollutant, octadecanoic (stearic) acid, under UVA irradiation (*Vilber-Lourmat*, 2 x 8 W, 365 nm, 1.2 mW $cm^{-2}$). The overall degradation reaction is given by Equation 2.1.

$$CH_3(CH_2)_{16}CO_2H + 26O_2 \xrightarrow[h\nu \geq E_{bg}]{TiO_2} 18CO_2 + 18H_2O \qquad (2.1)$$

Each different film was dip-coated with a thin layer of stearic acid using the same conditions described in the previous section. The photocatalytic study was evaluated by following the photodegradation of the C-H bonds of stearic acid, with IR bands at 2958, 2923 and 2853 $cm^{-1}$ (**Figure 2.17(a)**), which were used to calculate their corresponding integrated areas (**Figure 2.17(b)**). The photoactivity rates and formal quantum efficiencies ($\xi$) (**Figure 2.17(c)**) were estimated and calculated following the conditions previously described.

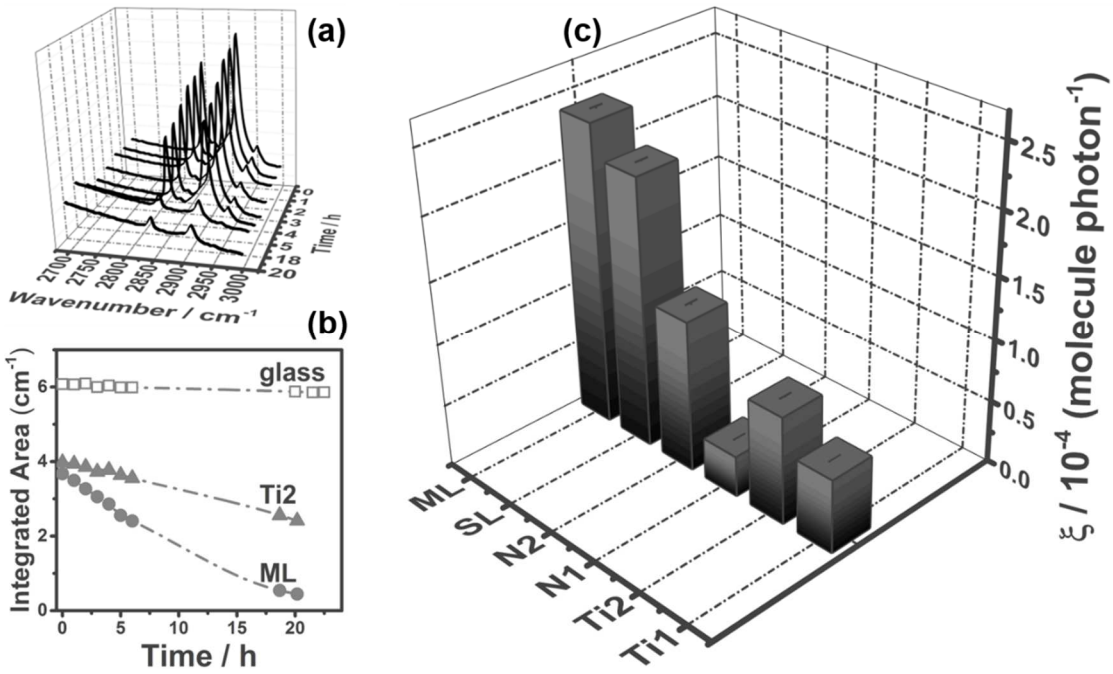


**Figure 2.17.** (a) FTIR spectra of a stratified multilayer N-$TiO_2$ thin film (ML), showing the photodegradation of stearic acid upon UVA irradiation (1.2 mW $cm^{-2}$). (b) Integrated areas, calculated from the photodegradation of stearic acid obtained, versus irradiation time of selected thin films, Ti2 (undoped $TiO_2$, full triangles) and ML stratified multilayer N-$TiO_2$, full circles). Plain glass (empty squares) is included as reference. (c) Formal quantum efficiencies (ξ), estimated as molecules degraded per incident photon, of selected thin films, undoped (Ti1, Ti2), non-stratified (N1, N2) and stratified doped (SL, ML) $TiO_2$ thin-films. Further sample and experimental details are given in Table 2.2.

The photocatalytic performance of selected thin films; non-stratified (N1, N2), single- (SL) and multi-layer (ML) stratified N-$TiO_2$ thin films, as well as their undoped $TiO_2$ analogues (Ti1 and Ti2) were tested by following the photodegradation of stearic acid using an UVA illumination source (**Figure 2.17(c)**). As previously mentioned, the effect of doping $TiO_2$ materials with high amounts of N was found detrimental from a photocatalytic point of view, as it can be observed in Figure 2.17(c) where the non-stratified N-$TiO_2$ film (N1) showed low photocatalytic efficiency when compared to the its undoped analogue. In contrast, the use of low concentrations of nitrogen to deliver non-stratified N-$TiO_2$ films (N2) resulted in an enhanced photocatalytic efficiency compared to that of their undoped analogues (Ti2). Interestingly, higher photocatalytic efficiencies were observed when nitrogen was added in specific regions

within the lattice of $TiO_2$, samples SL and ML, being extremely pronounced for multi-layer N-$TiO_2$ thin films. This behaviour was found unusual from a structural point of view, because the regions containing high amounts of nitrogen in the stratified N-$TiO_2$ films may also create disordered areas, which would lead to speed up the recombination process of the photogenerated carriers and thus decreasing their photocatalytic efficiency. It is worth noting that XRD analysis of the multi-layer stratified thin films and their undoped analogues showed comparable patterns (**Figure 2.18(a)**). Therefore, it could be expected that these highly disordered areas would be very narrow (within short-range order), if present at all, for the as-synthesised multi-layer stratified thin films. Instead, the concentration of nitrogen within the N-doped thin films could be correlated with the photocatalytic changes, suggesting that the nature and amount of nitrogen in $TiO_2$ thin films have an important role in their photocatalytic performance.

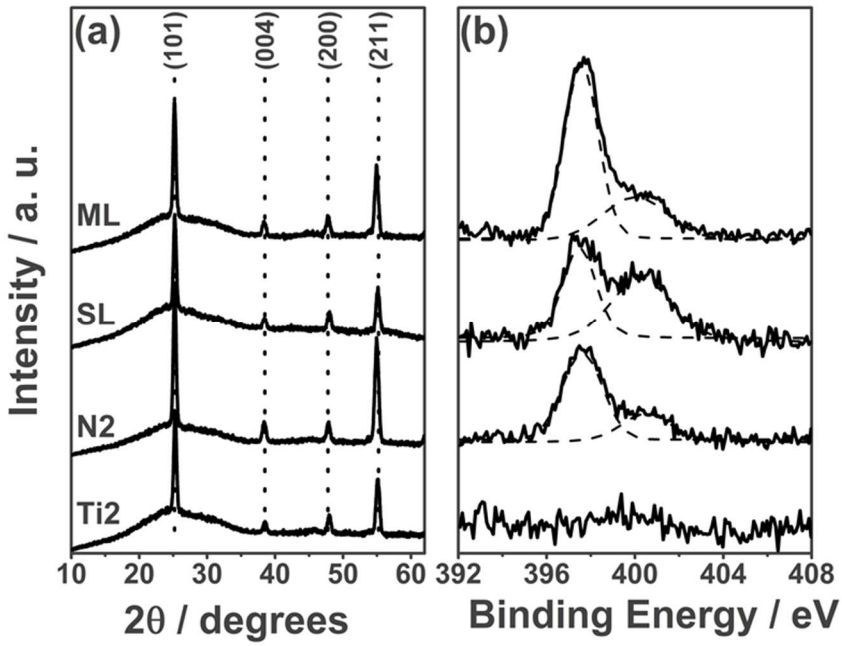


**Figure 2.18.** X-ray diffraction (XRD) and X-ray photoelectron spectroscopy (XPS) analyses of selected N-$TiO_2$ thin films, non-stratified (N2), single-layer (SL) and multi-layer (ML), as well as their undoped analogue (Ti2). XPS data was collected from depth-profile analysis of the entire thin films and averaged using comparable thicknesses.

As mentioned in the previous section, the influence of N species on the photocatalytic performance of dope $TiO_2$ photocatalysts has been widely studied, being a source of debate and/ or great controversy in the literature.[35] As previously mentioned, nitrogen can be added to the lattice of $TiO_2$ materials, either as substitutional ($N_s$, oxygen lattice site) and/ or interstitial ($N_i$) species, with binding energies of 397 and 399 – 400 eV, respectively.[88,91,126] The role of these species on the photocatalytic response of N-doped $TiO_2$ materials has been widely investigated and discussed;[25,124] unfortunately, despite the great number of works based on these materials no agreement has been reached. Indeed, the photocatalytic study of our N-doped thin films within the UV range (**Figure 2.17(c)**) could not be correlated to a specific role of either $N_s$ or $N_i$ species. XPS analysis of the thin films used in this section showed that the amount of $N_s$ (397 eV) within the ML sample was very high compared to that of the SL film and non-stratified N2 films (**Figure 2.18(b)**), which could have enhanced its photocatalytic performance. However, the concentration of substitutional nitrogen within both SL and N2 samples was comparable, despite the different photocatalytic efficiencies observed (**Figure 2.17(c)**). In addition, the presence interstitial nitrogen ($N_i$, 400 eV) could not be also clearly correlated with the enhancement of the photocatalytic efficiency, as similar $N_i$ concentrations were observed for both ML and N2 samples and only slightly higher amounts for SL sample (**Figure 2.18(b)**).

As previously mentioned, nitrogen species adsorbed to the surface of N-$TiO_2$ films may affect their photocatalytic efficiency. The role of these adsorbed species could be associated to a synergistic interaction among bulk and adsorbed species for an enhanced photocatalytic performance of these N-doped photocatalysts.[120] In this chapter, surface XPS analyses of the N 1s environment showed a single peak at 400 eV, which are widely acknowledged as surface adsorbed nitrogen species ($\gamma$-$N_2$, $NO_x$, $NH_x$).[35] It is

important mentioning that the nature and concentration these species were similar among the films investigated in this chapter, and no trace of other nitrogen-containing species ($N^-$, $NO_3^-$, etc.) was detected beyond instrumental error.

It is also worth mentioning that different groups[35,127,128] have emphasised that the nitrogen doping process could lead to create oxygen vacancies within the $TiO_2$ lattice ($V_o$s), which could play an important role in the visible light activity of N-doped $TiO_2$ materials. These $V_o$s are intrinsically created when nitrogen ($N^{-3}$) replaces oxygen ($O^{-2}$) within the $TiO_2$ structure and also formed under the reductive conditions typically used during nitrogen doping. These works also reported that visible light activity of N-$TiO_2$ materials is correlated with an optimum number of $V_o$s. However, upon exceeding this optimum value, they would act as carrier recombination centres decreasing the photocatalytic performance of the N-doped materials. Additional photocatalytic tests were performed by using regular indoor fluorescent lamps (visible range irradiation); however, no photocatalytic response was found for any of the selected thin films used in this section. Generally, any activity of N-$TiO_2$ photocatalysts observed in the visible range is in detriment of their UV activity.

As previously mentioned, the presence of high levels of nitrogen within the structure of doped $TiO_2$ films, has a detrimental role on their structural and functional properties. However, there is a beneficial correlation between photocatalytic efficiency and the total amount of nitrogen, when it was incorporated in specific regions within the lattice of $TiO_2$. These nitrogen rich regions within the multi-layer stratified films could act as *buffer* layers,[122] promoting the photogeneration of charge carriers. Therefore, the astonishing photocatalytic efficiency of the stratified N-$TiO_2$ films can be explained in terms of high mobility of the photogenerated charge carriers. In this section, stratified films were designed and engineered to combine highly ordered N-doped layers,

enhancing the creation of photogenerated charge carriers, and undoped layers with high-mobility and band like-conduction behaviour,[129] (**Figure 2.19**). In contrast, non-stratified films with non-ordered high levels of nitrogen resulted in the enhancement of recombination processes,[127] decreasing the photocatalytic performance of these thin films.

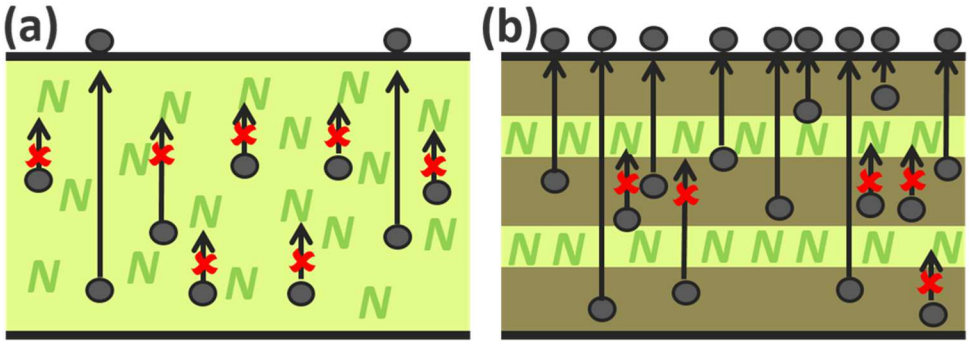


**Figure 2.19.** Scheme representing the potential photogenerated charge carrier mobility and recombination suggested for (a) non-stratified and (b) stratified N-$TiO_2$ thin-films. In the scheme N represents the addition of nitrogen ions to the non-stratified and stratified N-$TiO_2$ films, the full dots represent the movement of photogenerated charge to the surface of the N-$TiO_2$ films.

### 2.4.4. Conclusions.

In this chapter, we have presented a new strategy to synthesise stratified doped $TiO_2$ films using atmospheric-pressure chemical vapour deposition (APCVD) processes. This has been, to the best of our knowledge the first use of APCVD to deliver precursors in a pulsed mode. High amounts of nitrogen were added in specific regions within the $TiO_2$ lattice, with minor changes of their physical properties, which were confirmed through XRD and SEM analyses. The photocatalytic performance of as-synthesised stratified films was explored during degradation of stearic acid under UVA illumination. The activity of these films was dramatically enhanced compared to similar non-stratified and undoped $TiO_2$ films. A possible explanation for this enhanced photocatalytic efficiency was proposed in terms of the combined effects of higher

charge carrier photogeneration and mobility, as well as low carrier recombination within the highly doped and undoped regions of the stratified films.

In this chapter, we presented a simple strategy to add controlled concentrations of nitrogen into the $TiO_2$ structure. This APCVD configuration can be used to produce materials with multiple layers using a wide range of dopants or mixtures of co-dopants. In this sense, the approach reported in this chapter is similar to that used in ALD processes and allowed to design multilayer stratified films for an enhanced charge carrier generation and mobility. Examples of advanced photocatalyst designs such as the one presented in this chapter would suggest to revise the synthesis of photocatalytic systems to achieve an optimum combination of physical and chemical properties. The selective incorporation of convenient levels of specific dopant precursors (or mixture of co-dopants) would increase the number of variables to the complexity of these systems.

In the following chapter, we will explore the chemical modification of $TiO_2$ thin films using chemical reagents, phosphorus and sulfur, which can be added to the lattice of $TiO_2$ either as anionic or cationic species. These phosphorus/sulfur-doped $TiO_2$ thin films will allow to investigate the effect that anionic and cationic species will have on the physical and functional properties of these doped $TiO_2$ thin films.

Chapter III

# NON-METAL (PHOSPHORUS AND SULFUR) DOPED $TiO_2$ THIN FILMS

*'The following chapter presents the results from a series of experiments for growing phosphorus and sulfur doped $TiO_2$ thin films via atmospheric pressure chemical vapour deposition (APCVD). These two dopant sources can be added to the lattice of $TiO_2$ either as anionic or cationic species. Therefore, the synthesis of these doped $TiO_2$ films was designed to investigate the effect that these two different species (anions and cations) will have on the physical and functional properties of these doped $TiO_2$ films.'*

## 3. Non-metal (phosphorus and sulfur) doped $TiO_2$ thin films.

### 3.1. Introduction.

As previously mentioned, $TiO_2$ and specially N-doped $TiO_2$ have been widely explored for photocatalytic applications.[17] Unfortunately, there is still a wide debate on whether nitrogen doping could deliver sunlight-active photocatalysts.[35,130]

In the last few decades, there have been vast investigations to find alternatives to the use of nitrogen to dope $TiO_2$. As such, different non-metal and metal species have been investigated to modify the optical properties of $TiO_2$ photocatalysts. The benefits of adding anion species to $TiO_2$ are well acknowledged, as previously discussed. However, in the last few years, there has been an increasing interest in using cationic species to improve the function of $TiO_2$.[131–133] Different theoretical and experimental works have reported that adding cationic species into the $TiO_2$ lattice would result in the formation of inter-band localised states above the valence band of $TiO_2$, promoting electron transition between the valence and conduction bands and hence inducing visible light activity.[25,37] This led us to explore the modification of $TiO_2$, by using non-metal species which can be added into the $TiO_2$ matrix either as cations or anions. However, it is worth mentioning that the performance of cation and/or anion doped $TiO_2$ materials is intimately associated to the synthetic conditions. For instance, *Yang et al*.[134] reported that oxygen rich conditions led to produce cation-doped $TiO_2$ materials and oxygen deficient conditions to anion-doped $TiO_2$ materials. In addition, it is important to bear in mind that these cation-doped $TiO_2$ materials are in a powder form, and thus it would be crucial to rule out any possible contribution from oxide species generated in the surface of the material, which can mask the optical and functional response of the doped-$TiO_2$ materials.

In this chapter, we will investigate the use of phosphorus and sulfur species to modify $TiO_2$ thin films. These two chemical elements could be considered as the most promising alternatives to the use of nitrogen, as both could be added to the lattice of $TiO_2$ either as cations or anions, allowing to investigate their effect on the physical and functional properties of $TiO_2$ thin films.

## 3.2. Experimental methods.

All chemicals were purchased from *Sigma-Aldrich*. Titanium tetrachloride ($TiCl_4$, 99.9 %) and ethyl acetate ($C_4H_8O_2$, 99.8 %) were used as titanium and oxygen source, respectively. Triethyl phosphate ($(C_2H_5O)_3PO$, 99.8 %) and allyl sulfide ($C_6H_{10}S$, 97 %) were used as phosphorus and sulfur sources, respectively. Nitrogen gas ($N_2$) was supplied by BOC. Glass substrates coated with a thin barrier of $SiO_2$ (50 nm), which prevents the diffusion of ions into the as-deposited coatings, were provided by the Pilkington *NSG* Group. Each glass substrate was carefully washed with acetone ($C_3H_6O$, 99 %), isopropanol ($C_3H_8O$, 99 %), distilled water and finally dried with air prior to their use.

### 3.2.1. Phosphorus and sulfur doped $TiO_2$ film synthesis.

As previously mentioned, a cold-wall atmospheric pressure chemical vapour deposition (APCVD) process was used to synthesise the phosphorus and sulfur doped $TiO_2$ films. APCVD is a thermal CVD process, where each different precursor source is added to a stainless-steel bubbler. These precursors are heated to obtain enriched vapours which are transported to the reaction chamber by an inert carrier gas ($N_2$). A schematic figure of the APCVD apparatus is shown in Figure 3.1.

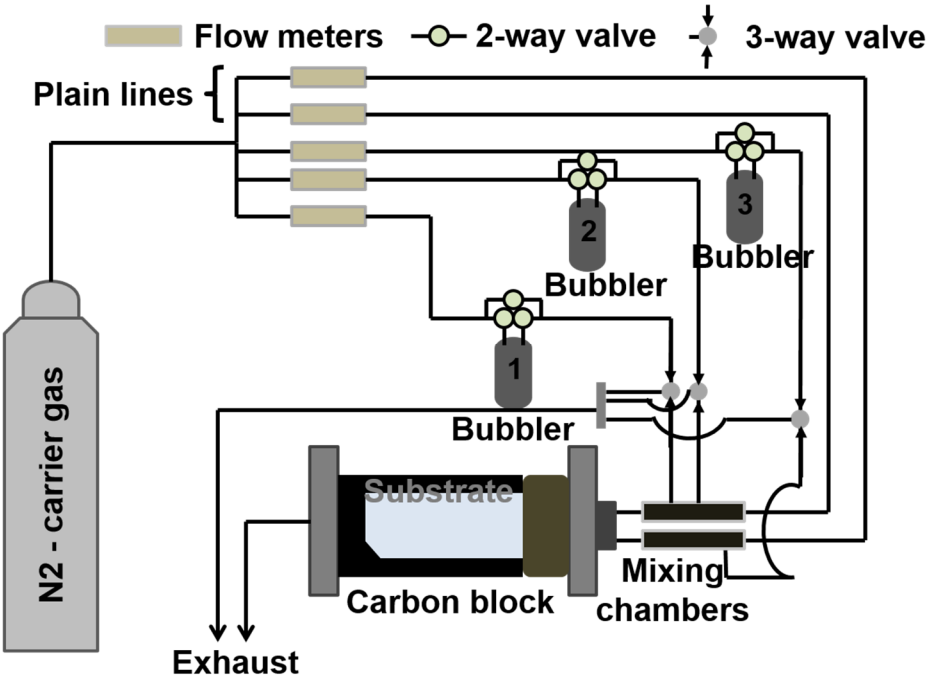


**Figure 3.1.** Schematic of the atmospheric pressure chemical vapour deposition (APCVD) apparatus. Undoped, P-doped and S-doped $TiO_2$ thin films were synthesised from volatile precursors, which were carried by $N_2$ gas from different bubblers; bubbler 1 contained $TiCl_4$, bubbler 2 contained ethyl acetate and bubbler 3 contained the dopant source used in this chapter (phosphorus and sulfur).

The CVD system was maintained at high temperature (200 °C). The gaseous reactants were mixed in stainless steel mixing chambers at 250 °C and transport through a triple baffle manifold into the reaction chamber using $N_2$ gas (pre-heated at 150 °C). The APCVD reaction chamber consisted of a 320 mm-long graphite block with three inserted heater cartridges (*Whatman*). The temperature of each individual APCVD component was controlled using Pt-Rh thermocouples. In a standard $TiO_2$ synthesis, the temperatures of the bubblers, containing the titanium and oxygen precursors, were held at 68 and 38 °C, respectively. The temperature used for each different dopant reactant was adapted to produce enough gaseous reactants. Low temperature, 8 °C, was used for sulfur, this temperature was achieved using an iced-bath. In contrast, the phosphorus source was heated at 90 °C.

### 3.2.2. Physical characterisation.

The structural properties of the as-synthesised thin films were explored using X-ray diffraction (XRD) and Raman spectroscopy analyses. XRD measurements were carried out using a Bruker-Axs D8 (Lynxeye XE) diffractometer, which consists of a monochromated Cu X-ray source ($K_{\alpha 1}$, 1.54 Å) and a glancing incident angle ($\theta$) 1°. Each different diffraction pattern was fit to the Le Bail method, using the anatase structure parameters from Joint Committee on Powder Diffraction Standards (JCPDS), through the GSAS and EXPGUI software suite. Raman spectroscopy was performed using a Renishaw 1000 sepectrometer equipped with a 633 nm laser, which was calibrated using a silicon reference. UV/vis spectroscopy analyses were carried out using a double monochromated Perkin Elmer Lambda 950 UV/Vis/NIR Spectrophotometer within the 250 – 2500 nm range. The UV/vis measurements were calibrated using a *Labsphere* reflectance standard. In addition, a Helios double beam instrument was used to record reflectance values within the range 300 – 2500 nm, at different positions, allowing to evaluate the thickness of the films via *Swanepoel* method.[85] This thickness measurements were also corroborated by side-view scanning electron microscopy (SEM). Two different SEM systems, a JEOL 6301 (5 KV) and a JEOL JSM-6700F field emission instruments, were used to collect data, the Oxford software INCA was used for EDS analysis. Atomic force microscopy (AFM) was performed using a Bruker Icon system running in PeakForce Quantitative Nanomechanical Property Mapping (QNM) mode. The topography of the samples was measured using 5 μm x 5 μm areas, and Bruker NCHV (etched silicon) tips in contact mode. X-Ray photoelectron spectroscopy (XPS) analyses were carried out using a Thermo K alpha spectrometer with monochromated Al K alpha radiation, a dual beam charge compensation system and constant pass energy of 50 eV. A binding energy range

of 0 – 1200 eV was used to collect survey scans. The principal peaks of the elements present in the as-synthesised films Ti (2p), O (1s), C (1s), P (2p), S (2p) and Si (2p), were investigated by acquiring high-resolution peaks. These peaks were used to evaluate the concentration of the different elements within the analysis region (spot size 400 μm). CASAXPS software was utilised to model the area underneath these peaks, using relative sensitive factors to calculate the thin film composition, these peaks were calibrated to adventitious carbon at a binding energy (B.E.) of 284.4 eV.

### 3.2.3. Characterisation of functional properties.

#### 3.2.3.1. Bandgap determination.

Transmittance spectra was recorded over the 300 – 2500 nm range on a Helios double beam instrument to determine band gap energies trough Tauc plots.[86]

#### 3.2.3.2. Transient absorption spectroscopy.

The dynamics of the photogenerated charge carriers of the undoped and doped $TiO_2$ films used in this chapter were measured using transient absorption spectroscopy (TAS) at room temperature (≈ 297 K) in the μs-s timescale. This TAS instrument has been previously explained in detail elsewhere.[135] In a few words, this system consist of a Xe lamp (75 W) which is employed as the probe beam to illuminate the samples, the Xe lamp has an integrated monochromator to allow the selection of specific wavelengths. A Si PIN photodiode is used to measure the changes in transmitted light upon the excitation of the sample by applying a UV laser excitation pulse, using the third harmonic of an Nd: YAG laser (355 nm, 6 ns pulse width). Reasonably low laser intensities were used (≈ 500 μJ $cm^{-2}$ $pulse^{-1}$) with a laser repetition rate of 1 Hz. Each TAS trace is the result of averaging between 50 and 500 scans.

### 3.2.3.3. Hall effect.

Hall Effect probe measurements were conducted at room temperature on an Ecopia HMS-3000 device in the Van der Pauw configuration. Measurements were acquired at 0.58 T with a variable current of 1 μA – 300 μA, on square cut samples with soldered indium-tin ohmic contacts, the integrity of which were tested prior to measurement.

### 3.2.3.4. Photocatalytic test.

A model organic pollutant, octadecanoic (stearic) acid (95 %, *Sigma-Aldrich*), was used to evaluate the photocatalytic response of the coating surfaces deposited in this chapter. A 0.05 M solution of stearic acid in chloroform was used to deposit a layer of the acid on the undoped and doped thin films, using a dip-coating process. UVA (*Vilber-Lourmat*, 2 x 8 W, 365 nm, 1.2 mW $cm^{-2}$) and/ or visible (*GE lighting 2D fluorescent GR10q-835 white, 28 W*) irradiation were used to evaluate the photocatalytic performance of the thin films photocatalysts. The loss of the dip-coated stearic acid layer was followed by measuring its characteristic C-H infrared bands at 2958, 2923 and 2853 $cm^{-1}$, which were integrated using a Perkin Elmer RX-I Fourier transform infrared (FTIR) spectrometer. The degradation of the stearic acid bands needs to be converted to the number of molecules of stearic acid degraded during the photocatalytic process. This conversion was performed following a work reported by Mills *at al*., [87] where it was estimated that 1 $cm^{-1}$ of integrated area corresponds to 9.7 x $10^{15}$ molecules of stearic acid. A linear regression of the degradation process, at its initial step (30 – 40 %), was used to assess the photocatalytic rate, which have shown to possess zero-order reaction kinetics above a critical stearic concentration. The photocatalytic response was expressed as formal quantum efficiency (ξ), which has been described as molecules of

acid degraded per incident photon (molec. photon$^{-1}$), and estimated accepting that all incident photons had the same energy (3.4 eV).

## 3.3. Multifunctional P-doped $TiO_2$ thin films. A new approach to self-cleaning, transparent conducting oxide materials.

### 3.3.1. Introduction.

As previously mentioned, $TiO_2$ have been deeply explored during the las few decades.[17,73,75,136] Unfortunately, $TiO_2$ materials present some drawbacks, being the most important its potential use in solar applications due to the *relatively* wide bandgap of its most photoactive $TiO_2$ polymorph, anatase. This has led to a large research driven to find different solutions to narrow the bandgap of $TiO_2$ and extend its photocatalytic response into the visible region, being the use of non-metal species, to chemically modify $TiO_2$ materials, the most explored.[76] From all different non-metal acceptor species, nitrogen has been the most studied dopant source,[88] however, there is still little consensus on its role to an overall improvement in visible light driven photocatalysis.[25,35,82,137,138]

In addition, the use of cations, with oxidation states higher than that of $Ti^{4+}$, have been also widely explored to modify the band structure of $TiO_2$ materials. It is worth mentioning that these dopant species do not reduce the visible light response of anatase $TiO_2$. These species act as electron donors, which can be injected into the conduction band of $TiO_2$, enhancing the use of $TiO_2$ as a transparent conducting oxide (TCO). A blue shift of the optical absorption of $TiO_2$, as well as a reduction in resistivity, are normally associated to the formation of these TCO materials. The use of these $TiO_2$ materials offers great advantages in the field of TCO applications due to its high transmittance in the infrared region, chemical stability and high refractive index, as well as an important reduction of its production cost.[139] Therefore, this application has been

widely explored during the last few decades, Nb, Ta, W and F have been the most common electron-donor dopants studied.[140–142] It is worth mentioning that Ta and Nb materials have shown promising optical and electrical properties, being comparable to that of ITO materials. In contrast, $TiO_2$ materials doped with F and W have not yielded low enough resistivities, being associated to a charge carrier concentration effect (*ie*. lower donation efficiency).[143] Interestingly, all these materials have shown a decrease of their photocatalytic performance.

In this section, we chose phosphorus as a dopant source, as it allowed the possibility to modify $TiO_2$ films with either cationic ($P^{5+}$) or anionic ($P^{3-}$) species, and further studying their effect on the function of $TiO_2$. It has been commonly acknowledged that phosphorus in the pentavalent state ($P^{5+}$) would induce a shift of its optical properties to lower wavelengths (blue-shift), as well as an increase in the number of free charge carriers within the P-doped $TiO_2$ films. In addition, P can be present as more attractive alternative to from a commercial point of view, as it is a much more earth abundant and cheaper dopant source than either Nb or Ta. Hence, the synthesis of P-doped films could be introduced as a new approach to deliver transparent conducting oxide materials.

P-doped $TiO_2$ films, hereafter P-$TiO_2$, have been already explored using sol-gel methods. These methods delivered P-$TiO_2$ materials with a single oxidation state in a cationic form, which was assigned to a phosphate state ($P^{5+}$).[144–147] Different photocatalytic methods, such as degradation of organic compounds (*n*-pentane and ethanol) and dyes (methyl orange (MO) and methylene blue (MB)) were used to evaluate the functional properties of these P-doped photocatalysts. However, different photocatalytic responses were observed, which could be correlated to varying concentration of $P^{5+}$ species and surface area within the different reported materials.

In this section, we investigated the use of APCVD methods to synthesise P-$TiO_2$ films.[52] This synthetic technique allows the growth of coatings at high temperature, avoiding the amorphous to crystalline transition associated to sol-gel methods which could drastically alter the nature and content of the dopant species.[144–146] Interestingly, we also found that APCVD can synthesise multi-valent P-doped $TiO_2$ films with cationic $P^{5+}$ and anionic $P^{3-}$ species,[35] which were used to study the effect that phosphorus had on the electronic and photocatalytic properties of P-$TiO_2$ films.

### 3.3.2. P-$TiO_2$ thin film synthesis.

P-doped $TiO_2$ thin films were deposited on float glass using an APCVD process, from the reaction of titanium (IV) chloride ($TiCl_4$), ethyl acetate (EtOAc) and triethyl phosphate ($(EtO)_3PO$) at 500°C (Equation 3.1).

$$TiCl_4 + CH_3COOC_2H_5 + ((C_2H_5O))_3PO \xrightarrow{500\,^oC} Ti_{1-x}O_{2-x}P_x + \text{by-products} \quad (3.1)$$

The reaction mechanism between EtOAc and $TiCl_4$ is not completely known. However, different reaction paths have been reported, being the most commonly acknowledge, the mechanism involving the hydrolysis of $TiCl_4$ (Equation 3.2)[148] *via* decomposition of ethyl acetate to form ketene and ethanol and subsequent dehydration of ethanol to form ethene and water.

$$CH_3COOC_2H_5 \longrightarrow CH_3CH_2OH + C_2H_2O \quad (3.2a)$$

$$CH_3CH_2OH \longrightarrow H_2O + C_2H_4 \quad (3.2b)$$

$$H_2O + TiCl_4 \longrightarrow TiO_2 + 4HCl \quad (3.2c)$$

P-$TiO_2$ films were synthesised by maintaining the temperature of the P stainless steel bubbler at 90 °C to control its vapour pressure. These P-$TiO_2$ films showed a thickness (measured from cross section SEM and Swanepoel method[85]) ranging between 450-

1050 nm. It is well acknowledged that $TiO_2$ thin films present different optical interference across the substrate, which each colour band corresponds to a different region of thickness.[149] Table 3.1 shows the corresponding phosphorus mass flow rates used to deliver the P-$TiO_2$ films. In addition, Table 3.1 also shows the atomic concentration of each phosphorus specie, $P^{5+}$ and $P^{3-}$, as observed by XPS studies, as well as the $P^{5+}/P^{3-}$ ratio. All films used in this section were adhesive and resistant to the Scotch tape test,[97] with no particles being peeled off, as well as resisting a scratch test using a steel scalpel[98] and were constantly stable in air. It is worth noting that all as-synthesised coating surfaces showed no pin-hole defects and no particulates were observed in the exhaust gas. Several samples (more than 30), from each different thin film, were synthesised to prove the reproducibility of the method synthetic method reported in this section However, only selected thin films, with comparable thickness and physical properties, are presented.

**Table 3.1.** Experimental and synthesis details of undoped and P-doped $TiO_2$ thin films. The metal ($TiCl_4$) and oxygen ($C_4H_8O_2$) precursors were used at constant temperature and mass flow conditions: 67 and 37 °C and 6.7 x $10^{-3}$ and 3.1 x $10^{-3}$ g $min^{-1}$, respectively. The temperature for the phosphorus source ($(EtO)_3PO$) was maintained at 90 °C.

| Sample | Experimental Details | | | | |
|---|---|---|---|---|---|
| | P Mass Flow ($10^{-3}$) (g $min^{-1}$) | $P^{5+}/P^{3-}$ ratio | $[P^{5+}]$ (*at*. %)* | $[P^{3-}]$ (*at*. %)* | [P] total (*at*. %)* |
| Anatase | -- | -- | -- | -- | -- |
| P:Ti1 | 0.13 | 1:0 | 0.50 ± 0.18 | -- | 0.50 ± 0.18 |
| P:Ti2 | 0.24 | 1:0 | 0.90 ± 0.37 | -- | 0.90 ± 0.37 |
| P:Ti3 | 0.38 | 1:1 | 1.17 ± 0.51 | 1.10 ± 0.65 | 2.27 ± 0.58 |
| P:Ti4 | 0.57 | 2:1 | 2.04 ± 0.68 | 0.94 ± 0.37 | 2.98 ± 0.62 |

*As determined by XPS analyses.

### 3.3.3. Results and discussion.

#### 3.3.3.1. X-ray photoelectron spectroscopy (XPS).

X-ray photoelectron spectroscopy (XPS) analysis was employed to evaluate the concentration and oxidation state nature of the P specie in all P-$TiO_2$ films used in this section. XPS is a surface-sensitive technique (≤ 10 nm),[150] therefore, several levels within the bulk were studied by etching the surface with argon sputtering. It has been previously reported that P can exist within the $TiO_2$ lattice as either, $P^{5+}$ cations which substitute $Ti^{4+}$ lattice sites or $P^{3-}$ anions which replace $O^{2-}$ lattice sites, these P oxidation states are commonly assigned to P 2p orbitals, with XPS binding energies of *ca*. 135 and 129 eV respectively.[144,151,152]

All P-doped $TiO_2$ films showed simply an individual peak at their surface, with binding energy of *ca*. 133.7 eV, which is generally assigned to phosphorus cations with an oxidation state of 5+ ($P^{5+}$, **Figure 3.2**).[144,146] It is worth noting that upon XPS surface

etching analysis a second P 2p environment was found within the bulk of the highly P-doped films (≥ 2.3 at. %). This second P 2p environment showed a peak at 128.8 eV, which has been reported by other groups as phosphorus anion species ($P^{3-}$, **Figure 3.2**).[152,153] It is commonly acknowledged that the XPS depth profile etching process can modify the oxidation state of elements,[154] however, this is unlikely due to the reduction of $P^{5+}$ to $P^{3-}$, since different phosphorus-based commercial powders with only $P^{5+}$ species were analysed by XPS depth-profiling, observing no changes in their oxidation state. The fact that solely $P^{5+}$ was present at the surface, even in samples that contained both $P^{5+}$ and $P^{3-}$ species in the bulk, was attributed to surface oxidation of $P^{3-}$ states at the surface on exposure to air.

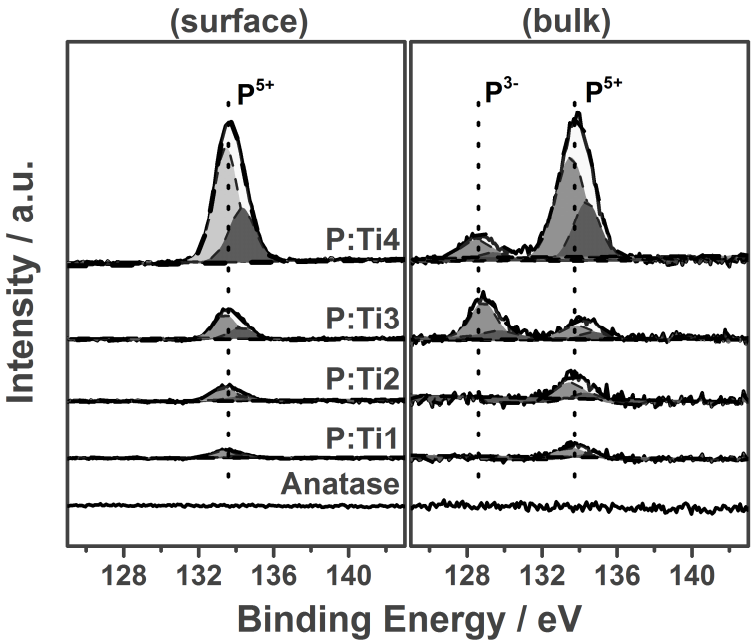


**Figure 3.2.** XPS analyses at the surface (left) and bulk average (right) showing the different P 2p environments found in the as-synthesised P-$TiO_2$ films. These films showed different $P^{5+}/P^{3-}$ ratios; P:Ti1 (1:0), P:Ti2 (1:0), P:Ti3 (1:1) and P:Ti4 (2:1). Anatase $TiO_2$ was used as reference. The experimental data is represented by solid lines and its deconvolution into each chemical state (2 $p_{3/2}$ and 2 $p_{1/2}$ environments) is represented by dotted lines. The film description and experimental details are given in Table 3.1.

As previously mentioned, we found that phosphorus can exist in the form of two different environments in P-$TiO_2$ films, $P^{5+}$ and $P^{3-}$, by using APCVD processes. Four

distinct P-$TiO_2$ samples were studied in this thesis in order to synthesise P-$TiO_2$ films with different P concentration, as well as different $P^{5+}/P^{3-}$ ratios. P:Ti1 and P:Ti2, using low concentrations of phosphorus, which resulted in the sole presence of $P^{5+}$ within the $TiO_2$ matrix. Likewise, samples P:Ti3 and P:Ti4, were synthesised using higher concentrations of phosphorus, which resulted in P-$TiO_2$ films with both $P^{5+}$ and $P^{3-}$ species. We observed a different $P^{5+}/P^{3-}$ ratio for these samples, being 1:1 for sample P:Ti3, and 2:1 for sample P:Ti4. Samples P:Ti1, P:Ti2, P:Ti3 and P:Ti4 showed a total content of phosphorus of 0.50, 0.90, 2.27 and 2.98 at. % (**Table 3.1**).

### 3.3.3.2. Structural properties of P-doped $TiO_2$ thin films.

The structural properties of all undoped and P-doped $TiO_2$ films, used in this chapter, were investigated using X-ray diffraction (XRD), these studies showed that all as-synthesised samples were only constituted of the anatase phase with no evidence of any other $TiO_2$ polymorph or additional phosphorus-based structure (**Figure 3.3**). It is worth mentioning that XRD analysis showed a considerable shift of the diffraction peaks upon phosphorus doping compared to that of their undoped analogues. These diffraction peaks were fit to a Le Bail refined model in order to quantify the lattice changes in the as-synthesised films, showing the widest changes in the tetragonal *c* axis. These changes were clearly observed in the films containing the lowest amount of P within the $TiO_2$ structure, sample P:Ti1, which presented the most contracted unit cell (135.7 ± 0.08 $Å^3$) relative to pure anatase (136.74 ± 0.08 $Å^3$). It is worth mentioning that the as-synthesised films with low concentration of phosphorus, P:Ti1 and P:Ti2 (0.50 and 0.90 at. % of phosphorus, respectively), showed a solely oxidation state, assigned to $P^{5+}$ states.[147] These $P^{5+}$ species would substitute $Ti^{4+}$ sites, resulting in a wide contraction of the unit cell, as $P^{5+}$ and $Ti^{4+}$ species have different ionic radii; where 6 coordinate

complexes of $P^{5+}$ and $Ti^{4+}$ show average ionic radii of 0.380 Å and 0.605 Å respectively. In contrast, an increase in the concentration of the dopant also increases the formation energy of the cationic dopant, resulting in P-$TiO_2$ films, samples P:Ti3 and P:Ti4, with two different P 2p environments, $P^{5+}$ and $P^{3-}$ species,[144,151,152,155] where the anionic species ($P^{3-}$) substituted $O^{2-}$ sites. The presence of these two P 2p environments resulted in the suppression of the unit cell contraction, showing values similar to the one of their undoped analogues.

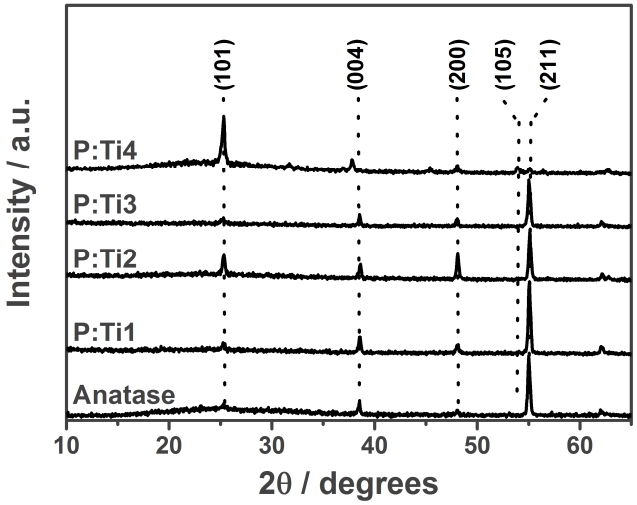


**Figure 3.3**. X-ray diffraction patterns of as-deposited P-$TiO_2$ films with different $P^{5+}/P^{3-}$ ratios; P:Ti1 (1:0), P:Ti2 (1:0), P:Ti3 (1:1) and P:Ti4 (2:1). XRD analysis of undoped anatase $TiO_2$ is included for comparison. The data was fit to a Le Bail refined model.

This was explained in terms of the bigger ionic radii of the $P^{3-}$ states (2.10 Å) compared to that of $O^{2-}$ sites (1.40 Å), compensating the unit cell contraction caused by the addition of $P^{5+}$ species. In addition, a change in preferred growth in specific diffraction planes was shown upon phosphorus doping. An anatase $TiO_2$ single crystal shows a typical growth in the (101) diffraction plane. However, the use of APCVD to synthesise $TiO_2$ films tends to substantially enhance the preferred growth in the (211) diffraction plane, as well as inhibiting growth in the (101) plane. However, it has been reported by Hyett *et al.*[156] that changes in the preferential growth did not substantially affect the photocatalytic response of $TiO_2$ films grown by APCVD. All undoped and P-doped,

with low amounts of phosphorus, $TiO_2$ films were grown preferentially in the (211) diffraction plane. However, the preferential growth was changed to the (101) diffraction plane (**Figure 3.3**) upon an increase in the concentration of phosphorus. A similar trend was also observed by Kafizas *et al*.[140] and Bhachu *et al*.[141] when APCVD was used to deposit Nb-$TiO_2$ films, where the preferential growth was modified from the (101) to the (211) plane at high concentrations of Nb.

The physical properties of the as-synthesised samples used in this section were also investigated using Raman spectroscopy. These analyses corroborated the results showed by XRD, where only $TiO_2$ anatase phase was found in all undoped and P-doped $TiO_2$ films. It is well acknowledged that anatase $TiO_2$ shows its major scattering $E_g$ band at 144 $cm^{-1}$, this band was shifted to lower wavenumbers upon phosphorus doping (**Table 3.2**). This band, $E_g$ mode, describes phonons operating primarily in the *a*-axis of the tetragonal unit cell.[157] It was found a clear trend between the level of $E_g$ band shift and then contraction of the unit cell volume observed by XRD analysis (**Table 3.2**), where the most red-shifted bands were found in the most contracted unit cells (*i.e.* samples P:Ti1 and P:Ti2; **Figures 3.4 and 3.5**).

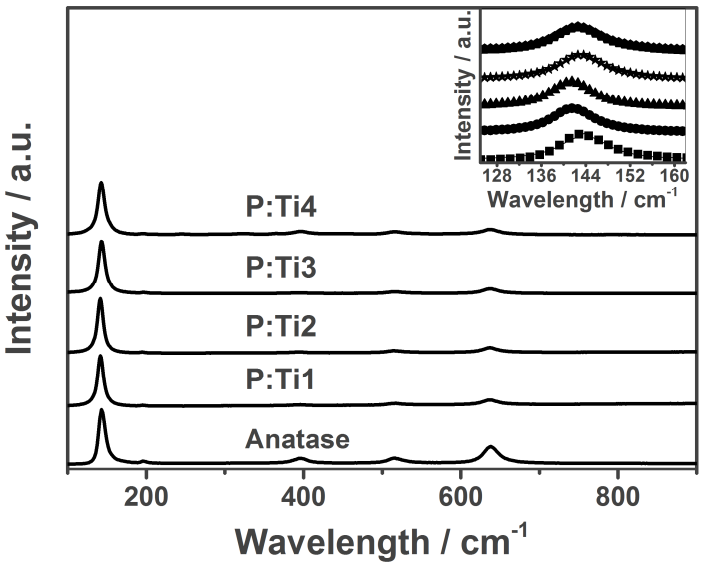


**Figure 3.4.** Raman spectroscopy spectra of undoped and P-doped $TiO_2$ films with different $P^{5+}/P^{3-}$ ratios and P content; P:Ti1 (1:0 and 0.50 at. %), P:Ti2 (1:0 and 0.90 at. %), P:Ti3 (1:1 and 2.27 at.%) and P:Ti4 (2:1 and 2.98 at.%). The inset highlights the red-shift of the major Raman scattering mode ($E_g$) observed in the P-$TiO_2$ films compared to undoped $TiO_2$ films.

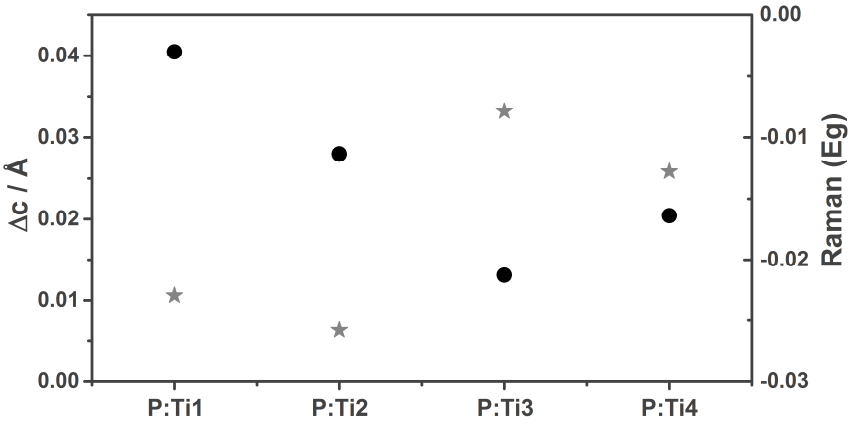


**Figure 3.5.** Comparison between the change in *c* lattice parameter (black circles) and the shift in the main Raman scattering mode ($E_g$) (grey stars) for all different P-doped $TiO_2$ films (P:Ti1, P:Ti2, P:Ti3 and P:Ti4).

**Table 3.2.** Structural and functional characterisation details of the as-synthesised films (undoped and P-doped) obtained *via* X-ray diffraction analysis (XRD), Raman spectroscopy, UV/Visible absorption spectroscopy, X-ray photoelectron spectroscopy (XPS), transient absorption spectroscopy (TAS), atomic force microscopy (AFM), photocatalytic degradation of stearic acid (SA) and Van der Pauw and Hall Effect electrical measurements.

| Sample | Physical Properties | | | | | | | |
|---|---|---|---|---|---|---|---|---|
| | X-ray Diffraction | | | Spectroscopy | | | | TAS |
| | a [Å] | c [Å] | Vol [Å$^3$] | $E_g$ (cm$^{-1}$) | Band gap (eV) | d[a] [nm min$^1$] | T % @ 2500 nm[b] | $t_{1/2}$ from 2 µs |
| Anatase | 3.787(1) | 9.533(6) | 136.74(6) | 143.9 | 3.22 | 305 | 73.2 | 58 |
| P:Ti1 | 3.782(1) | 9.505(6) | 135.67(4) | 141.7 | 3.36 | 315 | 66.8 | -- |
| P:Ti2 | 3.780(1) | 9.492(5) | 135.93(8) | 141.4 | 3.39 | 350 | 67.3 | 14 |
| P:Ti3 | 3.785(2) | 9.520(6) | 136.39(6) | 143.2 | 3.28 | 385 | 72.3 | 3.1 |
| P:Ti4 | 3.788(1) | 9.512(2) | 136.53(3) | 142.7 | 3.24 | 450 | 74.8 | 19 |

| | Functional properties | | | | Electrical properties | |
|---|---|---|---|---|---|---|
| | AFM | Photocatalysis | | | Hall effect probe | |
| | Surf. area (µm$^2$) | $\xi$ ($10^{-4}$) | FQY ($10^{-4}$) | $\rho$ (Ω cm) | $\mu$ (cm$^2$ V$^{-1}$ s$^{-1}$) | n ($10^{19}$ cm$^{-3}$) |
| Anatase | 29.3(4) | 0.86(1) | 1.34(2) | -- | -- | -- |
| P:Ti1 | -- | 0.33(1) | 0.65(2) | 1.69 ± 0.42 | 0.81 ± 0.13 | 0.49 ± 0.21 |
| P:Ti2 | 29.0(2) | 0.47(2) | 0.78(3) | -- | -- | -- |
| P:Ti3 | -- | 0.01(1) | 0.01(1) | 8.18 ± 2.13 | 0.10 ± 0.04 | 2.21 ± 1.76 |
| P:Ti4 | 30.1(6) | 0.55(2) | 0.82(2) | 6.49 ± 1.89 | 0.09 ± 0.05 | 1.54 ± 1.11 |

[a]d = film thickness; [b]average between 0 and 2500 nm. Numbers in parentheses represent the error on the last digit.

### 3.3.3.3. P-$TiO_2$ thin films morphology.

The structural morphology of all samples used in this section were studied *via* Scanning electron microscopy (SEM) analyses. These analyses showed that the morphology of the undoped $TiO_2$ films consisted of well-defined shell-shaped aggregated particles

(**Figure 3.6(a)**). However, a severe change in the structural morphology was found when phosphorus was added into the $TiO_2$ structure. It is worth mentioning that these changes were associated to the concentration of phosphorus. At low levels of P-doping, sample P:Ti2, larger particles were observed that were more jagged in shape (**Figure 3.6(b)**). Moreover, upon an increase in the concentration of phosphorus, sample P:Ti4, even bigger and more rounded bulb-shaped particles were observed (**Figure 3.6(c)**). Therefore, it can be concluded that the particle size of P-$TiO_2$ films is increased by the doping process.

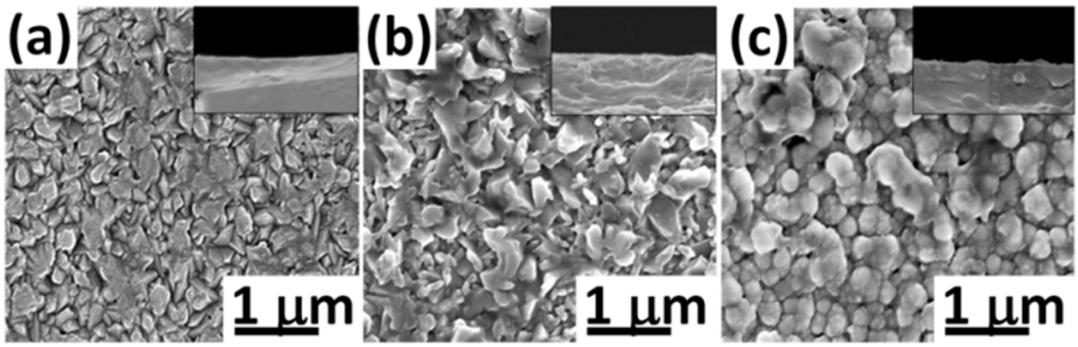


**Figure 3.6.** Scanning electron microscopy (SEM) images of typical (a) undoped $TiO_2$, (b) low concentration and (c) high concentration P-TiO2 films. The inset shows cross-section SEM images of the films.

The morphology of the undoped and P-doped films was further complemented by using atomic force microscopy (AFM). These AFM analyses were performed using a contact (PeakForce) scanning mode, with a 20 nm special frequency on scan areas of 5µm x 5µm. These measurements were locally performed six times for each sample. The average of the surface area projected by each different sample as used to work out the roughness induced surface area increase. These studies corroborated the changes in morphology observed by SEM, with progressively larger and more rounded particles upon P-doping (**Figure 3.7**). The root mean squared roughness increased significantly from 16 nm for undoped $TiO_2$ to 51 nm for high levels of P doping. However, the projected surface area showed only a slight increase as the peaks became sparser, the

calculated surface areas ranged from just 29.35 ± 0.39 $\mu m^2$ in undoped $TiO_2$ films, to 29.00 ± 0.18 $\mu m^2$ and 30.13 ± 0.63 $\mu m^2$ in $P^{5+}/P^{3-}$ = 1:0(b) and $P^{5+}/P^{3-}$ = 2:1 samples, respectively (**Table 3.2**).

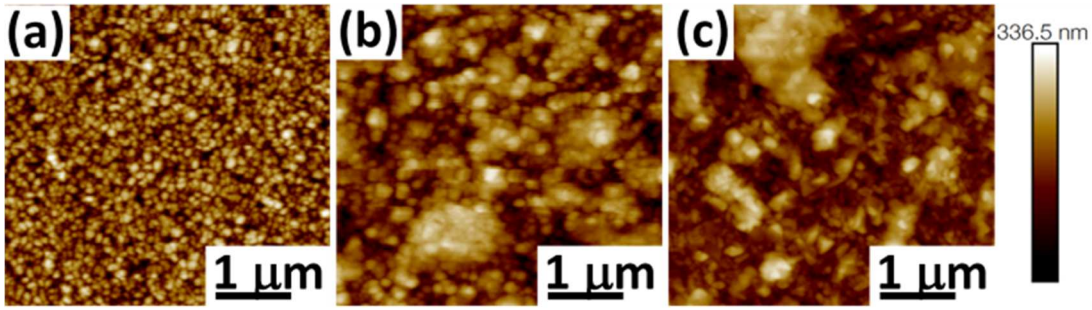


**Figure 3.7.** Atomic force microscopy (AFM) analysis of selected samples (a) undoped and P-doped $TiO_2$ films, with (b) low levels of phosphorus (P:Ti2, 0.90 at. %) and (c) high levels of phosphorus (P:Ti4, 2.98 at. %).

### 3.3.3.4. Optical properties.

All undoped anatase $TiO_2$ thin films, used in this section, showed high transparency with absorption onset values of ~ 380 nm (**Figure 3.8**). Interestingly, it was observed that upon the addition of low levels of phosphorus (< 1 at. %) the films acquired a blue/yellow tinge, slightly dipping their transmission within the green-red absorption region from ≈ 600 to 2000 nm (**Figure 3.8**). It is worth noting that doping with low concentrations of phosphorus resulted in a small of the absorption edge of P-$TiO_2$ films into the UV region, Tauc plot analysis (**Figure 3.8, inset**) corroborated this changes in the optical properties of the P-doped films showing bandgap energies of *ca.* ~ 3.4 eV compared to their undoped analogues (~ 3.2 eV). Interestingly, the addition of high levels of phosphorus (> 1 at. %) resulted in the synthesis of P-$TiO_2$ films with bandgap energies like that of their undoped analogues. This change in the optical properties of the P-doped films could be explained in terms of the different properties of the two oxidation states of phosphorus ($P^{5+}$ and $P^{3-}$) in the $TiO_2$ structure. The presence of

cationic phosphorus ($P^{5+}$) resulted in a blue-shift and bandgap enhancement of the P-doped films. However, this behaviour would not be expected upon the insertion of anionic phosphorus ($P^{3-}$) which replace oxygen lattice sites ($O^{2-}$). It is well acknowledged that density of states of $TiO_2$ materials is composed of O 2p orbitals in the valence band and Ti 3d orbitals in the conduction band. Anions, such as the $P^{3-}$ species found in the films explored in this section naturally replace $O^{2-}$ sites, modifying the $TiO_2$ valence band. As previously mentioned, it has been widely reported that $N^{3-}$ species substitute $O^{2-}$ sites, this process is followed by a mixing process where N 2p and O 2p orbitals the valence band is pushed upwards, narrowing their bandgap energy (*i.e*. red-shift of absorption spectrum).[88,99,124] The enhancement of the bandgap energy of P-$TiO_2$ films might be easily associated to a Moss-Burstein shift effect, which is produced when the enhancement of the carrier concentration is high enough to cause degeneracy and raise the conduction band minimum by occupancy. Nevertheless, the charge carrier concentration was found to be significantly low when merely $P^{5+}$ was present ($n \approx 5 \times 10^{18}$ $cm^{-3}$) compared to those recorded at high P levels ($1 \times 10^{19} \leq n \leq 5 \times 10^{19}$ $cm^{-3}$), where both $P^{5+}$ and $P^{3-}$ were presented. These charge carrier concentration measurements were investigated by Hall Effect probe analysis. Therefore, the blue-shift in bandgap energy of the P-doped film containing only $P^{5+}$ species cannot be explained in terms of a Moss-Burstein shift was the reason for a blue-shift in band-gap energy, as the same behaviour should also have been observed for the P-doped films containing both phosphorus species. Another possibility is that these differences in bandgap were due to changes in unit cell volume. However, as previously mentioned there were no significant changes in the lattice of P-$TiO_2$ films when both $P^{5+}$ and $P^{3-}$, coexisted within $TiO_2$ films. In contrast, films with solely $P^{5+}$ species resulted in the expansion of their unit cell volume expansion, due to the greater average

distance between the ions within the lattice and thus widened density of states. The intrinsic disorder caused by having a significant proportion of both $P^{5+}$ and $P^{3-}$ anions in the structure could also have an impact on the measure band gaps.

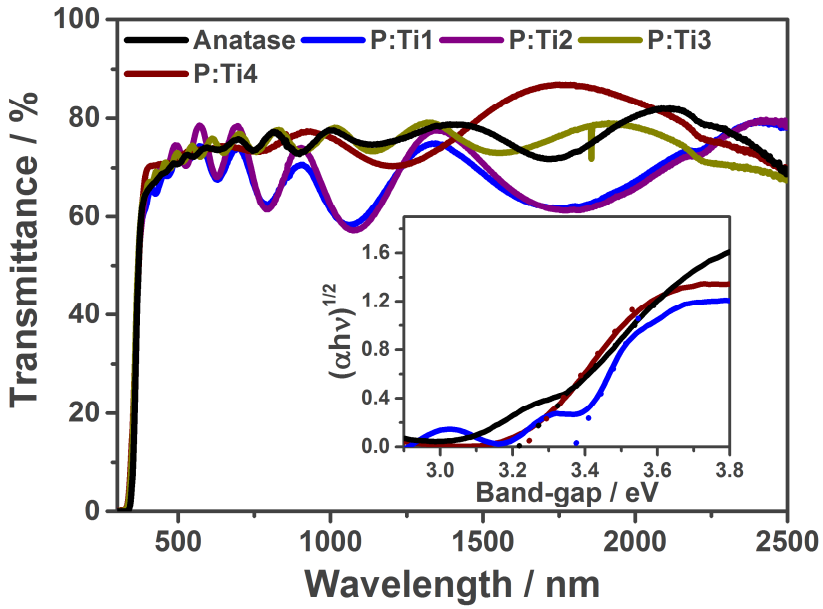


**Figure 3.8.** UV-Vis spectra of selected P-$TiO_2$ films with different $P^{5+}/P^{3-}$ ratios; P:Ti1 (1:0), P:Ti2 (1:0), P:Ti3 (1:1) and P:Ti4 (2:1), undoped $TiO_2$ (black solid line) is included as reference. The inset shows bandgap measurements derived from a Tauc plot, for P-doped films with low (P:Ti1, 0.50 at. %) and high P levels (P:Ti4, 2.98 at. %).

The lifetime and population of photogenerated charge carriers of P-$TiO_2$ films and their undoped analogues, was investigated *via* transient absorption spectroscopy (TAS) analysis, from the microsecond to second time-scale (**Figure 3.9**). This technique is a form of laser flash spectroscopy that tracks transient changes in absorption after an excitation pulse, in many semiconductor photocatalysts, these transient changes in absorption have been shown to be directly related to transient changes in photogenerated charge.[158–160] It has been previously demonstrated that kinetics and charge population of photogenerated electrons and/ or holes could be investigated in $TiO_2$ materials by recording transient absorbance switches at specific wavelengths.[24] TAS analyses were carried out using an inert environment (argon), to avoid photocatalytic processes during the process and therefore and thus, the photogenerated

charge carriers could only recombine. This recombination process would lead to a decrease in transient absorption towards zero net change (*i.e.* complete recombination of charge). The velocity of this recombination process dictates the natural lifetime of photogenerated charge carriers in a given photocatalyst. It has been well acknowledged that in anatase $TiO_2$ materials, photogenerated charge carriers recombine naturally within 100 ms and show a power law decay typical of the trap/ de-trapping movement of charge.[135] Each undoped and P-doped film was measured from the µs to s timescale, this region does not cover the initial stage where charge generation and trapping (fs to ps timescale) occurs but includes the timescale region where most photocatalytic processes typically occur such as the reduction of $O_2$,[161] the oxidation of NO[162] and the oxidation of water.[163]

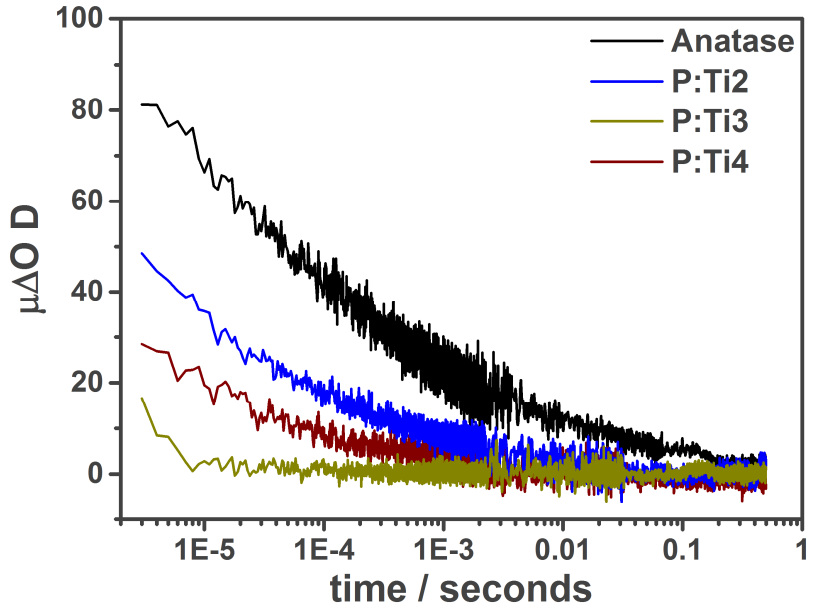


**Figure 3.9.** Transient absorption kinetic decays on the microsecond to second time-scale, normalised at 2 µs, was used to investigate the lifetimes of photogenerated charge carriers for undoped (black line) and P-doped, P:Ti2 ($P^{5+}/P^{3-}$ ratio = 1:0 and 0.90 at. %, blue line), P:Ti3 ($P^{5+}/P^{3-}$ ratio = 1:1 and 2.27 at. %, green line) and P:Ti4 ($P^{5+}/P^{3-}$ ratio = 2:1 and 2.98 at. %, burgundy line) $TiO_2$ films.

These TAS studies were carried out by using a 355 nm pulse laser, which was utilised to photoexcite the as-synthesise films used in this section, producing photogenerated

charges in the semiconductor alongside a transient change in absorption (**Figure 3.9**). It can be observed in Figure 3.8 that the films explored in this section showed similar levels of absorption at 355 nm, allowing a fair comparison in population changes. Figure 3.9 shows that the undoped $TiO_2$ film showed the highest absorbance at 2 μs. This meant that the undoped films could produce more photogenerated charge carriers at this time-scale compared with the P-doped samples, despite that all films would have absorbed a similar level of light from the laser pulse. Likewise, the decreasing of the initial absorption signal at 2 μs to half of its value ($t_{1/2}$) was also slowest for undoped $TiO_2$ (**Table 3.2**), showing a lifetime with a $t_{1/2}$ of 58 μs. In contrast, the addition of phosphorus decreases the lifetime of the photogenerated charge carriers, being the next longest lived charges for samples P:Ti4 and P:Ti2, with a $t_{1/2}$ of 19 and 14 μs respectively. The shortest lived photogenerated charge was found in sample P:Ti3, with a $t_{1/2}$ of 3.1 μs.

In summary, it can be concluded that P-doping increase recombination processed within P-$TiO_2$ films, decreasing the lifetime of photogenerated charge in $TiO_2$. It is often argued that doping $TiO_2$ typically encourages recombination, where the dopant sites act as centres for this recombination.[164] Interestingly, it was observed that the recombination rate changed substantially in our P-doped $TiO_2$ materials. The results obtained did not allow to completely correlate the recombination rate and levels of phosphorus; however, the results observed in this chapter do suggest that a faster recombination rate occurs when the $P^{5+}$ and $P^{3-}$ concentration are equivalent.

### 3.3.3.5. Functional properties of P-$TiO_2$ thin films.

#### 3.3.3.5.1. Electrical properties: Hall Effect Probe.

The electrical properties of the as-synthesised films used in this section were explored using Hall Effect probe measurements, at room temperature, in the van der Pauw configuration on samples made with soldered indium-tin contacts. Different positions in each of the P-doped $TiO_2$ films with low, mid and high levels of phosphorus, were investigated. In addition, area-specific XPS analysis data was collected to correlate the level and nature of the phosphorus species and their electrical properties. The median values, as well as their corresponding standard errors, for carrier density and mobility and resistivity as a function of total P concentration and relative presence of $P^{3-}$, of the P-doped films and their undoped analogue, are shown in Figure 3.10. All films investigated in this section displayed n-type conductivity, with different electrical conductivity properties depending on the oxidation state of the dopant ($P^{5+}$ and $P^{3-}$). It is worth noting that the doping process seems to produce changes in the electrical conductivity properties of the P-doped $TiO_2$ films, depending on the phosphorus environment specie added to the $TiO_2$ lattice; therefore, the presence of the $P^{3-}$ state (substituting $O^{2-}$ lattice site and neutralising any electrons in the system) corresponds to a decrease in both resistivity and charge carrier density whilst the $P^{5+}$ state (substituting on the $Ti^{4+}$ site and liberating an electron) effects an increase in electrical conductivity. Only at low phosphorus doping levels is the $P^{5+}$ state present alone (< 1 at. %), whereas at higher doping levels (from ≈ 2 at. %) the $P^{3-}$ state is also detectable.

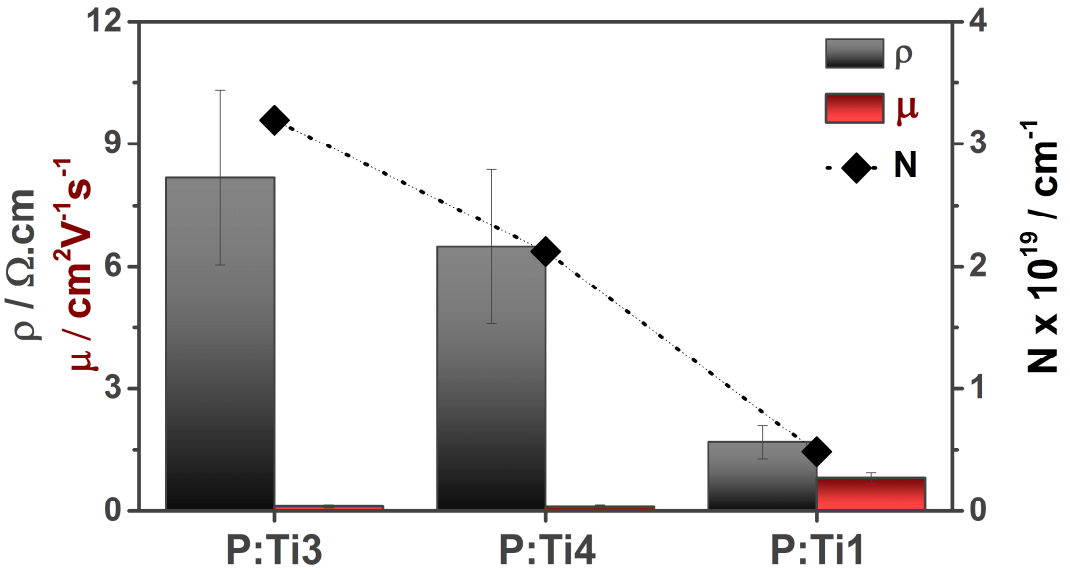


**Figure 3.10.** A comparison of Hall Effect probe measured resistivity (grey bars), charge carrier mobility (burgundy bars) and carrier density (full diamonds) for P-doped $TiO_2$ thin films; P:Ti3 ($P^{5+}/P^{3-}$ ratio = 1:1 and 2.27 at. %), P:Ti4 ($P^{5+}/P^{3-}$ ratio = 2:1 and 2.98 at. %), and P:Ti1 $P^{5+}/P^{3-}$ ratio = 1:0 and 0.50 at. %). Standard errors are included for median electrical property values.

It could be finally concluded that P-doping enhances charge carrier density values, inducing a crossover into semiconductor degeneracy, leading to a more 'metallic' character in accordance with the Mott metal-to-insulator transition. These levels of charge carrier concentration are not achievable in theoretical undoped $TiO_2$ films that allow conduction through oxygen vacancies. In contrast, in P-doped films the transfer of charge carriers is thought to proceed *via* a band process. Carrier density shows a typical transition from high resistivity, to low resistivity at an idealised dopant level (≈ 1 at. %), followed again by an increase in resistivity.

This could be explained in terms of the different roles of the phosphorus species within the doped $TiO_2$ films. When $TiO_2$ thin films are doped using low amounts of P, they will enter the lattice in the Ti site, with an oxidation state of 5+. These cationic species have an ionic radius of six coordinated $P^{5+}$ of *ca.* 0.380 Å, which is relatively smaller than that of $Ti^{4+}$ (0.605 Å), facilitating the replacement of the Ti lattice position. However, anionic species, $P^{3-}$, present a much larger ionic radius than $O^{2-}$ species,

which will be detrimental for their rapidly addition into $TiO_2$. As the concentration of dopant is increased, the formation energy of the cationic dopant, which acts as a shallow donor and is in the $P_{Ti}^{+1}$ charge state (**Figure 3.11**), increases over the range of the bandgap. P on an oxygen site, however, acts as a p-type dopant, with the hole state localized on the p-states of the P dopants. At high Fermi levels, however, $P_O^{-1}$ will start to become favourable. Once the concentrations of P dopant exceed ~ 1%, the $P_O^{-1}$ starts to dominate, acting as an electron killer, and pinning the Fermi level above just the conduction band minimum (CBM). Any further increase of the P doping concentration will just result in the decrease of the number of electrons in the system.

Whilst the effective carrier density values are fairly impressive; 0.5 – 2.2 x $10^{19}$ $cm^{-3}$ (especially as compared to other non-metal dopants such as fluorine), the carrier mobilities were low (≈ 0.1 - 0.8 $cm^2V^{-1}s^{-1}$) and attributed to ionised impurity scattering. Overall, the current effective resistivities (of the order of $10^0$ Ω.cm) were found to be too high for conventional TCO applications.

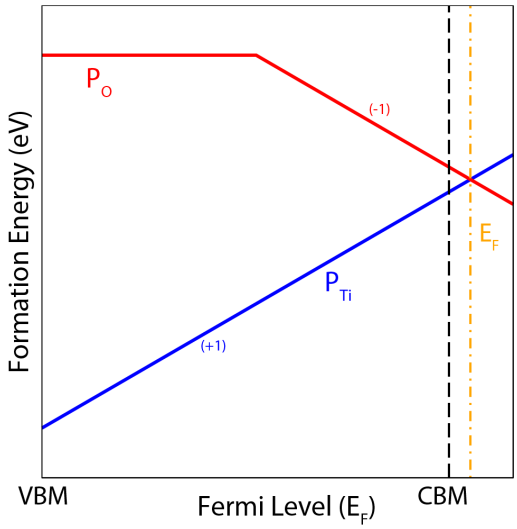


**Figure 3.11.** Schematic showing the mechanism of dopant self-compensation as the P-doping level is increased. The y-axis displays the formation energy of the defect species, and the x-axis shows the position of the Fermi level relative to the VBM and CBM for anatase $TiO_2$. For high doping levels (above the CBM), the Fermi level gets trapped (Orange dot-dash vertical line) by the formation of $P_O^{-1}$.

It can be concluded that the doping process explored in this section showed a decrease in mobility upon phosphorus doping, due to a heavy ionised impurity scattering effect (whether direct or indirect) of the dopant. However, it is worth noting that this decrease can be associated to the presence of the $P^{3-}$ species within $TiO_2$ films. Certainly, whether the lower mobility is due to the use of high levels of the phosphorus dopant, leading to form $P^{3-}$ species above a threshold value, or to the presence of the anionic specie resulted difficult to address. Nevertheless, the results reported in this section indicate that the presence of high levels of anionic species resulted in a severe loss of the mobility, at similar levels of total P-doping.

#### 3.3.3.5.2. Photocatalytic Activity.

As previously mentioned, the use of different synthetic methods to deliver P-doped $TiO_2$ materials resulted in a varying photocatalytic performance. It is worth mentioning that sol-gel methods can deliver materials with a varying phosphate content and surface area, which could potentially affect the photocatalytic efficiency of the material.[144–147] In contrast, the use of APCVD processes allow delivering films with homogeneous bulk phosphorus content, as well as comparable surface area morphology. These as-synthesised films were also used to thoroughly study the influence of the different P species in their photocatalytic response, which was tested during the photodegradation of stearic acid under UVA irradiation (1.2 mW $cm^{-2}$).[87] The overall photocatalytic reaction is given by Equation 3.3.

$$CH_3(CH_2)_{16}CO_2H + 26O_2 \xrightarrow[h\nu \geq E_{bg}]{TiO_2} 18CO_2 + 18H_2O \qquad (3.3)$$

The photoactivity efficiency of the films investigated in this section was explored using Fourier infrared spectroscopy, FTIR, this technique was used to monitor the loss of stearic acid characteristic C-H modes, present at 2958, 2923 and 2853 $cm^{-1}$. A linear regression of the curve integrated area *vs*. irradiation time, at the initial photocatalytic process (30 – 40 %), was used to assess the photocatalytic performance rates of the as-synthesised undoped and P-doped thin films. The corresponding rates were expressed as formal quantum efficiencies, $\xi$, defined as molecules of stearic acid degraded over incident photons (units, molecule $photon^{-1}$) (**Figure 3.12**). It is worth noting that all undoped and P-doped films used in this section showed comparable physical and structural properties, as previously discussed; hence any variation of the $\xi$ values should not be attributed to differences in their physical or morphological properties. With the exception of sample $P^{5+}/P^{3-}$ = 1:1, which showed no activity, most P-$TiO_2$ films showed moderate activities compared to undoped $TiO_2$ films. This finding is unusual for highly conductive samples, since is well acknowledged that for semiconductor materials there is a decrease in photocatalytic activity upon an increase of their electrical conductivity.[140]

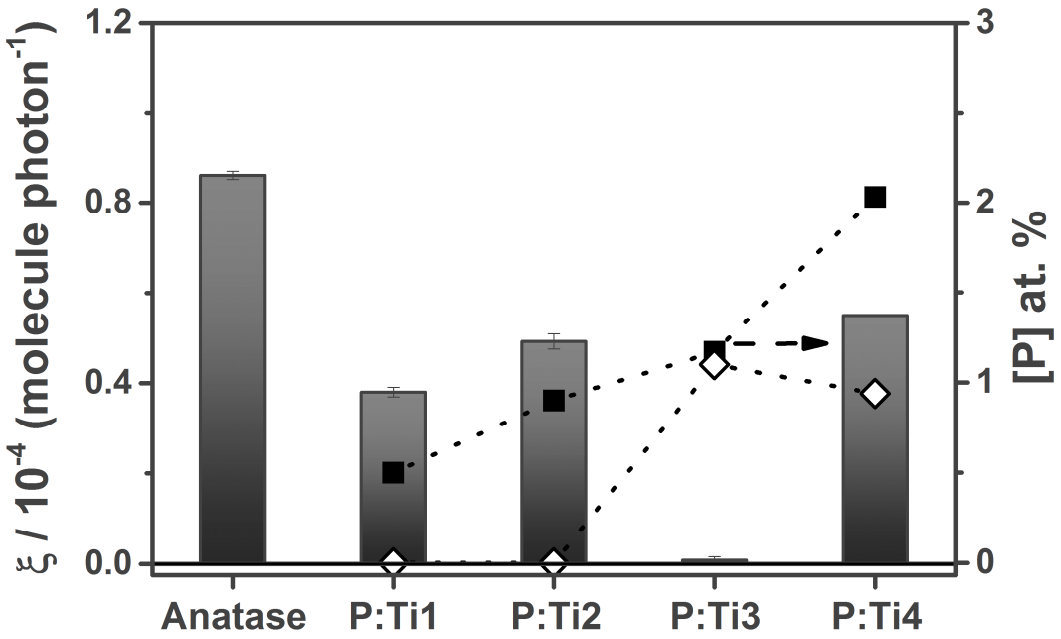


**Figure 3.12.** Formal quantum efficiencies obtained during photodegradation of stearic acid under UVA irradiation of selected P-$TiO_2$ films and undoped $TiO_2$ film used as reference. The relative levels (%) of cation phosphorus ($P^{5+}$, full squares) and anion phosphorus ($P^{3-}$, empty diamonds) are indicated for comparison. The film description and experimental details are given in Table 3.1.

The photocatalytic response of the films (**Figure 3.12**) could be directly correlated with photogenerated charge carrier lifetimes (**Figure 3.9**), where films with higher carrier lifetime showed the highest photocatalytic activity, being pure anatase $TiO_2$ (undoped) the most active film ($\xi$ = 0.86 molecule photon$^{-1}$; $t_{1/2}$ = 58 μs), followed by P:Ti4, P:Ti2 and P:Ti1 doped films ($\xi$ = 0.55, 0.47 and 0.33 molecule photon$^{-1}$; $t_{1/2}$ = 19, 14 and *na* μs, respectively). In contrast films with a similar ratio between anionic and cationic species, sample P:Ti3 ($P^{5+}/P^{3-}$ = 1:1), showed the lowest lifetime ($t_{1/2}$ = 3.1 μs) and no photocatalytic activity could be observed. These findings were correlated to the kinetics of the photocatalytic process in $TiO_2$ materials. It is commonly acknowledged that photocatalysis on $TiO_2$ proceeds through the generation of electrons and holes, which are diffused to the photocatalyst surface to react with air and water present in the environment in two different pathways: (i) holes reacting with $H_2O$ present in the surface of the materials to produce highly reactive hydroxyl radicals that subsequently degrade nearby organics or (ii) electrons reacting with $O_2$ to create superoxide species,

also highly reactive, which will also degrade nearby organics.[17] The mechanism of these two reactions take place at different time-scales, being demonstrated that (i) holes can react with $H_2O$ within 2 μs and (ii) electrons react with $O_2$ from 10 – 900 μs.[165] As previously mentioned, TAS analyses of the as-synthesised films showed that the undoped $TiO_2$ film was the sample with longest-lived photogenerated charge. However, it is worth noting that these charge carriers were reduced to half of their initial value from just 2-58 μs. Therefore, the low photocatalytic efficiency (*ca.* ~ 1.4 %) can be correlated to the slow reaction of electrons with $O_2$, where the rate of charge carrier recombination is higher than $O_2$ reduction.

Interestingly, the results observed in this section showed that the predominant presence of $P^{5+}$ species was beneficial in terms of high photocatalytic activity and electrical conductivity, whilst an equivalent presence of $P^{3-}$ and $P^{5+}$ resulted in a decrease of the functional properties of the P-doped films, where both photocatalytic and electrical properties were negligible. This effect can be correlated to an enhanced electron-hole recombination within $P^{3-}$ sites, where the lifetime of photogenerated charge carriers for the most $P^{3-}$-rich sample (P:Ti3) showed a faster decay, almost 20 times, than that of its undoped analogue film (anatase), and thus decreasing its photocatalytic efficiency (**Figure 3.13**).

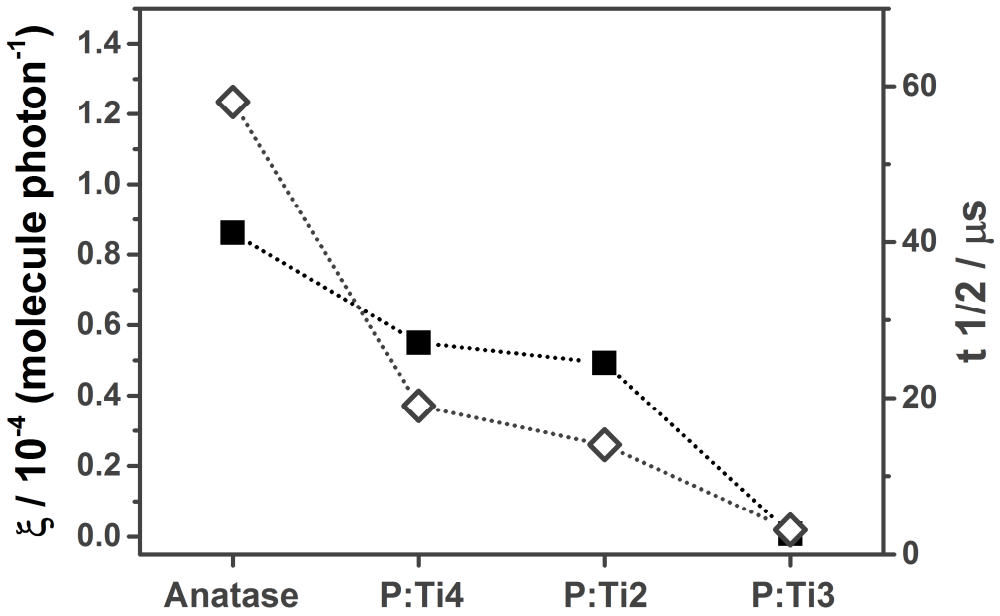


**Figure 3.13.** Comparison between photocatalytic efficiency (given as formal quantum efficiency, full squares) and the lifetime of photo-generated charge carriers (empty diamonds) for anatase and P-doped $TiO_2$ films; P:Ti2 ($P^{5+}/P^{3-}$ ratio = 1:0 and 0.90 at. %), P:Ti3 ($P^{5+}/P^{3-}$ ratio = 1:1 and 2.27 at. %) and P:Ti4 ($P^{5+}/P^{3-}$ ratio = 2:1 and 2.98 at. %).

### 3.3.4. Conclusions.

In this section, we presented a new route to synthesise P-doped $TiO_2$ films (either $P^{5+}$ doped or $P^{5+}$ and $P^{3-}$ doped) using atmospheric pressure chemical vapour deposition (APCVD). This is the first example of APCVD synthesis to incorporate anionic phosphorus ($P^{3-}$) in $TiO_2$.

In addition, we have used transient absorption spectroscopy (TAS) to investigate the transfer of the photogenerated charge carriers within the bulk of P-doped $TiO_2$ films. We observed an increase of the recombination of photogenerated charge carrier, decreasing their charge carrier lifetime upon the addition of phosphorus within the $TiO_2$ lattice, especially when the concentration of $P^{3-}$ species is higher than $P^{5+}$ species. These anionic species, $P^{3-}$, resulted also detrimental in the photocatalytic response of P-doped $TiO_2$ films, investigated during the mineralization of stearic acid. Therefore, it can be

concluded that $P^{3-}$ species contribute to increase the recombination of photogenerated charge carriers, being almost 20 times faster, for P-$TiO_2$ films with high $P^{3-}/P^{5+}$ ratio, than that of their undoped $TiO_2$ analogue. In addition, the charge carrier recombination of $P^{3-}$-rich films was also almost 6 times faster than the corresponding $P^{5+}$-rich samples.

Hall Effect probe measurements were also used to study the electrical response of the as-synthesised P-doped films. These measurements showed that the electrical conductivity was higher in samples rich in $P^{5+}$ species as well. The results reported in this chapter are significant, since electrical conductivity often arises to the detriment of photocatalytic activity, and it could mean a step forward in the formation of novel multifunctional materials, with an optimal balance between self-cleaning and TCO properties.

In the next section of this chapter, we will investigate the addition of sulfur species to $TiO_2$ films using APCVD, and its effect on the physical and functional properties of $TiO_2$ materials.

## 3.4. S-doped $TiO_2$ thin films.

### 3.4.1. Introduction.

As previously mentioned, non-metal doping has been the most commonly approach used to dope titania materials. Nitrogen has been historically the most explored dopant to red-shift the light absorption properties of $TiO_2$ materials.[25,88] However, these materials have engendered wide debates to explain either their enhanced UV activity,[35,99,164] and visible-light,[75,91,99] driving the scientific community to investigate alternative non-metal dopants.

Along with the use of nitrogen, sulfur has also been extensively investigated as an alternative to red-shift the absorption onset of $TiO_2$ materials from UVA to the visible light range.[166,167] Different techniques have been explored to synthesise these S-$TiO_2$ materials; such as, atomic layer deposition (ALD),[168] annealing of $TiS_2$ in air,[169] as well as mechanochemical treatment.[166] However, only a few groups have tried and successfully synthesised S-$TiO_2$ materials using atmospheric pressure chemical vapour deposition (APCVD),[170] a well-known technique widely used to manufacture float glass, which could be seen as a rapid and facile way to scale-up the synthesis of these photocatalytic materials.

In this chapter, the addition of sulfur to the $TiO_2$ lattice using an APCVD approach is reported. The results observed in the previous chapter and section of this chapter, when $TiO_2$ was doped with nitrogen and phosphorus, respectively, as well as previous S-doped $TiO_2$ reports, makes this chemical element a promising dopant source to replace oxygen within the $TiO_2$ lattice to narrow its band gap and enhance its photocatalytic response. It is commonly assumed that non-metal elements with a potential energy higher than that of O 2p atomic orbitals can widen the valence band of $TiO_2$,[171] narrowing its band gap. In addition, it has been reported that S can be added to $TiO_2$ either as anionic or cationic species,[108,172] both S oxidation states have been reported beneficial to red-shift the optical properties of $TiO_2$ and produce visible-light active photocatalytic materials.[173,174] However, it is worth mentioning that the contribution of these anionic and cationic species on the enhanced properties of $TiO_2$ is still not clear, being a subject of debate. In this chapter, we will evaluate the effect of adding sulfur into the $TiO_2$ lattice through different physical and optical techniques.

### 3.4.2. S-$TiO_2$ thin films synthesis and appearance.

S-doped and undoped $TiO_2$ thin films were synthesised using APCVD. Undoped $TiO_2$ thin films were synthesised using titanium tetrachloride ($TiCl_4$) and ethyl acetate ($C_4H_8O_2$) as titanium and oxygen sources, respectively. Sulfur-doped films were growing using allyl sulfide ($C_6H_{10}S$) as the sulfur source, following Equation 3.4.

$$TiCl_4 + CH_3COOC_2H_5 + C_6H_{10}S \xrightarrow{500\ ^oC} TiO_{2-x}S_x + \text{by-products} \qquad 3.4$$

As previously mentioned all precursors are contained in stainless steel bubblers at appropriate temperatures and the APCVD system is maintained at 200 °C. The enriched vapour reactants are transferred using pre-heated $N_2$ to the stainless steel mixing chambers (250 ºC) and carried through a triple baffle manifold into the CVD reaction chamber. In a standard S-$TiO_2$ synthesis, the temperature of the bubblers, containing the titanium, oxygen and sulfur sources were hold at 68, 38 and 8 ºC, respectively. The latter temperature was achieved using an ice bath. The corresponding mass flow rates of titanium and oxygen sources were 6.7 x $10^{-3}$ and 3.1 x $10^{-3}$ g $min^{-1}$. The flow rate conditions of the S precursors are indicated in Table 3.3. The films were deposited at 500 °C on float glass substrates (225 x 90 x 4 mm; length x width x thickness).

**Table 3.3.** Experimental and synthesis details of undoped and S-doped $TiO_2$ thin films. The temperature and mass flow conditions were constant for metal ($TiCl_4$) and oxygen ($C_4H_8O_2$) precursors: 68 and 38 °C and 6.7 x $10^{-3}$ and 3.1 x $10^{-3}$ g $min^{-1}$, respectively. The temperature for the phosphorus source ($C_6H_{10}S$) was maintained at 8 °C.

| **Sample** | **Experimental Details** | | | |
|---|---|---|---|---|
| | **S Mass Flow ($10^{-3}$) (g $min^{-1}$)** | **Deposition Time (s)** | **d (nm $min^{-1}$)** | **[S] (at. %)** |
| Undoped $TiO_2$ | - | 120 | 350 | - |
| S1 | 0.02 | 120 | 315 | 0.15 |
| S2 | 0.03 | 120 | 300 | 0.20 |
| S3 | 0.05 | 120 | 285 | 0.45 |

The S-$TiO_2$ thin films synthesised in this chapter were transparent, showing a slight yellow tinge, with thicknesses (as determined from cross-section SEM and *Swanepoel* method)[85] varying between 250-450 nm depending on the flow rate of the sulfur precursor. This variation in the thickness is correlated to the presence of different optical interference bands across the substrate, where each colour band corresponds to a different region of thickness.[149] All thin films used in this section were adhesive and resistant to the Scotch tape test,[97] with no particles being peeled off, as well as resisting a scratch test using a steel scalpel[98] and were constantly stable in air. It is worth noting that all as-synthesised coating surfaces showed no pin-hole defects and no particulates were observed in the exhaust gas. Several samples (more than 25), from each different thin film, were synthesised to prove the reproducibility of the method synthetic method reported in this section However, only selected thin films, with comparable thickness and physical properties, are presented.

### 3.4.3. Results and discussion.

#### 3.4.3.1.1. Physical and optical properties of S-$TiO_2$ thin films.

X-ray diffraction and Raman spectroscopy analyses showed that the use of low concentrations of sulfur did not modify the structural properties of $TiO_2$, presenting peaks that match in position to those expected from anatase $TiO_2$ crystal phase. However, we observed that increasing the amount of sulfur, loaded in the $TiO_2$ matrix, induced an anatase-to-rutile phase transfer, agreeing previous sulfur-doped works. Pore *et al.*[168] reported the synthesis of S-doped $TiO_2$ materials by atomic layer deposition (ALD), finding that sulfur had a drastic impact on the $TiO_2$ growth, inducing the presence of the rutile crystal phase. This could be explained as the $S^{2-}$ states (1.85 Å)

that replaces $O^{2-}$ sites (1.40 Å) were larger, modifying the lattice of $TiO_2$. This modification on the $TiO_2$ structure could decrease the temperature for the anatase-to-rutile transformation process. Sabyrov *et al.*[175] also reported that a decrease in the particle size, as well as an increase of the acidic conditions of the reaction environment, could contribute to increase the growth of the rutile crystal phase in $TiO_2$ materials. Therefore, our S-doped $TiO_2$ films might be affected by this anatase-to-rutile transfer effect, as the use of sulfur can lead to reduction of the pH of the CVD reaction chamber affecting the $TiO_2$ film synthesis.

All samples showed similar peak area ratios ([101]/[211]) in the range of 1.6-2 and FWHM of 0.5° which match in position to those expected for anatase $TiO_2$. The crystallinity of the S-$TiO_2$ films, as evaluated by XRD, was probably affected by incorporation of $S^{2-}$ anions in the structure, as expected from large size ions (**Figure 3.13**). In addition, possible atomic segregation of sulfur ions from the bulk to the surface of the films will be discussed below in terms of X-ray photoelectron spectroscopy (XPS) results.

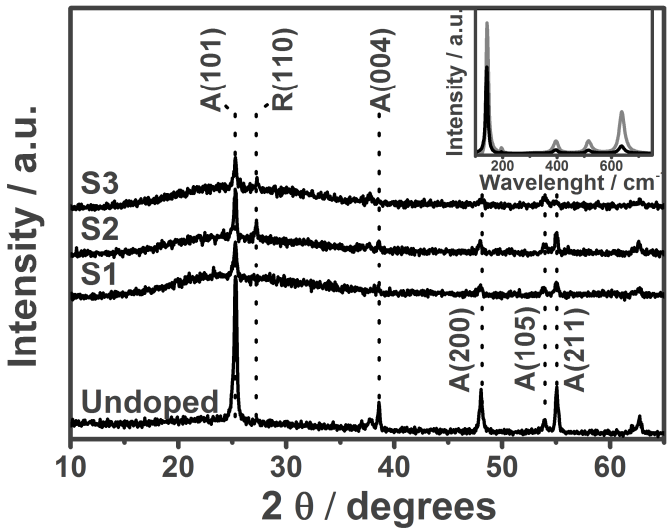


**Figure 3.13.** X-ray diffraction patterns of as-deposited S-$TiO_2$ films with different concentrations of sulfur, low sulfur loading (S1, 0.15 at. %, and S2, 0.20 at. %) and high loading of sulfur (S3, 0.45 at. %). Undoped $TiO_2$ XRD pattern was included for comparison. The inset shows Raman spectroscopy analysis of representative S-doped and undoped $TiO_2$ thin-films.

Undoped and S-doped $TiO_2$ thin films showed thicknesses within the range 300-700 nm, through cross-section scanning electron microscopy and *Swanepoel* method analyses. Scanning electron microscopy (SEM) analysis of undoped $TiO_2$ thin films (**Figure 3.14**) revealed a relatively rough surface formed of large diamond-like aggregated particles. In contrast, S-$TiO_2$ films showed a change in the morphology of the films with smaller flat particles apparently merged together, particularly in the case of S-$TiO_2$ films deposited using low concentrations of sulfur. Furthermore, the use of high concentrations of sulfur revealed a drastic change in the morphology of the S-$TiO_2$ films, the results observed in this chapter agree with previous works reported in the literature.[170]

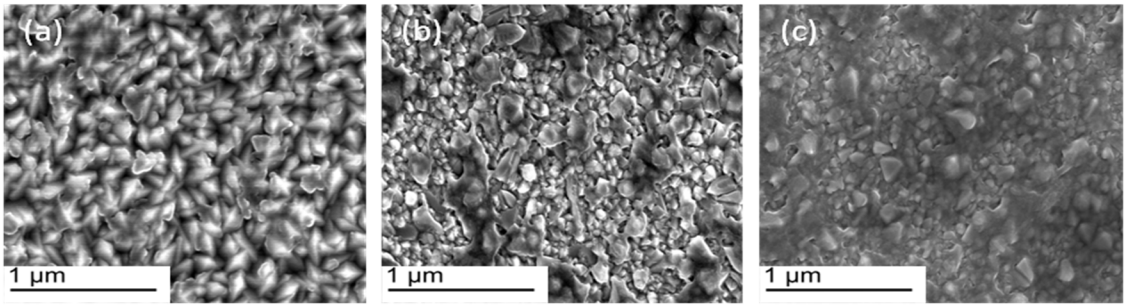


**Figure 3.14.** Scanning electron microscopy (SEM) images of (a) undoped and S-doped $TiO_2$ thin films, using low (b) and high (c) concentration of the sulfur source.

The undoped $TiO_2$ films used in this chapter were uncoloured and transparent, with absorption edges at ~ 380 nm (**Figure 3.15**), characteristic of anatase $TiO_2$ materials. The incorporation of S into the $TiO_2$ resulted in films with a yellow tinge, suggesting a potential change in the S-$TiO_2$ light-absorption properties. This was evidence by a bump and a red-shift in the absorption tail onset (**Figure 3.15**), similar to the one showed by interstitial nitrogen ($N_i$) species in N-$TiO_2$ materials, this red-shift of the tail onset is associated to the formation of intermediate states in N-$TiO_2$ materials,

facilitating the electron-hole photoseparation.[34,37] In contrast, it can be observed in Figure 3.15 that upon an increase in the S concentration, the absorption edge was also red-shifted. This could be explained in terms of the replacement of O sites by S which mixed the valence band O 2p orbitals with S 2p orbitals, resulting in the raising of the valence band energy and concomitant narrowing of the bandgap energy, similar to the effect showed by nitrogen substitutional ($N_s$) species in N-$TiO_2$ materials.[34]

It is worth mentioning that the S-doped films reported in this chapter showed the presence of sulfate species in the surface of the S-$TiO_2$ films, upon oxidation of the S dopant species. It is worth mentioning that these sulfate groups could be optically active in the visible region,[176] therefore, the optical red-shift observed in our S-$TiO_2$ films may be assigned to these surface groups. The presence and effect of these surface sulfate species will be discussed in detail in the next section of this chapter.

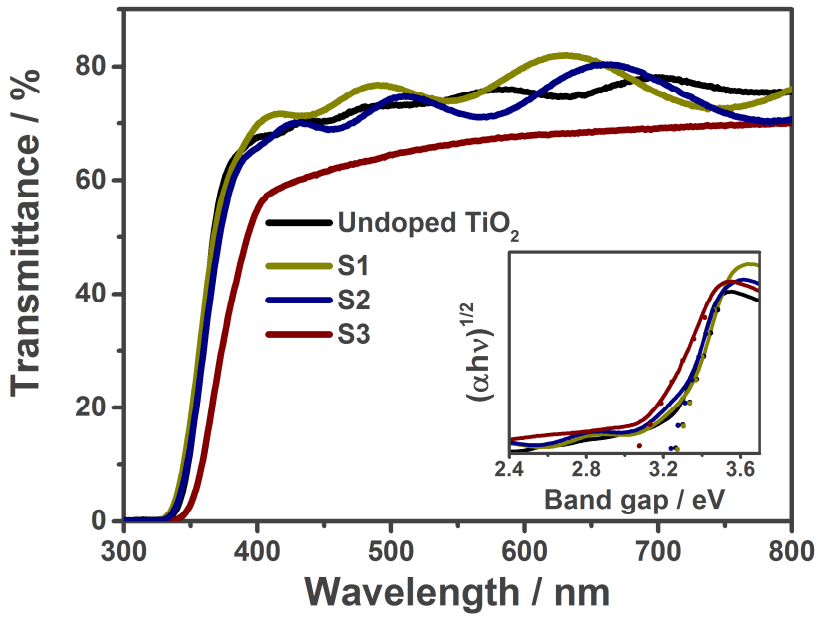


**Figure 3.15.** UV-Vis spectra of selected S-$TiO_2$ films using low (S1, 0.15 at. %, and S2, 0.20 at. %) and high (S3, 0.45 at. %) sulfur content, undoped $TiO_2$ (black solid line) is included as reference. The inset shows a comparison of the bandgap measurements, derived from Tauc plot analysis, between undoped and S-doped $TiO_2$ films.

#### 3.4.3.1.2. Influence of sulfur on the activity of S-$TiO_2$ thin films.

X-ray photoelectron spectroscopy (XPS) analysis was used to study the nature and concentration of the sulfur dopant in our S-$TiO_2$ thin-films. The addition of S species into $TiO_2$ materials has been widely studied in the last few decades. Both theoretical and experimental studies have reported that sulfur could be added to $TiO_2$ as two different oxidation state environments, either as a cation or an anion. Several groups have shown that S can be added as $S^{6+}$ ($SO_4^{2-}$) or $S^{4+}$ ($SO_2$) species, which replaced Ti within the lattice of $TiO_2$ materials, with typical binding energies values within 166-170 eV.[133,167,173] However, it is worth mentioning that the cationic species observed in these S-$TiO_2$ materials could be directly associated to the synthesis method. These S-doped materials were synthesised using an annealing step which would oxidise the S species present in the photocatalyst surface. In addition, it was observed that no cationic species were found within the bulk of $TiO_2$ upon XPS depth profiling analysis, suggesting that these species are mainly attached to the surface of the photocatalyst more than inserted into its matrix. Likewise, anionic species ($S^{2-}$) substituting $O^{2-}$ lattice sites were also assigned to S 2p binding energies between 160-163 eV.[167,172] It is also important mentioning that these anionic species were only observed through XPS surface analysis of S-$TiO_2$ materials synthesised using titanium disulfide ($TiS_2$) as the precursor source, and without post-heat treatment involved, suggesting that these $S^{2-}$ species could be assigned to the incomplete oxidation of the $TiS_2$ precursor.

As previously mentioned, XPS is a surface-sensitive technique ($\leq$ 10 nm),[151] thus all S-doped $TiO_2$ films reported in this chapter were investigated using several depths within the bulk by etching the sample with argon sputtering. Our S-$TiO_2$ films showed a single surface peak at 169 eV, which is commonly assigned to $S^{6+}$ ($SO_4^{2-}$) species (**Figure 3.16**).[133,167,177] Surface etching revealed extremely low concentration values of $S^{2-}$

replacing $O^{2-}$ species (**Figure 3.16**), represented by the presence of a weak peak at 162 eV.[167,172,178,179] This effect could be explained in terms of the important difference in the atomic size between O and S, which could play an important role to hamper the insertion of S into the bulk of $TiO_2$, encouraging atomic segregation from the bulk to the surface of our S-$TiO_2$ thin films. In addition, it should be mentioned that the etching process can change the oxidation state of elements during XPS depth profiling,[151] however, this point is unlikely in the hypothetical case of a reduction from $S^{6+}$ to $S^{2-}$, since argon sputtering typically encourages oxidation. The fact that solely $S^{6+}$ was present at the surface was attributed to surface oxidation on exposure to air.[154] It is important to note that the presence of these sulfate groups will create strong acidic sites on the surface of the $TiO_2$ thin-films, enhancing the acidity of S-$TiO_2$. As previously mentioned this increase in acidity would reduce the temperature of the anatase-to-rutile transfer process. In addition, it has been found that the presence of acidic sites on the surface of $TiO_2$ will have an important role in its photocatalytic response, which will be discussed in detail below.

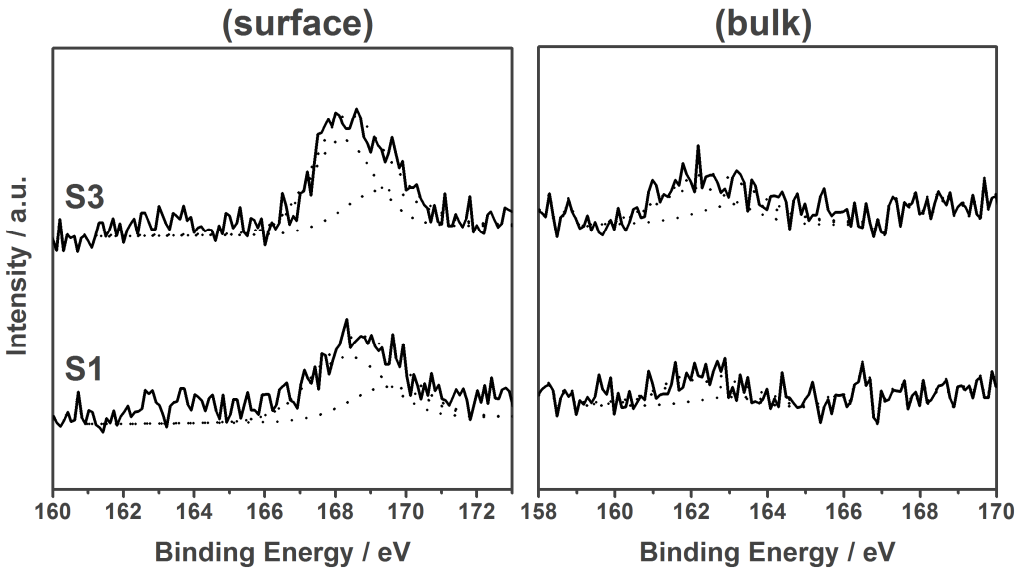


**Figure 3.16.** XPS spectra of surface (left) and bulk average (right) species in the $S_{2p}$ environment (assignments included) of S-$TiO_2$ films with low concentration of sulfur (S1, 0.15 at. %) and high concentration of sulfur (S3, 0.45 at. %). The solid lines

represent experimental data and dotted lines represent the deconvolution of each chemical state into its respective 2 $p_{3/2}$ and 2 $p_{1/2}$ environments.

The effect on the photocatalytic performance of $TiO_2$ materials upon sulfur doping has been widely investigated in the last few decades, showing very different experimental observations. Typical synthesis methods, such as sol-gel and hydrothermal techniques, may perform materials with varying sulfur content and surface area, affecting the photocatalytic performance of S-$TiO_2$ materials.[108,173,180] In contrast, APCVD allows the synthesis of thin films with a homogenous insertion of the dopant species across the bulk and also comparable surface properties. The photocatalytic activity of the S-$TiO_2$ samples was evaluated during the degradation of stearic acid under UVA irradiation (1.2 mW $cm^{-2}$).[87] The photocatalytic reaction is given by Equation 3.5.

$$CH_3(CH_2)_{16}CO_2H + 26O_2 \xrightarrow[h\nu \geq E_{bg}]{TiO_2} 18CO_2 + 18H_2O \qquad (3.5)$$

The photocatalytic test was performed following the loss of the stearic acid C-H modes at 2958, 2923 and 2853 $cm^{-1}$ *via* FTIR. A linear regression of the curve integrated area *vs*. irradiation time, at the initial photocatalytic process (30 – 40 %), was used to assess the photocatalytic performance rates of the undoped and S-doped films explored in this section. The corresponding rates were expressed as formal quantum efficiencies (ξ), defined as molecules of stearic acid degraded over incident photons (units, molecule $photon^{-1}$) (**Figure 3.17**). The variation in the ξ measurements was discarded to be due to differences in physical properties of the films, since all films investigated in this work, undoped and S-doped $TiO_2$, showed similar thicknesses and comparable crystallinity, based on XRD analysis (**Figure 3.13**).

In this chapter, we observed that the addition of S to $TiO_2$ is beneficial from a photocatalytic point of view. Figure 3.17 shows that except for sample S3, (synthesised using high mass flows of S) which performed a slightly lower photoactivity than

undoped $TiO_2$ films, all S-$TiO_2$ samples showed enhanced activities compared to undoped anatase $TiO_2$ films. This finding was astonishing, since sulfur seems to have a dramatic impact on the physical properties of S-$TiO_2$ materials (**Figure 3.13**), which has been usually associated with a decrease of the photocatalytic efficiency of $TiO_2$ materials.[181]

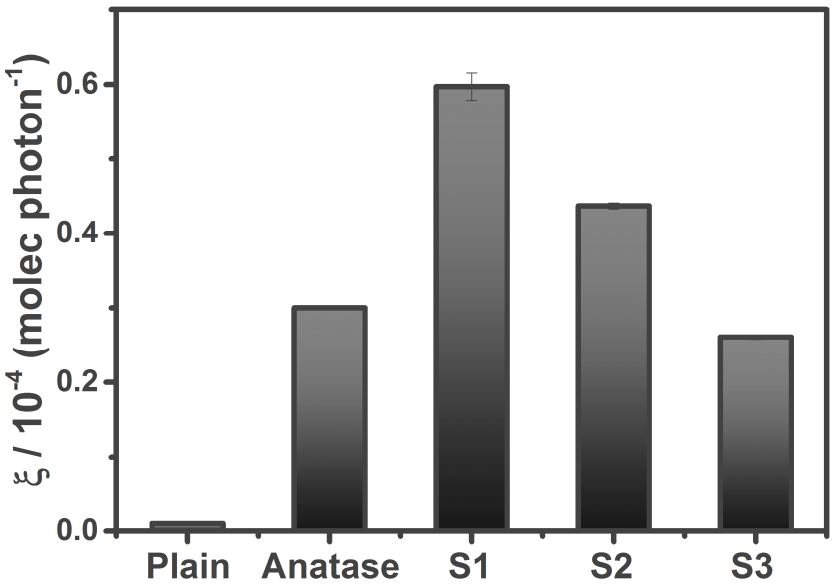


**Figure 3.17.** Formal quantum efficiencies obtained during photodegradation of stearic acid under UVA irradiation of undoped $TiO_2$ film (anatase) and S-doped $TiO_2$ films with different dopant concentration; low concentration of S (samples S1, 0.15 at. %, and S2, 0.20 at. %) and high concentration of S (sample S3, 0.45 at. %). Plain glass (Plain) was used as reference.

A general increase in activity, compared to undoped $TiO_2$ films, was observed for the S-$TiO_2$ films (**Figure 3.17**). As previously mentioned, the *relatively* big size of $S^{2-}$ (1.85 Å) was found a limiting factor to achieve a complete insertion of the S species into the $TiO_2$ lattice, being the majority of the S species segregated to the surface and subsequently oxidised. Therefore, the enhanced photocatalytic activity could be tentatively explained in terms of the presence of these sulfate species ($S^{6+}$) in the surface of the S-$TiO_2$ films. *Wang et al.*[182] demonstrated that the presence of sulfate species in $TiO_2$ materials, increased its surface acidity. This enhanced acidity generates Lewis acidic sites, generating more surface chemisorption centres for reactants and oxygen. It

is generally acknowledged that photocatalysis on $TiO_2$ proceeds through the reaction of photogenerated holes with $H_2O$ and photogenerated electrons with $O_2$ to form reactive hydroxyl radicals that will degrade nearby reactants, thus the increase of $O_2$ adsorbed to the S-$TiO_2$ surface will result in an enhancement of the active hydroxyl radicals.

Interestingly, XPS analysis showed that the concentration and nature of these sulfate species ($S^{4+}$) were similar for all different S-$TiO_2$ films, including low and high concentration of S (**Figure 3.16**). Therefore, the difference in UV photoactivity of S-$TiO_2$ thin films should be attributed to the different concentration of $S^{2-}$, replacing O sites, within the bulk of $TiO_2$. This finding suggests that using high amounts of S species, to dope $TiO_2$, would increase the amount of *impurities* added to the $TiO_2$ lattice, increasing the number of recombination centres. In addition, the use of high mass flows of S resulted in drastic changes in the structural and physical properties of $TiO_2$ (**Figure 3.13 and 3.14**), which was found detrimental for the photocatalytic performance of S-doped films. It is worth noting that a similar effect was observed in N-$TiO_2$ films, where the use of high mass flows of the dopant source was beneficial to narrow the band gap of the materials, but this effect generally compromises their photocatalytic response.[130]

### 3.4.4. Conclusions.

Allyl sulfide was used to synthesise S-doped $TiO_2$ thin-films by atmospheric pressure chemical vapour deposition (APCVD). The use of this chemical precursor to dope titania materials could facilitate the scale-up of S-$TiO_2$ films, as allyl sulfide is easier to handle and less toxic than reagents previously used via APCVD (hydrogen sulfide and carbon disulfide).

In this chapter, we found that the incorporation of sulfur within the lattice of $TiO_2$ was beneficial to alter the optical properties of $TiO_2$ films. We observed that having S-$TiO_2$ films, with low concentrations of S, performed a red-shift of the absorption tail onset increasing the photoactivity efficiency in the UV region. This effect could be explained in terms of mid-gap states between the valence and conduction band of the materials, promoting the photogenerated electrons and holes to the surface of the material. The use of high concentrations of S showed a red-shift in the absorption maximum onset, however, the photoactivity efficiency was decreased upon this enhancement in the amount of S; as more impurities were added to the material, increasing the number of recombination centres.

To summarise, we have found that the use of sulfur to dope $TiO_2$ films could be seen beneficial from a photocatalytic point of view. However, the relatively bigger atomic size of $S^{2-}$ compared to $O^{2-}$ species, drives to a great disorder within the structure of $TiO_2$ films, affecting drastically the crystallinity of the S-$TiO_2$ films. It is worth mentioning that no visible activity was observed for any of the S-$TiO_2$ films used in this chapter. Despite the different reports claiming visible light activity from S-$TiO_2$ materials, it is still not clear whether this enhanced activity is due to the presence of S within the bulk of $TiO_2$ or due to the generation of sulfate species on the surface of $TiO_2$. Acquiring visible light materials involves to control different parameters, such as controlling the type of surface species present in the photocatalyst surface, as well as having a restricted number of lattice defects for the promotion of photogenerated charge diffusion.

In the next chapter, APCVD will be used to investigate the synthesis of rutile/anatase $TiO_2$ heterojunction films. The synthesis of these heterojunction films was designed by adding an amorphous $TiO_2$-based interlayer to allow direct vapour deposition of anatase

on a rutile substrate. An organic model acid (stearic acid) was used to test the photocatalytic performance of these heterojunction films. In addition, silver (Ag) metal particles will be photodeposited on the surface of the heterojunction films, to investigate the effect, that the synergistic interaction between the two $TiO_2$ crystalline polymorphs, has on the photocatalytic activity of the heterojunction films.

Chapter IV

# RUTILE/ANATASE $TiO_2$ HETEROJUNCTION THIN FILMS

*'The following chapter presents the results from a series of experiments for growing rutile/anatase $TiO_2$ heterojunction films via atmospheric-pressure chemical deposition (APCVD). This synthesis was designed by introducing an amorphous $TiO_2$-based interlayer to allow direct vapour deposition of anatase on a rutile substrate, which otherwise would be hindered by templating. This resourceful approach and the subsequent crystallisation of the amorphous layer after heat-treatment of the films allowed investigation on the impact of an efficient interface contact of the two rutile and anatase phases in the photodegradation of a model organic pollutant. The enhanced photocatalytic properties of these films could possibly be explained by the high synergistic effect between both polymorphs. This chapter also presents clear evidence on the interfacial charge flow, involving electron transfer from rutile to anatase, which is in agreement with theoretical and electronic paramagnetic resonance data'.*

## 4. Heterojunction rutile/anatase $TiO_2$ thin films. An innovative approach to an efficient photogenerated charge carrier separation.

### 4.1. Introduction.

As previously mentioned $TiO_2$ materials have been widely used in photocatalysis.[17] However, the main limitation of these photocatalytic materials is its *relatively* wide band gap (*ca.* ~ 3.2 eV), limiting their use to UV-light driven applications. Many routes have been investigated during the last few decades to extend the photocatalytic response of $TiO_2$ into the visible region, being the chemical modification of $TiO_2$, addition of cations and anions to its lattice, the most explored approach. Although successful red-shifts have been observed, there is no general agreement as to which dopant is more beneficial. And in many cases, there is inherent problems associated to the addition of *impurities*, resulting in an increase in the number of the recombination centres with the concomitant decrease of the photocatalytic properties. In addition, as previously discussed, chapters 2 and 3, this chemical modification would not be durable to several photocatalytic cycles, due to a photoconsuming process of the dopant species during the photocatalytic process, decreasing its photocatalytic response.

Therefore, alternative solutions to extend and enhance the photocatalytic response of $TiO_2$ have been investigated. Despite the vast number of approaches to enhance the activity of $TiO_2$, which include nanostructuring and the addition of co-catalysts, arguably, the most successful would be to form a heterojunction system. This system would generated an interface region which promotes vectorial transfers, enhancing the lifetime of the photogenerated charge carriers and their availability on the surface of the photocatalyst to form active radicals with the associated increase of the photocatalytic performance.[31,38] This approach could be considered as a new and facile route to synthesise highly active photocatalysts, as well as a long-lasting solution to

overcome the low durability associated to doped materials. In addition, depending on the respective band energies, a heterojunction can increase photocatalytic efficiency through the complementary absorption of solar radiation.

In this section, the improvement of $TiO_2$ by forming a heterojunction between rutile and anatase $TiO_2$ polymorphs is presented. It has been commonly acknowledged that composites of these two polymorphs will enhance the photocatalytic properties of titania; following a similar mechanism to P25 Evonik, still the most common benchmark photocatalyst, where the synergy between the two polymorphs enhances the charge carrier separation.[183] However, the synergy between anatase and rutile phases has created a constant debate,[184,185] especially concerning the relative position of their corresponding conduction bands. It is worth mentioning that rutile has been commonly considered as an electron sink in the anatase-rutile system (**Figure 4.1(a)),** however, a recent theoretical model[31] has proposed a type II energy band alignment (staggered) with electrons being transferred from rutile to anatase (**Figure 4.1(b)**), which agrees a previous work based in electron paramagnetic resonance (EPR) data.[183] In this chapter an investigation to shed light on this rutile – to – anatase electron transfer based on standard photocatalytic tests is presented.

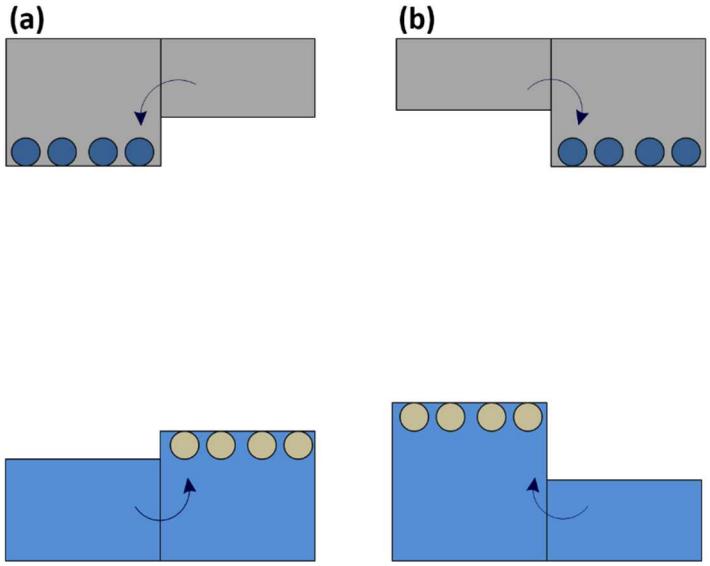


**Figure 4.1.** The two models proposed for the relative position of the conduction bands of rutile and anatase $TiO_2$ polymorphs (adapted from ref. **31**): (A) consensual model denoting rutile as an electron sink; (B) recent configuration proposing electron transfer from rutile to anatase. This work presents evidence that supports model (B).

Atmospheric pressure chemical vapour deposition (APCVD) was used to produce rutile (R) and anatase (A) materials, as well as rutile/anatase (R/A) heterojunction films, with an effective interface contact. When the synthesis of these multilayer films was designed, we found that there is an inherent limitation to deposit an anatase layer on rutile using APCVD (**Figure 4.2**). This rutile substrate would always act as a template, inducing formation of a single-phase rutile film. This issue was bypassed by intercalation of a $TiO_2$-based layer at relatively low temperature (~ 300 °C), producing an amorphous (Am) layer which blocks the templating effect of the rutile substrate (**Figure 4.2**). The deposition of the amorphous interlayer in the rutile/amorphous/anatase (R/Am/A) multilayer films and its thermally-induced crystallization, resulting in rutile/anatase (R/A) films, allowed evaluating the effect of an effective synergy at the interface, and the photocatalytic performance of the heterojunction films by monitoring the photodegradation of a model organic pollutant (stearic acid). Additionally, the synergistic contact between both layers and the rutile – to – anatase electron transfer was also investigated during photodeposition of silver

(Ag), allowing direct evidence of a drastic increase in electron density on the anatase surface of A/R films, which agrees with theoretical and experimental studies.[31]

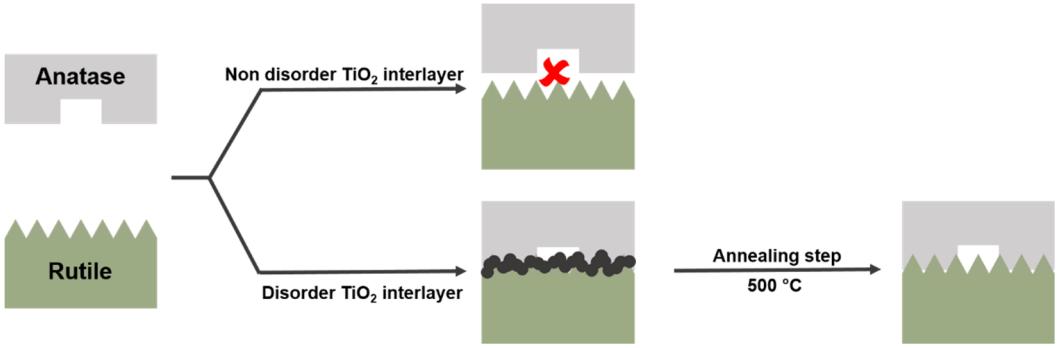


**Figure 4.2**. Scheme to explain the synthesis of the multilayer $TiO_2$ films. It can be observed how the first path would lead to have a pure single rutile film, as it would hinder the deposition of any crystalline $TiO_2$ phase. On the contrary, in the second route the use of a non-crystalline $TiO_2$-based material as interlayer and its successive crystallisation, allowed to deliver rutile/anatase films.

## 4.2. Experimental methods.

All chemicals were purchased from *Sigma-Aldrich*. Titanium tetrachloride ($TiCl_4$, 99.9 %) and ethyl acetate ($C_4H_8O_2$, 99.8 %) were used as titanium and oxygen source, respectively. Nitrogen gas ($N_2$) was supplied BOC and was used as the inert carrier gas. Quartz substrates were purchased from *MultiLab*. Each quartz substrate was thoroughly cleaned using acetone ($C_3H_6O$, 99 %), isopropanol ($C_3H_8O$, 99 %), distilled water and finally dried with air prior to their use. Octadecanoic (stearic) acid ($C_{18}H_{36}O_2$, 95 %) was used as the organic layer to be degraded during the photocatalytic test.

### 4.2.1. Physical characterisation.

X-ray diffraction analysis was performed using a Bruker-Axs D8 (Lynxeye XE) diffractometer, which consist of monochromated Cu X-ray source ($K_{\alpha 1}$, 154 Å) and a glancing incident angle ($\theta$) of 1°. Raman spectroscopy was performed using a Renishaw 1000 spectrometer equipped with a 633 nm laser, which was calibrated using a silicon reference. UV/vis spectroscopy analyses were carried out using a double

monochromated Perkin Elmer Lambda 950 UV/Vis/NIR Spectrophotometer within the 250 – 2500 nm range. These UV/vis measurements were calibrated using a *Labsphere* reflectance standard. Two different scanning electron microscopy (SEM) systems, a JEOL 6301 (5 kV) and a JEOL JSM-6700F field emission instruments, were used to collect data, the Oxford software INCA was used for EDS analysis. Likewise, SEM was also utilised to measure the thickness of the heterojunction thin films, and their single component analogues, *via* side-view SEM analysis. Transmission electron microscopy (TEM) images were collected using a high resolution TEM instrument, JEOL 2100, which consists of a $LaB_6$ source at an acceleration voltage of 200 kV. A Gatan Orius Charge-coupled device (CCD) was used to acquire and record the micrographs. The samples were prepared by scrapping them off the quartz substrate using a diamond pen, followed by a sonicating process in chloroform and drop-casted onto a 400 Cu mesh lacy carbon film grid (Agar Scientific Ltd.). Energy-dispersive X-ray spectroscopy (EDS) analysis was carried out using a JEOL JSM-6700F and secondary electron image on a Hitachi S-3400 field emission instruments (20 kV) and the Oxford software INCA. X-ray photoelectron spectroscopy (XPS) analyses were carried out using a Thermo K alpha spectrometer with monochromated Al K radiation, a dual beam charge compensation system and a constant pass energy of 50 eV. A binding energy range of 0 – 1200 eV was used to collect survey scans. The principal peaks of the elements present in the as-synthesised films Ti (2p), O (2p) and C (1s) were investigated by acquiring high-resolution peaks. These peaks were used to evaluate the concentration of the different elements within the analysis region (spot size 400 μm). CASAXPS software was utilised to model the area underneath these peaks, using relative sensitive factors to calculate the thin film composition, these peaks were calibrated to adventitious carbon at a binding energy (B.E.) of 284.4 eV.

### 4.2.2. Functional characterisation. Photocatalytic test.

A model organic pollutant, octadecanoic (stearic) acid, was used to evaluate the photocatalytic response of the coating surfaces deposited in this chapter using UVA irradiation. This organic pollutant is highly stable under UV light (in the absence of an underlying effective photocatalyst) and its loss can be easily followed by measuring its characteristic C-H infrared bands at 2958, 2923 and 2858 $cm^{-1}$ *via* infrared spectroscopy. The loss of stearic acid was integrated using a Perkin Elmer RX-I Fourier transform infrared (FTIR).

The investigation of the charge carrier flow was evaluated following the deposition of silver (Ag) metal particles upon reduction of $Ag^{+}$ ions by photogenerated electrons trapped on the surface of the selected films used in this chapter. The films were immersed in 40 ml of aqueous silver nitrate solution ($AgNO_3$) under strong stirring conditions for 2.5 h. The vessel, containing the sample and the $AgNO_3$ solution, was irradiated using solar simulator (75 W Xe lamp, Am 1.5 air mass filter), the solution was purged with argon (Ar) for 30 min prior to illumination. The presence of Ag metal particles was evaluated using energy-dispersive X-ray spectroscopy (EDS) and monitored *via* back-scattered SEM images.

## 4.3. Rutile/Anatase $TiO_2$ thin films synthesis.

Titanium (IV) chloride ($TiCl_4$) and ethyl acetate ($C_4H_8O_2$) were used as metal and oxygen sources, respectively.[52] The precursors were heated to achieve a particular vapour pressure, so that the enriched vapours could be transported to the reaction chamber by a pre-heated inert carrier gas ($N_2$, 200 °C). As previously explained the APCVD reactor consisted of a quartz tube containing a 320 mm-long graphite block with three inserted Whatman heater cartridges. The temperature of the entire system

was controlled by Pt-Rh thermocouples. All pipelines of the APCVD system were maintained at 200 °C, to inhibit condensation of the precursors in their way to the pre-mixing chamber. This chamber was kept at 250 °C, where the two gas streams of $TiCl_4$ and ethyl acetate met before passing to the reaction chamber through a triple baffle manifold. In a standard $TiO_2$ synthesis, the temperatures of the bubblers, containing the titanium and oxygen sources, were held at 70 and 40 °C, respectively. These temperatures allowed to set a gas flow of 1.2 L $min^{-1}$ / 70 °C and 0.25 L $min^{-1}$ / 40 °C for $TiCl_4$ and $C_4H_8O_2$, respectively.

The rutile $TiO_2$ layer was deposited with a growth rate of *ca.* 0.25-0.3 μm $min^{-1}$, on quartz slides (25 x 25 mm) at 500 °C, due to temperature limitation of the CVD rig the as-synthesised $TiO_2$ layer consisted of the anatase phase. Therefore, the rutile layer was achived by heat-treating the as-synthesised anatase film at 1050 °C during 5 h. The presence of only pure rutile phase, with no traces of anatase or any other crystalline phases, was corroborated by X-ray diffraction and Raman spectroscopy studies. As previously mentioned, an interlayer to avoid the templating of the rutile layer was synthesised. This interlayer was performed by lowering the temperature of the reacton chamber to 300 °C, allowing to synthesise an interlayer of amorphous $TiO_2$. This amorphous $TiO_2$ interlayer was deposited using different deposition times (growth rate, 0.1 μm $min^{-1}$) to deliver heterojunction films with variable interlayer thickness. The final $TiO_2$ layer (0.25 – 0.3 μm $min^{-1}$), which consisted of solely pure anatase phase, was deposited at 500 °C. The as-synthesised heterojunction films were heat-treated at 500 °C during 5 and 10 h. The quartz slides were only kept in the reactor during the actual deposition time of the amorphous interlayer (a few minutes) and the anatase phase (2 min) to avoid the potential crystallization of the amorphous $TiO_2$ layer.

**Table 4.1.** Film description and experimental details for the deposition of the rutile/anatase heterojunction films and the single-semiconductor analogues. The temperature and mass flow conditions were constant for the metal ($TiCl_4$) and oxygen ($C_4H_8O_2$) precursors: 68 and 38 °C and $6.7 \times 10^{3-}$ and $3.1 \times 10^{-3}$ g $min^{-1}$, respectively.

| Sample | Description | Physical properties | | Functional properties | |
|---|---|---|---|---|---|
| | $TiO_2$ crystal phase | Rutile and Anatase $TiO_2$ d [μm $min^{-1}$] | Amorphous $TiO_2$ d [μm $min^{-1}$] | Total d [μm $min^{-1}$] | FQE ($10^{-3}$ molecule $photon^{-1}$) |
| A1 | Anatase | 1.0 | -- | 1.0 | 0.75 ± 0.025 |
| A2 | Anatase | 1.3 | -- | 1.3 | 0.09 ± 0.021 |
| Am | Amorphous | -- | 0.3 | 0.3 | 0.15 ± 0.013 |
| R/Am | Rutile/Amorphous | 0.5 | 0.3 | 0.3 | 0.06 ± 0.025 |
| Am/A | Amorphous/Anatase | 0.5 | 0.3 | 0.3 | 0.62 ± 0.032 |
| Am/A-T10 | Amorphous/Anatase annealed 10 h | 0.8 | -- | 0.8 | 0.42 ± 0.014 |
| M1 | Rutile/Amorphous/Anatase | 0.5 | 0.1 | 1.1 | 1.79 ± 0.028 |
| M1-T10 | Rutile/Amorphous/Anatase annealed 10 h | -- | -- | 1.1 | 3.25 ± 0.037 |
| M2 | Rutile/Amorphous/Anatase | 0.5 | 0.3 | 1.3 | 3.25 ± 0.011 |
| M2-T10 | Rutile/Amorphous/Anatase annealed 10 h | -- | -- | 1.3 | 4.38 ± 0.017 |
| M3 | Rutile/Amorphous/Anatase | 0.5 | 0.4 | 1.4 | 4.38 ± 0.034 |
| M3-T10 | Rutile/Amorphous/Anatase annealed 10 h | -- | -- | 1.4 | 6.06 ± 0.035 |

## 4.4. Results and discussion.

### 4.4.1. Structural properties.

Scanning electron microscopy (SEM) analysis was used to investigate the structural morphology of the as-deposited films, as well as to demonstrate the presence of the different layers of rutile, amorphous and anatase $TiO_2$ within the multilayer films. Side-view SEM analysis of a typical as-deposited rutile/amorphous/anatase $TiO_2$ multilayer film is shown in Figure 4.3(a), where the three different layers can be clearly identified. These multilayer samples were annealed at 500 °C for 10 h to induce the crystallisation of the amorphous interlayer, resulting in rutile/anatase $TiO_2$ films with high intimate contact (**Figure 4.3(b)**). In addition, this heat treatment seemed to promote formation of a well-defined particulate structure on the surface of the films (**Figure 4.3(c)**). However, it is worth noting that by following the photocatalytic behaviour of the amorphous/anatase $TiO_2$ control sample, before and after the annealing step, it can be ruled out that the enhanced photocatalytic efficiency, of the films investigated in this chapter, was due to heat-induced changes in the morphology of the films, further details are given in the photocatalytic section.

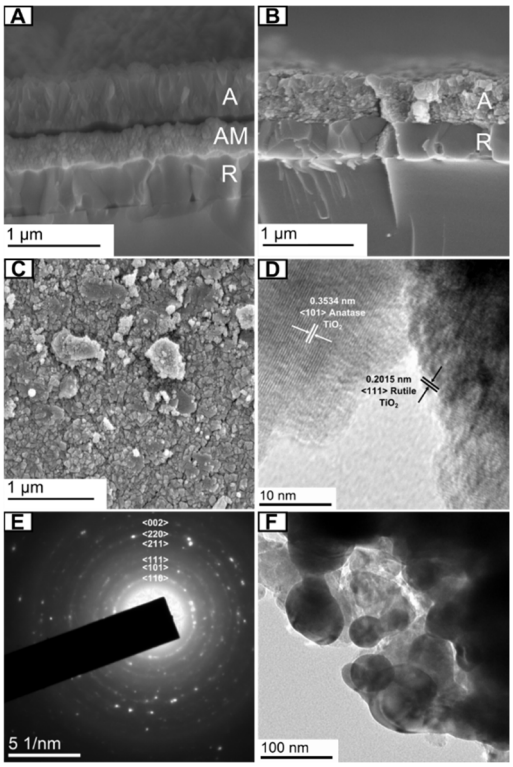


**Figure 4.3.** Scanning electron microscopy (SEM) images of (a) as-synthesised rutile/amorphous/anatase heterojunction $TiO_2$ film with thickness of *ca.* ~ 1.5 µm; (b) heat-treated rutile/anatase heterojunction $TiO_2$ film at 500 °C during 5 h, with thickness of *ca.* ~ 1.2 µm; (c) Top down view SEM image of a selected rutile/anatase heterojunction $TiO_2$ film. High-resolution transmission electron microscopy (HRTEM) images of (d) anatase and rutile crystalline phases in the heat-treated rutile/anatase heterojunction film and their corresponding interplanar distances, (101) and (111) planes for anatase and rutile, respectively; (e) electron diffraction pattern of rutile; (f) small rutile particles (< 100 nm) identified in R/A films.

High-resolution transmission electron microscopy (HRTEM) was also utilised to study the synergy between rutile and anatase crystalline phases on the annealed rutile/anatase films. HRTEM analysis showed large areas of highly crystalline material, with interplanar distances $d_A$ [101] = 3.5 Å and $d_R$ [111] = 2.0 Å assigned to anatase and rutile, respectively (**Figure 4.3(d)**). The two polymorphs were also identified by electron diffraction (**Figure 4.3(e)**). As it can be observed in Figure 4.3(d), anatase and rutile phases may be in intimate contact, this condition was emphasised by *Hurum et al.*[183] as essential to promote an efficient electron transfer from rutile to anatase. This work also proposed that the electron transfer could be rapidly promote between the two

titania polymorphs when atypically small rutile crystallites in small size aggregates (< 200 nm) were present, which can be clearly identified in the rutile/anatase heterojunction films synthesised in this chapter. Figure 4.3(f) showed the presence of small rutile particles (< 100 nm).

### 4.4.2. Physical and optical properties.

Raman spectroscopy analysis was also used to confirm the presence of the different $TiO_2$ phases. Pure crystalline phases of rutile and anatase, with no traces of any other crystalline phases, were identified in the materials. The presence of anatase phase was confirmed by a very strong band at 144 $cm^{-1}$ and three other Raman active-modes at 397, 515 and 639 $cm^{-1}$ (**Figure 4.4(e)**). In addition, rutile was also corroborated by the lack of a strong band in the 140 – 150 $cm^{-1}$ region and showing only Raman active-modes at 445 and 609 $cm^{-1}$ (**Figure 4.4(a)**).

Raman spectroscopy was also employed to monitor each deposition step. The presence of the amorphous $TiO_2$ modification was identified by significant baseline intensity in the Raman spectra of the rutile/amorphous $TiO_2$ control sample (**Figure 4.4(b)**) compared to that of pure rutile (**Figure 4.4(a)**). Further analysis of as-deposited amorphous $TiO_2$ on glass showed broad peaks at ca. 150 and 630 $cm^{-1}$, which are likely related to characteristic $E_g$ modes (144 and 638 $cm^{-1}$) of the anatase phase (**Figure 4.4(c)**). The presence of both $TiO_2$ polymorphs, rutile and anatase, was also clearly identified in the multilayer films by the presence of the characteristic $E_g$ modes associated to each individual crystalline phase (**Figure 4.4(d)**).

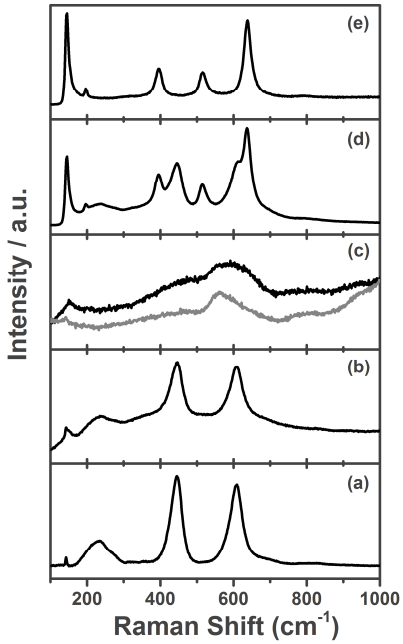


**Figure 4.4**. Raman spectroscopy patterns of (a) rutile $TiO_2$ on quartz. (b) Amorphous $TiO_2$ layer as deposited on rutile. (c) Amorphous layer on plain glass (black line) and corresponding spectrum of the glass substrate (grey line); (d) typical rutile/anatase heterojunction film; (e) pure anatase $TiO_2$ film on glass.

X-ray diffraction analysis (XRD) was also used to demonstrate the presence of both crystalline phases in the films (**Figure 4.5**). XRD is a technique sensitive to thin-films of atomic dimensions to thicknesses of many tens of microns. It is usually a non-destructive technique that requires no sample preparation. All these features make it a very facile and straight forward route to obtain structural information of multilayer thin-films. XRD analysis showed solely pure rutile and anatase phases, and no traces of any other crystalline phases were identified in any of the as-synthesised films. XRD patterns for the control sample, amorphous/anatase $TiO_2$ layered film, showed strong diffraction peaks at 25° and 48° which are associated to pure anatase $TiO_2$ materials (**Figure 4.5(b)**). It can also be observed that the as-deposited multilayer samples, rutile/amorphous/anatase $TiO_2$ films, showed these characteristic peaks as well as diffraction peaks at 27°, 36° and 55° which are commonly assigned to rutile materials (**Figure 4.5(a)**). It is worth noting that despite annealing these multilayer films, there

were no significant changes in the diffraction peaks (**Figure 4.5(a)**). This finding can be also applied to the control amorphous/anatase sample (**Figure 4.5(b)**) and, as it will be discussed below, it implies that the different photocatalytic behaviour of the heat-treated heterojunction films cannot be simply associated to a thermally-enhanced crystallinity.

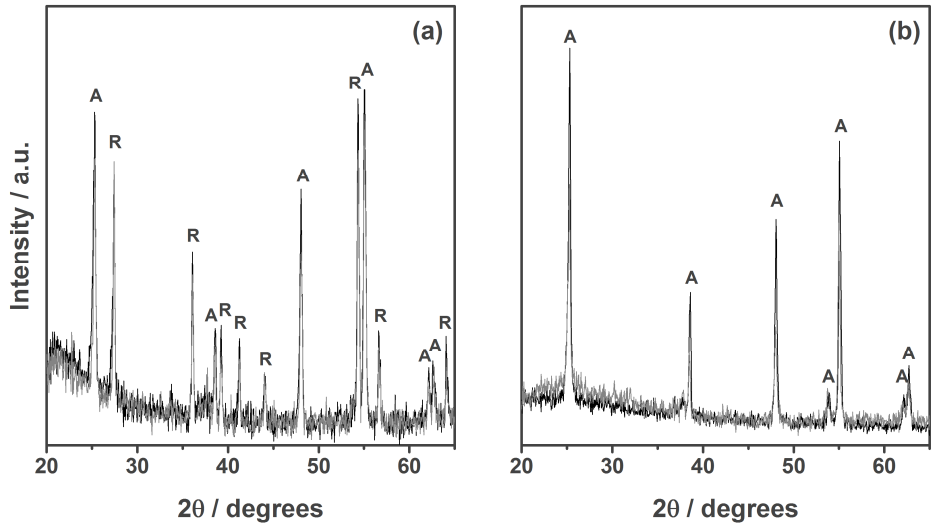


**Figure 4.5.** X-ray diffraction spectra of selected films (a) as-synthesised R/Am/A heterojunction thin film and (b) control Am/A film (black lines in graphs a and b). The grey lines show XRD patterns of the selected films, after being heat-treated at 500 °C for 10 h. This heat treatment process resulted in the complete crystallisation of the amorphous layer (Am), resulting in a R/A heterojunction film and a single component anatase film (A), respectively.

Optical properties for each individual sample were studied using UV-Vis measurements. It is well acknowledged that rutile and anatase polymorphs have two different absorption edges, with rutile absorbing at higher wavelengths. It can be clearly observed in Figure 4.6 that the absorption onset maximum of pure rutile is red-shifted by 40 nm respect to pure anatase. Figure 4.6 shows the bandgap energies of rutile and anatase phases, estimated from Tauc plot analyses (*ca*. 2.94 and 3.21 eV, respectively), which agrees with values reported in the literature. Figure 4.6 also shows that the absorption spectra of a typical rutile/amorphous/anatase heterojunction film resulted in

a combination of the spectra of the isolated crystalline phases, with a bandgap energy comparable to that of rutile (*ca.* 3 eV). This would be in agreement with values predicted in the literature, where the heterojunction of rutile and anatase phases would produce materials with an absorption onset red-shifted from the pure metal oxides.[31] Unfortunately, the high scattering component, inherent to $TiO_2$ films, in the absorption spectra of the annealed R/A film (**Figure 4.6**) hindered an accurate estimation of the bandgap energy for a comparison with reported values.

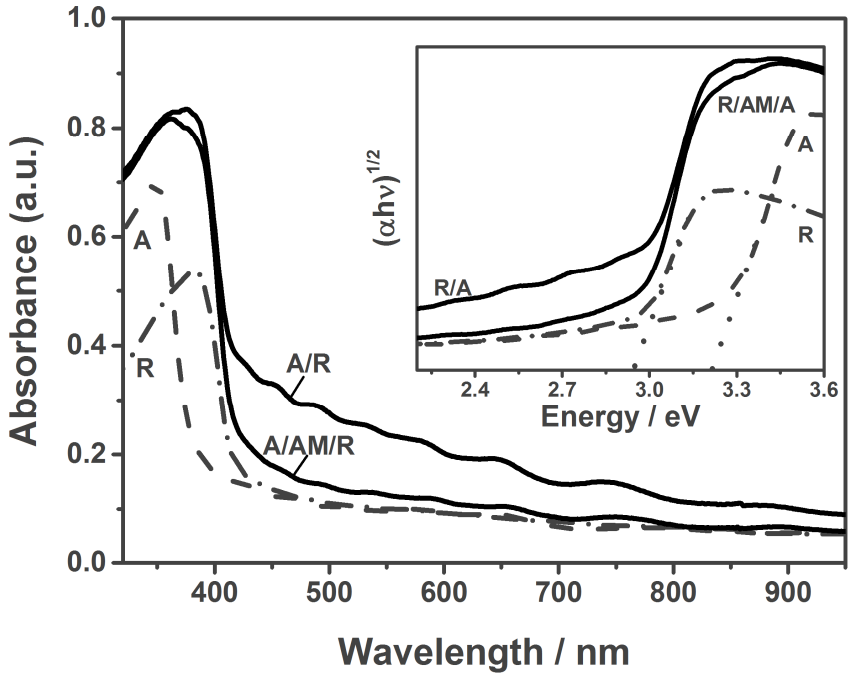


**Figure 4.6.** UV/vis spectroscopy analysis, showing the optical absorption of anatase (A), rutile (R) and rutile/anatase heterojunction films before (R/Am/A) and after (R/A) heat treatment at 500 °C for 10 h. The inset shows the approximate bandgap energy values of the rutile (R) and anatase (A) crystalline phases.

### 4.4.3. Photocatalytic activity.

Photocatalytic tests were conducted on all as-synthesised films using a model organic pollutant, octadecanoic (stearic) acid.[87,186–188] The overall degradation reaction is given by Equation 3.1 and can be easily followed for transparent samples via Fourier

transform infrared spectroscopy (FTIR), monitoring the loss of the C-H bands of acid at 2958, 2923 and 2853 $cm^{-1}$ (**Figure 4.7(a)**).

$$CH_3(CH_2)_{16}CO_2H + 26O_2 \xrightarrow[h\nu \geq E_{bg}]{TiO_2} 18CO_2 + 18H_2O \qquad (4.1)$$

The number of acid molecules degraded are estimated using a conversion factor from the literature,[87] 1 $cm^{-1} \equiv 9.7 \times 10^{15}$ molec $cm^{-2}$). A linear regression of the curve integrated area vs. irradiation time, at the initial photocatalytic process (20 – 30 %), was used to assess the photocatalytic performance rates of the as-synthesised films (**Figure 4.7(b)**). These rates were expressed as formal quantum efficiencies (ξ), which calculate the number of acid molecules photodegraded per incident photon (units, molec $photon^{-1}$). In this estimation, all photons irradiating the surface of the sample are considered to be absorbed by the photocatalyst, with a constant energy of *ca*. 3.4 eV (365 nm).

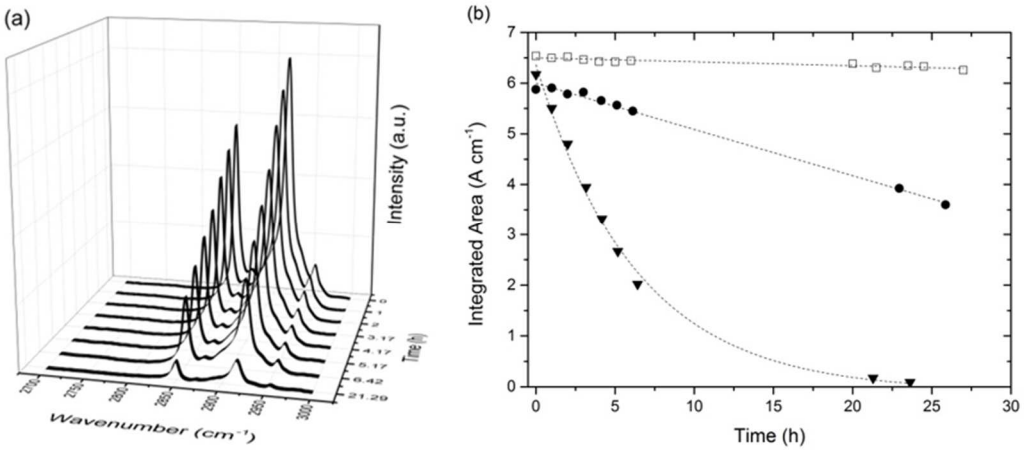


**Figure 4.7.** (a) FTIR spectroscopy measurements showing the loss of C-H modes of stearic acid upon UVA illumination (1.2 mW $cm^{-2}$) on a selected R/A heterojunction film. (b) Integrated areas obtained during illumination of R/A (full triangles) and control Am/A (full circles) films. A blank test corresponding to stearic acid on plain glass is included for reference (empty symbols).

A range of different rutile/amorphous/anatase films (samples M1, M2 and M3) was designed by keeping a similar thickness of the crystalline phases (anatase and rutile, *ca.* 0.5 – 0.6 μm) and modifying the thickness of the amorphous $TiO_2$ interlayer (*ca.* 0.1, 0.3 and 0.4 μm, respectively). A thin film of stearic acid was dip-coated onto the surface of all different films, control and multilayer samples, from a 0.05 M stearic acid solution in chloroform. The photocatalytic performance of all different films was assessed using UVA irradiation (BLB lamp, 1.2 mW $cm^{-2}$) before and after the heat treatment process at 500 °C for 5 and 10 h (**Figure 4.8**). For each single film, the photocatalytic efficiency was always increased after being heat-treated at 500 °C for 5 h (samples M1-T5, M2-T5 and M3-T5). This enhancement in photocatalysis could be easily associated to the annealing process, however, a control amorphous/anatase film was annealed at 500 °C for 10 h without showing changes in its photocatalytic activity (**Figure 4.8**). Since no structural changes were observed in the films before and after heat treatment, as observed by XRD analysis (**Figure 4.5**). The enhanced activity showed by the multilayer films could be directly attributed to the crystallisation of the amorphous interlayer and thus, to an intimate contact between the two crystalline rutile and anatase polymorphs. In addition, all multilayer films (M1-T5, M2-T5 and M3-T5) were annealed again to investigate the synergistic contact between rutile and anatase. It was observed that the activities did not increase further after a second annealing step (samples M1-T10, M2-T10 and M3-T10) (**Figure 4.8**), which could be attributed to the complete crystallisation of the amorphous $TiO_2$ interlayer after the first annealing step (5 h).

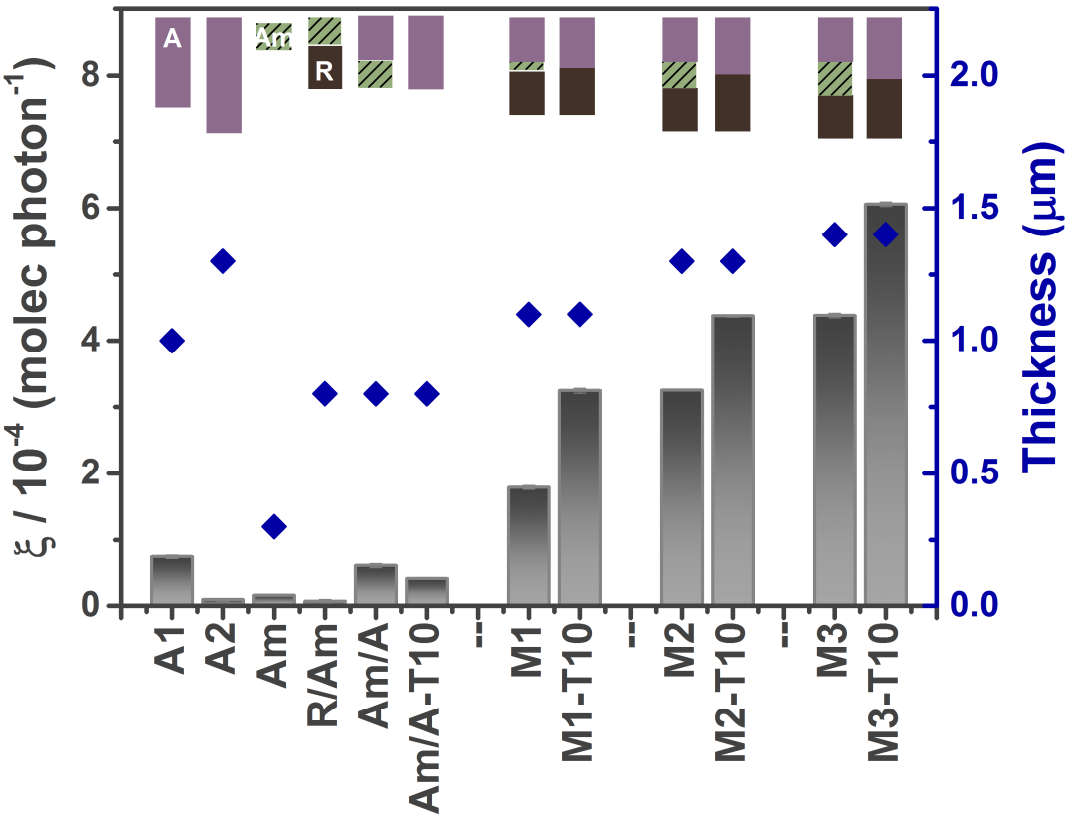


**Figure 4.8.** Formal quantum efficiencies (ξ) obtained from the photocatalytic evaluation of the as-synthesised heterojunction thin films and their single component analogues using UVA illumination (1.2 mW $cm^{-2}$). Three different rutile/amorphous/anatase heterojunction films (M1, M2, M3) with comparable thicknesses (0.5 – 0.6 μm) of the rutile and anatase layers but different thicknesses of amorphous interlayers (0.1, 0.3 and 0.4 μm) were photoevaluated. The layers included in each individual film are schematically represented for guidance. Anatase layers are represented by light purple frames (A), rutile layers by dark brown frames (R) and the amorphous interlayer by green patterned frames (Am). Each different frame was scaled per the approximate thickness of the corresponding layers; the total thickness of each single film is represented by blue full diamonds. The different heat treatment time (5 and 10 h, 500 °C) are labelled as T5 and T10, respectively. Two single component analogues (A1 and A2) with different thickness were used for reference. The thickness of sample A1 (~1 μm) was found optimal for single component films in this chapter, based on ξ values. In addition, three more control samples were tested and included as reference. An amorphous/anatase film (consisting of solely amorphous and anatase layers only), as well as amorphous $TiO_2$ deposited on glass (Am) and rutile (R/Am). Further experimental and film description details are given in Table 4.1.

The photocatalytic efficiency of the as-synthesised R/Am/A heterojunction films (samples M1, M2 and M3, before the heat treatment process) were significantly higher than those of their single component analogues (samples A1 and A2) (**Figure 4.8**). When using APCVD it was found that the formal quantum efficiencies of single

component anatase thin films is positively correlated with film thickness within a range below 1 μm.[156,189] However, an increase in thickness above this value was found detrimental from a photocatalytic point of view, showing poor photoactivity efficiency (comparison between pure anatase films with different thickness, samples A1 and A2 in Figure 4.8). This effect can be attributed to an enhanced charge carrier recombination associated to thicker films, were the charge carriers must travel farther distances to reach the photocatalyst surface. Therefore, the enhanced photocatalytic activity showed by the heterojunction films M1, M2 and M3 can be attributed to an effective separation and transfer of the charge carriers, with a potential contribution of the Am interlayer in the carrier dynamics. This positive contribution of the Am layer is reinforced by the direct correlation between the thickness of the amorphous $TiO_2$ layer and the activities of samples M1, M2 and M3 (**Figure 4.8**).

However, this was unexpected since it has been commonly reported that non-crystalline $TiO_2$ coatings promote the recombination of photogenerated charge carriers,[190] therefore, it would be expected for the amorphous interlayer to inhibit electron transfer between the two crystalline layers. It is worth noting that the amorphous $TiO_2$ coatings synthesised in this chapter showed negligible activity (**Figure 4.8**). It is also worth mentioning that, as remarked by *Ohtani*,[191] amorphous $TiO_2$ samples reported by different groups should not be extended to all non-crystalline $TiO_2$ modifications, which may differ in structure and composition. The nature of the amorphous $TiO_2$ layer in the rutile/amorphous/anatase heterojunction films may differ from that of the amorphous coating deposited on glass (Figure 4.4(c)). This amorphous $TiO_2$ interlayer, enclosed between rutile and anatase, may be a highly distorted modification of either anatase or rutile polymorph and its potential role in the charge carrier transfer between the crystalline rutile and anatase phases is not known. In fact, the existence of a highly

distorted interface between rutile and anatase has been suggested in the literature.[183,192,193] These interface regions have been suggested as nucleation sites, which favour the rapid electron transfer between the two polymorphs.

### 4.4.4. Synergistic interaction between rutile and anatase polymorphs.

The photocatalytic enhanced observed when comparing samples before and after annealing, could be associated to the synergistic interaction between the $TiO_2$ crystalline polymorphs. Nevertheless, this was effect was reported as *necessary* but not *sufficient* in the argument of electron transfer in the rutile/anatase system. Photogenerated holes and electrons react in the surface of the photocatalyst to form hydroxyl and hydroperoxyl radicals (•OH, $•O_2H$), respectively, as well as oxo species. Subsequently, these highly reactive radicals degrade nearby organic compounds.[17,191,194]

Further studies on the direction of the photogenerated charge carrier flow were carried out following the photodeposition of silver metal particles (Ag) by photoreducing $Ag^+$ ions with photogenerated electrons diffused and trapped on the surface of photocatalytic material.[195,196] The two $TiO_2$ polymorphs used in this chapter, rutile and anatase, present a very different capability to photoreduce $Ag^+$ ions. It has been reported that high amounts of small Ag metal particles normally coat the surface of rutile materials (**Figure 4.9**). However, more large Ag particles, forming aggregates (*lumps*) are commonly showed by pure anatase materials (**Figure 4.9(b)**). This observation is indicative of active sites (*hot spots*) involving accumulation of photogenerated electrons trapped on the anatase surface.[197]

All different samples were coated simultaneously under solar simulator irradiation conditions (75 W Xe Lamp, Am 1.5 air mass filter) in 40 ml of aqueous silver nitrate

solution ($AgNO_3$, purged for 30 min with Ar prior irradiation) under strong stirring conditions during 2.5 h. Energy-dispersive X-ray spectroscopy (EDS) using a back-scattering configuration, was used to investigate the presence of Ag metal particles within the surface of the films (**Figure 4.9**). Four different films were investigated, a single component rutile and anatase films, as-synthesised rutile/amorphous/anatase heterojunction (before heat treatment) and a rutile/anatase heterojunction (after heat treatment). The anatase film (initially Am/A but heat-treated at 500 °C for 10 h) showed lumps of Ag metal particles, scattered across the film surface, as expected from results reported in the literature (**Figure 4.9**). The rutile/amorphous/anatase heterojunction showed similar Ag aggregates across the anatase surface (top layer of the heterojunction film) (**Figure 4.9**); however, a high concentration of Ag particles coated the whole surface, suggesting an increase in the density of photogenerated electrons. This result is consistent with the photocatalytic enhancement of the as-synthesised rutile/amorphous/anatase heterojunction films compared to that of their single component anatase analogue (**Figure 4.8**). Interestingly, a dramatic enhancement in the Ag particle density was observed upon the heat treatment process to produce the annealed rutile/anatase heterojunction films (**Figure 4.9(d)**). This can be explained in terms of an effective synergy between the rutile and anatase polymorphs. The Ag particles were photodeposited as needles and large aggregates and they are presumably the result of alternating electronic and ionic events, commonly described by Equation 4.2.[196] It could be clearly postulated that the changes observed in the photodeposition of Ag showed that electron transfer occurs from rutile to anatase.

$$Ag^0 + Ag^+ \longrightarrow (Ag)_2^+ \xrightarrow{e^-} Ag_2 \xrightarrow{Ag^+} (Ag)_3^+ \xrightarrow{e^-} Ag_3 \longrightarrow \ldots \longrightarrow Ag_m \qquad (4.2)$$

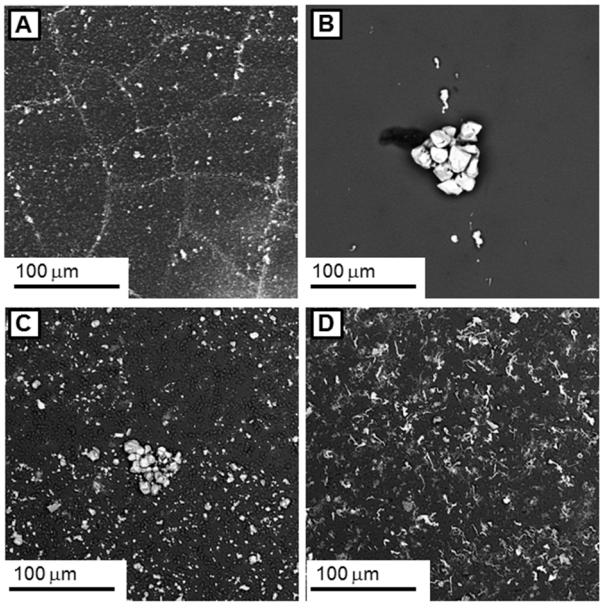


**Figure 4.9.** Backscattered SEM images of selected films (20 kV, x300) after photodeposition of Ag particles. (A) Rutile; (B) Anatase; (C) as-synthesised rutile/amorphous/anatase heterojunction film; (D) heat-treated rutile/anatase heterojunction film (500 °C, 10 h). Ag particles (light grey) can clearly observed against the $TiO_2$ background (dark grey). EDS analyses were also used to confirm the presence of Ag particles across the film surface.

It is worth mentioning that *Kawahara et al*.[198] reported SEM photodeposition of Ag particles on rutile/anatase patterned films, which were synthesised from sol–gel anatase stripes on sputtered rutile substrates, with both phases exposed to the testing environment. The authors observed large Ag aggregates on the anatase surface and a cloud of small Ag particles on the rutile side of the boundary region. The authors noticed the apparent inactivity of rutile, which was attributed to possible structure insensitivity of the [110] crystal plane of the sputtered rutile phase. These rutile/anatase patterned films showed an enhancement of the Ag particle size towards the rutile-anatase interface. In this work, the authors proposed an electron transfer from anatase to rutile phase, based on the scale of the diffusion length of electrons in solids, estimated as being of the same order (5.1 μm) than the extent of the Ag cloud on the rutile side. It is worth mentioning that this finding could be associated to the presence of deep trapping sites within the films, reversing the predicted electron transfer direction. Nevertheless, the enhanced number of Ag particles photodeposited, found in Kawahara

work, could also be explained by the increased density of photodeposited electrons towards the rutile-anatase interface, where a *tail* rather than a *cloud* of particles may be expected. Therfore, the findings observed by *Kawahara et al*.[198] could been considered in agreement with the proposed theoretical model and with the experimental observations reported in this chapter.

### 4.5. Conclusions.

In this chapter, APCVD was used to synthesise rutile/anatase $TiO_2$ layered films. This is the first time in which rutile/anatase heterojunction films were synthesised by APCVD techniques. The traditional impediment to deposit directly anatase on a rutile substrate via APCVD was surpassed by developing a novel synthesis approach to avoid a direct contact between both polymorphs, rutile and anatase, by intercalating an interlayer consisted of a non-crystalline $TiO_2$-based material. In addition, upon the synthesis of the multilayer films heat-treatment process at 500 °C was carried out for several hours to deliver rutile/anatase $TiO_2$ films through a complete crystallisation of the amorphous $TiO_2$ interlayer.

These $TiO_2$ heterojunction films showed a high level of interaction between rutile and anatase phases, as well as an atypical size of rutile particles, enhancing drastically the photocatalytic performance of $TiO_2$ materials. Our layered rutile/anatase films showed a 3-fold increase compared to N-doped $TiO_2$, being by the time they were synthesised one of the most active titania-based materials ever reported. Comparison between the behaviour of the layered films and the pure polymorphs of $TiO_2$, rutile and anatase, during photodeposition of silver particles allowed conclusions to be drawn on the directional flow of photogenerated electrons.

In the following chapter, we will use APCVD to investigate solid solutions of heterojunction films of two different metal oxides, $WO_3$ and $TiO_2$. Although the photoinduced wettability and photocatalytic degradation of dyes have been studied for these $WO_3/TiO_2$ heterojunctions, to the best of our knowledge, its effect on the photocatalytic degradation of organic compounds has not been reported. We will use an organic model acid (stearic acid) to test the photoactivity of these materials. In addition, theoretical and hard X-ray photoelectron spectroscopy (HAXPES) will be utilised to model the flow of the photogenerated charge carriers.

Chapter V

# NANOSTRUCTURED $WO_3/TiO_2$ HETEROJUNCTION THIN FILMS

*'The following chapter presents the results from a series of experiments for growing nanostructured $WO_3/TiO_2$ heterojunction films using chemical vapour deposition (CVD) processes. A nanostructured semiconductor host, consisting of nanorods of $WO_3$, was grown via an aerosol-assisted CVD method. This host was subsequently coated conformally with a layer of anatase $TiO_2$ using atmospheric-pressure CVD – with nanoscale precision of the coating's thickness. These $WO_3/TiO_2$ heterojunction films showed an unprecedented photocatalytic activity for a thin film in the degradation of a model organic pollutant. The enhanced photocatalytic properties of this system can be explained by the synergistic effect of charge separation between both metal oxide layers. This is supported by hybrid density functional theory (DFT) and hard X-ray photoelectron spectroscopy (HAXPES) studies, which suggest clear evidence of the importance of the vectorial charge separation in heterojunction systems.'*

## 5. Nanostructured $WO_3/TiO_2$ thin films: A facile solution to a highly active photocatalyst.

### 5.1. Introduction.

As previously mentioned, $TiO_2$ is the most studied photocatalytic material, either for UV[17] and/ or solar applications (by modifying its electronic structure).[24] Its solar application has been commonly explored by adding anionic and/ or cationic dopants into the $TiO_2$ structure.[25] Nevertheless, as previously reported, chapters 2 and 3, this approach often comes at the expense of structural properties and may compromise the overall performance of the photocatalyst. For instance, doping can yield increases in visible light activity but is often coupled with a decrease in UV light activity, meaning there is little or no overall benefit for outdoor use.[32,35] More recently, many new strategies for enhancing the activity of $TiO_2$ have been explored, including nanostructuring,[26,27] the addition of co-catalysts[28,29] and the use of heterojunction systems.[33,199]

A heterojunction is the interface that occurs when two dissimilar semiconductors are coupled. Such junctions have been explored extensively in the field of photovoltaics and in organic and dye sensitized solar cells.[30] More recently, heterojunction materials have also received considerable attention in the field of photocatalysis, especially for water splitting applications.[33,199] The fact that the most active form of $TiO_2$, P25 *Evonik* (formally known as Degussa), is a heterojunction system, as well as the results reported in chapter 4, supports this approach. P25 *Evonik* is composed of ~ a 3: 1 ratio of the anatase and rutile phases and is considered the benchmark material for comparing photocatalytic activity.[40,200] In a heterojunction system, the band structures of the two joining semiconductors can align favourably, causing photogenerated electrons and holes to migrate in separate directions across the heterojunction boundary. This spatial

separation in charge can inhibit electron-hole recombination and increase photocatalytic efficiency.[31,32,38] The benefits of using a heterojunction in photocatalysis have been demonstrated for a wide range of heterojunction systems, including $Cu_2O/TiO_2$,[41] $WO_3/BiVO_4$,[42] and $ZnO/BiVO_4$,[43] which have all shown synergetic enhancements in their photoresponse compared to that of their individual analogues.

At the same time, the nanostructuring of semiconductor materials often results in increases in photocatalytic activity. This has been attributed to both an increase in the degree of contact between the photocatalyst and the pollutant as well a decrease in the distance photogenerated charges must travel to react at the surface.[26,27,38,201] Over the last few decades, a wide range of high-surface-area photocatalytic materials, such as nanotubes, porous materials, 3D frameworks, *etc*. have been investigated.[38] Unfortunately, issues related to the supporting of these materials within photoreactors and the scalability of many of these synthetic processes represent additional challenges to future commercialisation.[70] A potential solution to this problem would be to produce high surface area photocatalysts directly onto a support using an upscalable technique. In this chapter, we explore the use of CVD, a roll-to-roll technique used heavily in industry for coating large- areas, for growing high surface area photocatalysts. In order to increase the efficiency of charge separation, and thus the efficiency of photocatalysis, the $WO_3$/ $TiO_2$ heterojunction system was explored. High surface area $WO_3$ nanorods were coated with conformal layers of anatase $TiO_2$. CVD has previously been used to conformally coat macrostructures,[202] however, the most commonly recognized method capable of delivering conformal coatings with nano-scale control is atomic layer deposition (ALD).[50,51] Unfortunately, factors associated with ALD processes, such as slow growth times, the requirement of high vacuum, low yields and high operation/ production costs, limit the commercialization of ALD methodologies for coating large

areas. Although CVD does not offer the same degree of controlled growth (such as the layer by layer growth ALD is capable of on the Angstrom scale), it can be used to grow films with nanoscale control. Also, CVD techniques are comparatively far cheaper, scalable and can deposit highly crystalline materials.[70]

In this chapter, we will investigate the nanostructuring of a well-known heterojunction system, $WO_3/TiO_2$, which has recently been extensively investigated by different groups,[203–205] who report enhancements in photogenerated charge carrier separation and function. Nevertheless, these $WO_3/TiO_2$ heterojunction systems were synthesised using techniques, such as hydrothermal, sol-gel and glancing angle deposition processes, less capable of mass-production. Therefore, we explore the application of CVD, a scalable method capable of producing robust coatings. We will report the synthesis of a semiconductor host with high specific area, nanorods of $WO_3$, synthesised by aerosol-assisted CVD (AACVD). Subsequently, this highly structured host will be conformally coated with $TiO_2$ with nano-scale control of its thickness, using atmospheric-pressure CVD (APCVD). In addition, we observed that coupling these $WO_3$ nanorods with $TiO_2$ results in the highest reported photocatalytic activity for a thin film during the degradation of stearic acid under UVA illumination. The investigation of these heterojunction $WO_3/TiO_2$ films will be complemented using state-of-the-art hybrid density functional theory (DFT) and hard X-ray photoelectron spectroscopy (HAXPES), to elucidate the electronic interaction at the heterojunction of the $WO_3$ and $TiO_2$ crystalline phases. The results reported in this chapter present evidence for the direction of charge separation in $WO_3$/ $TiO_2$, and provide important insights on the influence of vectorial charge separation in heterojunction systems as a whole.

## 5.2. Experimental methods.

Tungsten hexacarbonyl ([$W(CO)_6$], 99% ), titanium tetrachloride ($TiCl_4$, 99.9 %) and ethyl acetate ($C_4H_8O_2$, 99.8 %), used as tungsten, titanium and oxygen source, respectively, were purchased from *Sigma-Aldrich*. Acetone (99%) and methanol (99.5%), used as the solvents for the aerosol-assisted CVD process, were purchased from *Emplura*. Nitrogen gas was supplied by BOC. Quartz glass substrates were purchased from *Multi-Lab*. Octadecanoic (stearic) acid ($C_{18}H_{36}O_2$, 95%), purchased from *Sigma-Aldrich*, was used as the organic layer to be degraded during the photocatalytic test.

### 5.2.1. Physical characterisation.

The structural properties of the as-synthesised thin films were explored using X-ray diffraction (XRD) and Raman spectroscopy analyses. X-ray diffraction measurements were carried out using a Bruker-Axs D8 (Lynxeye XE) diffractometer, which consist of a monochromated Cu X-ray source ($K_{\alpha 1}$, 1.54 Å) and a glancing incident angle ($\theta$) of 1°. Each different diffraction pattern was fit to the Le Bail method, using structure parameters from Joint Committee on Powder Diffraction Standards (JCPDS), through the GSAS and EXPGUI software suit. Raman spectroscopy was performed using a Renishaw 1000 spectrometer equipped with a 633 nm laser, which was calibrated using a silicon reference. UV/vis spectroscopy analyses were carried out using a double monochromated Perkin Elmer Lambda 950 UV/Vis/NIR Spectrophotometer within the 250-2500 nm range. The UV/vis measurements were calibrated using a *Labsphere* reflectance standard. Two different scanning electron microscopy (SEM) systems, a JEOL 6301 (5 kV) and a JEOL JSM-6700F field emission instruments, were used to collect data, the Oxford software INCA was used for EDS analyses. Likewise, SEM

was also utilised to measure the thickness of the $WO_3/TiO_2$ heterojunction films, as well as their single component analogues, *via* side-on view SEM analysis. Transmission electron microscopy (TEM) images were collected using a high resolution TEM instrument, JEOL 2100, which consist of a $LaB_6$ source operating at an acceleration voltage of 200 kV. A Gatan Orius Charge-coupled device (CCD) was used to acquire and record the micrographs. Each sample was prepared by scraping them off the quartz substrate using a diamond pen, followed by a sonicating process in chloroform and drop-casted onto a 400 Cu mesh lacy carbon film grid (Agar Scientific Ltd.). Energy-dispersive X-ray spectroscopy (EDS) analysis was carried out using a JEOL JSM-6700F and secondary electron image on a Hitachi S-3400 field emission instruments (20 kV) and the Oxford software INCA. Atomic force microscopy (AFM) was performed using a Bruker Icon system running in PeakForce Quantitative Nanomechanical Property Mapping (QNM) mode. The topography of the samples was measured using 5 μm x 5 μm areas and Bruker NCHV (etched silicon) tips in contact mode. X-ray photoelectron spectroscopy (XPS) analyses were carried out using a Thermo K alpha spectrometer with monochromated Al K alpha radiation, a dual beam charge compensation system and constant pass energy of 50 eV. A binding energy range of 0 – 1200 eV was used to collect survey scans. The principal peaks of the elements present in the as-synthesised heterojunction films Ti(2p), W (4f), O (O1s) and C (1s) were investigated by acquiring high-resolution peaks. These peaks were used to evaluate the concentration of the different elements within the analysis region (spot size 400 μm). CASAXPS software was utilised to model the area underneath these peaks, using relative sensitive factors to calculate the thin film composition, these peaks were calibrated to adventitious carbon at binding energy (B.E.) of 248.4 eV.

### 5.2.2. Theoretical methods.

All calculations were performed using the Vienna Ab initio Simulation Package (VASP),[206–209] a periodic plane wave density functional theory (DFT) code where the interactions between the core and valence electrons are dealt with using the Project Augmented Wave (PAW) method.[210] Both the plane wave basis set and k-point sampling were checked for convergence, with a cut-off of 560 eV and k-point grid of Γ-centred 4 x 4 x 4, for the 32 atom monoclinic unit cell of $WO_3$ found to be sufficient. Geometry optimisations were performed using the Heyd-Scuseria-Ernzerhof (HSE06) hybrid DFT functional.[211] The structures were deemed to be converged when the forces on all the atoms totalled less than 10 meV $Å^{-1}$. In the plane wave formalism, due to the presence of periodic boundary conditions, the electrostatic potential of a crystal is not defined with respect to an external vacuum level and, as such, the absolute electronic eigenvalues from different calculations are not comparable. In order to align the energies to the vacuum level, a slab-gap model (128 atom, 15.5 Å slab, 20 Å vacuum) was constructed and the corresponding electrostatic potential averaged along the *c*-direction, using the MacroDensity package.[212] Consistent with previous studies of $WO_3$ surfaces,[213] a $(\sqrt{2} \times \sqrt{2})R45°$ reconstruction of the (001) surface was cleaved using the METADISE code.[214]

### 5.2.3. Functional characterisation. Photocatalytic test.

A model organic pollutant, octadecanoic (stearic) acid, was used to assess the photocatalytic response of the coating surfaces deposited in this chapter using UVA irradiation. This organic pollutant is highly stable under UV light (in the absence of an underlying effective photocatalyst) and its loss can be easily followed by measuring its characteristic C-H infrared bands at 2958, 2923 and 2858 $cm^{-1}$ *via* infrared

spectroscopy. The loss of stearic acid was integrated using a Perkin Elmer RX-I Fourier transform infrared (FTIR).

### 5.3. Synthesis of $WO_3/TiO_2$ heterojunction films.

This chapter reports the improvement of a well-known heterojunction photocatalytic system, $WO_3/TiO_2$, by using CVD processes. These films were produced as a two-step process, where nanorods of $WO_3$ (~ 650 nm length), deposited using AACVD, were coated with a layer of anatase $TiO_2$ (with varying thikness ~ 30, 45 and 100 nm) from APCVD. All different deposition parameters (bubbler and reactor temperatures, flow rates, deposition times, etc.) were controlled in order to achieve nanorods of $WO_3$ and anatase $TiO_2$ films. Likewise, two control samples, $WO_3/C/TiO_2$ and P25 *Evonik* films, were synthesised to evaluate the photocatalytic performance of $WO_3/TiO_2$ heterojunction films.

#### 5.3.1. Aerosol-assisted chemical vapour deposition (AACVD): $WO_3$ nanorods.

Tungsten hexacarbonyl (0.060 g) ($[W(CO)_6]$, 99%) was dissolved in 15 ml of a 2:1 mixture of acetone (99%) and methanol (99.5%). The solution containing the precursors was moistened using an ultrasonic humidifier (*Liquifog, Johnson Matthey*), operating at 2 MHz, to produce aerosols which were transported to the reaction chamber an inert carrier gas ($N_2$), controlled by a mass flow controller. Pure tungsten trioxide ($WO_3$) nanorods were deposited as a thin film at a set temperature of 375 °C (the actual temperature ranged between 339–358 °C) on quartz slides (*Multi-Lab*). Both the reactor heater and humidifier were switched off, after the thin film deposition, and the AACVD reactor was naturally cooled under a $N_2$ flow to room temperature. The inlet to the cold-wall reactor of the AACVD system was equipped with a water jacket to avoid the

overheating of the aerosol precursor, which could lead to its decomposition prior to entering the reaction chamber. The exhaust was directly vented into the extraction system of the fume cupboard. Each single quartz substrate was thoroughly cleaned using acetone (99 %), isopropanol (99.9 %) and distilled water and dried in air prior to use.

### 5.3.2. Atmospheric-pressure chemical vapour deposition (APCVD): Anatase $TiO_2$ coating.

After the synthesis of the $WO_3$ nanorods, an anatase $TiO_2$ overlayer was deposited at 500 °C from titanium tetrachloride ($TiCl_4$, 99%) and ethyl acetate ($C_4H_8O_2$, 99.8%) using APCVD. Each precursor was heated in stainless steel bubblers at 70 and 40 °C, respectively, and their flow rates set at 1.2 and 0.25 L $min^{-1}$, respectively. Pre-heated $N_2$ (~200 ºC) was used as inert carrier gas. The precursors were mixed in a stainless steel chamber (250 ºC) before accessing the reactor. The cold-wall APCVD reactor consisted of a 320 mm-long heating graphite block accommodated in a quartz tube, with three inserted *Whatman* heater cartridges. The temperature of the entire system was controlled by Pt-Rh thermocouples.

Figure 5.1 shows a scheme representing the synthesis of $WO_3$ nanorods *via* AACVD and their subsequent coating using an APCVD method. As it can be observed from Figure 5.1 and Figure 5.2(b), the specific flow rate conditions in the deposition of $TiO_2$ ensured the conformal coating of the $WO_3$ nanorods, preserving their original microstructure. In the following section, it will be discussed in detail the potential application of APCVD processes to deliver conformal coatings of nanostructured semiconductors.

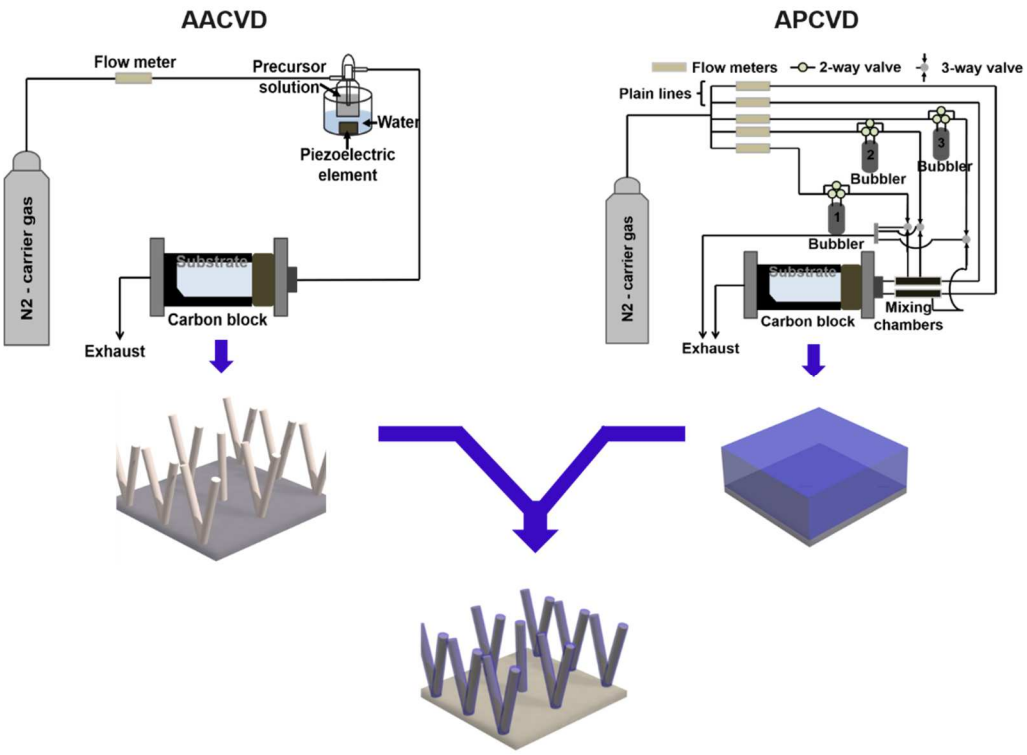


**Figure 5.1.** Schematic illustration of the use of AACVD and APCVD to deliver nanostructured $WO_3/TiO_2$ heterojunction films.

### 5.3.3. Synthesis of control sample: $WO_3/C/TiO_2$ thin film.

The conditions described above for the $WO_3/TiO_2$ film synthesis were reproduced with the incorporation of a thin carbon interlayer, which was sputtered over the $WO_3$ nanorods before the deposition of the $TiO_2$ layer. This carbon interlayer inhibited direct contact between $WO_3$ and $TiO_2$ phases, whilst preserving the microstructure of the original $WO_3/TiO_2$ film (**Figure 5.2(c)**). This approach was used to ascertain whether the enhancement in activity was due to synergistic interaction between the two semiconductors and to rule out the potential influence of an increasing specific area of the $TiO_2$ by using a high-surface-area host ($WO_3$). This effect will be discussed in detail in the photocatalytic section of this chapter.

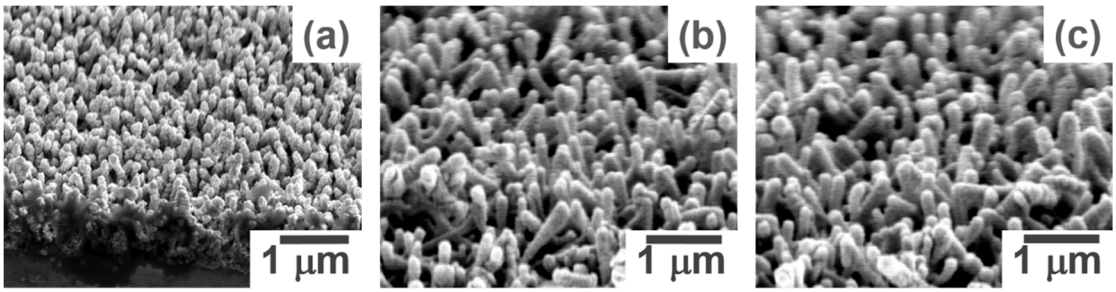

**Figure 5.2**. Scanning electron microscope (SEM) images of $WO_3$ nanorods thin-film (a), $WO_3/TiO_2$ heterojunction film (b) and $WO_3$ nanorods sputtered with a carbon (c) layer to avoid a synergistic contact between $WO_3$ and $TiO_2$ (W/C/Ti).

### 5.3.4. Synthesis of control sample: P25 *Evonik* film.

A film of P25 Evonik $TiO_2$ was deposited on borosilicate microscope glass slides (75 x 25 x 1 mm, *VWR International*) by dip-coating into a 5 *wt%* aqueous dispersion of the powders, following the optimum conditions reported by Mills *et al*.[107] In this work the samples were immersed for 10 s and then withdrawn at 120 mm $min^{-1}$. The film was dried at 30 °C for 30 min and then at 100 °C for 1 h, before washing it with water and left it to dry in air. Before the deposition of a layer of stearic acid, the $TiO_2$ coating on the back of the slide was removed by wiping it with cotton wool soaked in a 5 M aqueous NaOH solution.[215]

## 5.4. Results and discussion.

### 5.4.1. Conformal coating of the $WO_3$ nanostructured substrate.

Under the deposition conditions described in the previous section, a range of different $TiO_2$ coatings, of varying thickness, were deposited onto the nanorods of $WO_3$. The different thicknesses were achieved by tuning the $TiO_2$ deposition time (from 5 to 120 s). This approach allowed us to investigate the potential use of APCVD processes to deliver conformal coatings of highly nanostructured substrate hosts. In this section, we

will demonstrate that the thickness of the $TiO_2$ layer is directly dependent upon the deposition time (**Figure 5.3**).

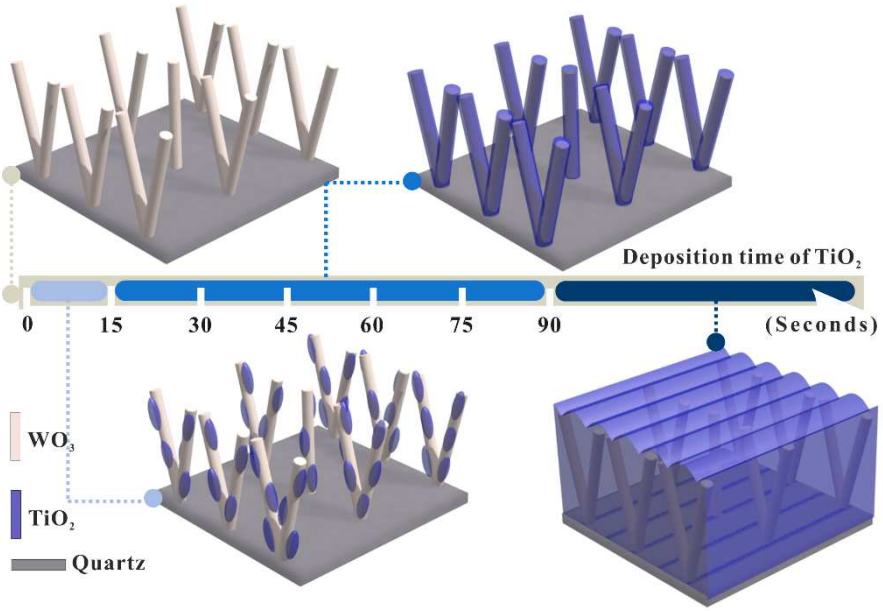


**Figure 5.3.** Model proposed for the growth of $TiO_2$ (blue colour) on $WO_3$ nanorods (grey colour) using APCVD. The $WO_3$ nanorods are grown on quartz substrates using AACVD. For deposition times below the *conformal* growth regime (< 15 s), the nanorods were only decorated with $TiO_2$ particles. Within the conformal growth regime (15–60 s), epitaxial growth of the $TiO_2$ layer was observed along the nanorods. For deposition times beyond the conformal growth regime (> 90 s), the nanorods were encapsulated within the bulk of a $TiO_2$ matrix.

We observed that the growth rate of $TiO_2$ within deposition times ranged between 15-60 s was approximately constant and estimated as 1.7 nm $s^{-1}$ (**Figure 5.4**), we observed that the $TiO_2$ growth rate achieved in this region was conformally controlled at a nanoscale level, herein called the conformal growth regime. In contrast, outside this conformal growth regime, the nanorods of $WO_3$ were either decorated with $TiO_2$ particles only ($TiO_2$ with deposition times < 15 s) or embedded within a bulk $TiO_2$ matrix ($TiO_2$ deposition times > 60 s), the latter conditions led to increased growth rates of 6.7 nm $s^{-1}$ (**Figure 5.4**). This growth rate is typical of flat $TiO_2$ films grown by

APCVD on glass (as opposed to a nanostructured substrate). In addition, $TiO_2$ depositions below 15 s showed a growth rate of 1.2 nm $s^{-1}$, resulting in the decoration of the $WO_3$ nanorods with $TiO_2$ particles (**Figure 5.4**). The films were labelled henceforth as W/Ti-*t*, where *t* indicates the deposition time (s) of the $TiO_2$ layer.

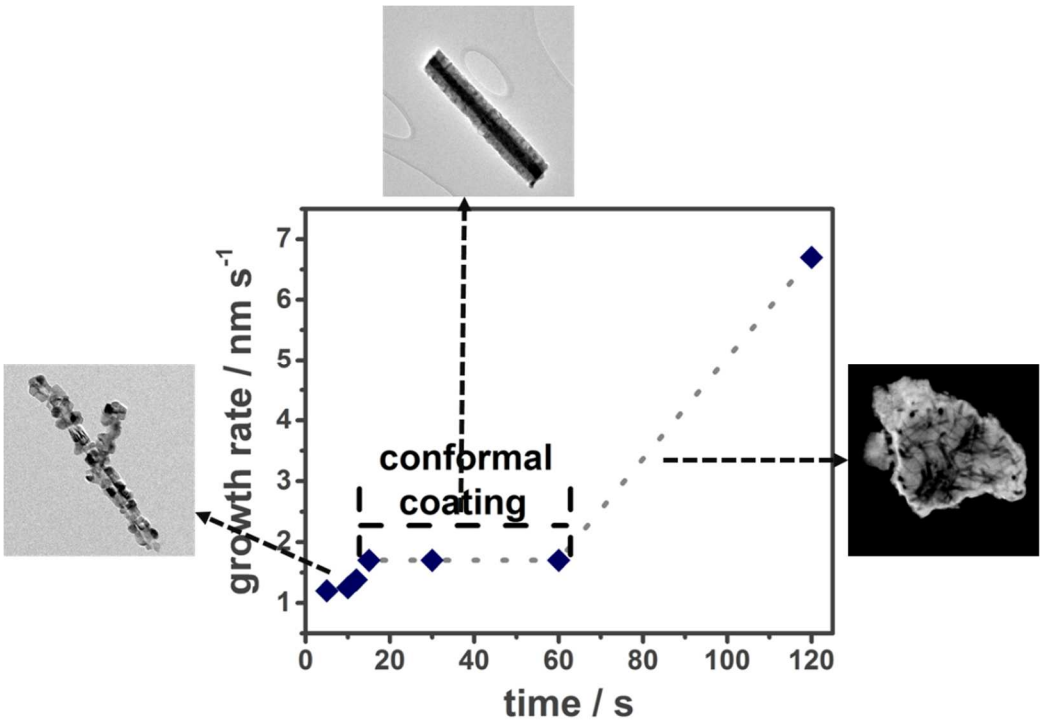


**Figure 5.4.** $TiO_2$ growth rates *vs.* deposition time on $WO_3$ nanorods. A conformal growth regime was established between 15-60 s with a constant rate of 1.7 nm $s^{-1}$. Below this regime, the $WO_3$ nanorods were decorated with $TiO_2$ nanoparticles whilst long deposition times resulted in bulk $TiO_2$ layers with embedded $WO_3$ nanorods.

### 5.4.2. $WO_3/TiO_2$ heterojunction films morphology.

Scanning electron microscopy (SEM) analysis was employed to investigate the microstructure of the $WO_3/TiO_2$ heterojunction films. Cross-sectional SEM studies showed that the microstructure of the nanostructured host was preserved for $TiO_2$ coatings grown for 60 s or less. (**Figure 5.5**). When the deposition time was increased to 120 s, an increase in growth rate was observed coupled with a loss in nanostructure,

resulting in a flat material, wherein nanorods of $WO_3$ were embedded within a bulk $TiO_2$ matrix (**Figure 5.5**). The complete encapsulation of the $WO_3$ nanorods by a $TiO_2$ overlayer was clearly observed using high-resolution transmission electron microscopy (HRTEM). It can be observed in Figure 5.5 that conformal $TiO_2$ coatings of 30, 45 and 100 nm were homogeneously deposited across the $WO_3$ nanorods at deposition times of 15, 30 and 60 s, respectively. However, depositions outside this range resulted in either particles of $TiO_2$ along the nanorods (< 15 s) or enclosing nanorods of $WO_3$ within $TiO_2$ (> 60s). For conformal structures, energy-dispersive X-ray spectroscopy (EDS) analyses across a $WO_3/TiO_2$ nanorod quantitatively showed how the $WO_3$ nanorods were completely covered by a conformal $TiO_2$ layer (**Figure 5.6**). A linear EDS cross-section, measured across a nanorod, confirmed the presence of W, Ti and O, with no other impurity elements. Moving across the rod, we consistently observe Ti, maximising at the edges of the rod, and as expected for a conformal coating. Also, W was only observed in the core, with no evidence of W diffusion into the $TiO_2$ layer. O was present throughout. EDS analysis also corroborated that the $WO_3$ nanorods were embedded within the bulk of a $TiO_2$ matrix when the conformal regime was surpassed (**Figure 5.6(d)**).

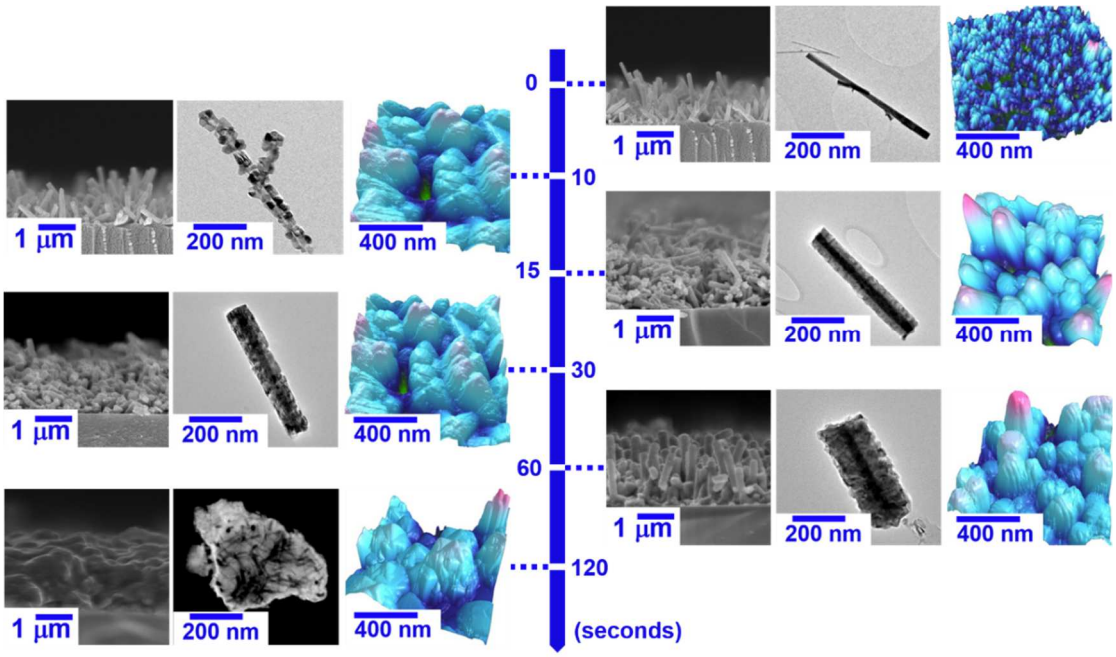


**Figure 5.5.** Cross-sectional scanning electron microscopy (SEM) (left column), transmission electron microscopy (TEM) (centre column) and atomic force microscopy (AFM) images (right column) of as-deposited and $TiO_2$-coated $WO_3$ nanorods, with $TiO_2$ coatings deposited for 0, 10, 15, 30, 60 and 120 s.

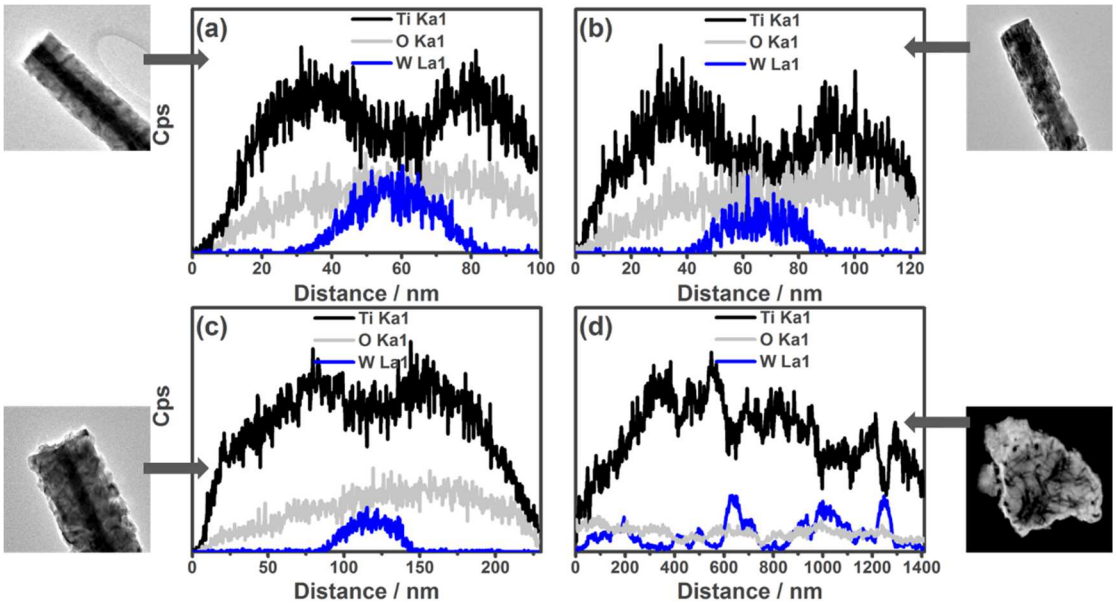


**Figure 5.6.** Energy-dispersive X-ray spectroscopy analysis (EDS) analysis across a $WO_3/TiO_2$ nanorod showing the presence of W, Ti and O elements, for the different $WO_3/TiO_2$ heterojunction films: (a) W/Ti-15; (b) W/Ti-30; (c) W/Ti-60 and (d) W/Ti-120.

### 5.4.3. Physical and optical characterisation.

X-ray diffraction (XRD) analyses of the different as-synthesised films showed pure monoclinic ($WO_3$) and anatase ($TiO_2$) structures (**Figure 5.7(a)**) with no trace of additional phases or impurities observed. XRD patterns were fit to a Le Bail refined model to quantify any changes in the lattice of both crystal phases. These patterns showed a strong diffraction peak at 25°, as well as additional peaks at 38°, 48° and 55°, which are associated with the anatase $TiO_2$ phase. It can also be observed a diffraction peak in all $WO_3/TiO_2$ heterojunction films, which is associated with the monoclinic $WO_3$ phase. From the lattice parameters (**Table 5.1**), it can be observed that there is no substantial change in unit cell volume (column = V % change) for either phase when compared with powder standards. This was further evidence of little or no W diffusion within the $TiO_2$ and *vice-versa*. The average crystal sizes did not change significantly either. Raman studies confirmed the results observed through XRD analysis, as solely anatase $TiO_2$ and monoclinic $WO_3$ crystal phases were present in all heterojunction and single-component films (**Figure 5.7(b)**). A weak band at 807 $cm^{-1}$ confirmed the presence of monoclinic $WO_3$. Also, the presence of anatase $TiO_2$ phase was confirmed by a very strong band at 144 $cm^{-1}$ and three other Raman active-modes at 397, 515 and 639 $cm^{-1}$. The position of the major scattering band of the anatase phase (at 144 $cm^{-1}$) did not change for any of the heterojunction films, where blue shifts in this band have previously been associated with W doping of the anatase phase.[149] As such, Raman analysis supported our EDS and XRD analyses in that no evidence for W diffusion into the anatase layer was observed.

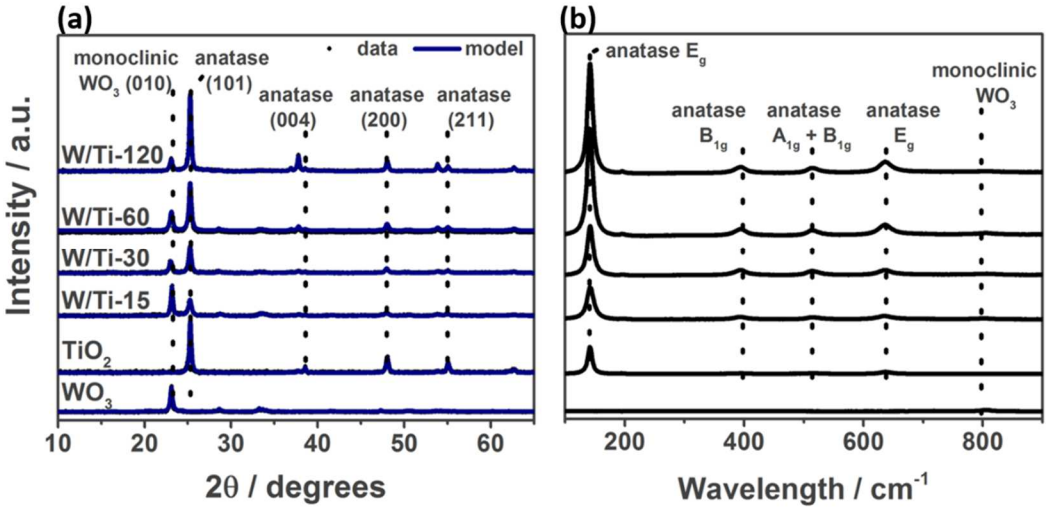


**Figure 5.7.** (a) X-ray diffraction spectra (dotted lines) of the as-synthesised $WO_3/TiO_2$ heterojunction films (W/Ti-15, W/Ti-30, W/Ti-60 and W/Ti-120) and their analogues, nanorods of $WO_3$ and anatase $TiO_2$. The data was fit to a Le Bail refined model (blue lines). (b) Raman spectroscopy analysis showing the presence of pure anatase $TiO_2$ and monoclinic $WO_3$ phases. The representative scattering bands of $TiO_2$ and $WO_3$ were accordingly labelled. Further experimental and film description details are given in Table 5.2.

**Table 5.1.** Unit cell lattice parameters derived from Le Bail refinement of XRD data. WRp is the weighed residual of least-squares refinement and V (%) is the lattice volume expansion relative to a powder standard. The unit cell of either phase did not expand more than 0.5 % relative to a powder standard. τ is the average crystallite size.

| **Sample** | | **X-ray diffraction-Le Bail refinement** | | | | |
|---|---|---|---|---|---|---|
| | | a [Å] | c [Å] | V (%) | wRp | τ (nm) |
| Standard | $WO_3$ | 7.301(1) | 7.670(1) | -- | -- | -- |
| | $TiO_2$ | 3.785(1) | 9.512(1) | -- | -- | -- |
| Pure phase | $WO_3$ | 7.287(3) | 7.701(1) | 0.02 | 0.12 | 27.3 |
| Pure phase | $TiO_2$ | 3.785(1) | 9.525(3) | 0.13 | 0.16 | 32.6 |
| W/Ti-15 | $WO_3$ | 7.312(3) | 7.684(1) | 0.02 | 0.93 | 33.2 |
| | $TiO_2$ | 3.793(1) | 9.527(6) | 0.62 | | 20.0 |
| W/Ti-30 | $WO_3$ | 7.254(6) | 7.721(1) | -0.25 | 0.92 | 21.7 |
| | $TiO_2$ | 3.792(1) | 9.540(4) | 0.68 | | 24.8 |
| W/Ti-60 | $WO_3$ | 7.301(6) | 7.710(1) | 0.49 | 0.12 | 23.2 |
| | $TiO_2$ | 3.788(1) | 9.515(2) | 0.22 | | 26.8 |
| W/Ti-120 | $WO_3$ | 7.264(4) | 7.708(1) | -0.13 | 0.13 | 22.1 |
| | $TiO_2$ | 3.790(1) | 9.520(1) | 0.39 | | 34.3 |

Numbers in parentheses represent the error on the last digit.

The optical properties were studied using UV-Visible absorption spectroscopy. It can be clearly observed in Figure 5.8(a) that the single-component $TiO_2$ film showed expected absorption edge values (~ 380 nm). Interestingly, $WO_3$ nanorods films showed an unexpected increase in light transmission, likely due to its nanostructured morphology. Smith *et al*.[216] reported that the synthesis of nanorods of $WO_3$ required the use of an oxygen deficient environment, which most likely introduced oxygen vacancies. It has been recently found by Ling *et al*.[217] that these oxygen vacancies within the nanorod localise electrons at $W^{6+}$ sites, forming polarons, which enlarge W-W bonds and shorten W-O bonds. This change in the structure of $WO_3$ will induce a spatial stress which is relaxed by a lattice displacement, resulting in the formation of dislocation loops (**Figure 5.9(a)**). These dislocation loops will induce a quantum confinement effect, increasing the light transmittance in $WO_3$ nanorods, as well as its bandgap. The presence of these oxygen vacancies within the nanorods of $WO_3$ can be demonstrated using XPS analysis. For charge neutrality, the presence of an oxygen vacancy results in the reduction of $W^{6+}$ states in $WO_3$ to $W^{5+}$. Our XPS analyses confirmed the presence of $W^{5+}$ states (**Figure 5.9(b)**).

Bandgap measurements were obtained from Tauc plot analyses,[86] as *ca*. 3.2 and 3.15 eV, for $TiO_2$ and $WO_3$ nanorods, respectively (**Figure 5.8(a), inset**). UV-Visible absorption spectra of the $WO_3/TiO_2$ heterojunction films showed band onsets that were substantially more red-shifted compared with each isolated analogue, in agreement with previous theoretical and experimental works, where it was found that the bandgap of heterojunction films is lowered with respect to the individual components.[31,32] Interestingly, a comparison of the UV absorption properties of a typical $WO_3/TiO_2$ heterojunction (W/Ti-60) with pure $TiO_2$ (**Figure 5.8(b)**) shows that the heterojunctions absorb substantially more UV light. Of note, our photocatalytic tests

were conducted using a 365 nm light source, where at this wavelength, heterojunction W/Ti-60 absorbed four times more light than pure $TiO_2$. However, as it will be explained in detail in the following section, the enhanced photocatalytic efficiency of the $WO_3/TiO_2$ heterojunction films cannot be explained only in terms of different light absorption.

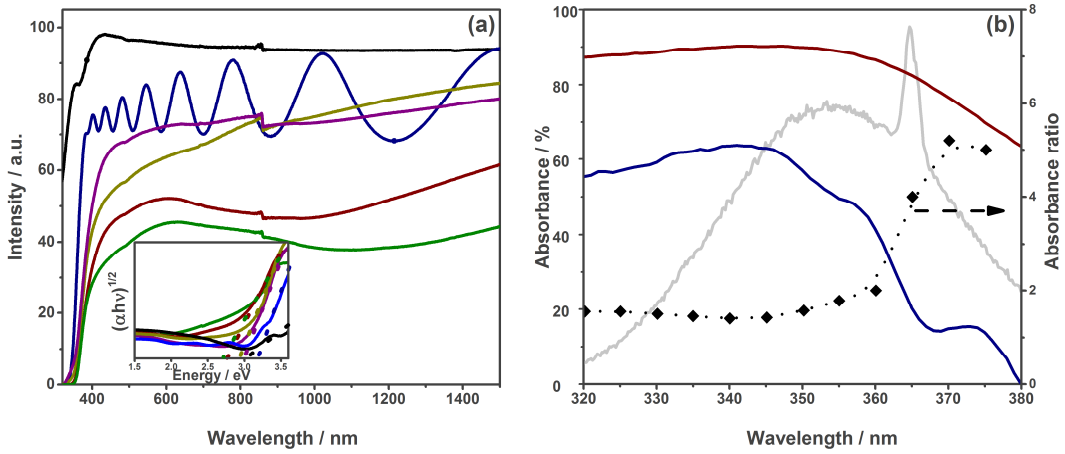


**Figure 5.8.** (a) UV-Vis spectra of pure metal oxides, $WO_3$ (black line) and $TiO_2$ (blue line), as well as the $WO_3/TiO_2$ heterojunction films; W/Ti-15 (purple line), W/Ti-30 (yellow line), W/Ti-60 (red line) and W/Ti-120 (green line). The inset shows bandgap measurements derived from Tauc plot analysis. (b) UV-Vis spectra of W/Ti-60 heterojunction film (red line) and its $TiO_2$ single-semiconductor analogue (blue line), highlighting the absorbance of both materials within the region (320-380 nm) of the emission spectrum of the light source used in our photocatalytic tests (grey line). The full symbols indicate the ratio between the corresponding absorbance of the two films. Further experimental and film description details are given in Table 5.2.

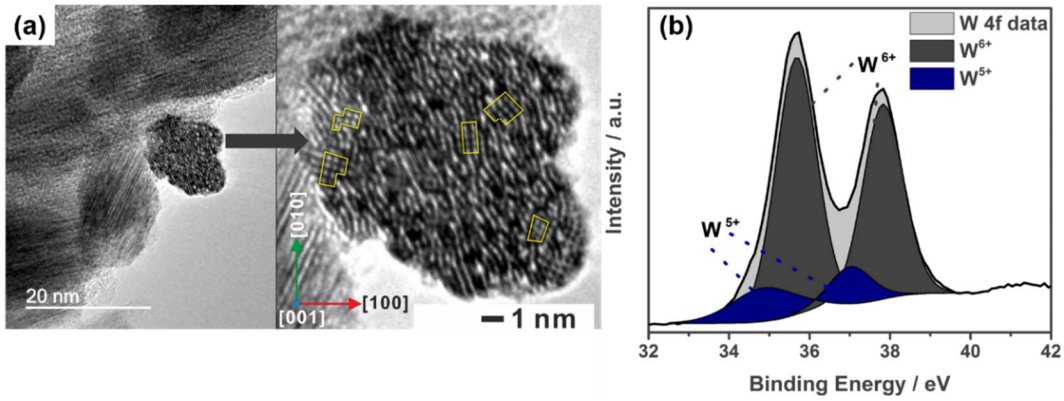


**Figure 5.9.** (a) High-resolution transmission electron microscopy (HRTEM) image of a typical nanorod of $WO_3$ and zoom in to show the strain within the lattice of the nanorods due to the presence of dislocation loops (yellow squares) within the lattice of $WO_3$ nanorods (image taken from Min Ling from his PhD work based on the study of the mechanism to grow $WO_3$ nanorods). (b) X-ray photoelectron spectroscopy (XPS) spectrum of the W 4f environment. The grey filling is assigned to $W^{6+}$ oxidation state and the blue filling is assigned to $W^{5+}$ oxidation state.

### 5.4.4. Hybrid density functional theory (DFT) and hard X-ray photoelectron spectroscopy (HAXPES) analyses.

The electronic interaction at the $WO_3/TiO_2$ heterojunction was studied from both theoretical and experimental standpoints. Density functional theory (DFT) has been widely used to explore the electronic band alignment between semiconductors.[218,219] The ionization potential of bulk $WO_3$ was calculated using the slab model,[212,220] using hybrid density functional theory (DFT) (HSE06 functional[211]) within the VASP code. In Figure 5.10, the alignment is plotted relative to the anatase $TiO_2$ band edges as calculated previously.[31] The HSE06 calculated ionization potential (7.65 eV) and electron affinity (4.91 eV) for $WO_3$ fits reasonably well with previous experimental measurements of $7.38 \pm 0.11$ and $4.10 \pm 0.11$ eV for $WO_3$ surfaces.[221] It should be noted that our calculated ionization potentials do not take into account the effects of interfacial strain and chemical interactions that may influence the band offset at a particular interface, however, they offer a reasonable first approximation, as demonstrated by the widespread application of Anderson's rule for estimating band offsets.[222] The calculated alignment, reported in this chapter, suggest spatial separation of holes moving into $WO_3$ (**Figure 5.10**). This idealised alignment is at variance with the commonly accepted $WO_3$-$TiO_2$ alignment motif in the literature.[203] The theoretical modelling, as well as the data interpretation and analysis of this section, were performed in collaboration with Dr. David O. Scanlon.

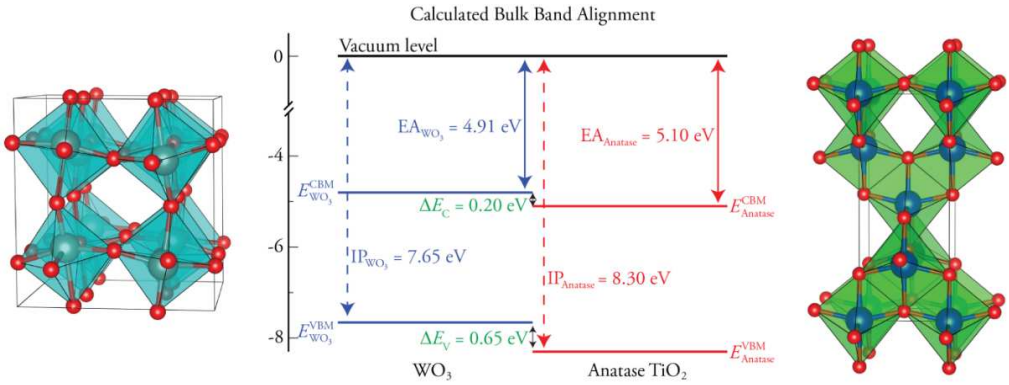


**Figure 5.10.** HSE06 calculated band alignment between $WO_3$ and anatase $TiO_2$. The electron affinities are calculated based on bandgaps of 2.74 and 3.20 eV for $WO_3$ and anatase $TiO_2$, respectively.

The electronic alignment at the $WO_3/TiO_2$ interface was also experimentally explored using hard X-ray photoelectron spectroscopy (HAXPES) measurements, which were carried out at Beamline I09 at Diamond Light Source. Figure 5.11 shows the valence band spectra measured from the W/Ti-15 film and the individual components. It is worth noting that no differences in the binding energy of either Ti 2p or W 4d were detected between the coated nanorods and the corresponding references (**Figure 5.11(b) and (c)**), indicating that the contact between $WO_3$ and $TiO_2$ does not alter the energy levels relative to the vacuum level on either side of the interface. The valence band alignment across the $WO_3/TiO_2$ interface could thus be determined directly from the valence band maxima of the $WO_3$ and $TiO_2$ references, which were extracted from Figure 5.11(a) to be 2.85 and 3.57 eV below the Fermi level, respectively, leading to a valence band offset of 0.72 eV. Figure 5.11(d) summarises the alignment of the energy levels derived from the HAXPES data, where the conduction band offset was estimated to be 0.26 eV, using previously reported bandgaps of 2.74 and 3.2 eV for $WO_3$ and $TiO_2$, respectively. The band edge of $WO_3$ is above that of $TiO_2$ for both conduction and valence bands, in excellent agreement with the DFT calculations previously reported. The HAXPES measurements, as well as the data interpretation and analysis

of this section, were performed in collaboration with Dr. Tien-Lin Lee and Dr. Pardeep Kumar at Diamond Light Source, Harwell Science and Innovation Campus.

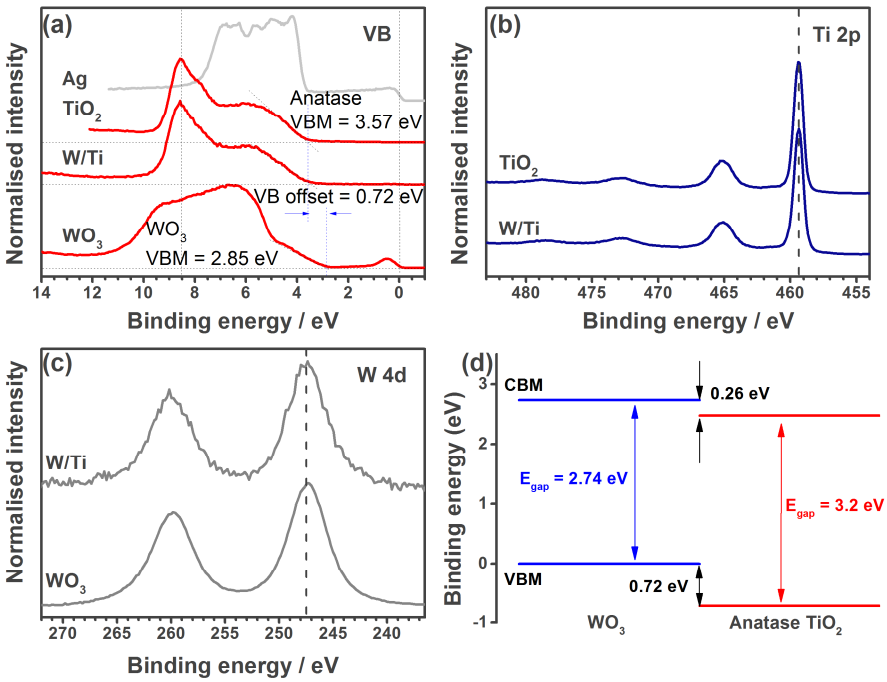


**Figure 5.11.** Results of the HAXPES measurements on $WO_3/TiO_2$ heterojunction film (W/Ti-15) and the individual components, $WO_3$ and anatase $TiO_2$. (a) Corresponding valence band spectra of all three materials. For each sample a silver Fermi edge was recorded to calibrate the binding energies. The blue dashed lines mark the valence band maxima of the $TiO_2$ and $WO_3$ references. (b-c) Ti 2p3/2 and W 4d5/2 peaks to show no detectable banding energy shifts between the samples. (d) Band alignment at the $WO_3/TiO_2$ interface derived from HAXPES results. Bandgaps reported from previous studies for $WO_3$ and $TiO_2$ are assumed for estimating the conduction band offset, values are relative to the VBM of $WO_3$.

### 5.4.5. Photocatalytic activity.

Photocatalytic tests were carried out in all individual single-component and heterojunction films during degradation of a model organic pollutant, stearic (octadecanoic) acid under UVA irradiation. The overall degradation reaction is given by Equation 5.1:

$$CH_3(CH_2)_{16}CO_2 + 26O_2 \longrightarrow 18CO_2 + 18H_2O \qquad 5.1$$

In a typical test, a thin layer of stearic acid was deposited onto the film using a home-made dip coater from a 0.05 M stearic acid solution on chloroform. The integrated areas of the bands were periodically estimated during UVA irradiation of the films ($I$ = 3.15 mW $cm^{-2}$). The light source was a blacklight-bulb lamp (BLB), 2 x 8 W (*Vilber-Lourmant*). The photoactivity rates were estimated from linear regression of the initial 30-40 % degradation steps (zero-order kinetics) of the curve of integrated areas (**Figure 5.12(b)**). The results are typically expressed in terms of the formal quantum efficiency, ξ, defined as the number of molecules degraded per incident photon (units, molecule x $photon^{-1}$). The number of acid molecules degraded were estimated using the conversion factor 1 $cm^{-1} \equiv 9.7 \times 10^{15}$ molecule $cm^{-2}$ from the literature.[87] The ξ values tend to underestimate the actual photocatalytic activity since not all incident photons are absorbed by the catalyst. In this estimation, it is also assumed that all the incident photons have the same energy, *i.e.* 3.4 eV (365 nm). The rates of degradation are typically expressed in terms of formal quantum efficiency (ξ), defined as molecules of stearic acid degraded per incident photon (molecule x $photon^{-1}$) (**Figure 5.13**).

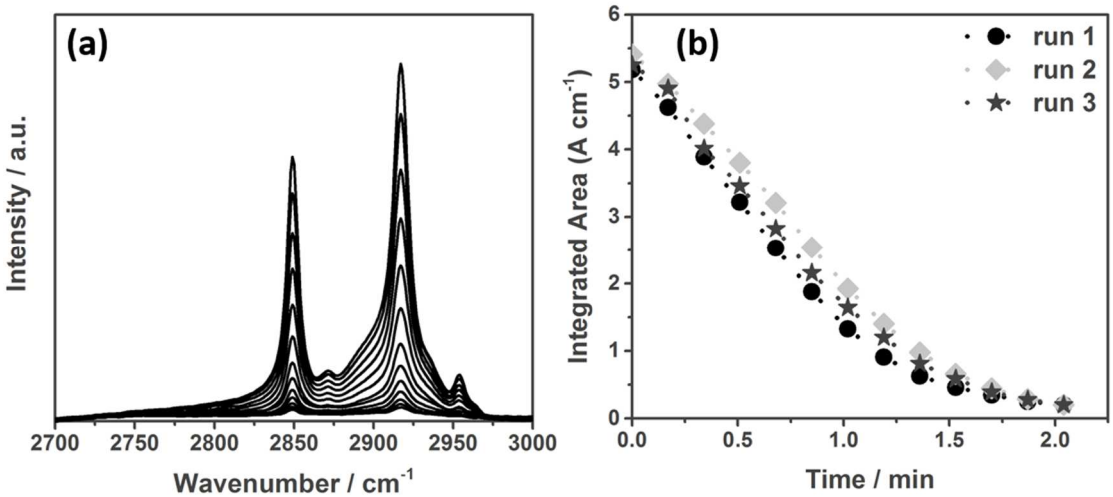


**Figure 5.12.** (a) IR spectra of stearic acid upon UVA illumination ($I$= 3.15 mW $cm^{-2}$) on a typical $TiO_2/WO_3$ heterojunction film. (b) Integrated areas obtained during sequential photocatalytic tests under UVA illumination of $WO_3/TiO_2$ heterojunction films.

The photocatalytic activity for our range of different heterojunction films (samples W/Ti-15, W/Ti-30, W/Ti-60 and W/Ti-120) were examined. As it can be observed in Figure 5.13, the formation of a heterojunction between $WO_3$ and $TiO_2$ results in an extremely beneficial enhancement in the photocatalytic efficiency. Within the conformal growth regime, the increase in activity correlated with the increasing thickness of the $TiO_2$ overlayer, this could be attributed to an enhancement of the light absorbed by the photocatalyst. However, beyond the conformal regime, the activity suddenly dropped to ξ values similar to those observed in pure $TiO_2$ films (**Figure 5.13, W/Ti-120**). These results were reproducible ((**Figure 5.13(b)**) and showed similar ξ values even after being storage in air for a year.

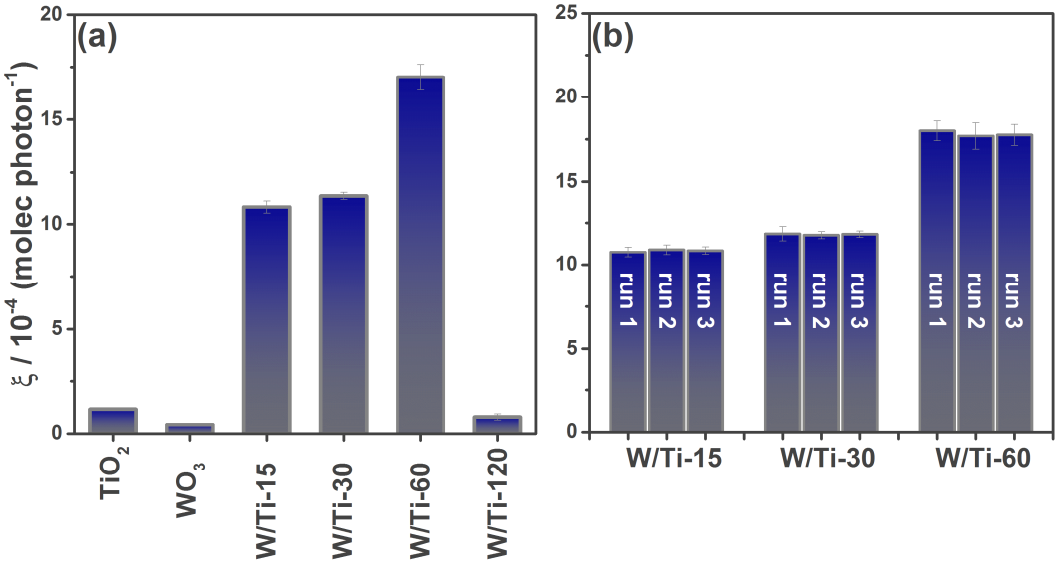


**Figure 5.13.** (a) Photocatalytic activities given as formal quantum efficiencies (ξ) of the different $WO_3/TiO_2$ heterojunction films with a varying $TiO_2$ overlayer; W/Ti-15 (30 nm of $TiO_2$), W/Ti-30 (45 nm of $TiO_2$), W/Ti-60 (100 nm of $TiO_2$) and W/Ti-120 (500 nm of $TiO_2$). The values are given as molecules degraded per incident photon (molecule × photon$^{-1}$) and were obtained from the rate of photodegradation of stearic acid under UVA illumination (3.15 mW·cm$^{-2}$). (b) Formal quantum efficiencies (ξ) obtained during sequential photodegradation of stearic acid on the three $WO_3/TiO_2$ heterojunction films obtained within the conformal growth regime (W/Ti-15, W/Ti-30 and W/Ti-60). The third test was carried out a year after the synthesis of the heterojunction films. Further experimental and film description details are given in Table 5.2.

The photocatalytic behaviour of the optimum $WO_3/TiO_2$ heterojunction film (W/Ti-60) was studied in detail, in order to achieve a better understanding of the effect of the synergetic interaction between the two metal oxides. The photocatalytic activity of the This heterojunction W/Ti-60 film was 17.1 x $10^{-4}$ molecule x photon$^{-1}$ (**Table 5.2**), which exceeded the record established by the rutile/anatase $TiO_2$ sample (10.7 x $10^{-4}$ molecule x photon$^{-1}$) reported in chapter 4. Surprisingly, the outstanding activity achieved by the W/Ti-60 heterojunction film was comparable to that of a dip-coated P25 *Evonik* film (16.8 x $10^{-1}$ molecule x photon$^{-1}$, **Figure 5.14**), with a film thickness considerably thicker (~1300 nm) than that of the W/Ti-60 film. This is a remarkable achievement for any thin film, since P25 *Evonik* is one of the best commercial polycrystalline $TiO_2$ photocatalysts, which is commonly used as a benchmark material for comparing photocatalytic activity.[223] As a reference, Figure 5.14 includes the $\xi$ values reported by a Pilkington Activ$^{TM}$ glass (0.2 x $10^{-4}$ molecule x photon$^{-1}$),[224] a commercially available self-cleaning coating, which was about 100-times lower in activity than that of the W/Ti-60 heterojunction film. In this chapter, a thorough comparison of the photocatalytic efficiency reported for different heterojunction systems, as well as chemically modified photocatalysts, was performed. However, it is worth mentioning that there is always an inherent difficulty when comparing photocatalytic materials produced by different synthetic methods and groups. This issue was bypassed by comparing *enhancement factors* as estimated from activity ratios between the heterojunction (or doped) material and their corresponding best-performing single (or pure) component. For instance, the enhancement factor for the system reported by Chatchai *et al*.,[225] $WO_3/BiVO_4$, was calculated by taking the IPCE values at 365 nm for the heterojunction system and the most active single-component, $BiVO_4$, these values being ~ 71 % IPCE and ~ 8 % IPCE, respectively, and thus the

estimated enhancement factor is ~ 9. As observed in Table 5.2 the corresponding enhancement factor of our $WO_3/TiO_2$ (W/Ti-60) system is ~ 14, which is the highest enhancement ever reported, to the best of our knowledge.

It is important to mention that heterojunction systems have been typically synthesised by sol-gel, electrodeposition, spin-coating and other thermal methods; which are commonly less capable of mass-production. Nevertheless, in this chapter we present the use of a well-known method, CVD, to produce high crystalline heterojunction systems that could be scaled up to online processes. In addition, it is also important mentioning that this $WO_3/TiO_2$ heterojunction system has been previously investigated by different groups,[203–205,226–228] where each single group reported an enhancement in the separation of the photogenerated charge carriers. Unfortunately, the photocatalytic properties presented in this chapter could not be compared with previous reports from the literature, as most of these works were based in hydrophilicity studies of the $WO_3/TiO_2$ system,[203,228] and in other works the chosen synthetic method performed composites instead of heterojunction systems.[227]

**Table 5.2.** Physical and functional details of the optimized $WO_3/TiO_2$ heterojunction film and relevant standards. As-synthesised $WO_3$ nanorods were ~650 x 70 nm (length x width).

| Sample | Physical Properties | | | Functional properties |
|---|---|---|---|---|
| | Spectroscopy | | AFM | Photocatalysis |
| | $d^b$ (nm) | $E_{bg}{}^d$ (eV) | Surface Area ($\mu m^2$) | $\xi$ / $10^{-4}$ (molecule × photon$^{-1}$) |
| $WO_3$ | -- | 3.10 | 11.1(3) | 0.4 ± 0.06 |
| $TiO_2$[a] | 650 | 3.21 | 4.6(4) | 1.3 ± 0.04 |
| W/Ti-15 | 30 | 3.02 | 9.5(6) | 10.8 ± 0.30 |
| W/Ti-30 | 45 | 2.95 | 8.0(6) | 11.3 ± 0.20 |
| W/Ti-60 | 100 | 2.80 | 7.6(7) | 17.1 ± 0.35 |
| W/C/Ti-60 | 100 | -- | 7.2(7) | 1.5 ± 0.07 |
| W/Ti-120 | 500 | 2.75 | 7.1(7) | 0.8 ± 0.08 |
| P25 *Evonik* | 1300 | -- | -- | 16.8 ± 0.03 |

[a]Values for an optimised $TiO_2$ CVD film deposited under identical flow/temperature conditions; [b]d = $TiO_2$ film thickness from TEM, SEM and profilometer measurements; [d]Bandgap energies ($E_{bg}$) estimated from Tauc plot analysis. Numbers in parentheses represent the error on the last digit.

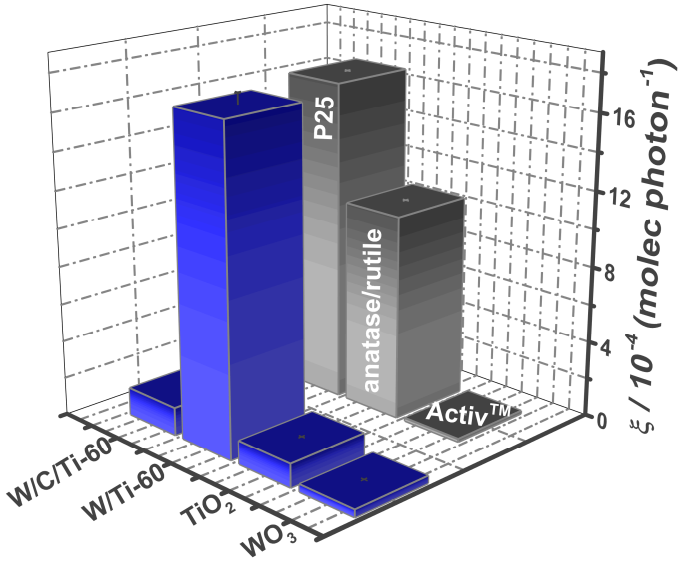


**Figure 5.14.** Photocatalytic activities given as formal quantum efficiencies ($\xi$) of the different heterojunction films, W/Ti-60 and W/C/Ti-60, as well as the individual components, $WO_3$ and $TiO_2$. The $\xi$ values are given as molecules degraded per incident photon (molecule x photon$^{-1}$). Typical $\xi$ values of relevant photocatalytic materials are included for reference. The activity of Pilkington Activ™ was obtained from ref. **224**

**Table 5.3.** Photocatalytic enhancement of representative photocatalytic materials (heterojunction and doped materials) reported in the literature. Synthesis method and photocatalytic test are included as reference. All photocatalytic materials were compared to their analogues.

| Photocatalyst | Synthesis method | Test[a] | λ | Enhancement factor[b] | Refs. |
|---|---|---|---|---|---|
| $WO_3/TiO_2$ | CVD | Stearic acid | UVA | 14 | **Chapter 5** |
| $WO_3/BiVO_4$ | Spin coating | IPCE | 365nm | 9 | **225** |
| $Cu_2O/TiO_2$ | Electrodeposition | IPCE | 365nm | 8 | **229** |
| $CaFe_2O_4$/ TaON | Electrophoretic dep | IPCE | 365nm | 8 | **230** |
| $V_2O_5$/N,S-$TiO_2$ | Solid state reaction route | IPCE | 365nm | 7.5 | **231** |
| $CdS/TiO_2$ | Anodization/ Electrodeposition | IPCE | 365nm | 7 | **232** |
| Rutile/Anatase $TiO_2$ | (AP)CVD | Stearic acid | UVA | 7 | **Chapter 4** |
| Nano-Au:Ag:$TiO_2$ | Sol-gel | Stearic acid | UVA | 7 | **136** |
| W:$TiO_2$ | Sol-gel | Stearic acid | UVA | 5 | **136** |
| $TiO_2/SrTiO_3$ | Hydrothermal synthesis | $H_2$ generation | UVC | 4.5 | **233** |
| $MoS_2/CdS$ | Electrodeposition/ Chem Bath | IPCE | 365nm | 4 | **234** |
| $Bi_2WO_6$/ Ag/N–$TiO_2$ | Spin coating | IPCE | 365nm | 4 | **235** |
| N:$TiO_2$ | (AP)CVD | Stearic acid | UVA | 3.5 | **Chapter 2** |
| $TiO_2/WO_3$ | Electrospinning/ Thermal evaporation/ Thermal annealing | Rh B | UVA | 3 | **226** |
| $TiO_2/SnO_2$ | (PE)CVD | Phenol | UV | 3 | **236** |
| $TiO_2/Cu_2O$ microgrid | Sol-gel/ Microsphere lithography | MB | UVA | 2.5 | **237** |
| $TiO_2/SnO_2$ | Electrospinning | Rh B. | UV | 2 | **238** |
| $WO_3/BiVO_4$ | Solvothermal/ Spin coating | IPCE | 365nm | 2 | **42** |
| $TiO_2/In_2O_3$ | Sol-gel | 2-CP | UV | 1.5 | **239** |
| $CeO_2/TiO_2$ | Colloidal templates/ ALD | MB | UVA | 1.5 | **240** |
| $ZnO/TiO_2$ | Thermal sputtering/ Anodization | IPCE | 365nm | 1.5 | **241** |
| $Bi_2S_3/WO_3$ | Solvothermal | IPCE | 365nm | 1.5 | **242** |
| Perovskite/ PCBM | Spin casting/ Thermal evaporation | IPCE | 365nm | 1.5 | **243** |

[a] IPCE: incident photo-to-current efficiency in water splitting; RhB: Rhodamine B; MB: methylene blue; 2-CP: 2-chlorophenol. [b]Approximate enhancement factors estimated from activity ratios between the heterojunction (or chemically-modified/doped) material and the corresponding active analogue (or pure) component.

As previously mentioned, the different $WO_3/TiO_2$ heterojunction films showed different light absorption. Therefore, it could be easily questioned whether the enhancement of the photoactivity efficiency is merely due to an increase in light absorption of the heterojunction films compared to the single-semiconductor analogues. This effect was investigated comparing the absorption spectra of the W/Ti-60 heterojunction film with that of its $TiO_2$ single-component analogue. Figure 5.8(b) shows the absorption spectra of the active components ($TiO_2$ on $WO_3$ and as a single layer) in these systems, within the relevant region (320-380 nm) of the emission spectrum of the light source (UVA BLB lamp). Indeed, the light absorption of the heterojunction film was 4-times that of the $TiO_2$ analogue at 365 nm (**Figure 5.8(b)**). However, considering a linear correlation between photon absorption and photocatalytic activity, the corresponding activity enhancement (a factor of 14) cannot solely be attributed to an increase in light absorption.

To ascertain whether the enhancement in activity was simply due to an increase in surface area of the $TiO_2$ by using a high-surface-area host ($WO_3$), a thin layer of carbon was sputtered over the $WO_3$ nanorods before the deposition of the $TiO_2$ layer, to inhibit direct contact between the oxide phases. The resulting $WO_3/C/TiO_2$ film showed a similar microstructure than that of the W/Ti-60 film (**Figure 5.3**), however, its photocatalytic activity was comparable to that of the single-semiconductor $TiO_2$ analogue (**Figure 5.14**). Therefore, it can be concluded that the enhancement observed for the $WO_3/TiO_2$ heterojunction films should be attributed to an electronic synergy upon a direct contact of the two phases. This synergistic effect most likely increased the lifetime of photogenerated charge carriers in $WO_3/TiO_2$ heterojunctions, reducing the detriment of charge carrier recombination, resulting in an enhanced photocatalytic activity.

## 5.5. Conclusions.

In this chapter, the use of CVD processes to synthesise $WO_3/TiO_2$ heterojunction films with high surface area by conformally coating nanorods of monoclinic $WO_3$ with anatase $TiO_2$ is reported. The use of CVD processes to synthesise heterojunction systems will be relevant for commercial applications, as it is a scalable method capable of producing robust coatings.

These $WO_3/TiO_2$ heterojunction films have shown the highest enhancement in activity for a $TiO_2$-based thin film photocatalyst. These heterojunction films are also durable to multiple photocatalytic cycles. Both theoretical and experimental work have provided a direct understanding of the enhanced activity, finding that a high level of electronic interaction between both, $WO_3$ and $TiO_2$, crystal phases is crucial to design highly active photocatalytic materials. Crucially, the synthesis of these highly active and durable photocatalytic surfaces has been achieved using an industrially upscalable method, CVD. These results reported in this chapter highlight not only a qualitative step forward in the engineering of photocatalytic heterojunction materials, but also the importance of the synthesis method and conditions employed, which should be optimised to ensure an effective contact between the semiconductor phases involved.

In the following chapter, we will summarise the results reported during this thesis. We will evaluate the use of CVD processes as a route to deliver robust surface coatings with high photocatalytic performance, as well as durable to several photocatalytic cycles. Finally, we will briefly suggest what we consider is necessary to improve the functional properties of thin film surface coatings.

Chapter VI

# CONCLUSIONS AND FUTURE WORK

*"The following chapter presents a summary of the results reported in this thesis. In this chapter, we will also present a brief introduction to the future work that we feel it could improve the application of photocatalysis to environmental treatment remedies."*

# 6. Conclusions and future work.

## 6.1. Summary of results.

As previously mentioned, enhancing the photocatalytic efficiency of $TiO_2$ has been intensely sought for more than five decades. This has led to a drastic increase on the number of publications from 1000 publications in 1970-2000 to almost 28000 publications in 2000-2015. Many different approaches, such as chemical modification, heterostructuring, nanostructuring, addition of co-catalysts, etc., have been investigated.

Although the vast number of methods studied, no approach has been more investigated than the chemical modification of $TiO_2$ using anionic and/ or cationic dopant species. This method modifies the electronic structure of the $TiO_2$ materials, allowing to tune its absorption features, and therefore, enhancing its photocatalysis. However, this solid solution depends extremely on the synthetic method and dopant source used, which have a direct influence on the nature of the species added to the structure of $TiO_2$, as well as the species adsorbed to its surface. The nature and effect of these dopant species on the photocatalytic performance of $TiO_2$ has created a historical debate, which is still unanswered. Atmospheric-pressure chemical vapour deposition (APCVD) has been used, in this thesis, to investigate the influence that anionic and cationic species had on the functional properties of $TiO_2$, by adding three different dopant species into the $TiO_2$ lattice, nitrogen (Chapter 2), phosphorus and sulfur (Chapter 3).

As previously mentioned, nitrogen can coexist within the $TiO_2$ lattice in the form of two different type of environments, by replacing substitutionally oxygen sites or sitting interstitially within the $TiO_2$ structure. This has led to a historical debate based on which nitrogen specie is the responsible of the photocatalytic enhancement of N-doped $TiO_2$

materials. Many authors have attributed the visible light activity as being due to the narrowing of the bandgap energy in the band structure of $TiO_2$ upon substitution of $O^{2-}$ by $N^{3-}$ species. It is worth mentioning that the visible light activity has been also assigned to the inherent formation of oxygen vacancies upon the incorporation of $N^{3-}$ anions. In contrast, the presence of interstitial nitrogen within the structure of $TiO_2$, forming N-O groups with lattice oxygen, has been observed beneficial to enhance the UV light sensitivity of N-doped $TiO_2$ materials. In addition, the use of nitrogen leads to obtain different nitrogen-based surface species, such as $NO_x$ groups, chemisorbed nitrogen ($\gamma$-$N_2$) and $NH_x$ species with similar binding energies to that of interstitial nitrogen, *ca*. ~ 400 eV; making even more difficult to identify the role of nitrogen in the N-$TiO_2$ photocatalysis.

In chapter 2 three different nitrogen sources (*tert*-butylamine, benzylamine and ammonia) were used to modify $TiO_2$ thin films. This allowed us to account the effect that nitrogen had on the physical and optical properties of N-$TiO_2$ films. In this chapter, we found that the presence of nitrogen enhanced the photocatalytic efficiency of $TiO_2$. However, after a thorough study of all different nitrogen-based species found on the surface of our N-$TiO_2$ films, it was found that these species had a main impact on the photocatalytic performance of the N-$TiO_2$ films under UVA light illumination. Therefore, the enhanced photocatalytic efficiency observed may be assigned to a sensitisation mechanism of $NH_x$ species (~ 400 eV). In addition, it was also found that the presence of nitrate ($NO_3^-$), nitrite ($NO_2^-$), as well as other N-O (N–O–Ti–O or O–N–Ti–O) groups had a dramatic effect on the photocatalytic response of N-$TiO_2$ films.

It has been commonly acknowledged that the chemical modification of $TiO_2$ normally requires the use of high amounts of the dopant specie, which will drastically affect the physical and functional properties of doped $TiO_2$ materials. In chapter 2, we bypassed

this issue through the design of stratified nitrogen-doped $TiO_2$ films, by adding the dopant specie locally within the $TiO_2$ structure. These stratified N-$TiO_2$ films combined N-doped and undoped $TiO_2$ layers which could be seen beneficial to increase photogenerated charge mobility and therefore, lower charge recombination. Atmospheric-pressure CVD was used in a pulsed precursor configuration to selectively incorporate high concentrations of nitrogen into the $TiO_2$ lattice, resulting in the synthesise of stratified N-doped $TiO_2$ films. These films showed enhanced photocatalytic efficiency without affecting the physical properties of N-$TiO_2$ films. Therefore, this APCVD configuration could be used to produce materials with multiple layers using a wide range of dopants or mixtures of co-dopants.

As previously mentioned the addition of cationic species to $TiO_2$ has been widely investigated. Many theoretical and experimental works have reported that cationic-doped $TiO_2$ materials could result in visible-active materials, by introducing inter-band localised states above the valence band of $TiO_2$, promoting the electron transition between the valence and conduction bands. In chapter 3, phosphorus and sulfur species were used to grow P and S-doped $TiO_2$ films and investigate the effect that cationic and anionic species have on the functional properties of $TiO_2$. It was found that the addition of cations, $P^{5+}$, to the $TiO_2$ structure resulted in an increase in the conductivity of the $TiO_2$ films, which agrees with the literature where it was reported that cationic dopants with higher oxidation state than $Ti^{4+}$ inject electrons into the conduction band of $TiO_2$, transforming it into a transparent conducting oxide (TCO). Interestingly, it was also observed that the cationic phosphorus specie ($P^{5+}$) did not decrease the photocatalytic efficiency of $TiO_2$. This was extremely relevant since electrical conductivity often arises to the detriment of photocatalytic activity. In addition, the incorporation of sulfur was also investigated. We found that the use of sulfur was beneficial from a

photocatalytic point of view. However, the relative big atomic size of sulfur resulted in disorder changes within the structure of $TiO_2$.

As previously mentioned, the inherent problems associated to the chemical modification of $TiO_2$ led to a vast investigation to find alternative routes to enhance the photocatalytic efficiency of $TiO_2$, being the use of heterojunction systems the most commonly accepted solid solution. In heterojunction systems, the band structures of the two joining semiconductors can align favourably, migrating photogenerated electrons and holes in separate directions across the heterojunction boundary. This vectorial charge separation can inhibit electron-hole recombination and enhance photocatalytic efficiency. In this thesis, we explored the design of two different heterojunction systems, rutile/anatase $TiO_2$ (Chapter 4) and nanostructured $WO_3/TiO_2$ (Chapter 5) heterojunctions to study the synergistic effect between the two joining metal oxides. The synthesis of rutile/anatase $TiO_2$ heterojunction films allowed us to investigate a well-studied heterojunction system, where an enhanced photocatalytic activity was observed compared to its single-semiconductor component (anatase $TiO_2$). This enhancement observed can be explained in terms of an effective photogenerated charge transfer promotion. In addition, the synthesis and investigation of nanostructure $WO_3/TiO_2$ heterojunction films, through theory, hard X-ray photoelectron spectroscopy and experiment, confirmed that the design of heterojunction systems with an electronic structure that promotes photogenerated charge transfer will result extremely beneficial to enhance the photocatalysis of $TiO_2$-based photocatalytic materials.

## 6.2. Future work.

We consider that further investigations into CVD processes may result in improved methods for depositing coatings with enhanced photocatalytic properties, especially the use of APCVD to produce conformal coatings. Although APCVD is a well-known technique, its potential application to deliver conformal coatings has not been explored in depth. We feel that continued application and investigation of this method could surely lead to further materials discovery, especially to produce new heterojunction systems if new combinations of metal oxide layers are applied. From looking at the literature, there is a wide number of non $TiO_2$-based photocatalysts including, $Fe_2O_3$, $Bi_2O_3$, $BiVO_4$, *etc*. that have been suggested to be visible-light active. Therefore, the optimisation of APCVD process, to coat these different metal oxides, will allow to engineer heterojunction systems with potential visible-light properties. In addition, we would also like to apply APCVD to produce stratified-doped metal oxides. We observed that the photocatalytic efficiency of stratified nitrogen-doped $TiO_2$ films was enhanced compared to that of undoped and non-stratified doped $TiO_2$ materials. Surprisingly, we found that these stratified nitrogen-doped materials did not affect their physical properties such as crystallinity. A possible explanation for this phenomenon was attributed an increase of charge carrier separation and mobility as charges move from the highly doped to undoped regions of the stratified films. Using APCVD we would like to assess the validity of this phenomenon by synthesising stratified $TiO_2$ thin films using a range of dopant sources, as well as investigating the design of heterojunction systems, to deliver robust self-cleaning surfaces with potential capabilities of water purification. We would also like to investigate upscalable routes to deliver low cost water splitting devices made by CVD methods.

## 7. References.


1. Thompson, T., Sobsey, M., Bartram, J. *International Journal of Enviromental Health Research*. **2003**, *13*, S89.
2. Richardson, S. D., Thruston Jr, A. D., Krasner, S. W., Weinberg, H. S., Miltner, R. J., Schenk, K. M., Narotsky, M. G., McKague, A. B., Simmons,J. E. *Journal of Toxicology and Enviromental Health, Part A*, **2008**, *71*, 1165.
3. Al-Karaghouli A., Kazmerski L. L. *Renewable and Sustainable Energy Reviews*, **2013**, *24*, 343.
4. Stackelberg, P. E., Furlong, E. T., Meyer, M. T., Zaugg, S. D., Henderson, A. K., Reissman, D. B. *Science of the Total Environment*, **2004**, *329*, 99.
5. Kim, J-S., Lee, C-H., Chang, I-S. *Water Research*, **2001**, *35*, 2137.
6. Le-clech, P., Chen, V., Fane, T. A. G. *Journal of Membrane Science*. **2006**, *284*, 17.
7. Comminellis, C. *Electrochimica Acta*, **1994**, *39*, 1857.
8. Tung, C-H., Shen, S-Y., Chang, J-H., Hsu, Y-M., Lai, Y-C. *Separation and Purification Technology*, **2013**, *117*, 131.
9. Deborde, M., von Gunten, U. Water Research, **2008**, *42*, 13.
10. Agustina, T. E., Ang, H. M., Vareek, V. K. *Journal of Photochemistry and Photobiology C: Photochemistry Reviews*. **2005**, *6*, 264.
11. Shon, H. K., Vigneswaran, S., Snyder, S. A. *Critical Reviews in Enviromental Science and Technology*, **2006**, *36*, 327.
12. Chong, M. N., Jin, B., Chow, C. W. K., Saint, C. *Water Research*, **2010**, *44*, 2997.
13. Wu, C-H., Chang, C-L. *Journal of Hazardous Materials B*, **2006**, *128*, 265.
14. Peternel, I. T., Koprivanac, N., Loncaric Bozic, A. M., Kusic, H. M. *Journal of Hazardous Materials*, **2007**, *148*, 477.
15. *Survey of Semiconductor Physics Surveyof Semiconductor Physics*.
16. Rothenberger, G., Moser, J., Gratzel, M., Serpone, N., Sharma, D. K. *Journal of the American Chemical Society*, **1985**, *107*, 8054.
17. Mills, A., Le Hunte, S. *Journal of Photochemistry and Photobiology A: Chemistry*, **1997**, *108*, 1.
18. Schwitzgebel, J., Ekerdt, G., Gerischer, H., Heller, A. *Journal of Physical Chemistry*, **1995**, *99*, 5633.
19. Pruden, A. L., Ollis, D. F. *Journal of Catalysis*, **1983**, *82*, 404.
20. Hsiao, C-Y., Lee, C-L., Ollis, D. F. *Journal of Catalysis*, **1983**, *82*, 418.
21. Goodeve, C. F., Kitchener, J. A. *Transactions of the Faraday Society*, **1938**, *34*, 570.
22. Fujishima, A., Rao, T. N., Tryk, D. A. *Journal of Photochemistry and Photobiology C: Photochemistry ReviewsI*, **2000**, *1*, 1.
23. Augustynski, J. *Electrochimica Acta*, **1993**, *38*, 43.
24. Fujishima, A., Zhang, X., Tryk, D. *Surf. Sci. Rep.*, **2008**, *63*, 515.
25. Zaleska, A. *Recent Patents on Engineering*, **2008**, *2*, 157.
26. Sun, Z., Kim, J. H., Zhao, Y., Bijarbooneh, F., Malgras, V., Lee, Y., Kang, Y-M., Dou, S. X. *Journal of the American Society*, **2011**, *133*, 19314.
27. Jin, B., Bang, H., Kamat, P. *Advanced Functional Materials*, **2010**, *20*, 1970.
28. Li, H., Bian, Z., Zhu, J., Huo, Y., Li, H., Lu, Y. *Journal of the American Society*, **2007**, *129*, 4538.
29. Tanaka, A., Nishino, Y., Sakaguchi, S., Yoshikawa, T., Imamura, K.,

Hashimoto, K., Kominami, H. *Chemical Communications*, **2013**, *49*, 2551.
30. Gratzel, M. *Journal of Photochemistry and Photobiology C: Photochemistry Reviews*, **2003**, *4*, 145.
31. Scanlon, D. O. *et al. Nature Materials*, **2013**, *12*, 798.
32. Quesada-Cabrera, R., Sotelo-Vazquez, C., Bear, J. C., Darr, J. A., Parkin, I. P. *Advanced Materials Interfaces*, **2014**, *1*, 1400069.
33. Moniz, S. J. A., Shevlin, S. A., Martin, D. J., Guo, Z.-X., Tang, J. *Energy Environmental Society*, **2015**, *8*, 731.
34. Di Valentin, C., Pacchioni, G., Selloni, A., Livraghi, S., Cozzi, V. R. *The Journal of Physical Chemistry B*, **2005**, *23*, 11414.
35. Emeline, A. V., Kuznetsov, V. N., Rybchuk, V. K., Serpone, N. *International Journal of Photoenergy*, 2008, 2008, 1.
36. Batzill, M., Morales, E., Diebold, U. *Physical Reviews Letters*, **2006**, *96*, 026103.
37. Serpone, N. *The Journal of Physical Chemistry B*, **2006**, *110*, 24287.
38. Wang, H. *et al*. *Chemical Society Reviews*, **2014**, *43*, 5234.
39. Di Fonzo, F., Casari, C. S., Russo, V., Brunella, M. F., Bassi, A. L. *Nanotechnology*, **2009**, *20*, 015604.
40. Ohno, T., Sarukawa, K., Tokieda, K., Matsumura, M. *Journal of Catalysis*, **2001**, *203*, 82.
41. Paracchino, A., Laporte, V., Sivula, K., Gratzel, M., Thimsen, E. *Nature Materials*, **2011**, *10*, 456.
42. Su, J., Guo, L., Bao, N., Grimes, C. A. *Nano Letters*, **2011**, *11*, 1928.
43. Moniz, S. J. A., Zhu, J., Tang, J. *Advanced Energy Materials*, **2014**, *4*, 1301590.
44. Wohler, F., U. L. *Liebigs Annalen*, **1855**, *94*, 255.
45. Aylsworth, J. W. *United States Patent* 553,296A **1896**.
46. De Lodyguine, A. *United States Patent* 575,002A **1897**.
47. Pilkington Brothers Ltd. , *Proceedings of the Royal Society of London Series A-Mathematical And Physical Sciences*, **1969**, *314*, 1.
48. Manasevit, H. M. *United States Patent* 4,368,098C **1983**.
49. Rai-Choudhury, P. *Journal of the Electrochemical Society*, **1969**, *116*, 1745.
50. Suntola, T., Antson, J. United States Patent 4,058,430A **1977**.
51. George, S. M. *Chemical Reviews*, **2010**,*110*, 111.
52. Neill, S. A. O., Clark, R. J. H., Parkin, I. P., Elliott, N., Mills, A. *Chemistry of Materials*, **2003**, *15*, 46.
53. Haga, K., Katahira, F., Watanabe, H. *Thin Solid Films*, **1999**, *343-344*, 145.
54. Hu, J., Gordon, R. G. *Solar Cells*, **1991**, *30*, 437.
55. Jensen, K. F., Graves, D. B. *Journal of the Electrochemical Society*, **1983**, *130*, 1950.
56. Potts, S. E. *et al. Organometallics*, **2009**, *28*, 1838.
57. Tabe, M. *Japanese Journal of Applied Physics*, **1982**, *21*, 534.
58. Cunningham, B., Chu, J. O., Akbar, S. *Applied Physics Letters*, **1991**, *59*, 3574.
59. Hou, B. X., Choy, K. *Chemical Vapour Deposition*, **2006**, *12*, 583. doi:10.1002/cvde.200600033
60. Knapp, C. E., Hyett, G., Parkin, I. P., Carmalt, C. J. *Chemistry of Materials*, **2011**, *23*, 1719.
61. Mungkalasiri, J., Bedel, L., Emieux, F., Dore, J., Renaud, F. N. R., Maury, F. *Surface & Coatings Technology*, **2009**, *204*, 887.
62. Silva, F., Hassouni, K., Bonnin, X., Gicquel, A. *Journal of Physics Condensed*

*Matter*, **2009**, *21*, 364202.
63. Zhang, Q., Yoon, S. F., Ahn, J., Gan, B., Yu, M-B. *Journal of Physics and Chemistry of Solids*, **2000**, *61*, 1179.
64. Huff, B. E., Moghadam, F. *United States Patent* 5,872,064A **1999**.
65. Hozumi, A., Takai, O. *Thin Solid Films*, **1997**, *303*, 222.
66. Haga, K., Kamidaira, M., Kashiwaba, Y., Sekiguchi, T., Watanabe, H. *Journal of Crystal Growth*, **2000**, *214/215*, 77.
67. Tsu, D. V., Lucovsky, G., Mantini, M. J. *Physical Review B*, **1986**, *33*, 7069.
68. Suresh, B. A., Anastasio, D., Burkey, D. *Chemical Vapour Deposition*, **2014**, *20*, 5.
69. Shaughnessy, W. S. O., Baxamusa, S., Gleason, K. K. *Chemistry of Materials*, **2007**, *19*, 5836.
70. Jones, A., Hitchman, M., Krumdieck, S. Chemical Vapour Deposition. Jones, A., Hitchman, M. editors. *Royal Society of Chemistry*, **2009**.
71. Choy, K. L. *Progress in Materials Science*, **2003**, *48*, 57.
72. Kodas, T. T., Hampden-Smith, M.Aerosol Processing of Materials. *Wiley-VCH:New York*, **1999**.
73. Page, K., Palgrave, R. G., Parkin, I. P., Wilson, M., Savin, S. L. P., Chadwick, A. V. *Journal Materials Chemistry*, **2006**, *17*, 95.
74. Kafizas, A., Dunnill, C. W., Parkin, I. P. *Journal of Materials Chemistry*, **2010**, *20*, 8336.
75. Dunnill, C. W. H., Aiken, Z. A., Pratten, J., Wilson, M., Morgan, D. J., Parkin, I. P. *Journal of Photochemistry and Photobiology A: Chemistry*, **2009**, *207* 244.
76. Korosi, L., Oszko, A., Galbacs, G., Richardt, A., Zollmer, V., Dekany, I. *Applied Catalysis B: Environmental*, **2007**, *77*, 175.
77. Asahi, R., Morikawa, T., Irie, H., Ohwaki, T. *Chemical Reviews*, **2014**, *114*, 9824.
78. Thompson, T. L., Yates, J. T. *Chemical Reviews*, **2006**, *106*, 4428.
79. Pelaez, M. *et al. Applied Catalysis B: Environmental*, **2012**, *125*, 331.
80. Taga, Y. *Thin Solid Films*, **2009**, *517*, 3167.
81. Paz, Y. *Applied Catalysis B: Environmental*, **2010**, *99*, 448.
82. Viswanathan, B., Krishanmurthy, K. R. *International Journal of Photoenergy*, **2012**, *2012*, 1.
83. Asahi, R., Morikawa, T. *Chemical Physics*, **2007**, *339*, 57.
84. Saha, N. C., Tompkins, H. G. *Journal of Applied Physics*, **1992**, *72*, 3072.
85. Swanepoel, R. *Journal of Physics E: Scientific Instruments*, **1983**, *16*, 1214.
86. Tauc, J. *Materials Research Bulletin*, **1968**, *3*, 37.
87. Mills, A., Wang, J. *Journal of Photochemistry and Photobiology A: Chemistry*, **2006**, *182*, 181.
88. Asahi, R., Morikawa, T., Ohwaki, T., Aoki, K., Taga, Y. S*cience*, **2001**, *293*, 269.
89. Morikawa, T., Asahi, R., Ohwaki, T., Aoki, K., Taga, Y. *Japanese Journal of Applied Physics*, **2001**, *40*, 561.
90. Kafizas, A., Crick, C., Parkin, I. P. *Journal of Photochemistry and Photobiology A: Chemistry*, **2010**, *216*, 156.
91. Diwald, O., Thompson, T. L., Zubkov, T., Walck, S. D., Yates, J. T. *The Journal of Physical Chemistry B*, **2004**, *108*, 6004.
92. Ihara, T., Miyoshi, M., Ando, M., Sugihara, S., Iriyama, Y. *Journal of Materials Science*, **2001**, *36*, 4201.

93. Balcerski, W., Ryu, S. Y., Hoffmann, M. R. *The Journal of Physical Chemistry C*, **2007**, *111*, 15357.
94. Nosaka, Y., Matsushita, M., Nishino, J., Nosaka, A. Y. *Science and Technology of Advanced Materials*, **2005**, 6, 143.
95. Maeda, M., Watanabe, T. *Journal of the Electrochemical Society*, **2006**, *153*, C186.
96. Miyauchi, M., Ikezawa, A., Tobimatsu, H., Irie, H., Hashimoto, K. *Physical Chemistry Chemical Physics*, **2004**, *6*, 865.
97. Mittal, K. L. *Electrocomponents Science and Technology*, **1976**, *3*, 21.
98. Butler, D. W., Stoddart, C. T. H., Stuart, P. R. *Journal of Physics D: Applied Physics*, **1969**, *3*, 877.
99. Yates, H. M., Nolan, M. G., Sheel, D. W., Pemble, M. E. *Journal of Photochemistry and Photobiology A: Chemistry*, **2006**, *179*, 213.
100. Serpone, N., Lawless, D., Khairutdinov, R. *The Journal of Physical Chemistry*, **1995**, *99*, 16646.
101. Lin, Z., Orlov, A., Lambert, R. M., Payne, M. C. *The Journal of Physical Chemistry B*, **2005**, *109*, 20948.
102. Peng, F., Cai, L., Yu, H., Wang, H., Yang, J. *Journal of Solid State Chemistry*, **2008**, *181*, 130.
103. Ananpattarachai, J., Kajitvichyanukul, P., Seraphin, S. *Journal of Hazardous Materials*, **2009**, *168*, 253.
104. Kuznetsov, V. N., Serpone, N. *The Journal of Physical Chemistry C*, **2009**, *113*, 15110.
105. Wu, P., Ma, C., Shang, J. *Applied Physics A Materials Science & Processing*, **2005**, *81*, 1411.
106. Rodriguez, J. A., Jirsak, T., Liu, G., Hrbeck, J., Dvorak, J., Maiti, A. *Journal of the American Chemical Society*, **2001**, *123*, 9597.
107. Mills, A., Wang, J. *Journal of Photochemistry and Photobiology A: Chemistry*, **1998**, *118*, 53.
108. Ohno, T., Mitsui, T., Matsumura, M. *Chemistry Letters*, **2003**, *32*, 364.
109. Shishido, T., Teramura, K., Tanaka, T. *Catalalysis Survey from Asia*, **2011**, *15*, 240.
110. Hao, E. *et al. Journal of Materials Chemistry*, **1998**, *8*, 1327.
111. Robel, I., Subramanian, V., Kuno, M., Kamat, P. V. *Journal of the American Chemical Society*, **2006**, *128*, 2385.
112. Vinodgopal, K., Wynkoop, D. E., Kamat, P. V. *Environmental Science and Technology*, **1996**, *30*, 1660.
113. Fujishima, A., Zhang, X. *Comptes Rendus Chimie*, **2006**, *9*, 750.
114. Wu, G., Nishikawa, T., Ohtani, B., Chen, A. *Chemistry of Materials*, **2007**, *19*, 4530.
115. Ni, M., Leung, M. K. H., Leung, D. Y. C., Sumathy, K.*Renewable and Sustainable Energy Reviews*, **2007**, *11*, 401.
116. Han, K. S., Lee, J. W., Kang, Y. M., Lee, J. Y., Kang, J. K. *Small*, **2008**, *4*, 1682.
117. Cao, J., Zhang, Y., Tong, H., Li, P., Kako, T., Ye, J. *Chemical. Communications*, **2012**, *48*, 8649.
118. Cao, J., Zhang, Y., Liu, L., Ye, J. *Chemical. Communications*, **2013**, *49*, 3440.
119. Tao, J., Yang, M., Chai, J. W., Pan, J. S., Feng, Y. P., Wang, S. J. *The Journal of Physical Chemistry C*, **2014**, *118*, 994.
120. Jung, Y. S. *et al. Advanced Materials*, **2010**, *22*, 2172.

121. Li, L., Rohrer, G. S., Salvador, P. A. *Journal of the American Ceramic Society*, **2012**, *95*, 1414.
122. Seo, H. O. *et al. The Journal of Physical Chemistry C*, **2011**, *115*, 21517.
123. Shim, W. H. *et al. Advance Materials*, **2011**, *23*, 519.
124. Finazzi, E., Di Valentin, C., Selloni, A., Pacchioni, G. *The Journal of Physical Chemistry C*, **2007**, *111*, 9275.
125. Okato, T., Sakano, T., Obara, M. *Physical Review B*, **2005**, *72*, 115124.
126. Cheung, S. H., Nachimuthu, P., Engelhard, M. H., Wang, C. M., Chambers, S. A. *Surface Science*, **2008**, *602*, 133.
127. Irie, H., Watanabe, Y., Hashimoto, K. *The Journal of Physical Chemistry B*, **2003**, *107*, 5483.
128. Emeline, A. V., Frolov, A. V., Ryabchuk, V. K., Serpone, N. *The Journal of Physical Chemistry B*, **2003**, *107*, 7109.
129. Tang, H., Prasad, K., Sanjinès, R., Schmid, P. E., Lévy, F. *Journal of Applied Physics*, **1994**, *75*, 2042.
130. Quesada-Cabrera, R., Sotelo-Vazquez, C., Darr, J. A., Parkin, I. P. *Applied Catalysis B: Environmental*, **2014**, *160-161*, 582.
131. Wang, Y., Wang, Y., Meng, Y., Ding, H., Shan, Y., Zhao, X., Tang, X. *The Journal of Physical Chemistry C*, **2008**, *112*, 6620.
132. Yang, K., Dai, Y., Huang, B., Whangbo, M-H. *The Journal of Physical Chemistry C*, **2009**, *113*, 2624.
133. Sun, H., Bai, Y., Cheng, Y., Jin, W., Xu, N. *Industrial and Engineering Chemistry Research*, **2006**, *45*, 4971.
134. Yang, K., Dai, Y., Huang, B. *The Journal of Physical Chemistry C*, **2007**, *111*, 18985.
135. Cowan, A. J., Tang, J., Leng, W., Durrant, J. R., Klug, D. R. *The Journal of Physical Chemistry C*, **2010**, *114*, 4208.
136. Kafizas, A., Kellici, S., Darr, J. A., Parkin, I. P. *Journal of Photochemistry and Photobiology A: Chemistry*, **2009**, *204*, 183.
137. Zhang, J., Wu, Y., Xing, M., Leghari, S. A. K., Sajjad, S. *Energy and Environmental Science*, **2010**, *3*, 715.
138. Asahi, R., Morikawa, T., Hazama, H., Matsubara, M. *Journal of Physics Condensed Matter*, **2008**, *20*, 064227.
139. Hitosugi, T., Yamada, N., Nakao, S., Hirose, Y., Hasegawa, T. *Physica Status Solidi (a)*, **2010**, *207*, 1529.
140. Kafizas, A., Noor, N., Carmichael, P., Scanlon, D. O., Carmalt, C. J., Parkin, I. P. *Advanced Functional Materials*, **2014**, *24*, 1758.
141. Bhachu, D. S. *et al. Advanced Functional Materials*, *24*, 5075.
142. Gillispie, M. A., van Hest, M. F. A. M., Dabney, M. S., Perkins, J. D., Ginley, D. S. *Journal of Materials Research*, **2011**, *22*, 2832.
143. Kafizas, A., Noor, N., Carmalt, C. J., Parkin, I. P. *Journal of Materials Chemistry C*, **2013**, 1, 6335.
144. Yu, J. C., Zhang, L., Zheng, Z., Zhao, J. *Chemistry of Materials*, **2003**, *15*, 2280.
145. Li, F., Jiang, Y., Xia, M., Sun, M., Xue, B., Liu, D., Zhang, X. *The Journal of Physical Chemistry C*, **2009**, *113*, 18134.
146. Korosi, L., Papp, S., Bertoti, I., Dekany, I. *Chemistry of Materials*, **2007**, *19*, 4811.
147. Gopal, N. O. *et al. The Journal of Physical Chemistry C*, **2012**, *116*, 16191.
148. Evans, P., Pemble, M. E., Sheel, D. W. *Chemistry of Materials*, **2007**, *18*, 5750.

149. Kafizas, A., Parkin, I. P. *Journal of the American Chemical Society*, **2011**, *133*, 20458.
150. Powell, C. J., Jablonski, A., Tilinin, I. S., Tanuma, S., Penn, D. R. *Journal of Electron Spectroscopy and Related Phenomena*, **1999**, *98-99*, 1.
151. Splinter, S. J., Rofagha, R., McIntyre, N. S., Erb, U. *Surface and Interface Analysis*, **1996**, *24*, 181.
152. Blackman, C., Carmalt, C. J., Parkin, I. P., O'Neill, S. *Chemistry of Materials*, **2002**, *14*, 3167.
153. Myers, C. E., Franzen, H. F., Anderegg, J. W. *Inorganic Chemistry*, **1989**, *24*, 1822.
154. Seah, M. P. *Surface and Interface Analysis*, **1980**, *2*, 222.
155. Lin, L., Lin, W., Xie, J. L., Zhu, Y. X., Zhao, B. Y., Xie, Y. C. *Applied Catalysis B: Environmental*, **2007**, *75*, 52.
156. Hyett, G., Green, M., Parkin, I. P. *Journal of the American Chemical Society*, **2006**, *128*, 12147.
157. Ohsaka, T., Izumi, F., Fujiki, Y. *Journal of Raman Spectroscopy*, **19789**, *7*, 321.
158. Pesci, F. M., Cowan, A. J., Alexander, B. D., Durrant, J. R., Klug, D. R. *The Journal of Physical Chemistry Letters*, **2011**, *2*, 1900.
159. Pendlebury, S. R., Wang, X., Le Formal, F., Cornuz, M., Kafizas, A., Tilley, S. D., Gratzel, M., Durrant, J. R. *Journal of the American Chemical Society*, **2014**, *136*, 9854.
160. Ma, Y., Pendlebury, S. R., Reynal, A., Le Formal, F., Durrant, J. R. *Chemical Science*, **2014**, *5*, 2964.
161. Peiro, A. M., Colombo, C., Doyle, G., Nelson, J., Mills, A., Durrant, J. R. *The Journal of Physical Chemistry B*, **2006**, *110*, 23255.
162. Devahasdin, S., Fan, C., Li, K., Chen, D. H. *Journal of Photochemistry and Photobiology A: Chemistry*, **2003**, *156*, 161.
163. Tang, J., Durrant, J. R., Klug, D. R. *Journal of the American Chemical Society*, **2008**, *130*, 13885.
164. Kafizas, A., Parkin, I. P. *Journal of Materials Chemistry*, **2010**, *20*, 2157.
165. Yamakata, A., Ishibashi, T., Onishi, H. *The Journal of Physical Chemistry B*, **2001**, *105*, 7258.
166. Zhang, Q., Wang, J., Yin, S., Sato, T., Saito, F. *Journal of the American Ceramic Society*, **2004**, *87*, 1161.
167. Umebayashi, T., Yamaki, T., Yamamoto, S., Miyashita, A., Tanaka, S., Sumita, T., Asai, K. *Journal of Applied Physics*, **2003**, *93*, 5156.
168. Pore, V., Ritala, M. & Leskela, M., Areva, S., Jarn, M., Jarnstrom, J. *Journal of Materials Chemistry*, **2007**, *17*, 1361.
169. Takeshita, K., Yamakata, A., Ishibashi, T., Onishi, H., Nishijima, K., Ohno, T. *Journal of Photochemistry and Photobiology A: Chemistry*, **2006**, *177*, 269.
170. Dunnill, C. W., Aiken, Z. A., Kafizas, A., Pratten, J., Wilson, M., Morgan, D. J., Parkin, I. P. *Journal of Materials Chemistry*, **2009**, *19*, 8747.
171. Tang, X., Li, D. *The Journal of Physical Chemistry C*, **2008**, *112*, 5405.
172. Ho, W., Yu, Y. C., Lee, S. *Journal of Solid State Chmistry*, **2006**, *179*, 1175.
174. Umebayashi, T., Yamaki, T., Tanaka, S., Asai, K. *Chemistry Letters*, **2003**, *32*, 330.
175. Sabyrov, K., Burrows, N. D., Penn, R. L. *Chemistry of Materials*, **2013**, *25*, 1408.
176. Hidalgo, M. C., Maicu, M., Navio, J. A., Colon, G. *The Journal of Physical.*

*Chemistry C*, **2009**, *113*, 12840.
177. Ohno, T., Akiyoshi, M., Umebayashi, T., Asai, K., Mitsui, T., Matsumura, M. *Applied Catalysis A: General*, **2004**, *265*, 115.
178. Hebenstreit, E. L. D., Hebenstreit, W., Diebold, U. *Surface Science*, **2001**, *470*, 347.
179. Gonbeau, D., Guimon, C., Pfister-Guillouzo, G., Levasseur, A., Meunier, G., Dormoy, R. *Surface Science*, **1991**, *254*, 81.
180. Tachikawa, T. *et al. The Journal of Physical Chemistry B*, **2004**, *108*, 19299.
181. Tanaka, K., Capule, M. F. V., Hisanaga, T. *Chemical Physics Letters*, **1991**, *187*, 73.
182. Wang, X., Yu, J. C., Liu, P., Wang, X., Su, W., Fu, X. *Journal of Photochemistry and Photobiology A: Chemistry*, **2006**, *179*, 339.
183. Hurum, D. C., Agrios, A. G., Gray, K. A., Rajh, T., Thurnauer, M. C. *The Journal of Physical Chemistry B*, **2003**, *107*, 4545.
184. Li, G., Gray, K. A. *Chemical Physics*, **2007**, *339*, 173.
185. Kumar, S. G., Devi, L. G. *The Journal of Physical Chemistry A*, **2011**, *115*, 13211.
186. Paz, Y., Luo, Z., Rabenberg, L., Heller, A. *Journal of Materials Research*, **1995**, *10*, 2842.
187. Ollis, D. *Applied Catalysis B: Environmental*, **2010**, *99*, 478.
188. Sawunyama, P., Fujishima, A., Hashimoto, K. *Langmuir*, **1999**, *15*, 3551.
189. Kafizas, A., Carmalt, C. J., Parkin, I. P. *Chemistry - A European Journal*, **2012**, *18*, 13048.
190. Ohtani, B., Ogawa, Y., Nishimoto, S.*The Journal of Physical Chemistry B*, **1997**, *101*, 3746.
191. Ohtani, B. *Chemistry Letters*, **2008**, *37*, 216.
192. Deskins, N. A., Kerisit, S., Rosso, K. M., Dupuis, M. *The Journal of Physical Chemistry C*, **2007**, *111*, 9290.
193. Penn, R. L., Banfield, J. F. *American Mineralogist*, **1999**, *84*, 871.
194. Hoffmann, M. R., Martin, S. T., Choi, W., Bahnemannt, D. W. *Chemical Reviews*, **1995**, *95*, 69.
195. Torimoto, T., Nakamura, N., Ikeda, S., Ohtani, B. *Physical Chemistry Chemical Physics*, **2002**, *4*, 5910.
196. Mohamed, H. H., Bahnemann, D. W. *Applied Catalysis B: Environmental*, **2012**, *128*, 91.
197. Farneth, W. E., Mclean, R. S., Bolt, J. D., Dokou, E., Barteau, M. A. *Langmuir*, **1999**, *15*, 8569.
198. Kawahara, T., Konishi, Y., Tada, H., Tohge, N., Nishii, J., Ito, S. *Angewandte Chemie*, **2002**, *114*, 2935.
199. Zhu, L., Fu Tan, C., Gao, M., Ho, G. W. *Advanced Materials*, **2015**, *27*, 7713.
200. Sun, B., Smirniotis, P. G. *Catalysis Today*, **2003**, *88*, 49.
201. Liu, Y., Tang, A., Zhang, Q., Yin, Y. *Journal of the American Chemical Society*, **2015**, *137*, 11327.
202. Crick, C. R., Bear, J. C., Kafizas, A., Parkin, I. P. *Advanced Materials*, **2012**, *24*, 3505.
203. Miyauchi, M., Nakajima, A., Watanabe, T., Hashimoto, K. *Chemistry of Materials*, **2002**, *14*, 4714.
204. Smith, W., Wolcott, A., Fitzmorris, R. C., Zhang, J. Z., Zhao, Y. *Journal of Materials Chemistry*, **2011**, *21*, 10792.
205. Higashimoto, S., Sakiyama, M., Azuma, M. *Thin Solid Films*, **2006**, *503*, 201.

206. Kresse, G., Hafner, J. *Physical Review B*, **1993**, *47*, 558.
207. Kresse, G., Hafner, J. *Physical Review B*, **1994**, *49*, 14251.
208. Kresse, G., Furthmuller, J. *Physical Review B*, **1996**, *54*, 11169.
209. Kresse, G., Furthmiiller, J. *Computational Materials Science*, **1996**, *6*, 15.
210. Kresse, G., Joubert, D. *Physical Review B*, **1999**, *59*, 11.
211. Krukau, A. V., Vydrov, O. A., Izmaylov, A. F., Scuseria, G. E. *The Journal of Chemical Physics*, **2007**, *125*, 224106**.**
212. Burton, L. A., Walsh, A., *Applied Physics Letters*, **2013**, *102*, 132111.
213. Oliver, P. M., Parker, S. C., Egdell, R. G., Jones, F. H. *Journal of the Chemical Society, Faraday Transactions*, **1996**, *92*, 2049.
214. Watson, G. W., Kelsey, E. T., Leeuw, N. H. De, Harris, D. J., Parker, S. C. *Journal of the Chemical Society, Faraday Transactions*, **1996**, *92*, 433.
215. Mills, A., Worsley, D., Davies, R. H. *Journal of the Chemical Society: Chemical Communications*, **1994**, 2677.
216. Smith, A. M., Kast, M. G., Nail, B., Aloni, S., Boettcher, S. *Journal of Materials Chemistry A*, **2014**, *2*, 6121.
217. Ling, M., Blackman, C. *Physica Status Solidi (a)*, **2015**, *12*, 869.
218. Hinuma, Y., Gruneis, A., Kresse, G., Oba, F. *Physical Review B*, **2014**, *90*. 155405.
219. Buckeridge, J. *et al. Chemistry of Materials*, **2015**, *27*, 3844.
220. Ganose, A. M., Butler, K. T., Walsh, A., Scanlon, D. O. *Journal of Materials Chemistry A*, **2016**, *4*, 2060.
221. Weinhardt, L., Blum, M., Bar, M., Heske, C., Cole, B., Marsen, B., Miller, E. L. *The Journal of Physical Chemsitry C*, **2008**, *112*, 3078.
222. Anderson, R. L. *IBM Journal of Research and Development*, **1960**, *4*, 283.
223. Ohtani, B., Prieto-Mahaney, O. O., Li, D., Abe, R. *Journal of Photochemistry and Photobiology A: Chemistry*, **2010**, *216*, 179.
224. Mills, A., Lepre, A., Elliott, N., Bhopal, S., Parkin, I. P., O'Neill, S. A. *Journal of Photochemistry and Photobiology A: Chemistry*, **2003**, *160*, 213.
225. Chatchai, P., Murakami, Y., Kishioka, S., Nosaka, A. Y., Nosaka, Y. *Electrochimica Acta*, **2009**, *54*, 1147.
226. Lu, B., Li, X., Wang, T., Xie, E., Xu, Z. *Journal of Materials Chemistry A*, **2013**, *1*, 3900.
227. Quesada-Cabrera, R. Q., Latimer, E. R., Kafizas, A., Blackman, C. S., Carmalt, C. J., Parkin, I. P. *Journal of Photochemistry and Photobiology A: Chemistry*, **2012**, *239*, 60.
228. Irie, H., Mori, H., Hashimoto, K. *Vacuum*, **2004**, *74*, 625.
229. Siripala, W., Ivanovskaya, A., Jaramillo, T. F., Baeck, S-H., McFarland, E. W. *Solar Energy Materials and Solar Cells*, **2003**, *77*, 229.
230. Kim, E. S. *et al. Journal of the American Chemical Society*, **2013**, *135*, 5375.
231. Martha, S., Das, D. P., Biswal, N., PArida, K. M. *Journal of Materials Chemistry*, **2012**, *22*, 10695.
232. Lai, Y., Lin, Z., Chen, Z., Huang, J., Lin, C. *Materials Letters*, **2010**, *64*, 1309.
233. Ng, B. J., Xu, S., Zhang, X., Yang, H. Y., Sun, D. D. *Advanced Functional Materials*, **2010**, *20*, 4287.
234. Liu, Y., Yu, Y-X., Zhang, W-D. *The Journal of Physical Chemistry C*, **2013**, *117*, 12949..
235. Xu, Q. C. *et al. Chemical Commouncations*, **2011**, *47*, 8641.
236. Cao, Y. *et al. Chemistry of Materials*, **2000**, *12*, 3445.
237. Zhang, J., Zhu, H., Zheng, S., Pan, F., Wang, T. *ACS Applied Materials and*

*Interfaces*, *1*, 2111.
238. Liu, Z., Sun, D. D., Guo, P., Leckie, J. O. *Nano Letters*, **2007**, *7*, 1081.
239. Shchukin, D., Poznyak, S., Kulak, A., Pichat, P. *Journal of Photochemistry and Photobiology A: Chemistry*, **2004**, *162*, 423.
240. Alessandri, I., Zucca, M., Ferroni, M., Bontempi, E., Depero, L. E. *Small*, **2009**, *5*, 336.
241. Shaheen, B. S., Salem, H. G., El-Sayed, M. A., Allam, N. K. Thermal *The Journal of Physical Chemistry C*, **2013**, *117*, 18502.
242. He, H., Berglund, S. P., Xiao, P., Chemelewski, W. D., Zhang, Y., Mullins, C. B. *Journal of Materials Chemistry A*, **2013**, *1*, 12826.
243. Jeng, J. *et al. Advanced Materials*, **2013**, *25*, 3727.